High harmonic generation with high energy femtosecond pulses

Ondřej Hort

université de BORDEAUX

THÈSE PRÉSENTÉE

POUR OBTENIR LE GRADE DE

DOCTEUR DE L'UNIVERSITÉ DE BORDEAUX

ÉCOLE DOCTORALE DES SCIENCES PHYSIQUES ET DE L'INGÉNIEUR

SPÉCIALITÉ LASERS, MATIÈRE ET NANOSCIENCES

Par Ondřej HORT

HIGH HARMONIC GENERATION WITH HIGH ENERGY FEMTOSECOND PULSES

Sous la direction de : Éric CONSTANT

Soutenue le 30 avril 2014

Membres du jury :

Président :	M. Philippe Tamarat	Professeur des universités, Université de Bordeaux
Rapporteurs :	M. Bertrand Carré	Directeur de recherche CEA Saclay
	M. Stéphane Sebban	Directeur de recherche CNRS, LOA
Examinateurs :	M. Gilles Chériaux	Ingénieur de recherche CNRS, LULI
	M. Íñigo Sola	Maître de conférences, Universidad de Salamanca
	Mme. Amelle Zair	Chargé de recherche EPSRC, Imperial College
Directeur de thèse :	M. Éric Constant	Directeur de recherche CNRS, CELIA

Résumé

Nous présentons nos travaux sur la génération d'harmoniques élevée (HHG) avec des impulsions térawatt femtosecondes. Nous avons effectué l'HHG avec les impulsions fondamentales de haute énergie et caractérisé l'émission de XUV spatialement et spectralement de manière monocoup et nous avons observé plusieurs structures dans le champ lointain. Ces structures sont très robustes et reproductibles et ont été observés dans de nombreux types de gaz et des géométries de génération. Sans caractérisation monocoup spatiale et spectrale les structures ne sont pas visibles. Nous avons développé des simulations simples pour identifier ces structures et nous avons pu observer des structures similaires. Nous les avons identifiés comme étant liées à la cohérence spatiale de la source XUV et la diffraction dans le champ lointain. Dans le champ proche, la phase et l'amplitude harmonique évoluent spatialement et temporellement et leurs profils sont fortement modulés. Ces profils modulés diffractent et créent des spectres structurés dans le champ lointain. Nous avons observé que la propagation dans un milieu générateur fin a peu d'influence sur les structures. Nous démontrons une mise en forme spatiale de l'impulsion fondamentale via l'optique adaptative et leur avantage pour HHG. Une optique adaptative nous permet d'avoir un faisceau à profil de phase régulier. Un tel faisceau est utilisé pour HHG avec un faisceau de grand diamètre et contrôle du faisceau XUV est démontrée. Nous avons développé une technique de post-compression de haute énergie, et nous avons obtenu des impulsions de 10 fs et 10 mJ dans un profil quasi gaussien. La technique repose sur l'automodulation de phase induite par l'ionisation et est compatible avec des impulsions niveau TW de haute énergie. Nous avons effectué des HHG avec ces impulsions et obtenu des spectres XUV quasi continu avec des structures spatiales et spectrales. Nous avons effectué des simulations simples et des simulations de SFA et nous avons observé des structures similaires même sans prendre en compte la propagation dans le milieu.

Mot clés : Génération d'harmoniques d'ordres élevés, Lasers femtosecondes, Impulsions attosecondes, Post-compression par ionisation, Structures XUV spatiales et spectrales

---

Abstract

We present our work on high harmonic generation with TW femtosecond pulses. We performed HHG with high energy femtosecond pulses and characterize the generated XUV emission spatially and spectrally at the single-shot basis and we observed many structures in spatially resolved XUV spectra in the far field. Those structures are very robust and reproducible and have been observed in many different gases and generation geometries. Without spatial and spectral characterization on the single-shot basis the structures are not visible. We developed simple simulations to identify those structures and we observed similar structures as experimentally. We identified them as a result of spatial coherence of the XUV source and the diffraction to the far field. In the near field, the harmonic amplitude and phase are spatially and temporally dependent and their profiles are strongly modulated. Such modulated profiles diffract to structured spatially resolved spectra in the far field. We observed that propagation of the XUV in the generating medium has little influence on the structures. We demonstrate spatial shaping of the driving pulses via adaptive optics and their advantage for HHG. An adaptive optics allows us to have the driving beam of regular spatial profile and phase even out of focus. Such a beam is used for HHG with a large diameter driving beam and control of the XUV beam is demonstrated. We developed a high energy TW post-compression technique and we obtained pulses of 10 fs and 10 mJ in a quasi-Gaussian spatial profile. The technique is based on ionization-induced self-phase-modulation and is compatible with high energy TW level pulses. We performed HHG with such TW pulses and obtained XUV quasi-continuum spectra with spectral and spatial structures. We performed simple simulations and SFA simulations and we observed similar structures even without considering the XUV propagation in the medium.

Keywords: High harmonic generation, Femtosecond lasers, Attosecond pulses, Ionization-induced post-compression, Spatial and spectral XUV structures

---

CELIA

Centre Lasers Intenses et Applications - UMR 5107

Résumé en français

La génération d'harmoniques d'ordres élevés (HHG) conduit à la génération des impulsions XUV attosecondes. Bien qu'il y ait nombreux usages scientifiques de cette source de lumière, une large diffusion des applications XUV est limitée par la faible énergie portée par ces impulsions XUV. La principale raison est le rendement de conversion faible du processus HHG. De nos jours, il y a beaucoup d'efforts pour produire des impulsions attosecondes haute énergie et nous avons poursuivi ce but en utilisant des lasers de forte énergie (lasers térawatt (TW).)

Dans ce travail, nous présentons des progrès scientifiques pour la génération d'impulsions attosecondes isolés de haute énergie. Notre principale motivation est de trouver comment générer des impulsions XUV attosecondes de haute énergie avec des impulsions femtosecondes infrarouges de haute énergie.

Nous présentons des HHG expérimentales obtenus avec des impulsions femtosecondes de haute énergie et nous mettons au point une simulation simple pour identifier les phénomènes physiques importants. Nous démontrons deux techniques de mise en forme spatiale des impulsions fondamentales et leur avantage pour HHG (masque de phase pour profil flat top et miroir déformable). Nous présentons également une nouvelle technique de post-compression haute énergie qui donne des impulsions de 10 fs et 10 mJ et nous permet de générer des harmoniques avec ces impulsions.

Nous disposons d'une chaîne de laser CPA Ti : Saphir qui délivre des impulsions de 75 mJ sur 55 fs centrée à 810 nm au taux de répétition de 10 Hz. Nous caractérisons les émissions XUV générée spatialement et spectralement avec un spectromètre XUV de champ plat équipé de MCP (40 mm diamètre) et nous estimons le nombre de photon XUV utilisant une photodiode XUV. Nous nous concentrons principalement sur les harmoniques de plateau car ils contiennent plus de photons que les harmoniques de coupure et la résolution du spectromètre est plus élevée pour les plus basses énergies de photon.

Notre installation permet d'obtenir des spectres XUV résolus spatialement de manière monocoup. Nous montrons qu'il s'agit d'une condition nécessaire pour observer de nombreuses structures dans les spectres XUV résolues spatialement dans le champ lointain. Ces

structures sont très robustes et reproductibles et ont été observés dans de nombreux types de gaz et des géométries de génération. Sans caractérisation spatiale et spectrale monocoup les structures ne sont pas visibles.

À haute énergie d'impulsions fondamentales, nous avons observé que la génération d'harmoniques dans un jet de gaz avec une très courte longueur de milieu maximise le nombre de photons XUV par rapport à la cellule de gaz et capillaire rempli de gaz. Les structures complexes sont généralement observées en régime de forte intensité.

Nous avons développé des simulations simplifiées pour identifier ces structures et nous avons observé des structures similaires. Nous les avons identifiés comme étant liées à la cohérence spatiale de la source XUV et la diffraction dans le champ lointain.

Dans le champ proche, la phase et amplitude harmonique varient spatialement et temporellement et leurs profils sont fortement modulés. Cette modulation provient surtout de la dépendance non linéaire de l'amplitude et la phase du dipôle harmonique sur intensité infrarouge. C'est pourquoi l'émission XUV qui en résulte est modulée dans l'espace, temps et fréquence. Aux intensités infrarouges très élevées la déplétion de l'état fondamental des émetteurs a également un fort impact sur la distribution spatiale et temporelle du dipôle harmonique dans le champ proche c'est-à-dire dans le milieu générateur.

Un profil spatio-spectral modulé dans le champ proche diffracte pour donner des profils structurés dans le champ lointain. Ces structures sont pour la plupart identifiés comme des interférences du chemin court avec lui-même par alfadIIR/dt et la déplétion de l'état fondamental des atomes dans le milieu générateur. En cas de forte intensité infrarouge le chemin long est généralement trop divergent et sa contribution au signal détecté est très faible. Nous avons observé que la propagation de la XUV dans le milieu générateur a peu d'influence sur les structures.

Nous simulons l'HHG en faisant varier des paramètres contrôlables expérimentalement et donnons les spectres expérimentaux correspondants. Il y a un bon accord entre nos simulations et les résultats expérimentaux.

Une structure expérimentalement détectée, appelé Red-Shifted Structure (RSS), a été expliquée comme due à la présence d'une pré-impulsion décalée spectralement vers le rouge.

En collaboration avec LPGP, nous avons effectué HHG dans capillaires remplis d'argon. Nous avons observé des harmoniques spectralement larges et décalées vers le bleu. L'ordre harmonique généré maximal était plus élevé que dans le cas du jet de gaz. Nous avons trouvé ce genre de source XUV bien adapté pour être injecté dans des amplificateurs de rayonnement X.

Comme nous avons observé une forte influence du profil spatial du faisceau sur la génération des harmoniques, nous avons développé une mise en forme spatiale d'un faisceau fondamental compatible avec impulsions femtosecondes de haute énergie.

Une optique adaptative nous permet d'avoir le faisceau à profil de phase régulier encore loin du foyer. Aux termes de la collaboration industrielle, nous avons développé un miroir déformable compatible avec impulsions femtosecondes de haute énergie. Nous avons corrigé notre faisceau. Les structures XUV dans le champ lointain étaient alors encore plus régulières. HHG était également réalisé loin du foyer et structures spatio-spectral très nettes ont été observés.

À l'aide de miroir déformable nous contrôlons directement la forme spatiale c'est-à-dire la phase spatiale du faisceau infrarouge et donc aussi la phase spatiale de la XUV du faisceau. Nous avons démontré cette possibilité prometteuse du contrôle XUV avec le faisceau infrarouge contenant une aberration contrôlée.

Différents profils spatiaux du faisceau peuvent être obtenus via un masque de phase. Un masque de phase réfléchissant est préférable d'éviter les effets non linéaires. Nous utilisons un miroir sphérique avec une marche épais de 200 nm dans le centre, appelé Two-Optical Paths (TOP) mirror. Cette technique permet d'obtenir un profil plat du faisceau dans le foyer. L'intérêt est double. Le foyer est plus grand que dans le cas de faisceau gaussien permettant l'utilisation des impulsions d'énergie plus élevées et l'émission XUV est confinée dans le temps. Cela signifie que le XUV est généré en même temps dans tout le diamètre de faisceau fondamental. Ce confinement est compatible avec la diffraction dans le champ lointain et nous montrons théoriquement que générer des harmoniques à l'aide de faisceau a profil plat de forte intensité avec des impulsions de 10 fs entraîne seulement 2 impulsions attosecondes ou même seulement à 1 impulsion lorsqu'on considère la propagation.

Comme les impulsions de 55 fs sont trop longues pour confiner le HHG même à très haute intensité, nous avons développé une technique de post-compression de haute énergie et nous avons obtenu des impulsions de 10 fs et 10 mJ dans un profil spatial quasi gaussien. La technique est basée sur auto modulation de phase induite par l'ionisation qui élargit le spectre des impulsions femtosecondes de haute intensité.

La dynamique de l'ionisation rapide provoque un décalage significatif vers le bleu de la longueur d'onde centrale. Le processus peut s'expliquer par l'indice de réfraction linéaire qui devient dépendant de d'intensité. Les impulsions sont ensuite positivement dérivées en fréquence et récompressées avec des miroirs a dérivé de fréquence. Un grand élargissement spectral est atteint même avec une faible pression de l'hélium jusqu'à 10 mbar gardant la puissance critique au-dessus des centaines de TW qui assure la compatibilité avec des impulsions de haute énergie. En réglant la pression d'hélium dans le capillaire on obtient une source de laser térawatt avec durée d'impulsion réglable.

Nous avons effectué des HHG avec ces impulsions et obtenu des harmoniques spectralement très larges. Avec une intensité plus élevée ou de plus courtes impulsions, le XUV quasi continuum apparaît. Les structures spatiales et spectrales robustes dans le champ

lointain ont été observées sous différents paramètres. Nous avons effectué des simulations simples et des simulations de SFA et nous avons observé des structures similaires même sans prendre en compte la propagation dans le milieu.

Nous avons montré que les structures spatiales sont principalement dues à la cohérence spatiale de la source XUV. Compte tenu de la déplétion du dipôle harmonique en raison de la forte intensité des impulsions fondamentales, le profil spatial du faisceau XUV en champ proche varie considérablement au cours de l'échelle de temps plus courte que la durée de l'impulsion fondamentale. Ce signal complexe en champ proche diffracte dans le champ lointain créant les franges spatiales. Les structures spectrales ont été expliquées à l'aide de la cohérence spatiale et déplétion du dipôle. Deux temps prédominants d'émission ont été observés dans le champ proche menant à franges spectrales dans le champ lointain.

Nous soulignons que ni les conditions correspondant à l'accord de phase ni la propagation du XUV dans le milieu générateur n'ont été inclus dans les deux types de simulations. Comme nous avons réussi à expliquer le comportement XUV sans l'accord de phase et la propagation de XUV dans le milieu, on peut conclure que ces effets ne jouent pas de rôle majeur dans les structures observées avec HHG générées à haute énergie dans un jet de gaz.

À l'avenir, les techniques développées doivent être couplés ensemble. Effectuant le HHG avec les impulsions de 10 fs et faisceau plat devraient générer des impulsions attosecondes isolé de haute énergie. Une approche alternative de HHG loin du foyer avec faisceau gaussien à l'aide de miroir déformable et avec des impulsions de 10 fs est également très prometteuse. Par la suite une caractérisation temporelle des impulsions attosecondes est nécessaire. Les techniques basées sur le temps (par exemple, XUV autocorrélation) sont préférables pour éviter l'influence des structures XUV spatio-spectrale sur la validité des mesures réalisées dans le domaine spectral qui nécessitent des faisceaux homogènes. Les structures dans les spectres XUV résolues spatialement pourraient aussi servir aussi à caractériser le processus HHG via l'imagerie inverse.

Avec des impulsions fondamentales plus courtes (que 55 fs d'original), des impulsions XUV plus courtes doivent être générées et il devrait être plus facile de générer des impulsions attosecondes de haute énergie qui seraient aptes à explorer de nouveaux domaines tels que les processus non linéaires induits par XUV.

Acknowledgments

One of the hardest part of this work is to name all persons that contributed to this work. During more than three years a lot of people helped me in the lab as well as outside. Even if their great contribution cannot be expressed using words I will try to point out at least the main reasons why I am so thankful to them.

On the first place I thank my friends from Celia for great ambiance and working conditions. Grand merci à Éric Constant, my supervisor, for his guidance, patience, open mind and the concept of «good enough». Whenever I needed help, he was there giving me a hand or advising me. He was not the only one to advise me, I thank Yann Mairesse and Baptiste Fabre for showing me that I really do not want to go for molecules, Éric Mével for revealing me another point of view on teaching, Dominique Descamps for cooling me down when having good results and discovering many problems in those good results (which way he kept me in reality), Stéphane Petit for introducing me the beauty of laser development, helping me explore the magic of french wine and countless discussions about other subjects. I'm glad that I took a beer with Fabrice Catoire, who was always ready to explain me theoretically whatever I asked, although I sometimes finished completely confused.

I cannot forget my student or former student colleagues. Merci à Antoine Dubrouil for lab training at the beginning of my PhD, for discussions of all kinds and for teaching me how to «call the things with right names» (in french). Merci à Charles Handschin for eternal jokes late at work and for his black lab humor when experiment does not work. Merci à Mathieu Dumergue for his help with LaTeX, Matlab and procrastination during endless thesis writing. I thank to Hartmut Ruf for opening my eyes to see important things (and persons). I thank Amélie Ferré for accepting, adopting and developing «macho» jokes that helps us all to survive our hard work.

My thanks belong also to the support team of Celia: Emmanuelle, Céline, Sophie, Loïc, Élodie, Laurent, Alain, Rodrigue et Anatoli. Merci!

I thank all my friends in Bordeaux, especially Marcelo, Mélody and Gratianne for what they are and how they accept the world and Anne, Noémie and Julie for their endless hope to make me a better French.

Finally, I thank a lot my family and Edita for great support and love.

I thank all the people that have enriched my life to make me a better person for that was the major goal of this work.

« Plus ça change, plus c'est la même chose. »

an old French proverb

Contents

Chapter 1

Introduction: State-of-the-art and main goals

The first laser has been built and operated in 1960. A ruby illuminated with flashlamps emitted a coherent beam of red visible light. Since then, many different laser media were investigated and, to date, the lasers cover spectrally an interval from ultraviolet (UV) to far infrared.

27 years after the first laser, High Harmonic Generation (HHG) was observed in 1987 and 1988 in two different places [McPherson 87, Ferray 88]. A medium (typically gaseous) illuminated with high intensity short laser pulse emits a coherent beam of high energy photons that correspond to odd harmonics of the fundamental pulse wavelength (high harmonics). As the wavelength of such radiation can reach few nm and therefore takes place in between soft X-rays and ultraviolet, we call the HHG radiation as XUV.

Now, in the year 2014, 27 years after the first HHG, we witness rapidly growing interest in generating high harmonics for Physics [Corkum 07, Krausz 09, Agostini 04, Papadogiannis 03, Morlens 06] and also in many others Physics-related field of research such as Biology or Chemistry [Nugent-Glandorf 01, Itatani 04, Stavros 05]. On the other hand, 27 years after the first observation of HHG, a commonly available commercial XUV source is still missing.

Such a drastic restriction of HHG to scientific laboratories has a large impact on the speed at which new phenomenons are observed, described and explained and also on the size of the XUV community. Indeed, HHG is extensively performed and examined only in few countries over the world often with a very few or just one XUV laboratory per country.

Under such conditions some ideas or paradigms[1] are commonly accepted in default and no more investigated. For instance, in XUV community the concept of phase-matching as a major driving phenomenon of HHG was extensively studied theoretically at the end of the

[1] A concept of scientific paradigms was first introduced and extensively explained in the excellent book «Structure of scientific revolutions» written by Thomas Kuhn and published in 1960.

last millennium and confirmed experimentally by a large number of experimental results [Balcou 97, Constant 99, Gaarde 99, Rundquist 98, Durfee 99, Mével 00, Kazamias 03a].

A holy grail of HHG, the generation of high energy isolated attosecond pulses seems to be close ahead. Besides better temporal resolution that is offered in pump-probe experiments, there is also a subjective notion, that a real «evolution» of very short femtosecond pulse development (that is indeed isolated) should be an attosecond pulse, isolated as well.

Therefore a lot of efforts were made for the generation of isolated attosecond pulse using various techniques and demanding various femtosecond driving lasers [Bouhal 98, Sekikawa 04, Cao 06, Pfeifer 07, Jullien 08, Abel 09, Ferrari 10, Hong 11, Zhao 12, Du 12, Takahashi 13]. To date, one of the best achievements seems to be the generation of isolated attosecond pulse using a GDOG technique applied on non-CEP-stabilized driving laser supplying femtosecond pulses as long as 28 fs [Feng 09].

While the single attosecond pulse generation is now a common task performed in many laboratories [Drescher 02, Uiberacker 07, Cavalieri 07, Schultze 10, Goulielmakis 10, Sansone 10], the energy contained in this isolated pulse is not high enough for many applications, restricting possible applications to scientific laboratories as mentioned.

Moreover, various efforts to generate high XUV photon flux via HHG are often counterproductive to the isolated attosecond pulse generation.

As the high energy high repetition rate lasers are commercially available today and some ultra-high repetition rate high intensity lasers are already developed and XUV performed in scientific laboratories even for much longer wavelength (4 µm), we feel that raising the number of generated XUV photons by using just more powerful driving laser will be more often on the daily schedule of researchers. In the light of such technical advances surprisingly little effort was devoted to characterize in detail the high harmonic generation with high energy high intensity pulses.

On our way towards high energy isolated attosecond pulse generation, we progressed in parallel in both aspects - using high energy femtosecond pulses and generating shorter attosecond pulse trains.

For the latter, we developed a new post-compression technique that is compatible with high energy femtosecond pulses.

While performing HHG with high energy femtosecond pulses (short as well as long) we observed unprecedented effects in form of robust and complex spatio-spectral structures in XUV single-shot profiles detected in the far field. Some of the structures characteristics suggest that the phase-matching conditions are not of the most important role during the HHG process in contradiction with commonly accepted paradigm.

Therefore, in this work we present a wide experimental study of HHG with high energy femtosecond pulses varying a large number of parameters. We suggest an approach

that allows us understanding the experimental results and perform a simple simulation to support our findings. We stress the importance of utilization of spatially and spectrally resolved XUV profiles on the single-shot basis.

An innovative high energy femtosecond pulse post-compression technique is also presented same as XUV spectra generated with post-compressed 10 fs TW pulses.

In order to provide a comprehensive insight, we start this work with a general description of HHG in gases (chapter 2). Microscopic as well as macroscopic features are briefly discussed and the chapter is finished with a description of commonly used XUV characterization instruments that we used in this work.

The following chapter n°3 compares HHG in various geometries such as gas jet and gas filled capillary. General experimental setup is also presented. We detail our simple simulation of HHG with respect to high energy femtosecond pulses. The XUV properties simulated using low intensity and high intensity are compared. Then the simulation is used to explain experimentally observed XUV characteristics and the most common XUV shapes are commented. We also performed HHG in a capillary in collaboration with LPGP, and this experiment is described at the end of the chapter 3.

In chapter n°4, spatial shaping of the driving infrared beam before HHG is considered using an adaptive optics and phase mask. Both techniques were developed with a special attention to be compatible with high energy pulses and have considerable effects on HHG.

Chapter 5 is devoted to the development of high energy post-compression technique that is unusually based on ionization rather than on Kerr effect. This approach allows us using very high energy pulses and obtaining 10 fs TW level pulses suitable for HHG that is presented in the following chapter n°6.

HHG with 10 fs TW pulses is presented with parametric studies. In this chapter n°6 our simple simulations are compared to complex SFA based simulations performed by Vasily Strelkov (RAS, Moscow).

Generally this whole work is devoted to HHG with high energy femtosecond pulses under various conditions and we feel that our findings are of major importance for design of future HHG experiments as some new XUV features have to be considered.

Note that most of the figures shown in this work were embedded into the pdf in vector format. Consequently they are presented as-they-are and by zooming into, the pixelization correspond to realistic experimental and simulation resolution.

Chapter 2

General overview of harmonic generation at high energy

High harmonic generation can be performed in gases, in solids [Dromey 06] and in plasmas [Quéré 06]. In all of these media, one generates large-bandwidth XUV radiation temporally formed in ultrashort pulses. However, conceptually all those technique differ a lot from each other.

In our work we are generating high harmonics only in rare gases. Wherever we use the term «HHG» we would mean HHG in rare gases if not specified otherwise.

In this chapter we explain some of fundamental microscopic characteristics of HHG. We would follow with phenomenons corresponding to propagation of XUV in the generation medium and the chapter will be finished with description of XUV characterization techniques.

Through this chapter, special attention will be payed on high driving pulse energy aspects of HHG.

2.1 Microscopic aspects of HHG

HHG in gases is obtained by focusing an ultrashort pulse in a gas medium. This generating pulse is commonly called «driving». The crucial parameter is the peak intensity of the driving pulse. It has to be at least of the order of $10^{14}\,{}^{\mathrm{W}}/_{\mathrm{cm}^2}$. Then the driving pulse field strength is comparable to the electric field between a core and an electron.

The emitted radiation typically of tens to hundreds of eV is spectrally formed into a series of spectral peaks as sketched on figure 2.1.

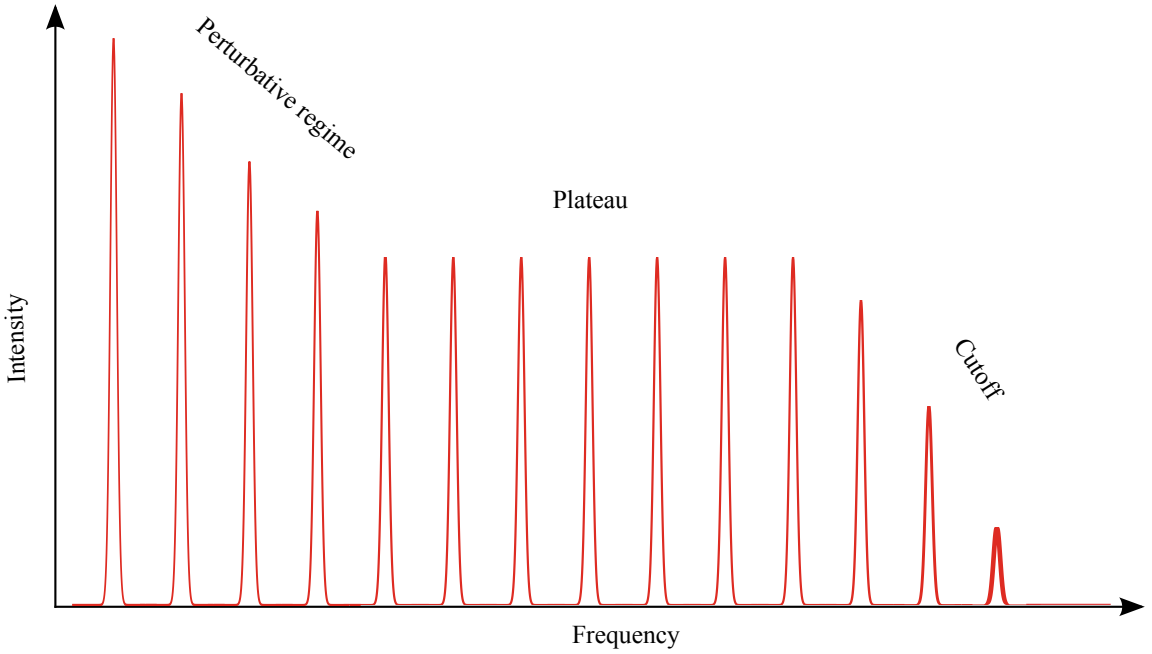

Figure 2.1 – Typical spectrum of HHG in gases whilst employing long driving laser pulses. There are 3 different regions: Perturbative, plateau and cutoff. Adapted from [Higuet 10]

The spectral peaks (each peak corresponds to one harmonic) form 3 different zones:

Perturbative regime where the harmonic peak intensity decreases rapidly,

Plateau where the harmonics have about equal intensity

Cutoff where the intensity drops rapidly to zero.

All three spectral regions are qualitatively and quantitatively different.

The perturbative region contains only small number of harmonics and typically is not used for applications.

Plateau spectral extent vary with the gas and intensity used and usually this part contains the most of the emitted energy in the XUV. The plateau is very often used for measurement and application.

Cutoff also contains only few harmonics and because of its special characteristics is used for some special applications.

To explain those characteristics the simple-man model was developed.

2.1.1 Simple-man model

The simple-man model (also known as «three step model») was developed and described in [Corkum 93, Schafer 93]. Although the model is 1D and semiclassical it predicts well

enough experimental observations.

2.1.1.1 Presentation of the model

The principle of this model is shown on figure 2.2.

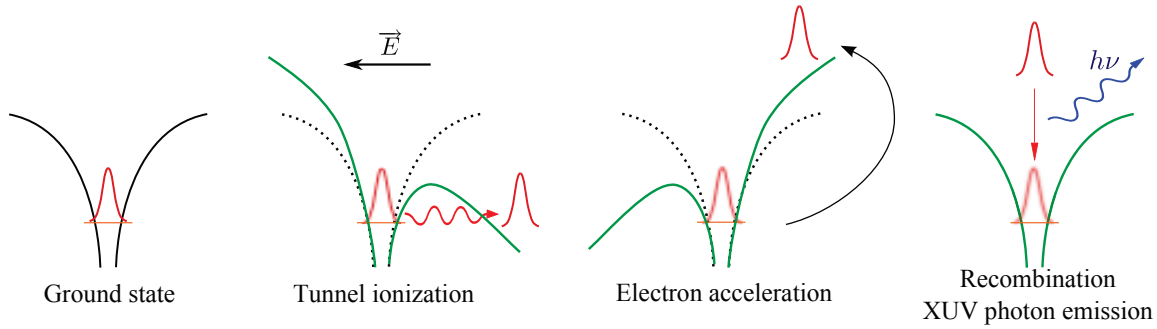

Figure 2.2 – (color) Simple-man model (1D). Electron wave function is denoted red and the atomic potential is green. Adapted from [Higuet 10].

One can describe the model first imaging the ground state atom before arrival of the driving pulse. The electron is in the potential well of the core. When the driving pulse arrives and interacts with the atom the three steps follow:

Tunnel ionization: The infrared field is strong enough to raise the potential on the one side and to lower it on the other side of the potential well of the atom. The electron then has a significant probability to tunnel out of the potential well.

Electron acceleration: Once the electron is ionized, it moves in the continuum. One should note that the electron is not bound but driven by the strong driving field. This infrared field is so strong that we can neglect the Coulomb attraction between the electron and the positive ion, the so-called «Strong-field approximation» (SFA). Basically the electron follows on the electric field direction. Practically it means that at first the electron is accelerated opposite to the ion location, then stopped and finally accelerated back towards the parent ion position. This step is shown in detail on figure 2.3.

Recombination & XUV photon emission: When the electron returns to the proximity of the parent ion it can recombine releasing all its kinetic energy in an XUV photon.

From the spatio-temporal point of view the simple-man model is presented on figure 2.3.

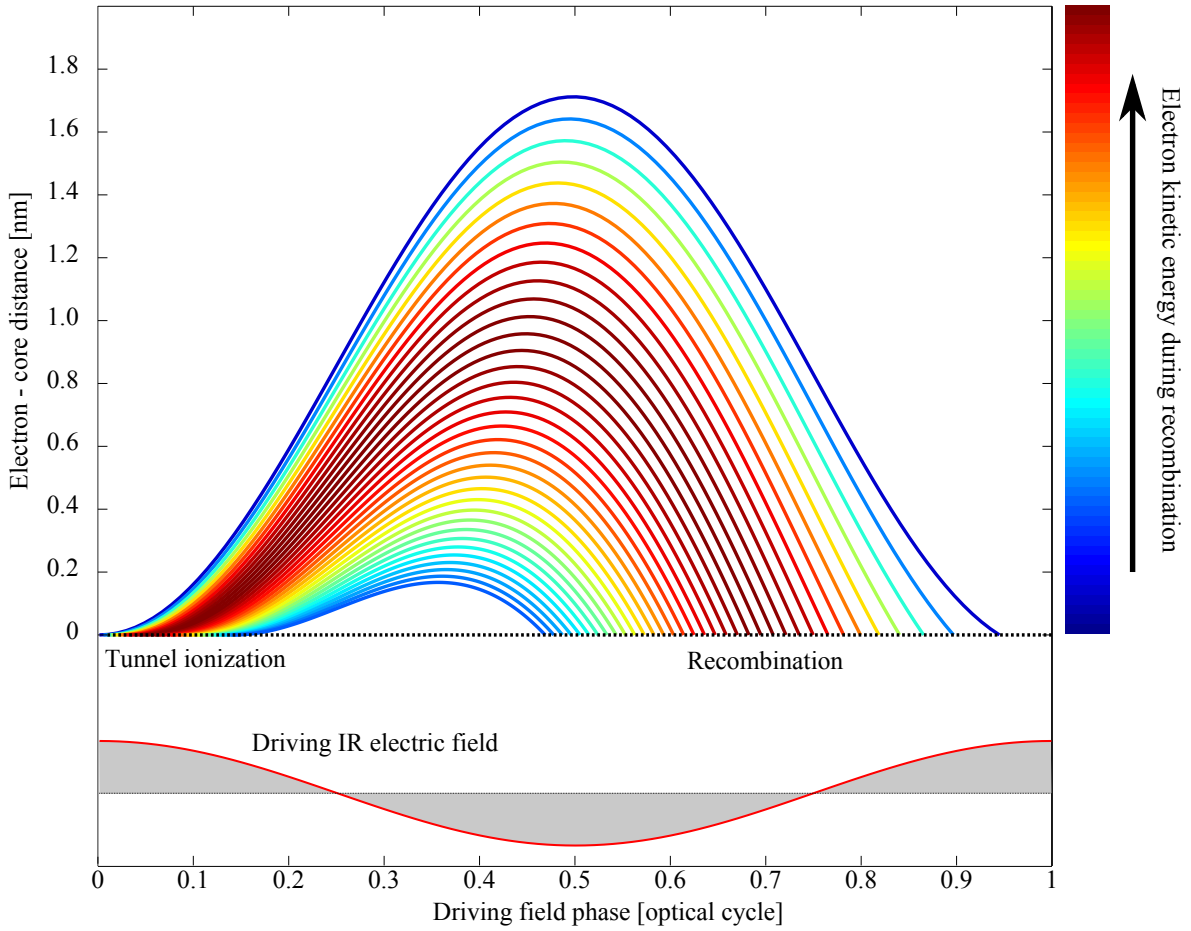

Figure 2.3 – (color) Simulated electron trajectories in the continuum. The generating and accelerating driving field is shown at the bottom of the image. The driving laser peak intensity was 10^{14} W/cm² with a central wavelength of 800 nm. The electron trajectories are shown for different ionization times corresponding also to different recombination times. The trajectory with the highest electron kinetic energy is the dark red one corresponding to the highest harmonic generated (cutoff). Adapted from [Higuet 10].

The figure presents simulated electron trajectories in the continuum. The generating and accelerating driving field is shown at the bottom of the image. The driving laser peak intensity was 10^{14} W/cm² with a central wavelength of 800 nm. The electron trajectories are shown for different ionization times corresponding also to different recombination times.

The trajectory with the highest electron kinetic energy is the dark red one corresponding to the highest harmonic generated (cutoff). We define short and long quantum trajectory (also called «path») relative to this cutoff trajectory.

Trajectories of electrons that are liberated into the continuum before the cutoff electron are called long trajectories because their trajectories duration are longer than the cutoff trajectory. The excursion time of the electron[1] in the continuum declines with harmonic's order rising.

[1]The excursion time of the electron is the time duration that the electron spends in the continuum.

Trajectories of electrons that are liberated into the continuum after the cutoff electron are called short trajectories because their trajectories duration are shorter than the cutoff trajectory. The excursion time associated with these trajectories raises with harmonic's order.

The short and long trajectories are very different. For instance the yellow path on figure 2.3 corresponding to kinetic energy of 8 eV goes up to 1.5 nm far away for the long path but only around 0.4 nm for the short path.

Short and long trajectories together present a temporal window of ionization (figure 2.4). Electrons liberated in this window may recombine emitting an XUV photon.

Beside that, there are many trajectories with ionization outside this window that correspond to electrons that never come back to the parent ion and thus those trajectories do not generate XUV photons.

The time-energetic point of view of the simple-man model is presented on figure 2.4.

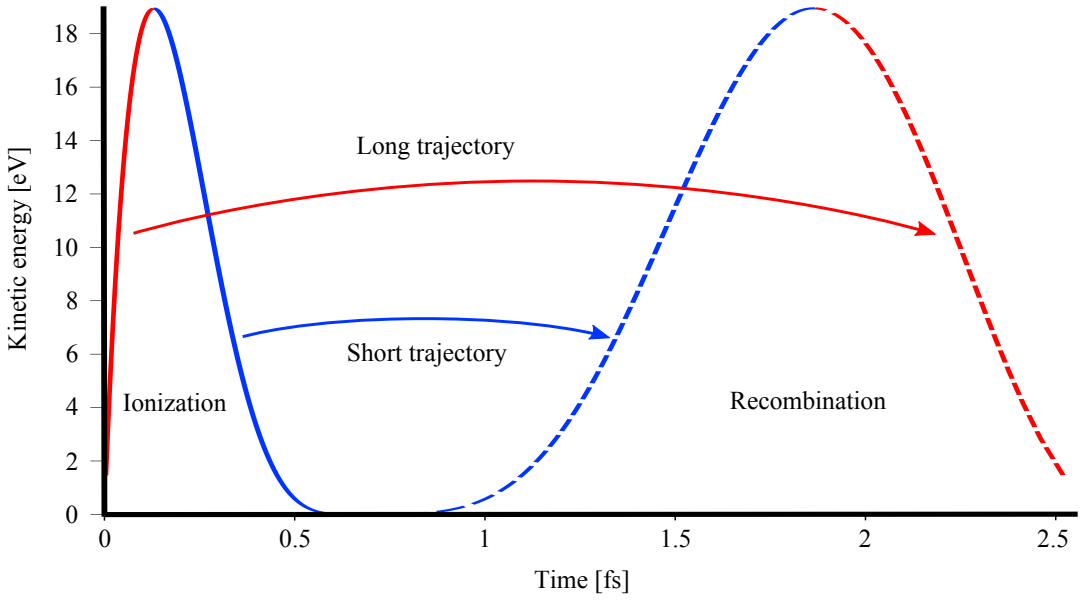

Figure 2.4 – (color) Simulated electron trajectories in the continuum that presents the electron kinetic energy at the recombination (dashed line) as a function of the time of ionization (solid line). The driving laser peak intensity was 10^{14} W/cm² with a central wavelength of 800 nm. The short trajectories (blue) and long trajectories (red) are distinguished. Adapted from [Higuet 10].

The figure represents the electron kinetic energy at the recombination as a function of the time of ionization. The driving laser peak intensity was 10^{14} W/cm² with a central wavelength of 800 nm. The short trajectories and long trajectories are «connected» via the point of highest kinetic energy of 19 eV. The ionization temporal window is slightly larger than 0.5 fs and the recombination window is larger than 1.5 fs. Also in here we can see the great difference between the short and the long path in terms of excursion time passed in the continuum.

The simple-man model runs every half-cycle $T_0/2$ of the driving field ω_0. The even harmonics though interfere destructively and the final spectrum contains only odd harmonics with spacing of $2\omega_0$ (where ω_0 denotes the driving laser angular frequency).

2.1.1.2 Important relations

In this work we will need to know some quantities to explain observed experimental features of HHG.

2.1.1.2.1 Barrier suppression intensity The first step of the simple-man model is the tunnel ionization (see figure 2.2). For a low intensity the atomic potential well is not lowered enough so the tunnel ionization probability is correspondingly low and there is no HHG. For intensity that is too high the potential barrier would be lower than the ground state energy of the electron so there would be no tunnel ionization neither.

The driving pulse intensity that lowers the potential barrier to the level of the electron ground state energy is called «barrier suppression intensity» and is denoted as I_{SB}. This intensity depends only on ionization potential I_p of the medium and can be expressed as [Augst 89]:

$$I_{SB} = \frac{cI_p^4}{128\pi} \tag{2.1}$$

giving $I_{SB}\,[10^{14}\mathrm{W/cm^2}] = 4\times10^{-5}\cdot I_p^4\,[eV]$. The formula is for singly charged ion. Values of barrier suppression intensity for rare gases are calculated on table 2.1.

Gas	$I_p\,[eV]$	$I_{p2}\,[eV]$	$I_{SB}\,[10^{14}\,\mathrm{W/cm^2}]$
Helium	24.58	54.40	14.62
Neon	21.56	41.07	8.65
Argon	15.76	27.63	2.47
Krypton	14.00	24.56	1.54
Xenon	12.13	21.20	0.87

Table 2.1 – Ionization potential, potential of double ionization and calculated barrier suppression intensity for 1 electron of rare gases [Augst 91, Lide 07].

2.1.1.2.2 Ponderomotive potential and Keldysh parameter From a static point of view an atom to be ionized has to interact with a driving field of appropriate intensity. However the field does not establish immediately but rises from 0 to its maximum in finite time. Also an electron does not tunnel immediately. Therefore the barrier has to be lowered for a time interval long enough for electron to tunnel. Intuitively for long wavelength of the driving field the electron would have enough time to tunnel out of the atom. For short wavelength the barrier would lower faster than the electron can «react».

To quantify that, the Keldysh parameter γ was introduced in [Keldysh 65]. The Keldysh parameter is dimensionless and can be expressed:

$$\gamma = \sqrt{\frac{I_p}{2U_p}}$$

where the ponderomotive potential U_p is defined (in joules) as

$$U_p = \frac{e^2 E^2}{4 m_e \omega_0^2} \tag{2.2}$$

where $e = -1.602 \times 10^{-19}\,\mathrm{C}$ is the electron electric charge, E stands for electric field, $m_e = 9.11 \times 10^{-31}\,\mathrm{kg}$ is the electron mass and ω_0 denotes the laser angular frequency[2].

The ponderomotive potential can be viewed as the mean kinetic energy of an electron oscillating in the electromagnetic field E with angular frequency ω_0.

Two cases of ionization are defined correspondingly to the value of γ:

1. $\gamma << 1$ the so called «tunnel ionization» occurs when the electron has enough time to tunnel.

2. $\gamma >> 1$ the so called «multiphoton ionization» occurs when the electron is released without tunneling.

In this work we use driving laser with central wavelength of 810 nm and high intensities. For instance, let's consider argon gas with its ionization potential $I_p = 15.76\,\mathrm{eV}$ and laser intensity $I = 1.29 \times 10^{14}\,\mathrm{W/cm^2}$ that gives the ponderomotive potential $U_p = 7.88\,\mathrm{eV}$. Than the Keldysh parameter $\gamma = 1$ and we are on the border between the tunnel and multiphoton ionization.

2.1.1.2.3 Cutoff intensity The highest harmonic (cutoff) that can be generated with a ponderomotive energy U_p in a medium of ionization potential I_p can be found as:

$$h\nu_{max} = I_p + 3,17U_p \tag{2.3}$$

where $3,17U_p$ is the kinetic energy of the recombining electron. Combining equations 2.2 and 2.3 one can yield the cutoff driving field for given harmonic, gas and driving laser frequency as:

$$E^2 = (h\nu_{max} - I_p)\,\frac{4 m_e \omega_0^2}{3.17 e^2} \tag{2.4}$$

[2]Giving $U_p\,[eV] = 6,12I\,\left[10^{14}\,\mathrm{W/cm^2}\right]$ for 810 nm

giving $I_{cutoff} = (h\nu_{max} - I_p)\frac{m_e\omega_0^2}{579.5e^2}$ where we used $E^2 = 2 \times 377 \times I_{cutoff}$. The values of cutoff intensity for different harmonics and gases are shown on table 2.2 and figure 2.5.

Harmonic	Helium	Neon	Argon	Krypton	Xenon
11			0,06	0,15	0,24
13			0,21	0,30	0,40
15		0,07	0,37	0,46	0,56
17	0,07	0,23	0,53	0,62	0,71
19	0,23	0,39	0,69	0,78	0,87
21	0,39	0,55	0,84	0,94	
23	0,55	0,70	1,00	1,09	
25	0,71	0,86	1,16	1,25	
27	0,86	1,02	1,32	1,41	
29	1,02	1,18	1,48		
31	1,18	1,33	1,63		
33	1,34	1,49	1,79		
35	1,49	1,65	1,95		
37	1,65	1,81	2,11		
39	1,81	1,97	2,26		
41	1,97	2,12	2,42		
43	2,13	2,28			
45	2,28	2,44			
47	2,44	2,60			
49	2,60	2,75			
51	2,76	2,91			
53	2,91	3,07			
123	8,44	8,59			
201	14,59				

Table 2.2 – Simulated cutoff intensity for different harmonic orders and rare gases. In units of 10^{14} W/cm^2.

In the table there are empty spaces for helium and neon where the equation 2.2 is no more valid. This is because of the validity of the Strong-Field Approximation.

The empty spaces for high orders of harmonics are due to the cutoff intensity that is higher than the intensity of the barrier suppression (equation 2.1).

The interesting issue of the figure 2.5 lies in the cutoff intensity compared between different gases. For instance, to generate harmonic 19 one needs more than three-times higher intensity in krypton than in helium. One can argue that experimentally it is much easier (with lower intensity) to generate harmonics in krypton than in helium. So we would like to stress here that table 2.2 and figure 2.5 show the cutoff intensity of defined harmonics, not the intensity to obtain comparable photon flux for different gases. That means that in gases with high ionization potential the low harmonics are already in the cutoff while no signal could be detected. Then when rising intensity, all the harmonics in

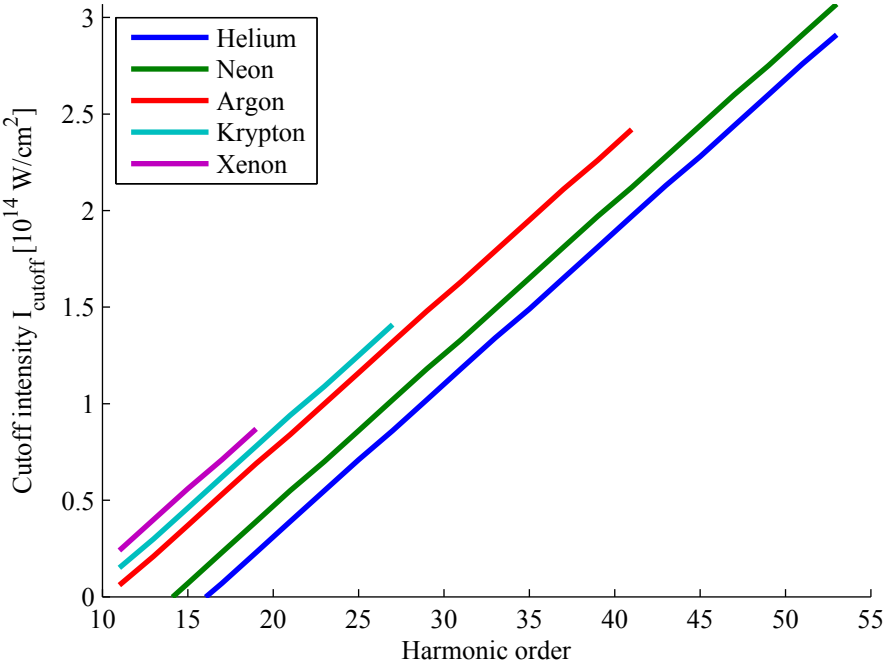

Figure 2.5 – (color) Simulated cutoff intensity for different harmonic orders and rare gases. For each gas the highest displayed harmonic order is the highest obtainable in the gas except for helium and neon.

the cutoff and plateau seem to appear instantaneously.

2.1.2 Quantum model

The semiclassical simple-man model is in good agreement with experiments. However, to sight deeper in underlying principles of HHG one has to use full quantum model. For example, one cannot explain coherence with the semiclassical model where the phase of emitted XUV photons depends only on the time spent in the continuum. Therefore the final phase can take arbitrary value making the HHG process apparently incoherent.

Note that temporal coherence is necessary condition for attosecond pulse generation.

The quantum model was developed in [Lewenstein 94, Lewenstein 95]. In difference to the semi-classical model the quantum model considers quantum effects during the tunneling ionization and the diffusion of the electron wavepacket in the continuum.

For purposes in our work the quantum model is not necessary to use therefore we will consider only simple-man model.

To illustrate the difference between semi-classical (figure 2.4) and quantum approach we plot the harmonic order as a function of time of ionization and recombination on figure 2.6.

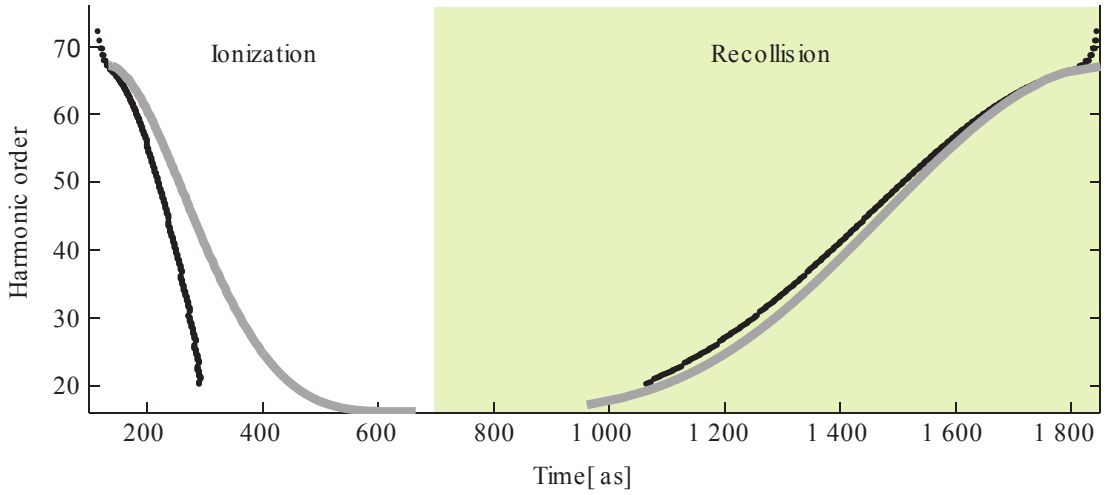

Figure 2.6 – Calculated semiclassical (gray) and quantum (black) dependence of the generated harmonic order on the ionization and recombination time. (adopted from [Shafir 12])

The recombination demonstrates a very good agreement between the semiclassical ([Corkum 93]) and quantum model. However, the lower harmonics promote a pronounced difference in the time of ionization. The quantum ionization window is about 100 as shorter than the semiclassical one. The difference between the two models can be also found in [Becker 02].

2.2 Macroscopic aspects of HHG

An arbitrary generating medium is of finite length and atomic density. The medium can alter the phase of both driving (IR) and generated (XUV) radiation via self phase modulation (SPM). The medium also absorbs the radiation. The coefficient of absorption are very high for XUV and corresponding coherence length typically vary between few μm and 1 mm depending on gas, gas pressure and harmonic order.

A detected XUV signal is a sum of the signals of all the emitters (atoms) in the volume of interaction that behave as described in previous section 2.1. The signals are coherent because the driving pulse is coherent and the process of HHG keeps the coherence. The signal combination is therefore also coherent.

In this way, in the observation plane in the far field some emitters can interfere constructively and some destructively. To maximize overall XUV signal it is favorable to keep the interferences constructive. That means to keep the phase difference of emitters lower than π and in ideal case equal to 0. Those conditions are commonly referred to as «phase-matching».

To quantify the overall constructive interferences in a generating medium as a whole we introduce a «coherence length» l_{coh}. The coherence length denotes the medium length

where the phase difference of emitters is lower than π i.e. the length of constructive interference. In the first approximation the phase-matching is accomplished when the length of the medium is lower than the coherence length $l_{med} < l_{coh}$.

To maximize XUV signal in [Constant 99] authors described a complex formula for overall XUV signal as a function of many parameters including coherence length that is given:

$$l_{coh} < \frac{\pi}{\delta k} \tag{2.5}$$

where δk denotes wave-vector mismatch between driving infrared pulse and generated XUV pulse. This mismatch is given by:

$$\delta k = q\left(\delta k_{at} + \delta k_{el} + \delta k_{Gouy}\right) + \delta k_{\varphi_{at}} \tag{2.6}$$

where k_{at} and k_{el} corresponds to the propagation in neutral atoms and free electrons, k_{Gouy} is connected with the geometrical phase advance due to focusing also known as the Gouy phase and $k_{\varphi_{at}}$ denotes the atomic phase gradient that also depends on the quantum path.

To maximize the XUV signal one should seek a compromise between the microscopic and the macroscopic effects. For instance, raising intensity would raise the microscopic signal but also could destroy the phase-matching by ionization.

One way to fulfill the inequality of equation 2.5 is to push δk as close to zero as possible. The terms in equation 2.6 are of different signs so theoretically the balance of positive and negative terms is possible.

The propagation through neutral atoms would influence δk_{at} through the gas type and neutral atoms density. This term would be always positive.

The electron dispersion δk_{el} depends on driving laser parameters and electron density as [Kazamias 11]:

$$\delta k_{el} = \frac{\omega}{c}\delta n_{el} = -\frac{\omega}{c}\frac{n_e}{2n_c}$$

where

$$n_e = \frac{\tau P}{k_B T}$$
$$n_c = \frac{\omega^2 m_e}{\mu_0 c^2 e^2}$$

where n_{el} is refractive index, n_e denotes electron density, n_c critical electron density, T

stands for thermodynamic temperature and τ denotes ionization degree of the medium ($\tau = 0$ in the case of no ionization and $\tau = 1$ in the case of completely ionized medium). Therefore the electron dispersion is always negative.

The Gouy phase term corresponds to driving beam focusing, but putting an iris into the input laser beam would have dramatic results on the Gouy phase as it will be discussed later in chapter n°3. This term can be both negative or positive.

The atomic phase term depends only on the driving intensity profile and the quantum trajectory though

$$\delta k_{\varphi_{at}} = -\alpha \nabla I\left(x, y, z, t\right)$$

where in the plateau the value of α equals $1 \times 10^{-14}\,\mathrm{cm^2/w}$ for short trajectory and twenty five times more e.g. $2.5 \times 10^{-13}\,\mathrm{cm^2/w}$ for long trajectory [Gaarde 02]. For $I_{IR} < I_{cutoff}$, $\alpha = 13 \times 10^{-14}\,\mathrm{cm^2/w}$. The value of $\delta k_{\varphi_{at}}$ can be negative or positive depending on spatial and temporal shape of the driving intensity.

Trying to put δk close to zero could be a difficult task when generating harmonics using high intensity driving pulses. The terms described above would become time and space dependent making the overall phase-matching practically impossible.

Another way to fulfill the phase-matching inequality (equation 2.5) is to reduce the medium length for instance using a thin gas jet. Under such conditions the macroscopic influence is much less important than with long medium. Those are the conditions that we choose experimentally and we developed a simulation that corresponds to that.

2.3 XUV radiation characterization techniques used in this work

As the XUV radiation has some special characteristics the characterization techniques commonly used in laser technology have no use in XUV spectral domain (although the XUV characterization techniques are in general based upon what is known from IR). From that point of view the most limiting properties of XUV are:

Short wavelength: XUV photon energy is typically of the order of tens to hundreds of eV. Such energetic photons are absorbed almost immediately in solids and even in gases of pressure more than 10 mbar. Consequently all HHG setups take place under vacuum. Also, with an exception of thin metal films there is practically no transmission optics for XUV. Reflection optics has problems with maximal obtainable reflectivity and surface roughness.

Low XUV intensity compared to IR: The HHG process efficiency is low. In argon typically 10^{-5}. That means that the «noise» (infrared pulse) is 5 orders of magnitude more intense than the XUV signal. Several techniques were developed to circumvent this issue.

Low XUV intensity for nonlinear optics: Even after getting rid of the infrared noise the signal is still low and high sensitivity instruments have to be used. Moreover the measurement techniques based on nonlinear effects (e.g. autocorrelation) are very difficult to perform.

The XUV characterization techniques presented were developed to consider all those issues.

2.3.1 Flat-field XUV spectrometer

A flat-field XUV spectrometer is a fundamental and most common instrument to characterize HHG. Principally it consists of 3 parts:

1. Slit
2. Grating
3. Imaging device

Schematic of our XUV spectrometer is shown on figure 2.7.

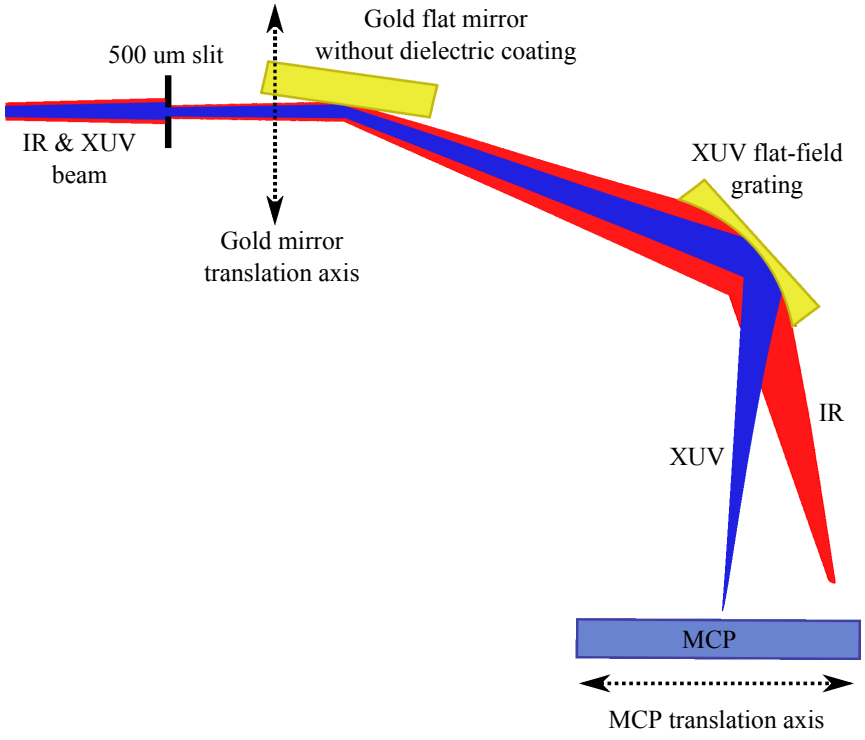

Figure 2.7 – (color) Schematic of the flat-field XUV spectrometer (adapted from [Dubrouil 11b])

2.3.1.1 Slit

A slit is the first element in the optical path of the beam that defines the XUV spectrometer resolution. Sometimes the slit is not used and the spatial discrimination is defined by the focal spot/generating medium size. In our spectrometer we use a 500 μm vertical slit at the distance of 188 cm from the beam focus.

2.3.1.2 Grating

The grating defines spectral resolution and spectral window. To provide spectral and spatial resolution, so called flat-field gratings are used. They often have variable groove spacing and are designed so that, despite the spatial width of the XUV beam, all the spectral components (of the first and higher orders of diffraction) are imaged in a plan and so the detector can be flat and the spectral image is not deformed.

There are two types of XUV gratings: transmission and reflexion.

Our spectrometer consists in a Hitachi reflective cylindrical concave gold grating with 1200 grooves per mm used at 87° grazing incidence. The grazing incidence is necessary to support the short XUV wavelength (that would need more grooves per mm when used at smaller angle of incidence). The concave grating images the slit with a magnification of 1 in the horizontal (spectral) dimension. The first order of the grating is diffracted to the detector while the zeroth order together with infrared beam are reflected, resp. diffracted towards a different directions and blocked carefully to reduce parasitic signal on the detector in the XUV case and to avoid any optics damage in the case of infrared driving beam.

2.3.1.3 Imaging device

There are mostly two types of imaging devices: MCP and CCD.

XUV CCD is a camera that is sensitive in XUV spectral domain. Typically it is actively cooled with water or air. The major advantage over microchannel plates is high dynamics and that the acquired image can be intensity-calibrated therefore giving information on the number of photons XUV detected. The biggest disadvantage is the sensitivity in the infrared region of the spectrum, so the driving beam has to be completely blocked including any reflections or diffusion in vacuum chambers. The chip is also typically smaller than a useful diameter of MCP.

Microchannel Plates (MCP) is a photon-multiplier that works in XUV range. A XUV photon creates bunch of electrons that are accelerated to the phosphor screen. Typically MCP are solar-blind i.e. they do not amplify visible and infrared component of the spectrum. For maximum gain one has to use two microchannel plates in inverse directions.

Our MCP were supplied by Photonis Inc. company. They have the imaging diameter of 40 mm and 10 μm pore size. The input connectors of the MCP were supplied with a high voltage supply of up to -2 kV. Typically we used it about -1.55 kV to avoid saturation of the MCP.

Our phosphor screen was made of Ce:YAG and emitted in green-yellow spectrum between 490 and 620 nm with a center on 530 nm. The decay time of light intensity from 90 % to 10 % is declared to be as short as 300 ns and from 10 % to 1 % it is 90 μs that makes it suitable for repetition rates up to 10 kHz. The phosphor screen was connected to +3kV high voltage supply.

To be able to save the spectra the phosphor screen was observed with a 12 bit CCD. As we already discussed the horizontal axis corresponds to the spectral resolution. In the vertical dimension, the beam propagation is not affected by the grating and this dimension allows us to observe the spatial profile of the XUV beam. The detection efficiency was high enough to characterize the harmonics both spectrally and spatially on a single-shot basis and the 12 bit CCD was able to acquire at a repetition rate of 10 Hz, that is the repetition rate of the laser.

2.3.1.3.1 Experimental implementation of the spectrometer Our XUV spectrometer with its implementation is shown on figure 2.8.

One can see the entrance slit and a gold mirror (on the left) are placed on a translation stage. That allows removing them to let the beam go straight for application. This translation stage can be controlled from outside the chamber in order to put the XUV spectrometer in and out of the beam path and thus without breaking the vacuum.

One should note that the central part of the chamber is free for the installation of an interferometer or other instruments.

A typical single-shot spatially and spectrally resolved far-field XUV spectrum measured by our flat-field XUV interferometer is on figure 2.9.

On figure 2.9 we show a spatio-spectral XUV profile generated in neon. The spatial integrated spectrum on figure 2.9 b) contains plateau and cutoff as already discussed in section 2.1.

2.3.2 Time-of-flight mass spectrometer

Time-of-flight (TOF) mass spectrometer is a second most common XUV characterization instrument. It uses the fact that the typical spectrum of XUV contains photons whose energy is higher than ionization potential of gases. Letting the XUV beam ionize the gas in the sensitive region of the TOF and detecting the produced ions or electrons would give also complementary information about the XUV beam. Moreover the TOF spectrometer is also

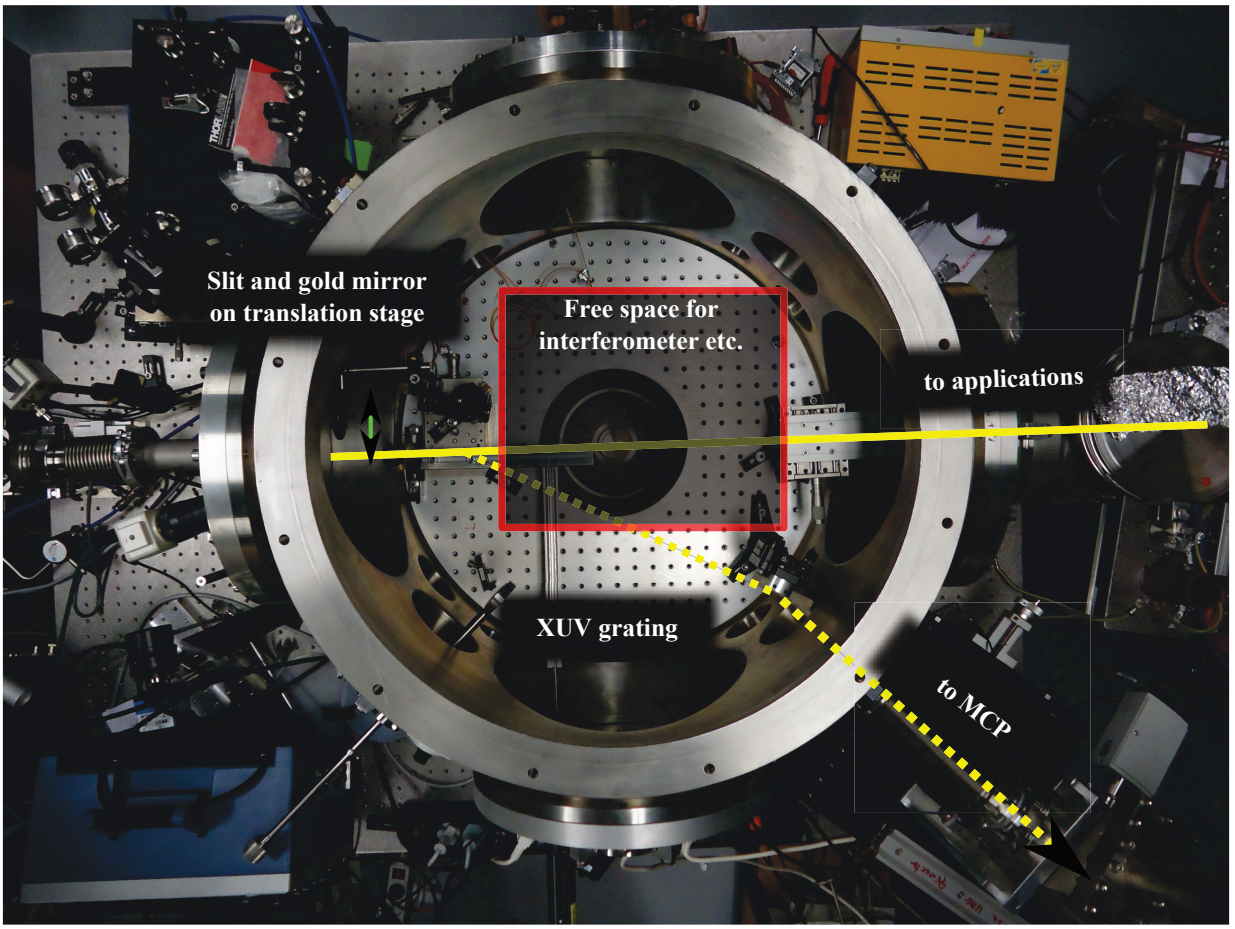

Figure 2.8 – (color) Photograph of opened characterization chamber (from above). Dashed the beam path to the MCP. Solid the liberated beam heading towards the applications. In the middle one can see a turbo pump and free space that is reserved for an interferometer setup.

well suitable to detect the gas ionized by infrared beam and therefore this instrument is very well fitted for pump-probe experiments. This advantage is a key feature for measurement techniques such as RABBIT [Paul 01].

2.3.2.1 General principle

The underlying principle of the TOF mass spectrometer is a measure of the time τ_{flight} needed for ions or electrons to go from the interaction zone to the detector (distance L) following an equation:

$$\tau_{flight} = 2L\sqrt{\frac{m}{qV}} \tag{2.7}$$

where m is the mass of an ion or electron, q stands for its charge ($q = e$ for electrons and $q = Ze$ for ions) and V is an acceleration potential.

The equation 2.7 sets the parameters that can be obtained by the TOF based principle.

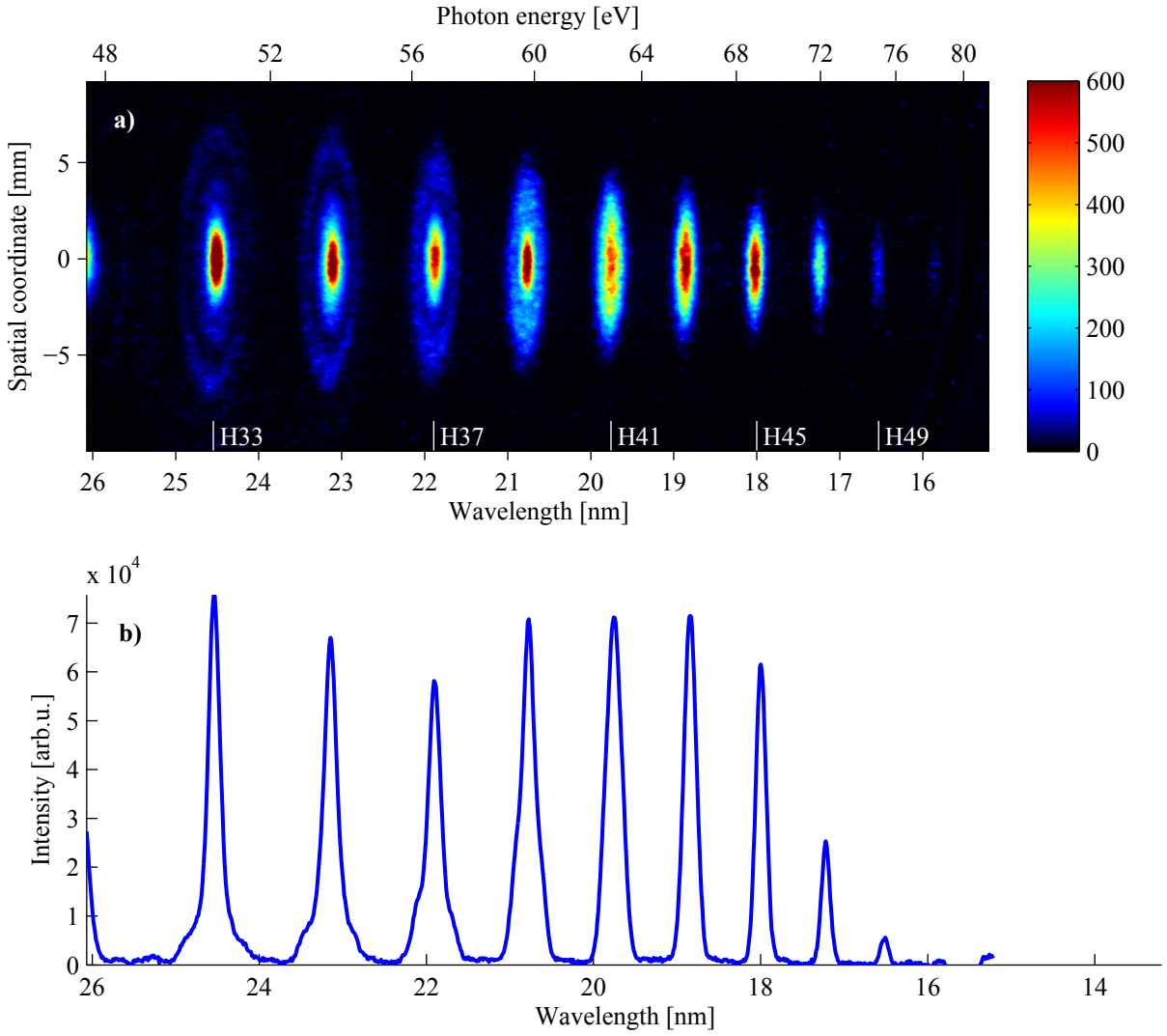

Figure 2.9 – (color) a) Single-shot spatially and spectrally resolved far-field XUV spectrum and b) its spatial integration. Neon jet (approx. 750 μm thick, pressure 30 mbar) was placed 4 mm after the focus, the iris diameter was 13 mm and the estimated intensity in the gas jet was 3×10^{14} W/cm^2.

Whilst it is used with ions, one obtain the mass spectrum (actually it is the $\frac{m}{q}$ spectrum) and whilst used with electrons, the result is the energy spectrum. Typically a TOF spectrometer resolution is high enough to distinguish isotopes of an element.

The principle of the TOF is on figure[3] 2.10.

The TOF mass spectrometer consists of vacuum chamber with at least 3 large electrodes and a detector of charged particles.

[3]The figure was created using SimIon software.

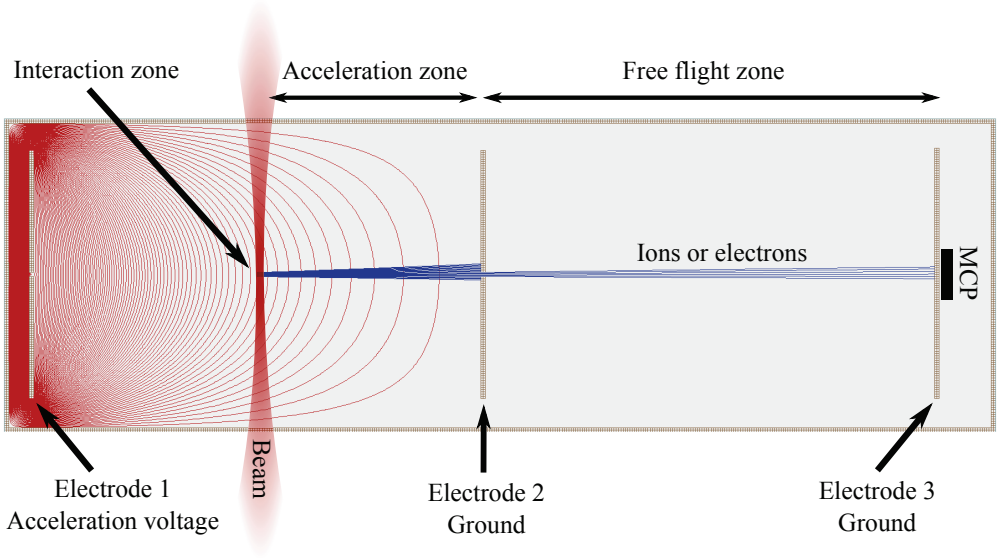

Figure 2.10 – (color) Principle schema of time-of-flight mass spectrometer

2.3.2.2 Charged particles acceleration

A space between the first and second electrode can accommodate IR or XUV beam, gas injection and the electrodes are set to provide an accelerating potential. Equipotential lines are shown on figure 2.10.

2.3.2.2.1 Injection of the IR beam The infrared or XUV beam is coming vertically on the figure and usually focused in the interaction zone of the TOF. The focusing is necessary to obtain high intensity in the interaction zone and to keep the interaction zone as small as possible. With large interaction zone the resolution of the TOF is decreasing.

In general there are two ways to focus the beam into the interaction zone. Either the focusing optics is before the TOF spectrometer, or it is in the spectrometer. In the first case the focusing optics is typically a toroidal mirror with grazing incidence and long focal length, the second case is typically a normal incidence spherical mirror with a very short focal length. The toroid mirror is very useful when there is a need to have the beam even after the interaction zone. However the proper alignment of an toroid mirror is tricky and difficult and it can induce aberrations [Bourassin-Bouchet 10]. The spherical mirror in the TOF is much compact than the toroid mirror and easier to use. However, the reflexion coefficient for XUV of normal incidence is very low (typically bellow 5% for gold mirror and harmonic 21[4]).

From the point of view of maximum obtainable intensity in the interaction zone the toroidal mirror provides a higher reflectivity but larger focal spot with aberrations and

[4]Wavelength of 38.5 nm.

the spherical mirror focuses the beam to much smaller spot but the reflectivity is poor. At the end, the final choice between the toroidal mirror placed before spectrometer and spherical mirror placed in the spectrometer, lies on special characteristics of the application or characterization method.

We choose the spherical mirror under normal incidence to have the smallest focal spot possible and high XUV intensity in the interaction zone.

2.3.2.2.2 Gas injection The gas to be measured is often injected with a needle under controlled pressure. Using a needle can profit from much higher gas density in the interaction zone and much less pressure in the acceleration zone. The point is to have enough particles to be ionized and no neutral particles that can interact with the charged particles in their way to the detector.

There is one needle issue to be considered. The needle, when placed close to interaction zone, can disturb significantly the equipotential lines in the interaction and acceleration zone. Therefore an optimal needle - beam distance is a trade-off between high signal corresponding to high pressure and disturbing the signal corresponding to accelerating potential that accelerates no more towards the detector. In our experiments the needle was placed 4 millimeters above the beam.

There is also one issue with the high pressure and intensity in the interacting zone. When ionizing a lot of atoms in a small volume, their distance is small enough to put the Coulomb force to play. The ions flying towards the detector repulse each other widening the transversal size of the ion bunch and, more importantly, accelerating the ions at the head of the bunch and decelerating ions at the tail. The phenomenon is called space charge effect and it decreases significantly the resolution of the TOF spectrometer.

2.3.2.2.3 Accelerating potential An acceleration potential is necessary to drive the charged particles to the detector. It is achieved by applying a high voltage on electrode 1 (see figure 2.10) and connecting the electrode 2 and the chamber to the ground. The typical voltage on electrode 1 was 2 kV for positive ions detection and -0.1 kV for electrons. Note that the effective potential in the interaction zone is much lower.

The gas is injected in the way that its kinetic energy is perpendicular to the electric field vector in the interaction zone. In the acceleration zone the trajectory of ions has a parabolic shape. Therefore on electrode 2 the ions arrive about 1 mm lower than if their initial velocity was zero. This value corresponds to 1 kV of acceleration potential and the atoms initial thermal velocity corresponds to 0.038 eV. Note that all the atomic species of the same charge would follow the same trajectory in the TOF spectrometer. For electrons this can be neglected.

As seen on figure 2.10 the equipotential lines are not straight but curved. It is caused by the size of the electrodes compared to their relative distance. To have the lines straight one should increase the size of the electrodes or decrease their distance or put the interacting zone closer to the first electrode.

2.3.2.3 Free flight and detection of particles

In our TOF spectrometer we choose to use a normal incidence spherical mirror to focus a beam into the interaction zone. The mirror was unprotected gold with a focal distance of 10 cm. That means that the large incoming beam pass the interaction zone before being focused by the spherical mirror.

For a differential pumping there is only a slit 1 mm thick and 10 mm high in the center of the electrode that separates the acceleration and the free flight zone. Because of the curved potential the effective size of the slit gives 1/3 of the original size in both dimensions.

The free flight zone is between two electrodes connected to the ground so there is no acceleration. The pressure in this zone should be the best possible to reduce noise on MCPs and with a turbomolecular pump we managed to achieve around 10^{-8} mbar.

2.3.2.3.1 Detection of particles We used MCP to detect charged particles. The MCP were in a double stack configuration for optimal gain. They were manufactured by Hamamatsu company [Hamamatsu 06] and their operating diameter was 25 mm. There is a metallic anode on the output of the MCP. The created signal was acquired by an 1 GHz oscilloscope connected to the anode. A photograph of the MCP with their support is on figure 2.11.

The maximum applicable voltage was 1 kV on each MCP giving 2 kV on the pair. We used this maximum voltage in order to get the highest signal possible. Note that due to very high vacuum there was practically no noise detected even on maximal allowed tension.

The wiring of the detection setup is shown on figure 2.12.

To detect positive ions we applied a -2.2 kV on the first stage of the MCP, -0.2 kV on the second stage (giving -2 kV of the difference to accelerate the created electrons) and the anode was connected directly to the oscilloscope (i.e. to the ground). That gives -0.2 kV to accelerate the electrons from the second stage of the MCP to the anode.

To detect electrons we have to apply a positive voltage on both stages of MCP that implies also a high positive voltage on the anode. But it is not possible to connect high positive voltage to the oscilloscope so we are forced to add a capacitance before the oscilloscope and the resulting wiring is on figure 2.12 b).

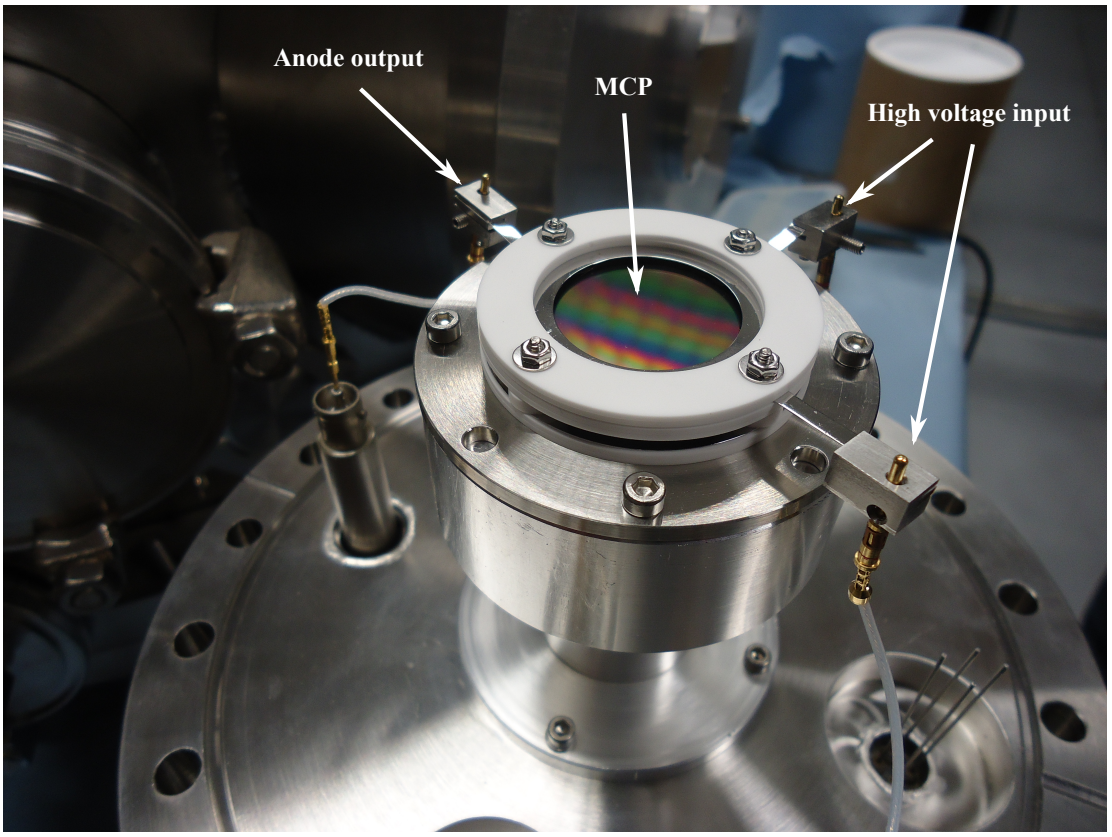

Figure 2.11 – (color) Photograph of MCP with its support.

2.3.2.3.2 Processing the TOF signal The MCP response to one ion is extremely nonlinear. In practice it means that signal can correspond to detection of one or more ions making the amplitude of the signal pulse meaningless. To circumvent this issue, we set the detection parameters such as beam intensity and pressure in the interaction zone so that, in average, we detect less than one event in one shot at a specific time of flight. Then a large statistics is needed to obtain a complete curve. To get rid of electronic noise we used a threshold in a postprocessing procedure. At the end each detection event was considered to be one ion.

A typical TOF spectrum is on figure 2.13.

On the figure 2.13 one can see a typical TOF spectrum acquired using argon as a detection gas. Note the atmospheric residuals as nitrogen, oxygen and water vapor, that is hard to pump. Also note that the Ar^{2+} position is $\sqrt{2}$ times lower than the position Ar^{+}, that is a direct consequence of equation 2.7.

2.3.3 XUV photodiode

XUV photodiode is a compact instrument to estimate the XUV photon flux. Our photodiode was manufactured by Osi optoelectronics and its product name is XUV-100. It has

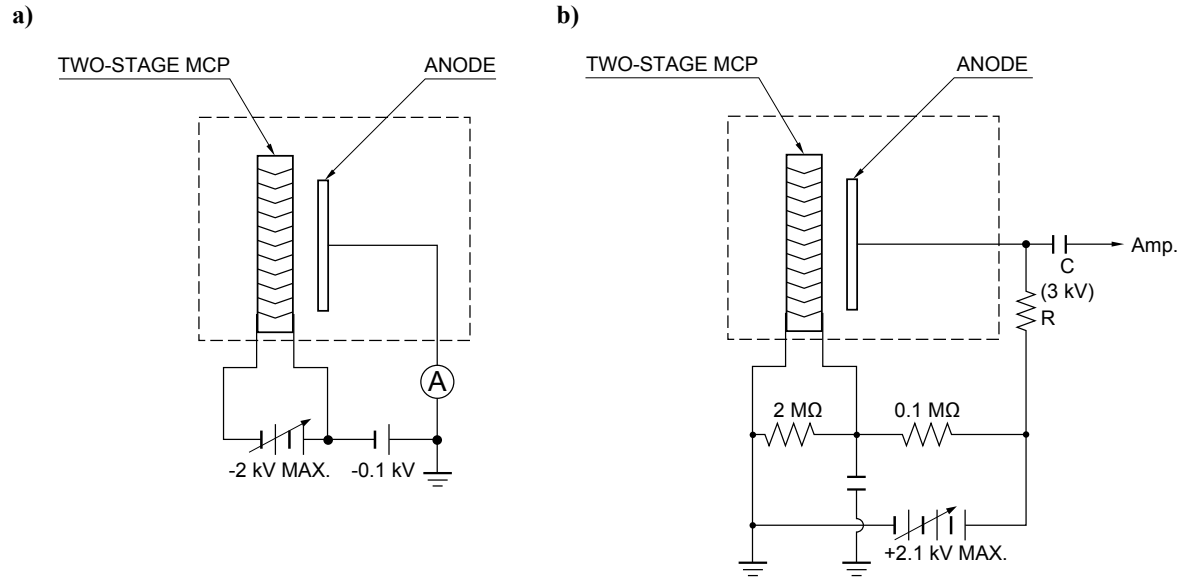

Figure 2.12 – Wiring of the MCP in the TOF a) When detecting positive ions b) When detecting electrons. (adopted from [Hamamatsu 06])

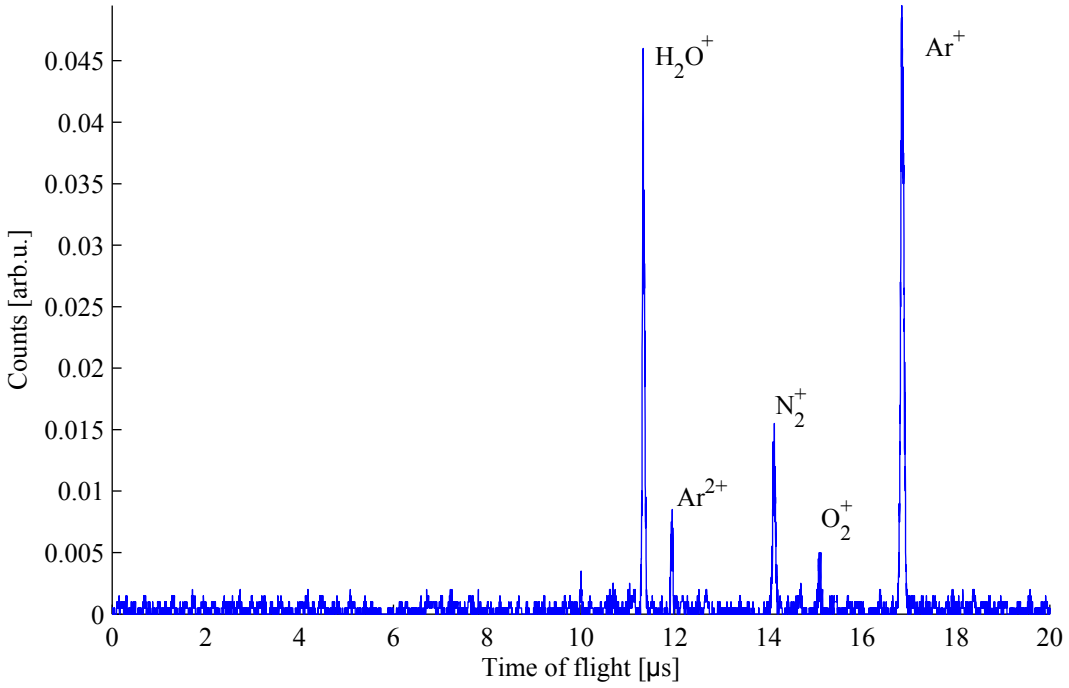

Figure 2.13 – TOF spectrum obtained with 10^{-6} mbar of argon in the TOF chamber injected by an needle. Note that the interaction zone pressure is much higher. XUV was generated in krypton jet.

a square shape with a size of 10 mm. We connect our photodiode directly to our 1GHz oscilloscope. The XUV photon number can be then calculated using «integral» function on the signal $\int U\mathrm{d}t$ typically in nV · s. Then the XUV photon number N_{ph} can be estimated by:

$$N_{ph} = \eta \frac{N_e}{h\nu_q}$$

where $\eta = 3.66\,\text{eV}$ is the energy needed to create one electron-hole pair that is provided by the manufacturer and $h\nu_q$ is the energy of harmonic measured. The number of electrons N_e can be estimated by:

$$N_e = \frac{Q}{e} = \frac{1}{Re} \int U \mathrm{d}t$$

where e is the electron charge and R is the oscilloscope resistance.

It is very important to block all the infrared radiation before the XUV photodiode. Usually this is achieved by mounting an aluminum filter in a vacuum valve. This way, the installation is leak-proof in terms of infrared beam. An aluminum filter transmits XUV radiation in the interval from 18 eV to 72 eV that corresponds to harmonic 13 to 47 in our case. We used two aluminum filters of thickness of 150 nm and 101 nm to block completely the IR radiation.

Maximal XUV photon number obtained with various geometries and gases is shown on table 2.3.

	Gas jet	8 mm cell	Pulsed 2.7 mm cell	Capillary
Neon	1.9×10^8			1.9×10^8
Argon	5.2×10^9	8×10^8	5.5×10^8	2.1×10^9
Krypton	3.1×10^9			
Xenon	3.3×10^9		5.5×10^8	1.2×10^9
Acetylene	2.2×10^9			

Table 2.3 – Maximal XUV photon number per shot generated in various geometries and gases. The value is an average of 100 shots and contains all the harmonics.

The table 2.3 shows the number of XUV photons detected by the XUV photodiode after consideration of aluminum filters transmission. Note that the values are low estimation as the photodiode is smaller than the XUV beam.

We can see that using cells to generate maximal number of photons is not the right way to go. One can obtain more photons with capillaries but most of XUV photons are generated in gas jet.

The choice of the gas is not so straightforward to maximize the photon flux. More gases provides high XUV photon number, argon can generate the most in all of the geometries tested.

Chapter 3

HHG with high energy long femtosecond pulses

As we have seen in previous chapter macroscopic effects play a major role in high harmonic generation process. In practice the most important macroscopic parameters that we are able to control are:

- Gas pressure: density of potential emitters in the volume of interaction
- Medium length: number of potential emitters and coherence length
- Laser intensity
- Laser focus position: Gouy phase and laser intensity spatial profile

For detection one adds:

- HHG medium to detector distance: XUV spatial size and profile on the detector
- XUV detector parameters (resolution, spectral acceptance, efficiency,...)

but detection parameters in general were not tuned[1] in this work.

3.1 Comparison of different generating geometries

Regarding parameters mentioned above there were three different HHG in gas implementation developed worldwide: gas jet, gas cell and gas filled capillary. Table 3.1 summarizes their general characteristics.

[1] With a very exception of spectral region of interest of the detector.

HHG source type	Gas jet	Gas cell	Gas filled capillary
Operational mode	Pulsed or continuous	Pulsed or continuous	Continuous
Medium length	Short(< 1 mm)	few mm to few cm	Long (few cm and more)
Medium pressure	Few tens of mbar	mbar to hundred of mbar	mbar to hundred of mbar

Table 3.1 – General comparison of HHG sources in gas

3.1.1 Gas jet

Gas jet is often used as a simple way to perform HHG. It is because of practically no need of beam alignment, robustness and relative ease of use. The main characteristics is the fact that the gas is not confined in the gas-laser interaction zone but expands freely into vacuum of HHG chamber.

The gas jet we used is called «Series 9 Pulse Valve» and was distributed by Sensortechnics company; its schematic drawing and photo can be found on figure 3.1.

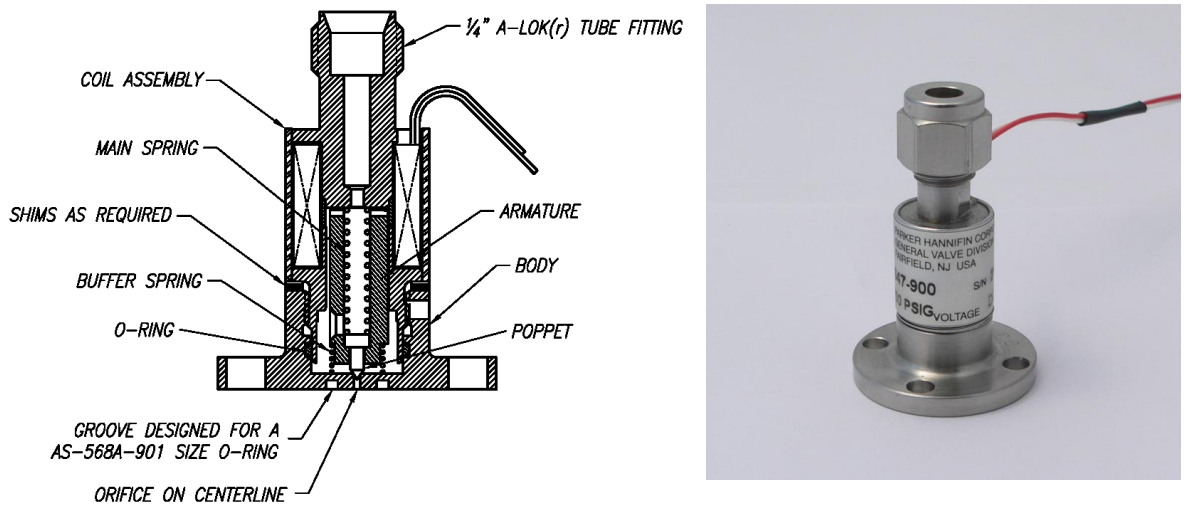

Figure 3.1 – Gas jet used in experiments

Gas jet power supply provides configurable electric pulses to an electromagnet whose core move upwards to open an exit orifice or downwards to close the exit when the current is off. That way the gas jet can be considered as a motorized binary (on/off) valve. Leaking is prevented by a contact of stainless steel orifice and a Teflon poppet - the end pike of the coil core.

A gas jet synchronization with laser pulses is obtained with a Stanford Pulse Generator triggered by laser chain masterclock signal. In most of the experiments the gas jet «go

open» trigger signal was set to 850 μs before the laser pulse[2]. This delay is caused by limited speed of valve opening and is not a limiting factor in our experiments at 10 Hz.

The opening time is typically 550 μs and the synchronization is set in the way that the laser pulse interacts with the expanding gas when its atomic density is close to maximum. Shorter opening time causes decrease of the maximum obtainable gas pressure while longer opening time doesn't raise significantly the gas pressure. Moreover it increases gas overall consumption and raise pressure in HHG vacuum chamber close to the maximum pumping load of turbomolecular pump and with heavier gases as krypton or xenon can lead to turbo pump overheat or damage.

The gas injection by the nozzle leads to a conical expansion with a cone angle of about 55° FWHM. The value was experimentally determined using a CCD camera acquiring a gas jet side image. The laser ionized the gas jet and the size of plasma was measured for several laser-nozzle distances. The gas was ionized by 60 mJ pulses clipped by 20 mm diameter iris in argon jet of backing pressure of 4.2 bar placed in the focus.

The nozzle head was machined to minimize more the jet-beam distance as shown on figure 3.2.

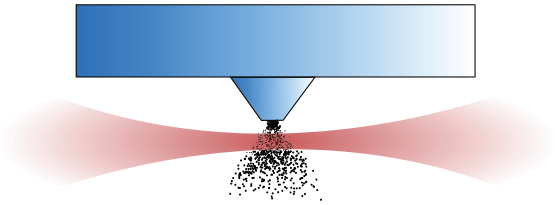

Figure 3.2 – Schematic detail of gas jet and laser beam configuration.

In that way, the atomic density in the interaction zone was maximized to optimize the XUV yield as it will be shown later. With a gas jet orifice of 250 μm the medium length is about 750 μm in the interaction zone.

This is important for the adjustment of several parameters:

1. The medium length (750 μm) is much smaller than infrared beam Rayleigh range z_R ($z_R = 10$ mm for fully open iris diameter of 30 mm, 2 m of focal length and collimated beam radius of $w = 10$ mm at I_{max}/e^2).

2. A spatial coherence of the beam is preserved

The last thing to consider is the asymmetry of the gas spatial profile. Using cylindrical orifice results in cone-shaped gas profile so that the part of the beam closer to gas nozzle

[2]Recall that the laser repetition rate is 10 Hz giving a time interval of 100 ms between two consecutive laser pulses.

interacts with shorter and denser medium than the opposite one. Considering the slope of the gas density (around 55 degrees the cone angle) and the small beam size (often near focus) this aspect is nearly always completely neglected in the literature and it will be neglected in this work as well. However, this assumption should be reconsidered when working with very large laser beam. The atomic density scales with $1/L^2$ where L stands for the medium length. The medium is shorter on the beam side close to gas jet nozzle making the atomic density much higher on one side of a large-diameter beam than on the other.

There are also other types of gas jet with a very low divergence of emitted gas (e. g. Even-Lavie) but the price is much higher than the price of ordinary gas jet (e. g. our gas jet) and they are also more delicate than our. The gas jet we used was very robust and this was an important advantage for us.

At working temperature (room temperature), our backing gas pressure (up to 6 bars) is too low to form clusters in the gas jet.

3.1.2 Gas filled capillary

Gas filled capillary promotes in many ways characteristics opposite to gas jet. The gas medium confined in the capillary is much longer than that of the gas jet and the infrared pulse spatial mode is strongly influenced by the coupling and guiding. Moreover the pulse propagates and ionizes the gas at the same time causing frequency and phase modulation. The critical experimental condition to fulfill is the proper injection alignment i.e. the beam has to be perfectly aligned in the capillary axis and the focal spot has to be placed at an entrance of the capillary.

The gas confinement in the capillary is obtained either by putting the capillary in the gas between two windows or by injecting the gas via a side hole. We used the latter option in order to avoid transmission through a material that can cause many nonlinear effects. Drilling a hole in the glass capillary cladding is a tricky task while special attention has to be taken to make the hole in the core as clean as possible and avoid any glass fragments remaining in the core.

The gas injection is continuous under a controlled pressure.

Depending on gas pressure there are two major types of HHG:

Low pressure permits harmonics generated at the beginning of the capillary to propagate through the sparse gas medium until the end and therefore they can be detected. In this case, the phase-matching counts strongly for spatio-spectral distribution of the harmonic signal because the effective medium length is high and δk is crucial [Rundquist 98].

High pressure does not allow the harmonics to propagate in the gas because of absorption length that is much smaller than the medium length [Constant 99]. All the generated XUV photons are almost immediately reabsorbed and therefore just the harmonics generated at the end of the capillary can be detected. Then the effective length is small and the case becomes similar to the gas jet. The difference is that the fundamental beam can be significantly perturbed by propagation before generation of high harmonics.

3.2 Experimental setup

We performed experiments with both geometries. The schematic principle of the experimental setup is on figure 3.3. The collimated infrared beam enters the vacuum in the

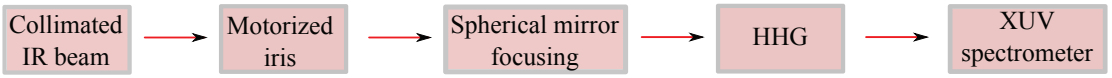

Figure 3.3 – Draft of the HHG experimental setup. The arrows represent beam propagation.

compressor and stays under a vacuum everywhere. When fitted with a Gaussian shape the size of the collimated infrared beam is $w = 10\,\text{mm}$ (a waist radius at I_{max}/e^2). The beam is clipped by an iris that is controllable under vacuum. The beam is focused with a 2 m focal length spherical mirror to a pulsed gas jet. Note that in this configuration high harmonics are generated at high intensity even in the loose focusing regime and the peak intensity can be above intensity of barrier suppression of the atomic target. The values of barrier suppression intensity I_{SB} are shown in table 2.1 on page 28.

An adjustable iris allows controlling the HHG parameters such as intensity and beam size in the generating medium. The gas jet (detailed in section 3.1.1) is operated under backing pressure of few bars depending on the gas used. After HHG, the XUV beam is transmitted through a differential pumping tube and propagates toward a mobile XUV spectrometer or applications. A $500\,\mu$m vertical slit is in the distance of 119 cm (from the gas jet) located at the entrance of a flat-field XUV spectrometer. The spectrometer is detailed in section 2.3.1 on page 35.

The figure 3.4 shows the detailed experimental setup. Vacuum chambers and beam path is shown to give a more definite idea of the experimental setup size. The second biggest chamber in the setup (HHG chamber) is based on DN200KF vacuum tubes (i.e. the inner diameter around 20 cm) where the gas jet is placed with 3-axis translation stages. The z-axis (the axis of the beam) translation stage range is 15 cm and the x and y-axis translation stages range of 25 mm. In that way we can move the gas jet over 7.5 cm around

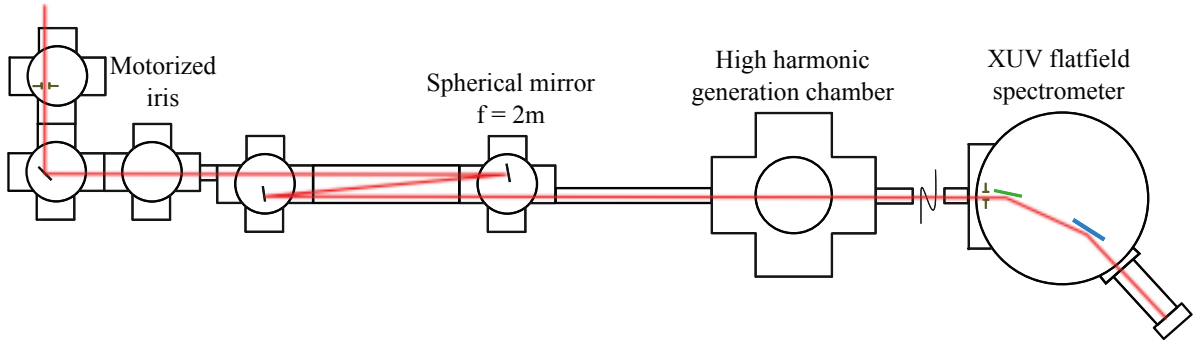

Figure 3.4 – Experimental setup in detail

the focus at z = 0 and change significantly the medium length and atomic density in the interaction zone.

The DN160KF vacuum chambers (i.e. the inner diameter around 16 cm) allow one to pass 3 beams while using standard supports of 2 inches mirrors or 2 beams using motorized supports.

The Z-shape beam path of a focusing mirror and the flat mirror before entering the HHG chamber is necessary because direct focusing to the gas jet is not possible due to small size of our experimental room that is only 5 by 6 meters. Note that while using this high energy femtosecond laser beam, no optics can withstand the fluency close to the focus, defining the minimum distance to the focus for focusing optics as well for characterization instruments (e.g. XUV spectrometer) and applications.

The importance of controllable iris is wide. One can easily tune the intensity and focal spot size in the generating medium and also the spatial phase (phase front) and intensity profile when the medium is not at focus. This would finally have a lot of influence on the generated XUV spectra as we will see later and also this is absolutely necessary for spatial shaping technique via reflective phase mask (section 4.2 on page 166).

3.2.1 Examples of experimental results

The experimental setup described above gives us an opportunity to observe spectrally and spatially resolved single-shot XUV profiles in the far field generated with high energy driving pulses. On figure 3.5 we show some examples of such XUV profiles.

The figure 3.5 shows experimental far-field spatially and spectrally resolved XUV profiles generated in argon and krypton in various conditions but with high energy long pulses (about 50 fs). The harmonics are of different shapes and contain spatio-spectral structures.

In literature such features are often assigned to phase-matching conditions via propagation of the XUV in the generation medium. Complex simulations of the propagation in the generating medium were also performed to explain such phase-matching.

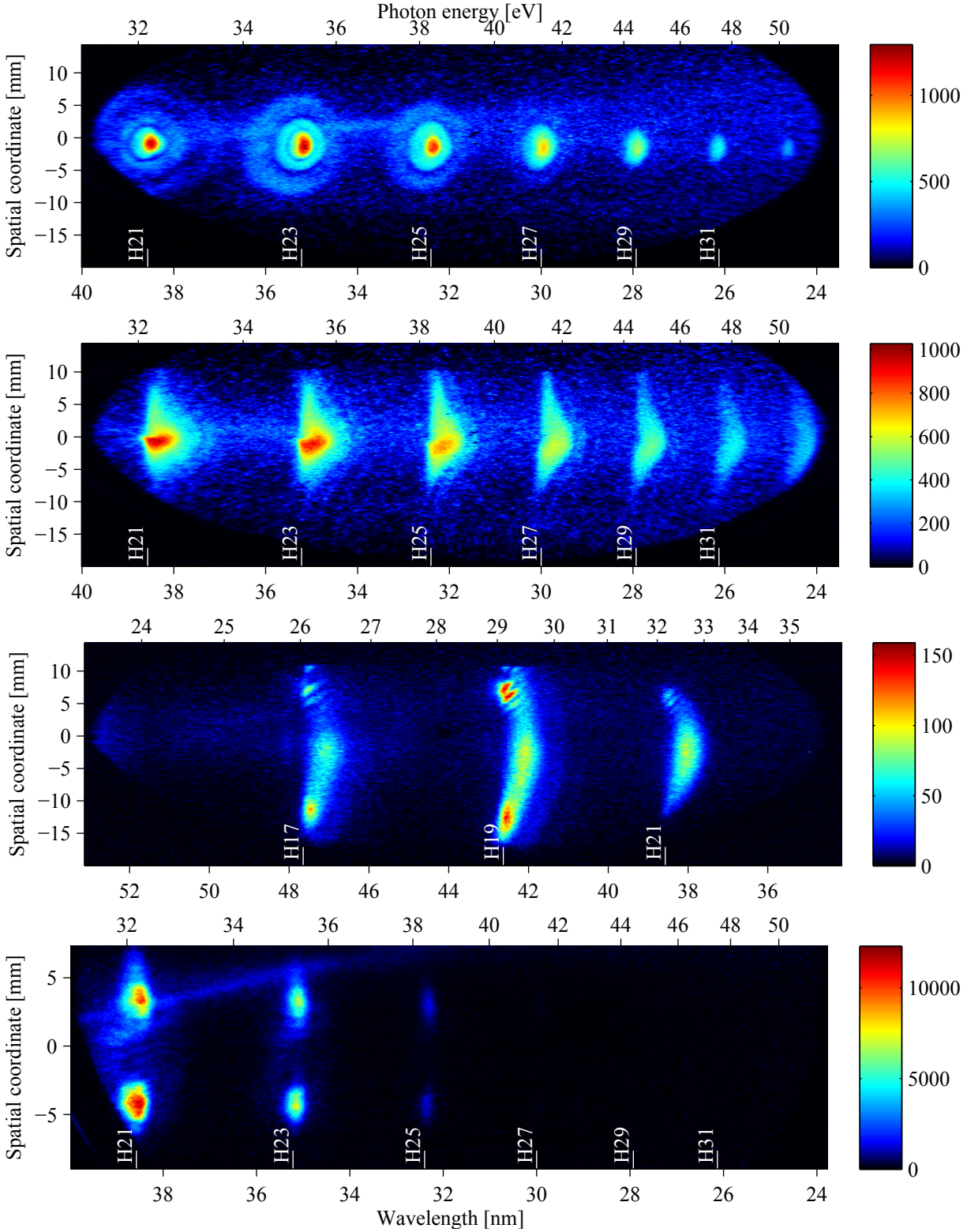

Figure 3.5 – (color) Experimental far-field spatially resolved XUV single-shot spectra generated in a) argon jet in the focus with 75 mJ before iris of 10 mm diameter, b) argon jet in the focus with 75 mJ before iris of 14 mm diameter, c) krypton jet 11 mm after the focus with 22 mm iris diameter and d) krypton jet 18 cm before the focus with 75 mJ before iris of 12 mm diameter. Note that the spectra were taken under different conditions and with different detection instruments. Therefore the intensity (colormap) should not be compared directly.

The structures present in XUV profiles on figure 3.5 are very regular and robust. Intuitively one feels that a simple explanation of such structures is more appropriate than complex propagation simulations that includes a lot of parameters.

The simulation of HHG without the propagation in the medium would reveal features in XUV profiles that are not caused by propagation. As generated in gas jet, one approach a case where the medium length is close to zero lowering the role of the propagation. The numerical model is described in following section.

3.3 Simulating the HHG

3.3.1 Simulation overview

To understand our results and get a deeper insight into HHG at high energy we performed simulations involving controllable experimental parameters. A wide study for harmonics generated in gases at high intensity is still missing in the literature so we decided to create a simulation for all the parameters that we used during our experiments.

Our simulations follow on schematic experimental setup presented on figure 3.3. We start with a Gaussian pulse in collimated Gaussian beam. The pulse is centered at 810 nm and is transform limited to 55 fs FWHM.

The infrared beam is clipped by iris and diffracted via Hankel transform to the position of the infinitesimally thin gas jet. For more details on Hankel transform see appendix A.

The XUV beam is then numerically «generated» from the infrared driving pulse/beam in the medium. As this is the heart of the whole simulation where the most of approximations are taken, we dedicate whole section 3.3.2 to it.

The XUV beam is then diffracted via Hankel transform to the observation plane representing the MCP in the XUV spectrometer.

To summarize the whole simulation let's recall that we begin with temporal Gaussian pulse in Gaussian beam. Then we perform (in the order) temporal Fourier transform, Hankel transform (including focusing and propagating to the gas jet), Fourier transform, HHG, Fourier transform and Hankel transform to retrieve our spatially resolved spectra on MCPs.

In that way, we should obtain reliable results where a lot of information could be obtained about spatially resolved XUV spectra and their homogeneity.

With 4096 points in the temporal/spectral axis and 512 points in spatial axis the calculation of one spatially resolved spectrum takes around 40 minutes.[3]

[3]Performed with 64-bit Intel Core i5 M450 processor and 4 GB of RAM.

Such high time consumption was also the main reason why we cannot simulate the radiation of less than 29 nm (more than 42 eV). Widening the spectral window would force us to raise the time/spectral number of points in order to avoid sampling issues. More points would raise the memory consumption and the time spent on each spectrum to too high levels.

Our spectral window can support up to harmonic order 25. We decided to stop at the order 21 to avoid spectrally cut the harmonic signal under certain parameters which can be very misguiding during interpretation. Anyway one should not forget that the first (H11) and last (H21) harmonic should be examined with special attention because they have neighbor harmonics only from one side. The interference patterns could be less structured therefore.

3.3.2 HHG calculation

The XUV beam is numerically «generated» in an infinitesimally thin layer located at the gas jet position by considering that an infrared field of intensity I_{IR} and phase φ_{IR} creates a harmonic field E_q with phase φ_q

$$E_q(t,r) = |E_{IR}(t,r)|^{q_{eff}(I_{IR})} \cdot e^{i\varphi_q(t,r)} \tag{3.1}$$

$$\varphi_q(t,r) = q\varphi_{IR}(t,r) - \alpha(I_{IR})\, I_{IR}(t,r) \tag{3.2}$$

where odd integer q denotes harmonic order and $q_{eff}(I_{IR})$ is an effective order of nonlinearity. We took $q_{eff} = 1.5$ [Heyl 11, Wahlström 93] for intensity higher than the specific harmonic cutoff intensity and $q_{eff} = q/4$ for the intensity below the cutoff [Wahlström 93] as illustrated on figure 3.6 a). It shows the infrared and XUV modulus with and without considering that the harmonics are generated for lower intensity than a cutoff intensity I_{cutoff} (see equation 2.4 on page 29) with the same q_{eff} i.e. with and without considering that the q_{eff} is independent on the driving field E_{IR}.

The figure 3.6 b) shows the harmonic dipole dependance on driving field intensity for harmonics 21, 19 and 17. Note that the part of the curve below the cutoff intensity was adjusted by a linear factor to equal the plateau curve at the cutoff intensity.

The equation 3.2 expresses the harmonic phase that is connected to infrared (driving) phase and that scales also with local intensity through the harmonic dipole phase (more in section 2.1 on page 23). In the plateau the value of α equals $1 \times 10^{-14}\,\mathrm{cm^2/W}$ for short trajectory and twenty five times more e.g. $2.5 \times 10^{-13}\,\mathrm{cm^2/W}$ for long trajectory [Gaarde 02]. For $I_{IR} < I_{cutoff}$ the $\alpha = 13 \times 10^{-14}\,\mathrm{cm^2/W}$. The relative weight of short and long trajectory was taken to be 1:1 in the instant of generation.

The relative weight of short and long trajectories in the generating medium depends on

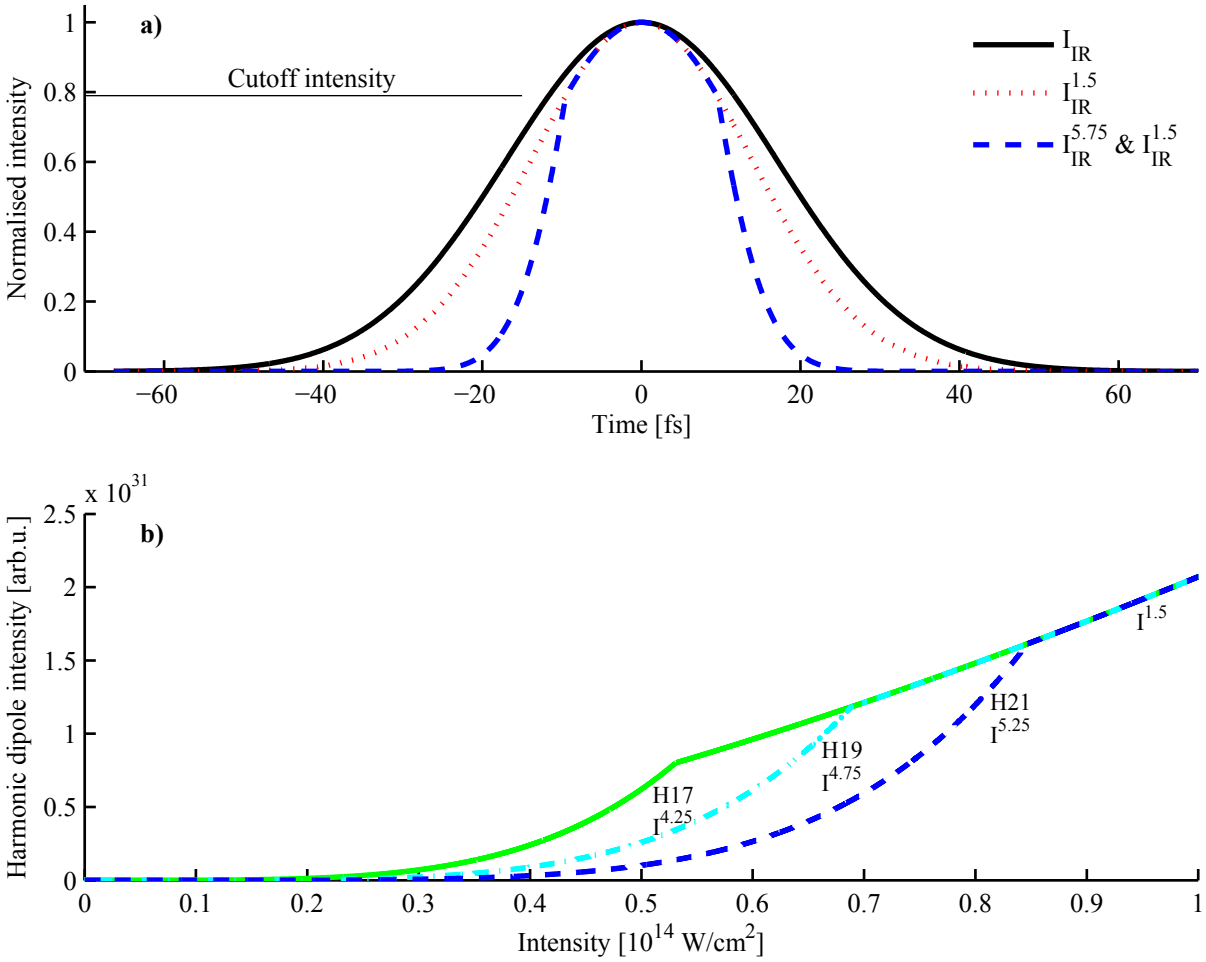

Figure 3.6 – (color) Calculated a) normalized harmonic dipole intensity (blue dashed) compared to driving beam intensity (black solid). This illustrative case is for pulses of 40 fs and intensity of 10^{14} W/cm² and harmonic 21 generated in argon. The red dotted curve stands for unreal case of «plateau everywhere» and is issued just for comparative purpose. b) Comparison of harmonic dipole intensity dependence on driving intensity for harmonics 17 (green solid), 19 (magenta dash-dotted) and 21 (blue dashed).

many parameters such as harmonic order, intensity and fundamental wavelength. It was published for H17 and H21 in [Strelkov 06a] where the author found the long trajectory contribution much less than in the original Lewenstein model (and in accordance with [Gaarde 02]). Calculating the quantum paths amplitudes for all harmonics and intensity interval of interest is possible via 3D TDSE and exceeds the purpose of this simulation so I took the quantum paths amplitude ratio as 1:1 as proposed in [Strelkov 06a].

Note that the intensity dependent phase in equation 3.2 induces directly the frequency shift of the harmonic wavelength. The angular frequency can be expressed as

$$\omega_q(t,r) = \frac{\mathrm{d}\varphi_q(t,r)}{\mathrm{d}t} = \alpha \frac{\mathrm{d}I_{IR}(t,r)}{\mathrm{d}t}$$

giving frequency blue shift at the rising edge of the driving IR pulse and a red shift at

the falling edge.

For higher intensities, where ionization degree reaches 100% during the pulse propagation it is important to suppress the HHG in places where there are no more neutral atoms e.g. no more emitters available.[4] In our simulation, this is achieved by calculating the ionization degree n_i in every point of our driving pulse through time and space and putting the HHG yield multiplied with $1 - n_i$. The ionization degree is defined between 0 and 1 corresponding to 0% and 100% of atoms ionized and was calculated in argon using improved ADK model by [Tong 05] that treats better the ionization under high intensity fields than original ADK model by [Ammosov 86].[5]

In our approach of the HHG approximation we do not consider:

Propagation in the generating medium. Our assumption is valid only for very thin medium and low gas pressure.

Attosecond chirp. As we saw in section 2.1 on page 23 all the harmonics are not generated at the same time during the driving field optical cycle. This is found to be a phase difference for different wavelengths - in other words the attosecond spectral chirp. This omission, however, does not affect the XUV spectra.

Short and long trajectory relative weight and phase difference. Short and long trajectory relative weight may not be equal and may even vary across the harmonics. The phase difference changes from cycle to cycle moving accordingly interference maxima and minima. This omission implies that interference patterns position is arbitrary.

Omitting such features one gets results on others features, that are included in the simulation.

In our experimental conditions of high energy driving pulses, we believe that driving beam spatial phase and intensity and depletion together with spatial coherence of XUV radiation have a major impact and impose **far-field** spatio-spectral harmonic profile even without propagation. Often in literature the far-field harmonic spatio-spectral profiles are linked to propagation in the generating medium. In our simulation we neglect propagation to highlight the other effects.

[4] With the intensity high enough one can generate harmonic even in the completely ionized medium - HHG in ions. We neglect the possibility of harmonic generation in ions mostly because the harmonic yield from ions is not well known to date so the signal coming from HHG in ions will present a poorly controlled additional parameter.

[5] The improved ADK model was successfully compared to TDSE calculations up to 2.5 times the barrier-suppression intensity threshold [Tong 05]. In our case it can be used for even higher intensities because at 2.5 times of barrier-suppression intensity the medium is already completely ionized suppressing the influence of further ADK calculations to zero.

3.3.3 HHG at low intensity driving pulses

To begin let's consider situation of HHG in argon at low intensity of $10^{14}\,\mathrm{W/cm^2}$ (compared to barrier suppression intensity I_{SB}) where the total ionization of the medium is well bellow 0.1%. The driving collimated beam size is $w = 10\,\mathrm{mm}$ (a waist radius at I_{max}/e^2) that is slightly clipped by a 30 mm diameter iris. The beam is then focused by 2m focal length mirror to a gas jet placed 10 mm before the focus. It gives a beam radius in the medium of $w = 64\,\mu\mathrm{m}$ @ I_{max}/e^2 and pulse energy 0.27 mJ. Those parameters were chosen as illustrative according to the real experimental setup where 30 mm corresponds to maximal aperture of 2" optics. The iris diameter and the gas jet position were chosen to support the infrared beam profile that is close to Gaussian one with a phase that is not disturbed too much. Moreover it eliminates the special case when the gas jet is in the focus so the beam profile is Gaussian with a flat phase.

3.3.3.1 Near-field spatio-temporal XUV profile

Figure 3.7 shows the spatio-temporal profile of the XUV generated in the gas jet (before diffraction).

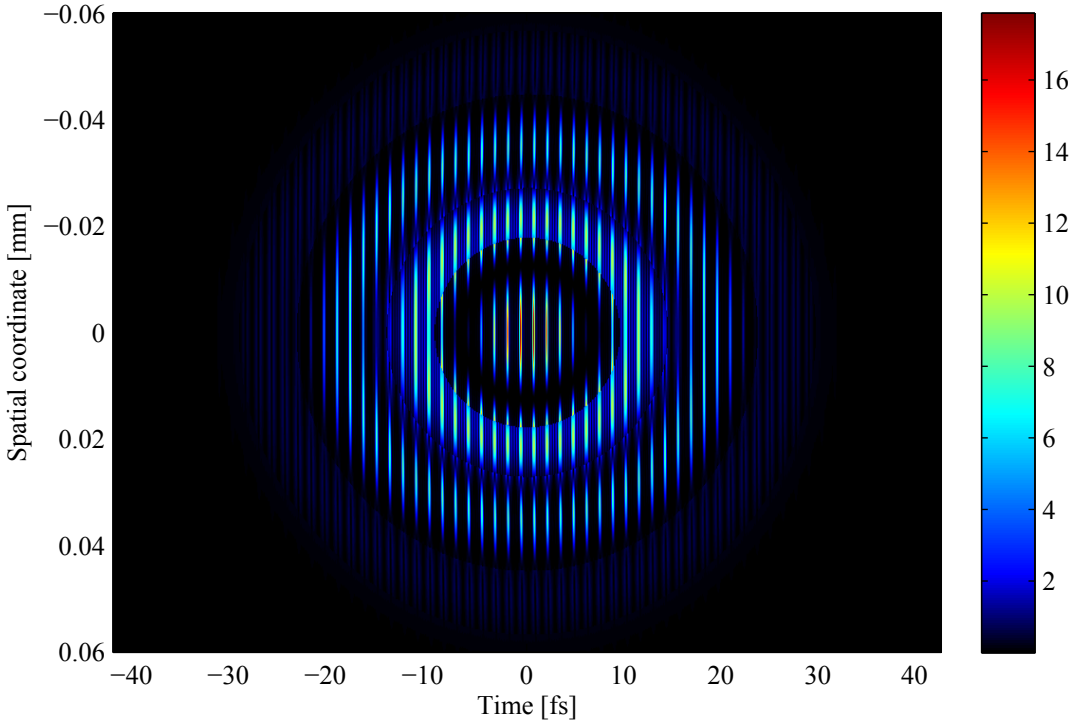

Figure 3.7 – (color) Simulated XUV spatio-temporal profile in the argon gas jet (near-field) for $I_{max} = 10^{14}\,\mathrm{W/cm^2}$. The spectral window is from 30 to 80 nm (harmonics 11 to 21). The colormap is linear and in arbitrary units.

The maximum of intensity is at center corresponding to the infrared pulse peak center

and we can also see a clear interference pattern evolving in time and space.

There are 2 things to notice. First, the XUV spatio-temporal intensity profile follows on driving pulse profile. This is the direct result of equation 3.1. Second, there are many temporal and spatial structures. To study quantitatively the temporal structures the XUV emission on axis is plotted on figure 3.8 and overall integrated spatial signal is on figure 3.9.

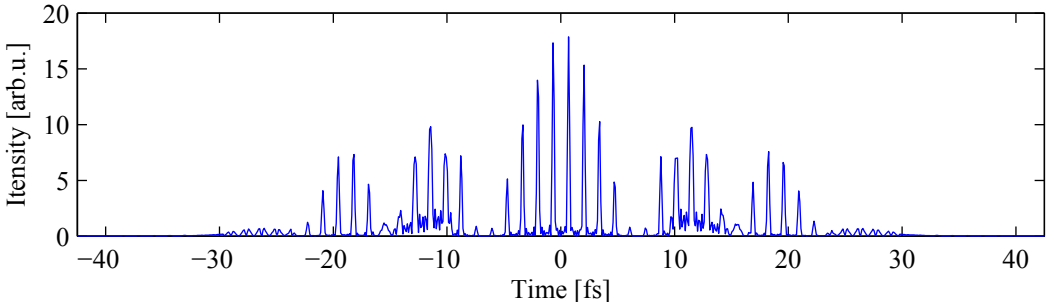

Figure 3.8 – XUV temporal profile on axis in the gas jet. Contains harmonics 11 - 21 and the peak IR intensity is $I_{max} = 10^{14}\,\mathrm{W/cm^2}$.

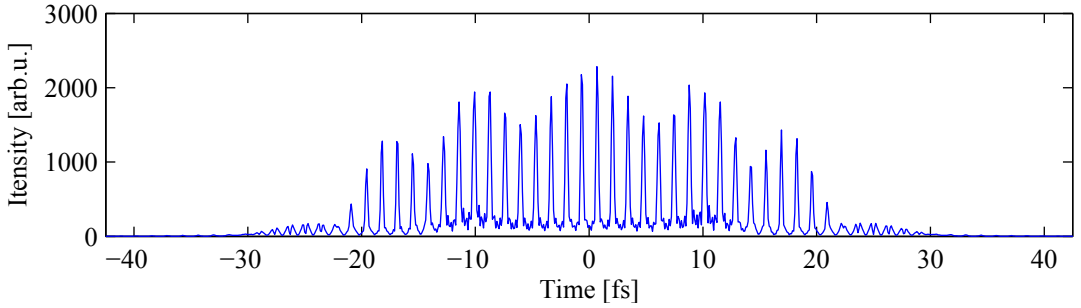

Figure 3.9 – XUV temporal integrated profile in the gas jet. Contains harmonics 11 - 21 and the peak IR intensity is $I_{max} = 10^{14}\,\mathrm{W/cm^2}$.

The small temporal fringes (attosecond pulse train) correspond to several harmonics beating. In other words summation of several electric fields of harmonic 11, 13, 15, 17, 19 and 21 defined by first term in equation 3.2 gives an interference pattern with characteristic duration of 1.35 fs corresponding to their spectral difference $2\omega_0$ where ω_0 denotes driving field central angular frequency corresponding to 810 nm.

From another point of view one expects one attosecond pulse to be generated twice during the driving pulse optical cycle (as discussed in section 2.1) giving also 1.35 fs between two maxima. Note that actually there should be 4 attosecond pulses emitted during a driving pulse - 2 for short path and 2 for long path. However, in our simulation both paths are created at the same time producing only 2 attosecond pulses per driving pulse optical cycle and a temporal fringes pattern with typical size of 7-10 fs.

The temporal fringes pattern with typical size of 7-10 fs in time and 20 μm in space is due to the second term of equation 3.2 revealing the interference between the short and

the long path $\alpha_{short} I - \alpha_{long} I$. The position of maxima and minima are just defined by their offset in the simulation. As we already discussed in section 3.3.2 this offset depends only on infrared intensity via $(\alpha_{short} - \alpha_{long})\, I_{IR}$. As we will see later this would change the interference pattern in near field but its importance largely vanishes in the far field where the relative weights are very different for the two trajectories.

To illustrate the influence of the short and long path, we first suppressed the long path (figure 3.10) and afterward the short path generation (figure 3.11).

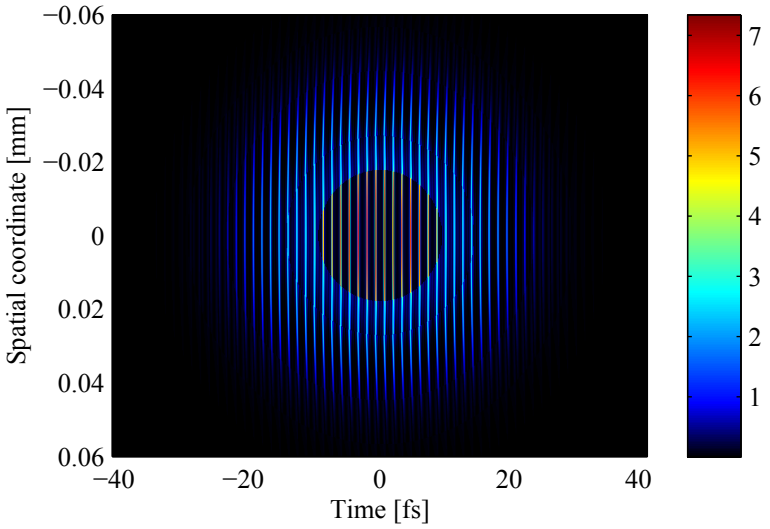

Figure 3.10 – (color) Simulated spatio-temporal profile of harmonics 11, 13, 15, 17, 19 and 21 in the gas jet (near-field) generated in argon at $10^{14}\,\mathrm{W/cm^2}$ with no long path ($\alpha = 1$ or $13 \times 10^{14}\,\mathrm{cm^2/W}$).

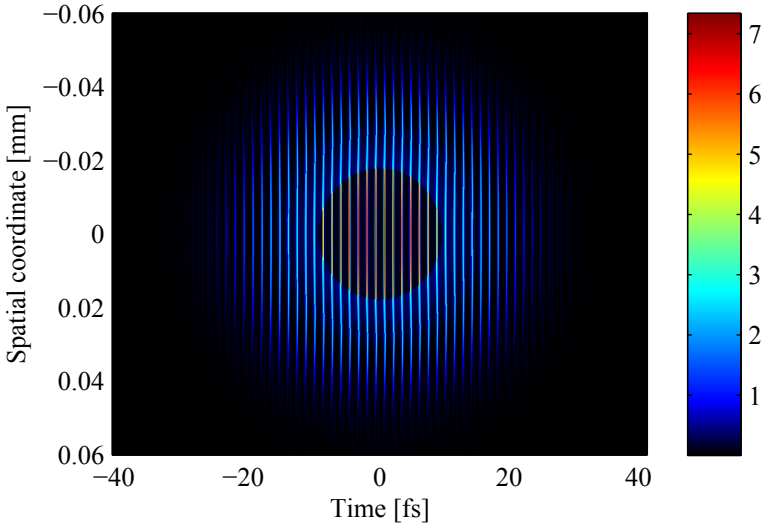

Figure 3.11 – (color) Simulated spatio-temporal profile of harmonics 11, 13, 15, 17, 19 and 21 in the gas jet (near-field) generated in argon at $10^{14}\,\mathrm{W/cm^2}$ with no short path ($\alpha = 13$ or $25 \times 10^{14}\,\mathrm{cm^2/W}$).

Important note on the nomenclature

As we will often exercise numerical results performed with and without short and long path, we would define the following terms:

No short path denotes spatio-temporal or spatio-spectral XUV profile where the short path is not included. Thus the simulation contains only long path for $I_{IR} > I_{cutoff}$ ($\alpha = 25 \times 10^{-14}\,\mathrm{cm^2/W}$) and for $I_{IR} < I_{cutoff}$ the $\alpha = 13 \times 10^{-14}\,\mathrm{cm^2/W}$. Note that this is very different from

Long path only, where $\alpha = 25 \times 10^{-14}\,\mathrm{cm^2/W}$ (corresponding to long path) independently on infrared pulse intensity I_{IR}. Correspondingly there is

No long path where the long path is not included but the short path ($\alpha = 1 \times 10^{-14}\,\mathrm{cm^2/W}$) is present for $I_{IR} > I_{cutoff}$ and for $I_{IR} < I_{cutoff}$ the $\alpha = 13 \times 10^{-14}\,\mathrm{cm^2/W}$.

Short path only, where $\alpha = 1 \times 10^{-14}\,\mathrm{cm^2/W}$ (corresponding to short path) independently on infrared pulse intensity I_{IR}.

No special term will be used in cases where there are both short and long paths present and for $I_{IR} < I_{cutoff}$ the $\alpha = 13 \times 10^{-14}\,\mathrm{cm^2/W}$.

Note that this nomenclature does not contain the value of the q_{eff} that will be specified.

We can see that omitting short path or long path suppresses the large interference patterns seen in figures 3.7 and 3.8.

We observe also noise between attosecond pulses even by considering a single path and still some modulation of the envelope (see figures 3.12 and 3.13).

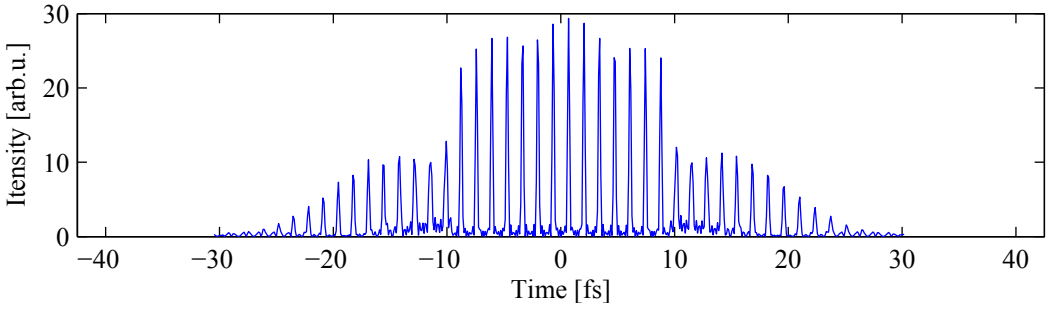

Figure 3.12 – XUV temporal profile on axis in gas jet for $I_{max} = 10^{14}\,\mathrm{W/cm^2}$ with no long path ($\alpha = 1$ or $13 \times 10^{14}\,\mathrm{cm^2/W}$). Contains harmonics 11 - 21.

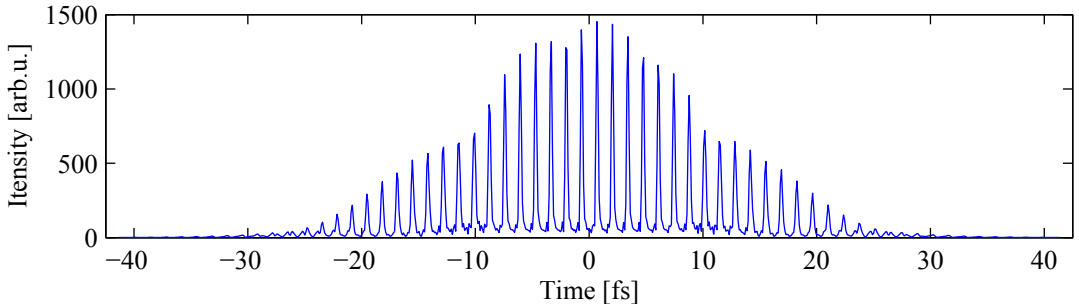

Figure 3.13 – XUV spatially integrated temporal profile in gas jet for $I_{max} = 10^{14}\,\mathrm{W/cm^2}$ with no long path ($\alpha = 1$ or $13 \times 10^{14}\,\mathrm{cm^2/W}$). Contains harmonics 11 - 21.

To understand this structures we changed the XUV dipole phase of the emission occurring at $I_{IR} < I_{cutoff}$ to the same value as short path. The results are shown on figures 3.14, 3.15 and 3.16.

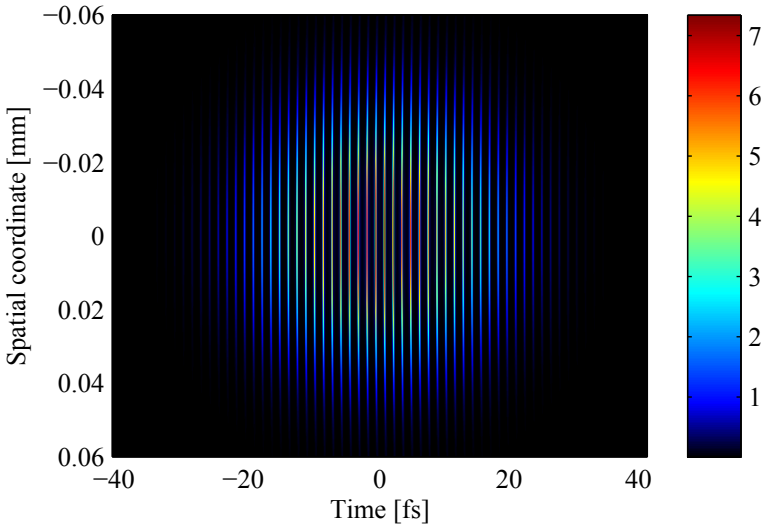

Figure 3.14 – (color) Simulated spatio-temporal profile in the gas jet of harmonics 11, 13, 15, 17, 19 and 21 generated in argon at $10^{14}\,\mathrm{W/cm^2}$ with short path only ($\alpha = 1 \times 10^{14}\,\mathrm{cm^2/W}$).

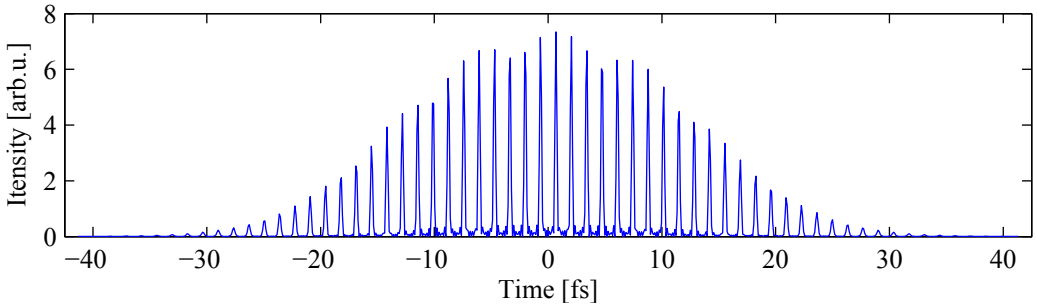

Figure 3.15 – Simulated XUV temporal profile on axis in the gas jet of harmonics 11, 13, 15, 17, 19 and 21 generated in argon at $10^{14}\,\mathrm{W/cm^2}$ with short path only ($\alpha = 1 \times 10^{14}\,\mathrm{cm^2/W}$).

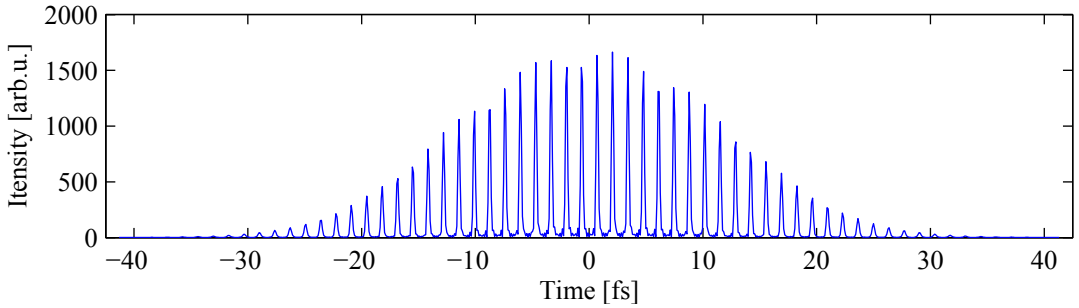

Figure 3.16 – Simulated XUV temporal spatially integrated profile in the gas jet of harmonics 11, 13, 15, 17, 19 and 21 generated in argon at 10^{14} W/cm² with short path only ($\alpha = 1 \times 10^{14}$ cm²/W).

All the structures in the envelope disappeared as can be seen on spatio-temporal profile on figure 3.14, on axis on figure 3.15 and in the spatially integrated temporal profile on figure 3.16. The attosecond pulses are still present as 6 different harmonics are considered. Note that the apparent small modulation of envelope is due to the resolution of the simulation.

Conclusion We have seen that long infrared pulses of 40 fs and low intensity of 10^{14} W/cm² would generate XUV radiation that is structured in time and space. We have observed attosecond pulses as temporally thin peaks. The envelope of attosecond pulses is highly modulated due to nonuniformity of harmonic dipole phase α that has different values when $I_{IR} < I_{cutoff}$ from $I_{IR} > I_{cutoff}$, with two different values corresponding to two different quantum paths. Coherent sum of all three different phase contributions results in large interference patterns in time for the envelope of attosecond pulses and also in space for each attosecond pulse.

3.3.3.2 Near-field spatio-spectral XUV profile

Performing temporal Fourier transform of the calculated spatio-temporal profile provides the near-field spatio-spectral XUV profile in the gas jet still at low intensity of 10^{14} W/cm² and practically no ionization in the medium.

The XUV profile resolved both spectrally and spatially is shown on figure 3.17. We can see spectrally narrow intense lines at the harmonic frequencies and spectrally broad structures around these lines. The spatio-spectral structures are direct result of structures of spatio-temporal profile.

To observe quantitatively XUV emission the on axis spectrum is shown on figure 3.18 and the spatial integration on figure 3.19.

The overall characteristic trend is that lower harmonics are brighter than the higher ones. But there is a slight modulation making the harmonic 15 weaker than harmonic 17.

Also a peak at the harmonic frequency is present except for harmonic 21 that consists

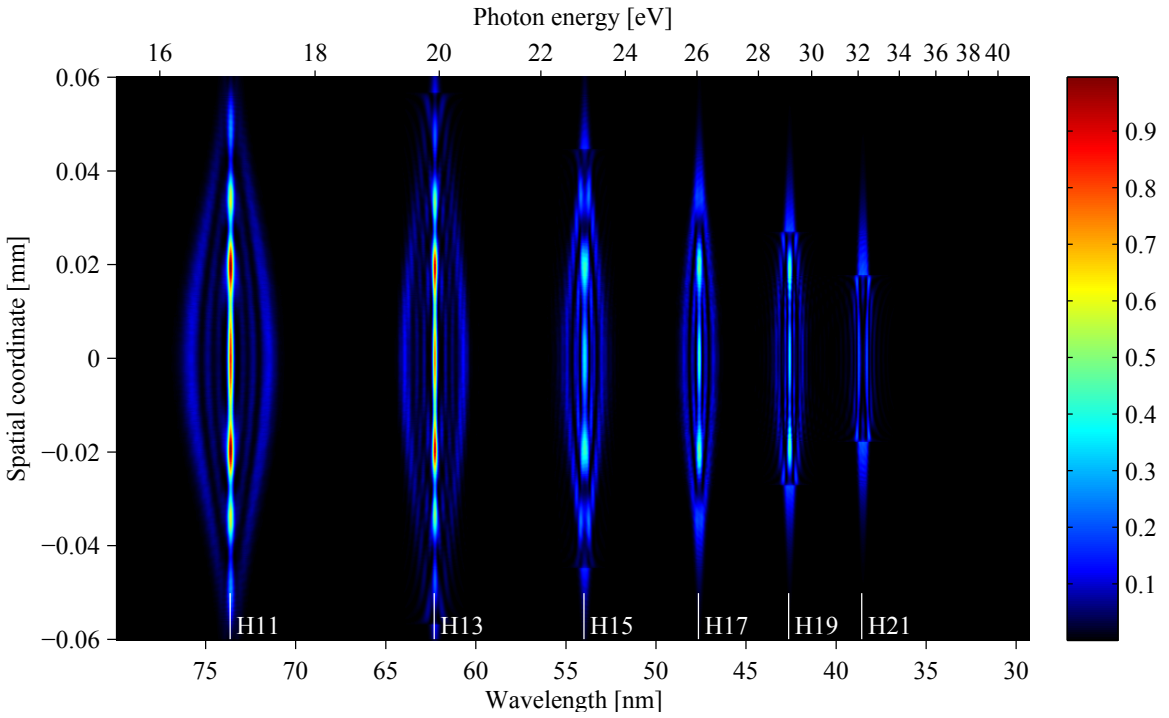

Figure 3.17 – (color) Simulated spatio-spectral XUV profile in the gas jet of harmonics (from left to right) 11, 13, 15, 17, 19 and 21 generated in argon at 10^{14} W/cm².

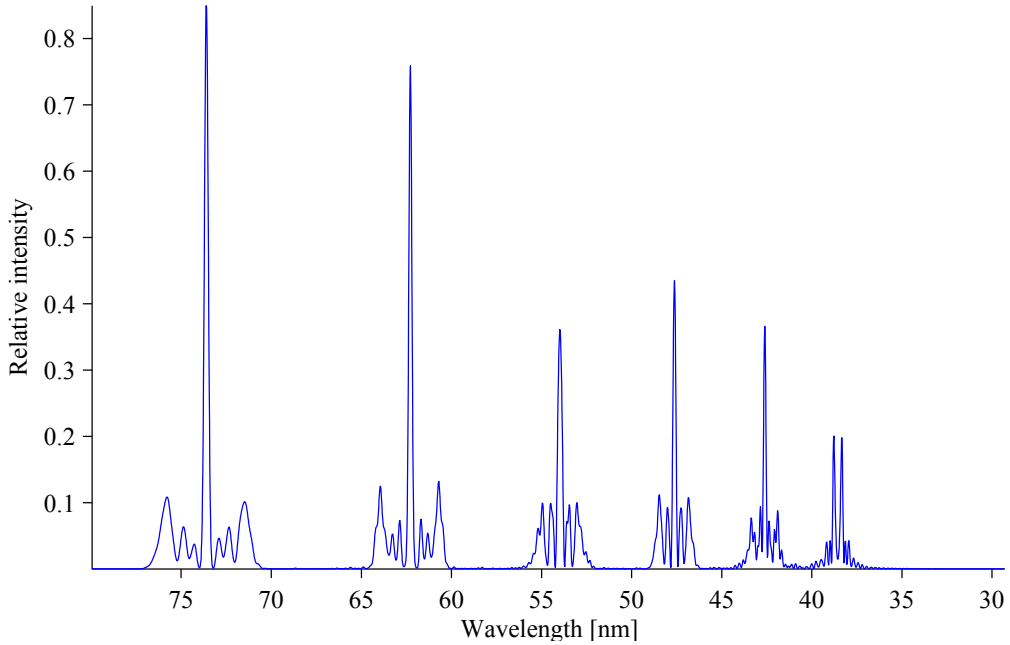

Figure 3.18 – Simulated on-axis XUV spectrum in the gas jet (near-field) generated in argon at 10^{14} W/cm². The considered harmonic orders are 11 - 21.

of two main peaks with a zero in between. With higher order of harmonics the spectrally wide structures approach the harmonic line causing interferences.

The spatial profile of harmonic 15 only is shown on figure 3.20.

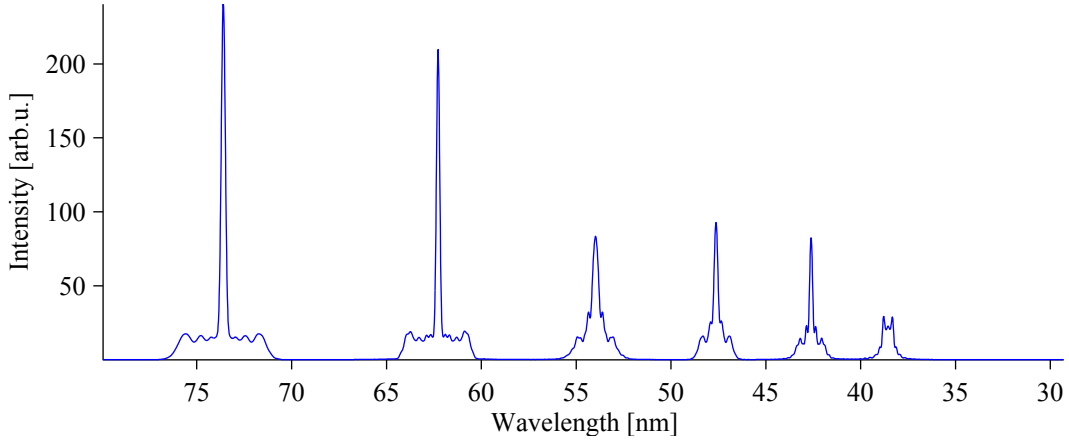

Figure 3.19 – Simulated spatially integrated XUV spectrum in the gas jet (near-field) generated in argon at 10^{14} W/cm². The considered harmonic orders are 11 - 21.

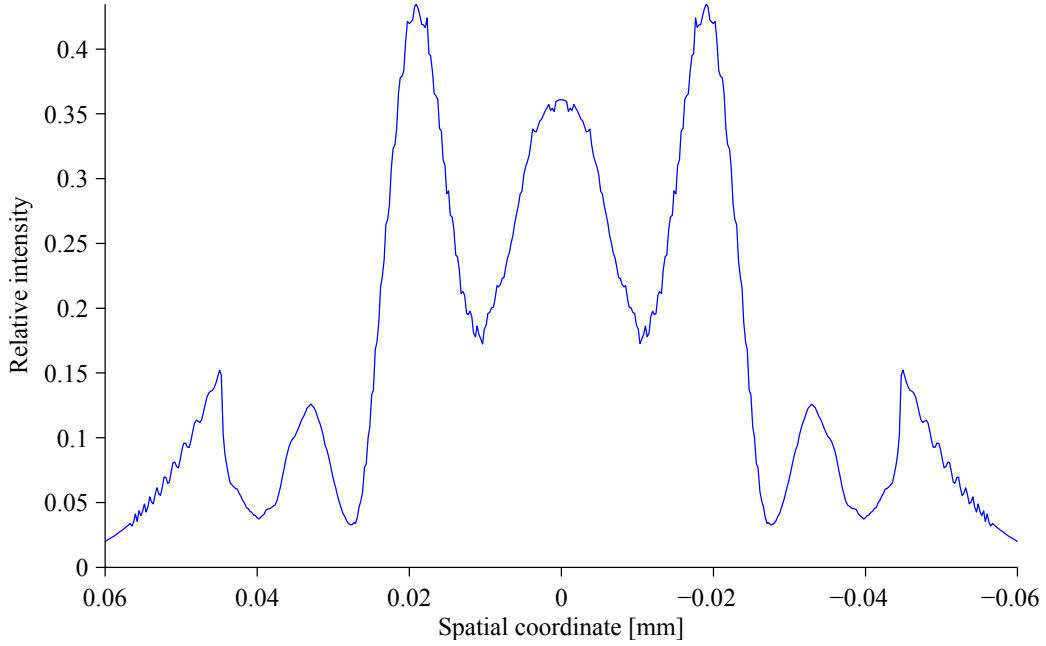

Figure 3.20 – Simulated spatial profile of harmonic 15 in the gas jet (near-field) generated in argon at 10^{14} W/cm².

The spatial profile (figure 3.20) of the harmonic 15 (the harmonic frequency only) is also well modulated and the maximum is not present on axis. Overall the modulation seems to be regular.

Spatio-temporal profile for short path and long path were the same. To distinguish the contribution of both paths in spatio-spectral profile, the spectrum without long path is on figure 3.21 and the spectrum without short path is on figure 3.22.

The short path contribution is limited to the spectrally narrow harmonic lines with almost zero signal between harmonics. This is even better seen on spectral profile on axis

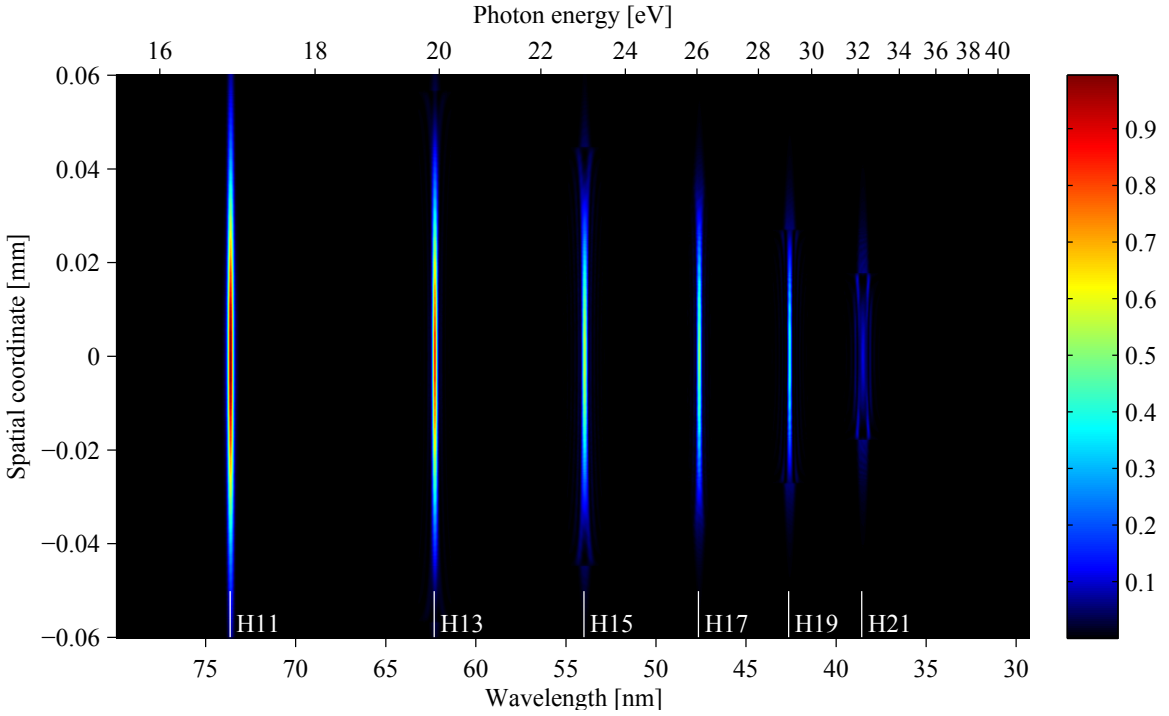

Figure 3.21 – (color) Simulated spatio-spectral XUV profile with no long path ($\alpha = 1$ or 13×10^{14} cm^2/W) in the gas jet generated in argon at 10^{14} W/cm^2.

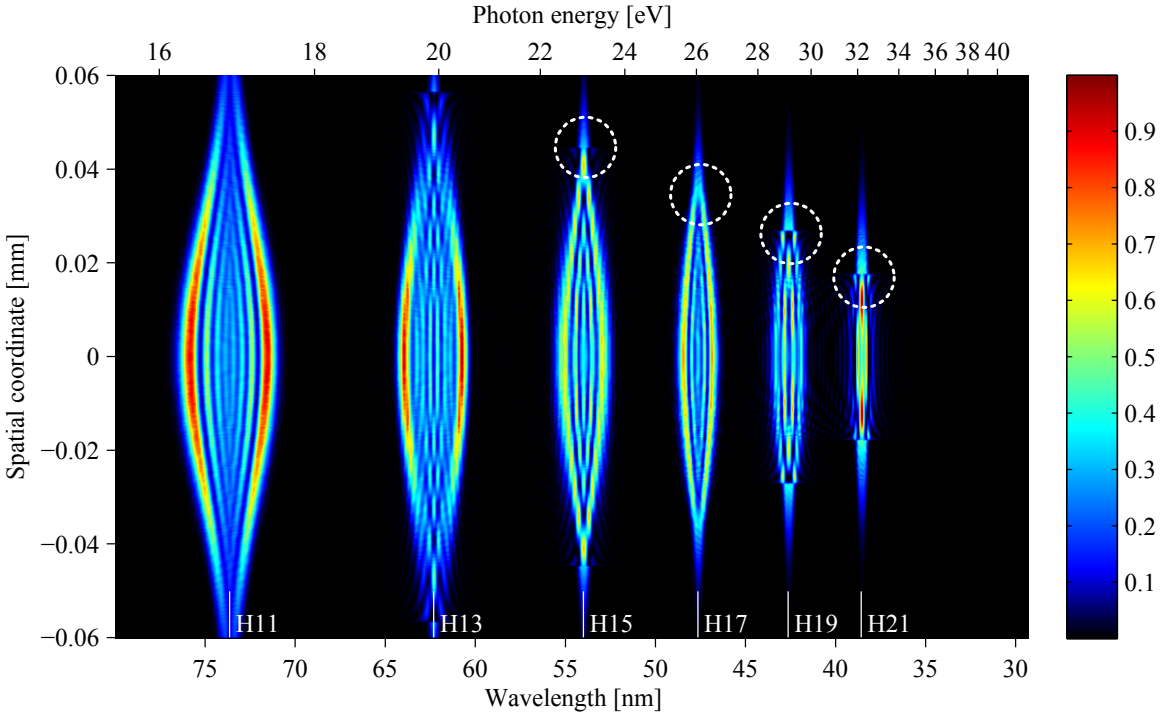

Figure 3.22 – (color) Simulated spatio-spectral XUV profile with no short path ($\alpha = 25$ or 13×10^{14} cm^2/W) in the gas jet (near-field) generated in argon at 10^{14} W/cm^2. Note the off-axis wings highlighted with white dashed circles.

on figure 3.23.

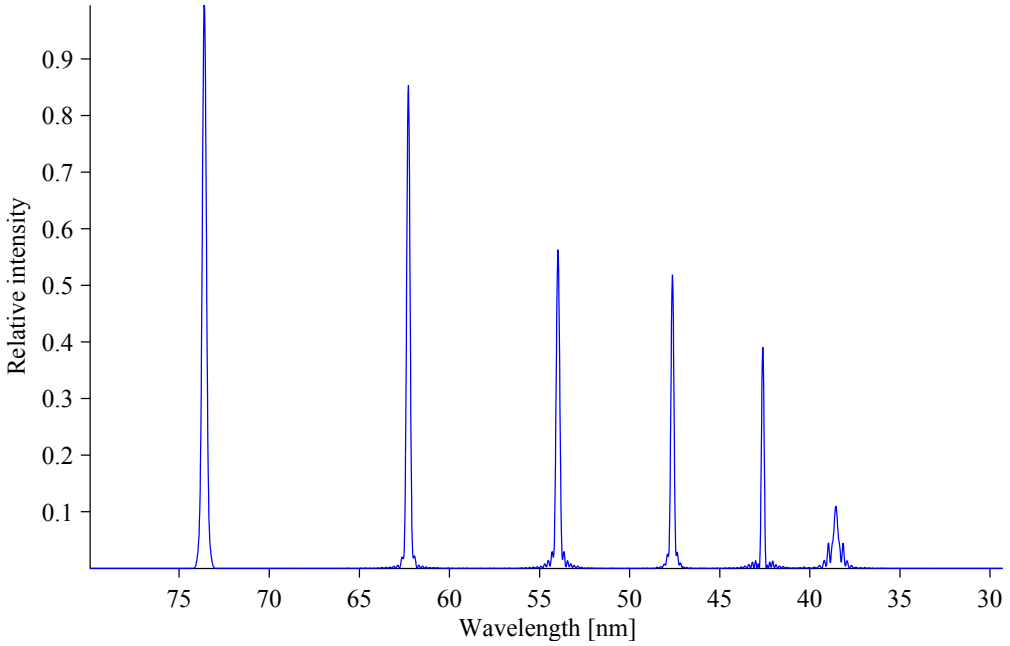

Figure 3.23 – Simulated spectral XUV profile in the gas jet (near-field) on axis with no long path ($\alpha = 1$ or 13×10^{14} cm^2/w).

The long path however is spectrally very broad and highly structured both in frequency and space.

There is also off-axis wings structures at each harmonic that appears at the same spatial position for short and long paths. Some of them are highlighted on figure 3.22 by dashed white rings. To quantitatively analyze them we plotted the spatial profile of harmonic 15 with no long path on figure 3.24.

The overall profile is similar to Gaussian noisy shape with two abrupt wings. The wing sharp peaks are located around 45 μm far from optical axis. At this spatial point the infrared driving beam intensity equals the cutoff intensity (see equation 2.4 on page 29) of harmonic 15. Therefore, the wings are likely due to a phase jump between harmonic dipole phase of $\alpha = 13 \times 10^{-14}$ cm^2/w for $I_{IR} < I_{cutoff}$ and $\alpha = 1 \times 10^{-14}$ cm^2/w for $I_{IR} > I_{cutoff}$.

To support this hypothesis, we examined the case with short path only ($\alpha = 1 \times 10^{-14}$ cm^2/w independently on intensity). Spatially resolved spectrum, on-axis spectral profile and the harmonic 15 spatial profile are shown on figures 3.25, 3.26 and 3.27.

The spectral profile of harmonics is very regular and structureless and there is no signal between individual harmonics. The spatial profile of every harmonics is clean and Gaussian-like as demonstrated in detail for harmonic 15. The off-axis wings are therefore due to destructive interference between the short path in the plateau ($\alpha = 1 \times 10^{-14}$ cm^2/w) and the cutoff phase ($\alpha = 13 \times 10^{-14}$ cm^2/w).

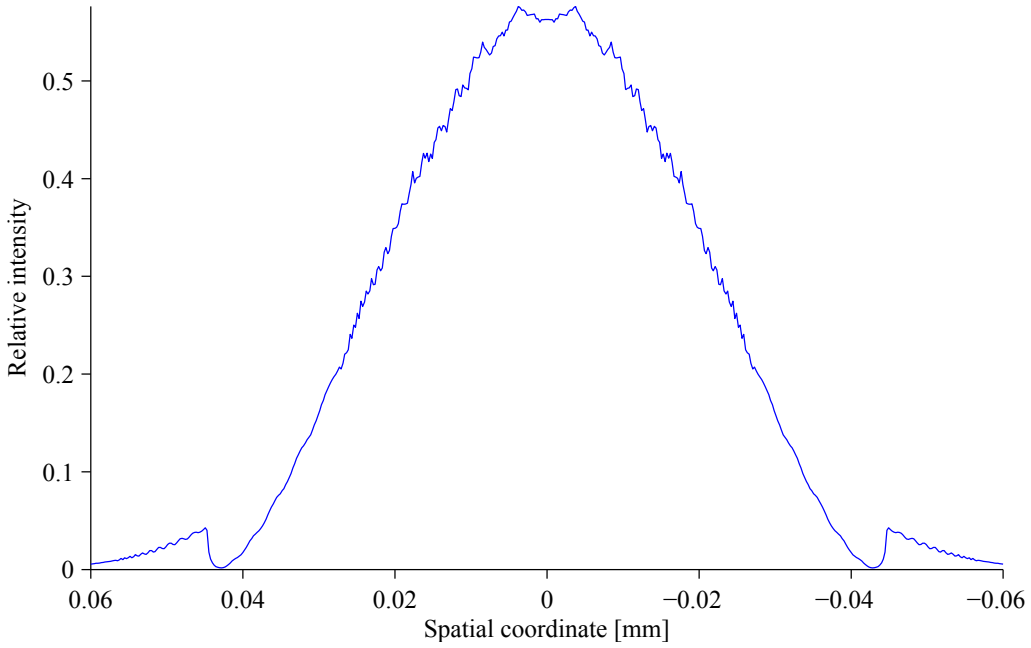

Figure 3.24 – Simulated spatial profile of harmonic 15 in the gas jet (near-field) without long path ($\alpha = 1$ or $13 \times 10^{14}\,\mathrm{cm^2/W}$) generated in argon at $10^{14}\,\mathrm{W/cm^2}$.

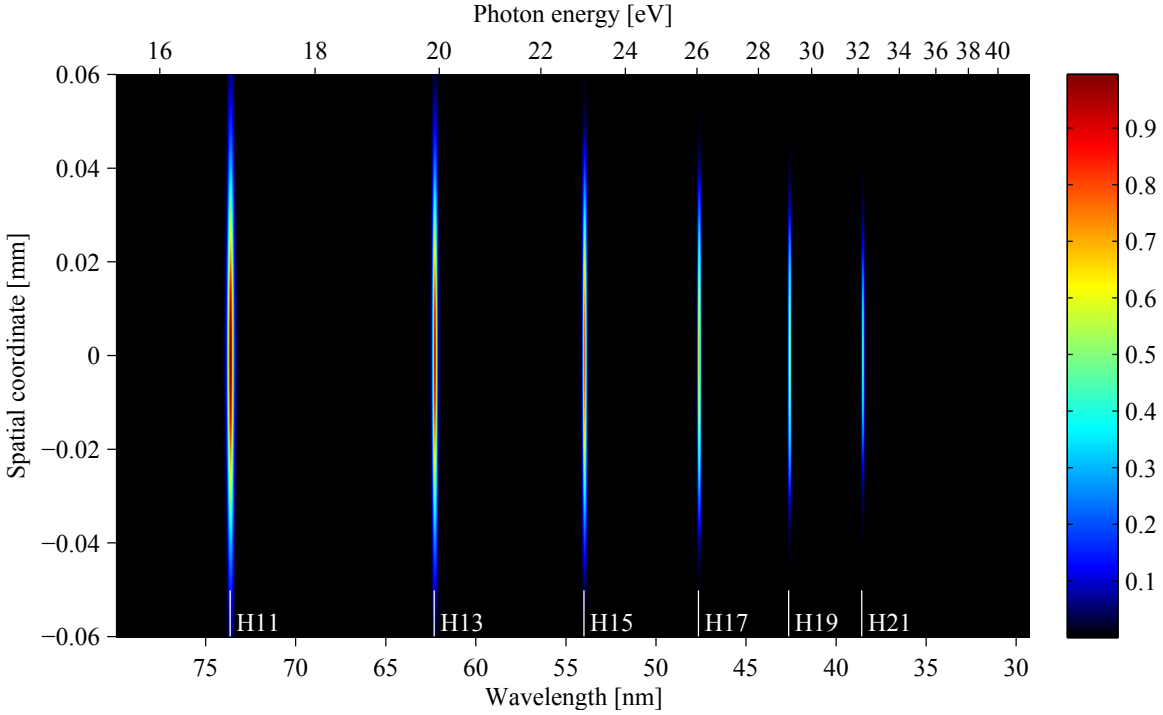

Figure 3.25 – (color) Simulated spatio-spectral XUV profile with short path only ($\alpha = 1 \times 10^{-14}\,\mathrm{cm^2/W}$ independently on intensity) in the gas (near-field) jet generated in argon at $10^{14}\,\mathrm{W/cm^2}$.

3.3.3.2.1 Conclusion for short path contribution At low intensity for plateau harmonics the short path is spectrally narrow and centered at the harmonic frequency.

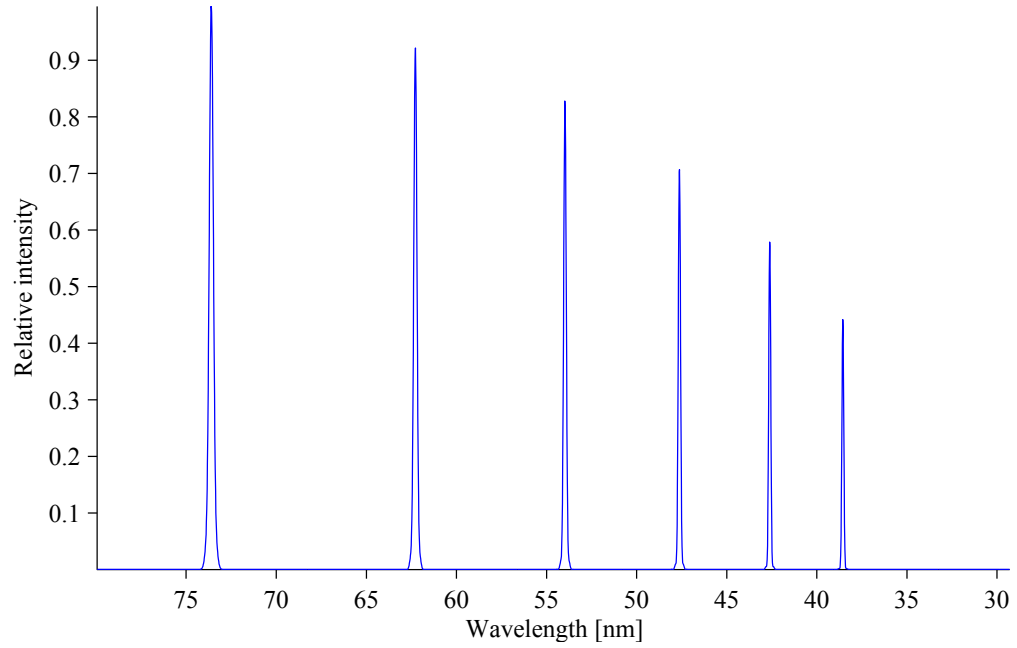

Figure 3.26 – Simulated spectral XUV profile on-axis in the gas jet (near-field) with short path only ($\alpha = 1 \times 10^{-14}\,\mathrm{cm^2/W}$ independently on intensity).

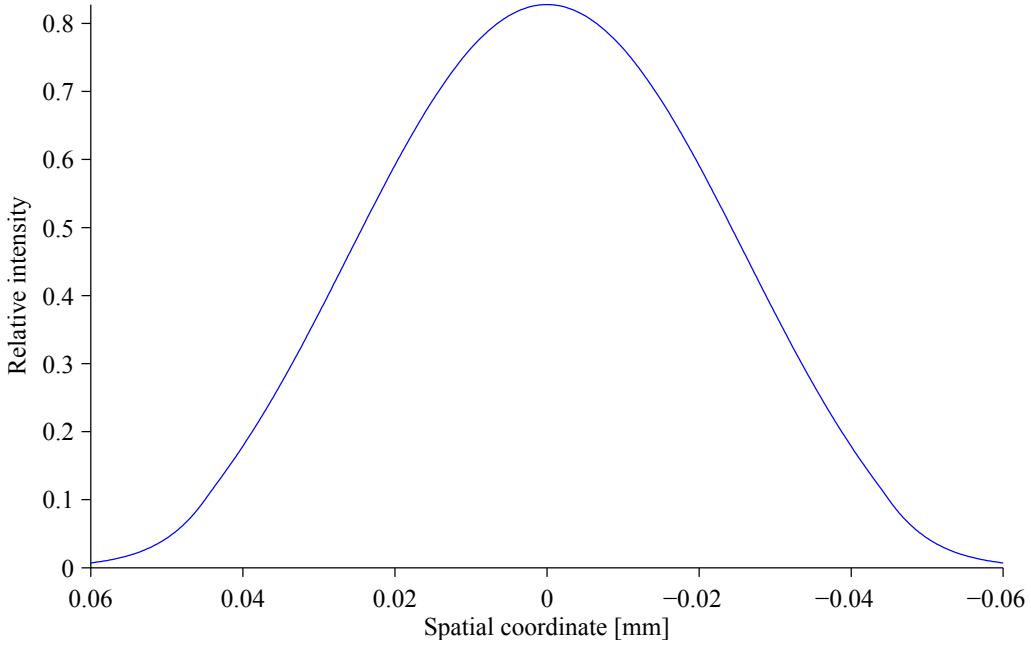

Figure 3.27 – Simulated spatial profile of harmonic 15 in the gas jet (near-field) short path only ($\alpha = 1 \times 10^{-14}\,\mathrm{cm^2/W}$ independently on intensity) generated in argon at $10^{14}\,\mathrm{W/cm^2}$.

When all contributions are considered, large spatial structures appear and they are due to interference with long path. Off-axis wings are due to emission where the infrared driving intensity is lower than the cutoff intensity of corresponding harmonic.

The relative weight of the cutoff emission ($\alpha = 13 \times 10^{-14}\,\mathrm{cm^2/W}$) increases when ap-

proaching the cutoff harmonics, that is the reason why without the long path the structures are the most visible for harmonic 21 - the highest simulated harmonics.

Also, we can conclude that the harmonic dipole amplitude nonuniform shape, given by discontinuity of the effective harmonic order q_{eff}, has practically no significant influence on spatio-spectral structures in the near field.

3.3.3.2.2 Origin of the long path structures We have obtained spectrally broad signal due to $\alpha\frac{dI}{dt}$ [Gaarde 99] and a lot of modulations when generating without short path (see figure 3.22). Moreover, the highest intensity is off the harmonic line. To distinguish whether the structures come from the long path itself or interaction with the cutoff phase component, we simulated long path only ($\alpha = 25 \times 10^{-14}\,\mathrm{cm^2/W}$ independently of intensity) on figure 3.28.

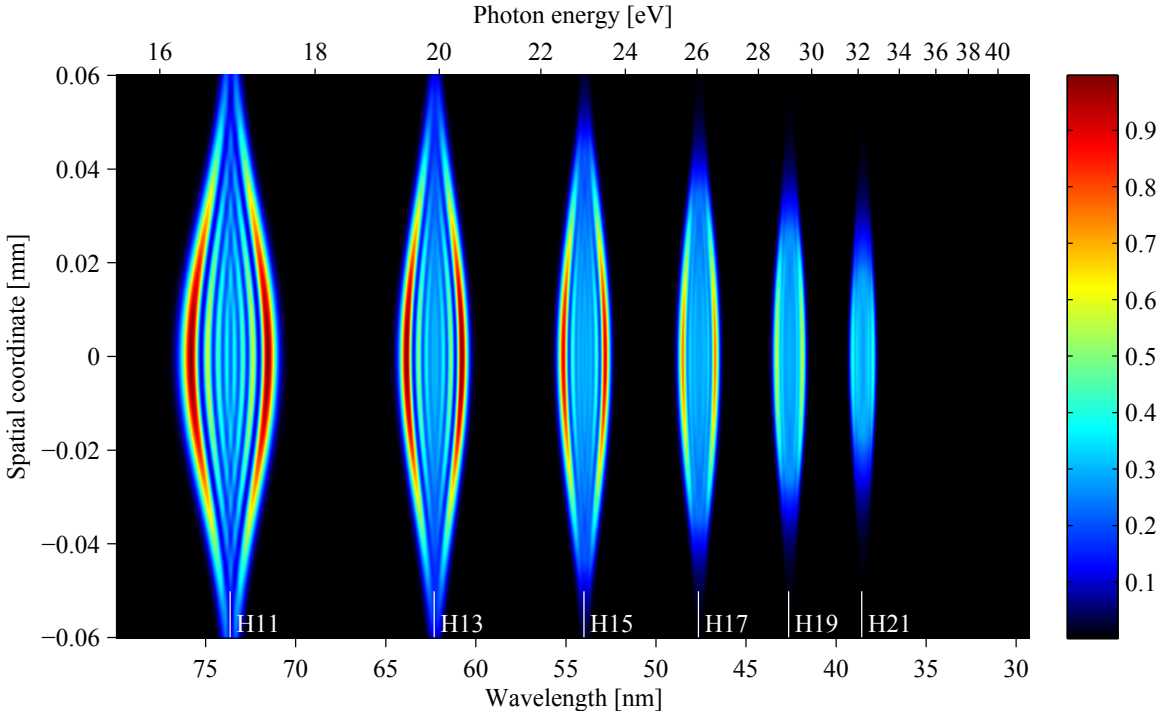

Figure 3.28 – (color) Simulated spatio-spectral XUV profile with long path only ($\alpha = 25 \times 10^{-14}\,\mathrm{cm^2/W}$ independently on intensity) in the gas jet (near-field) generated in argon at $10^{14}\,\mathrm{W/cm^2}$.

To check the influence of the intensity dependent harmonic effective order we plot on figure 3.29 the same harmonic with only long path on 45% of peak infrared intensity. In that way, harmonics 11, 13 and 15 take place in the plateau and harmonics 17, 19 and 21 are in the cutoff i.e. the peak infrared intensity is lower than the cutoff intensity for harmonics 17, 19 and 21.

To better see the spectral modulations, the spectral profile on axis is on figure 3.30 and the spatially integrated spectrum is on figure 3.31.

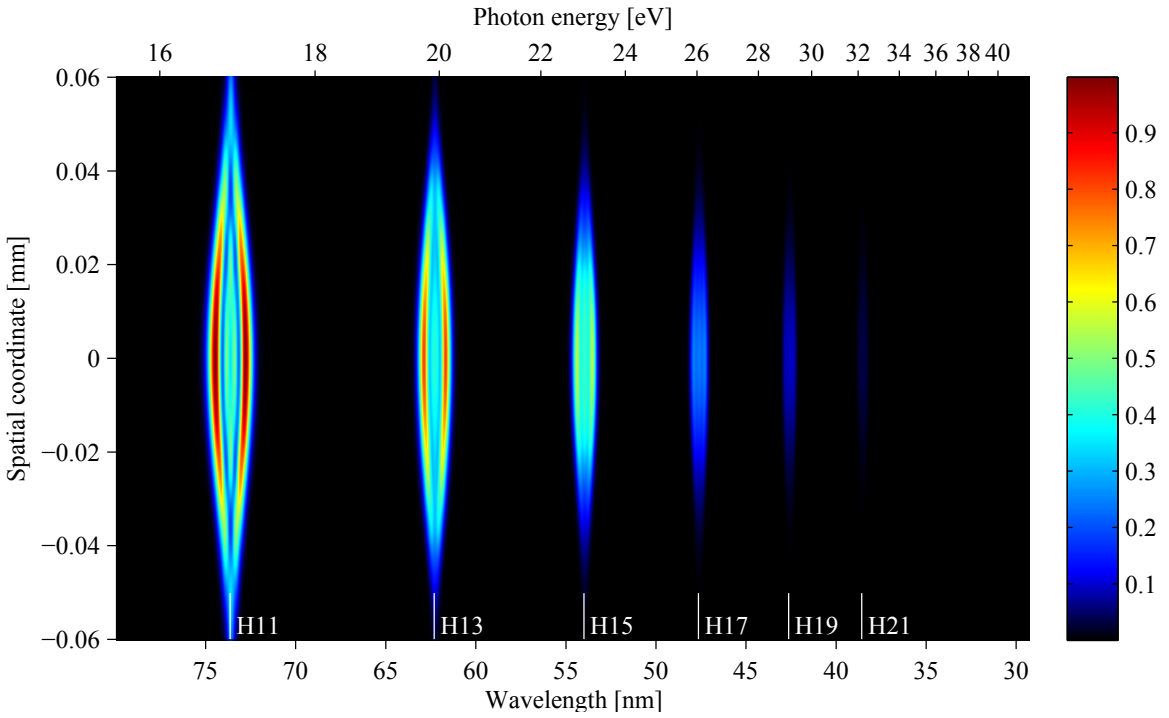

Figure 3.29 – (color) Simulated spatio-spectral XUV profile with long path only ($\alpha = 25 \times 10^{-14}\,\mathrm{cm^2/W}$ independently on intensity) in the gas jet (near-field) generated in argon at $0.45 \times 10^{14}\,\mathrm{W/cm^2}$.

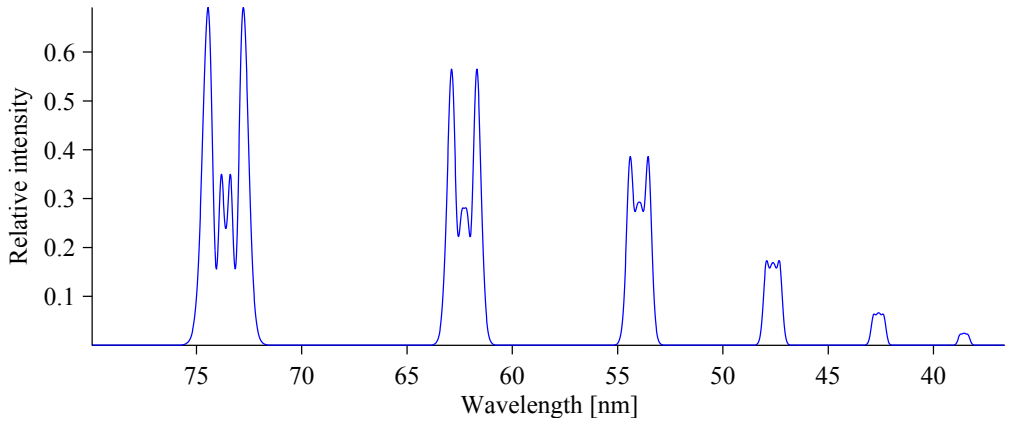

Figure 3.30 – Simulated spectral XUV profile on axis in the gas jet (near-field) with long path only ($\alpha = 25 \times 10^{-14}\,\mathrm{cm^2/W}$ independently on intensity) generated at $0.45 \times 10^{14}\,\mathrm{W/cm^2}$.

The structures contrast decreases with high harmonic order. The cutoff harmonics are of super-Gaussian shape with only a small modulation at the top. Therefore this small spectral modulation cannot be due to the spatial discontinuity of the harmonic effective order q_{eff}.

We have already eliminated nearly all possible causes for such structures. Thus those structures have to be only long path-long path interferences.

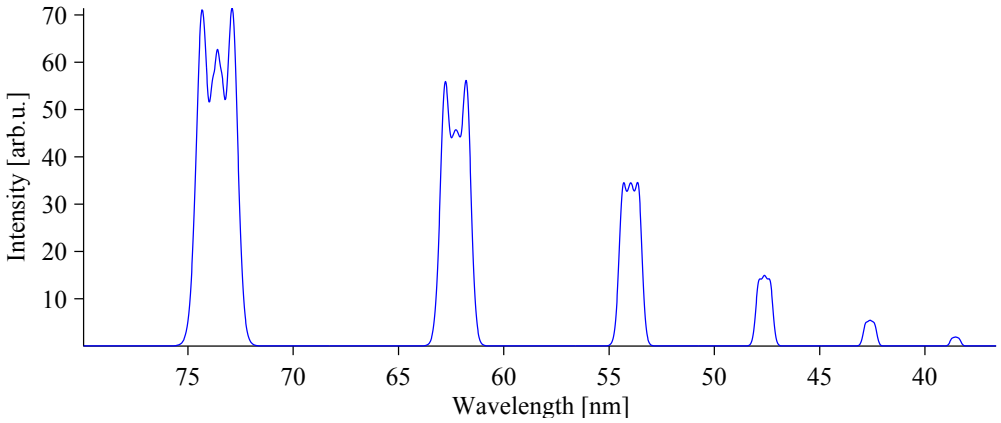

Figure 3.31 – Simulated spatially integrated spectral XUV profile in the gas jet (near-field) with long path only ($\alpha = 25 \times 10^{-14}$ cm^2/W independently on intensity) generated at 0.45×10^{14} W/cm^2.

3.3.3.2.3 Conclusion At low intensity where the generating medium is not ionized, we can clearly distinguish the contributions of short and long trajectories in the near-field spatio-spectral XUV profiles.

The short trajectory is spectrally very narrow and located at the harmonics wavelength. The spectrum of the short path is regular without modulation. The long path is spectrally much broader than the short path and the spectrum is very modulated. Those modulations are explained by interferences of the long trajectory with itself. As the spectrally narrow short path contains the same amount of signal as the spectrally broad long path, the spectral intensity of the short path is much higher than the spectral intensity of the long path.

Cutoff radiation has very reduced contribution to the spectral structures.

We can observe spatial structures where the short and long path overlap and also in the long path only, where again they are due to interference of the long path with itself. The cutoff radiation creates spatial structures in the off-axis wings of the XUV beam, where the IR intensity is around the cutoff intensity.

3.3.3.3 Far-field spatio-spectral XUV profile

The near-field XUV profile cannot be experimentally detected but is important for understanding the HHG dynamics. To compare theory and experiment, one has to simulate XUV profiles in the far field. This approach is equivalent to detection by MCPs in the XUV spectrometer. In here, we limit our figures spatially from -20 to 20 mm as 40 mm is the diameter of the real MCPs used in the experiment.

We note that the MCP response can be nonlinear [Hamamatsu 06] and therefore we show both linear and logarithmic spectra.

The far-field spatially resolved harmonic spectrum generated in argon at 10^{14} W/cm^2 is

shown on figure 3.32 in linear scale and on figure 3.33 in logarithmic scale.

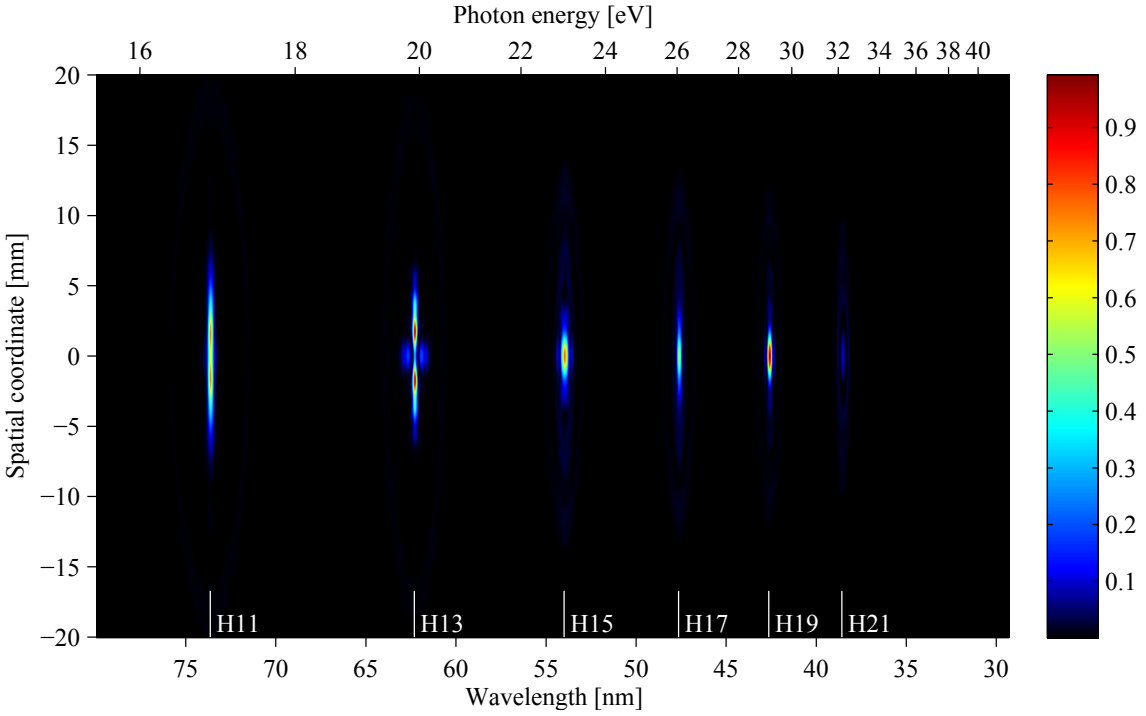

Figure 3.32 – (color) Simulated spatially resolved far-field harmonic spectra generated in argon at 10^{14} W/cm² 1 cm before the focus.

The harmonics are spectrally narrow with some spatial and spectral modulations. The maximum of intensity is on axis for harmonics 15 to 21 and off axis for harmonics 11 and 13. There are also weak ellipse-like structures that can be barely seen on linear scale on figure 3.32.

Logarithmic scale reveals also plenty of fine structures that fill completely the spatio-spectral space between the harmonics but because they are about 4 orders of magnitude weaker than the brightest part they cannot be seen on linear scale.

To be more quantitative we plotted the spectra on axis on figure 3.34 and spatially integrated spectra on figure 3.35.

The on-axis spectrum reveals a lot of structures and irregular harmonic peak amplitude. An interesting fact is that some harmonics (as 11, 17 and 19) are much less structured than others (such as 13, 15 and 21) and harmonics are not the same from one to another. On the other hand, spatial integration washes out most of differences showing similar spectrum for all the harmonics - there is an intense peak on the harmonic line and spectrally broad pedestal of low amplitude.

3.3.3.3.1 Origin of the short path structures in the far field To understand the impact of different parameters we plotted the same spectra without long path on figures

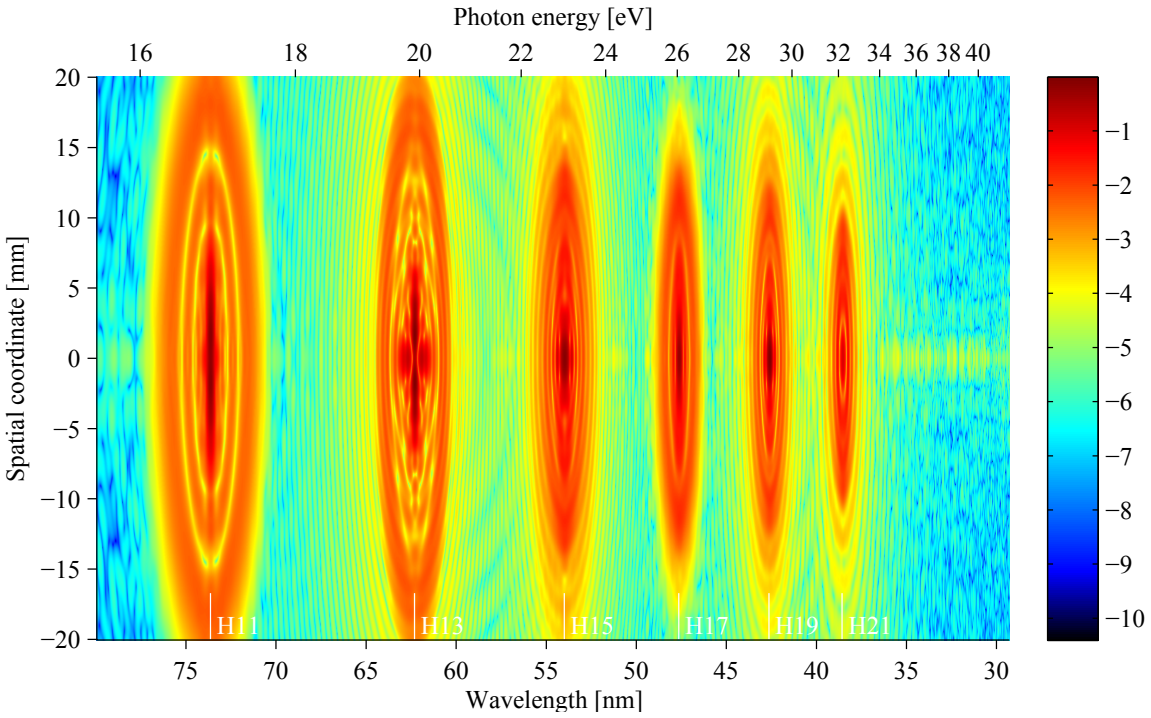

Figure 3.33 – (color) Simulated log scale far-field spatially resolved XUV spectrum (argon, peak intensity is 10^{14} W/cm^2, the gas jet is placed 1 cm before the focus).

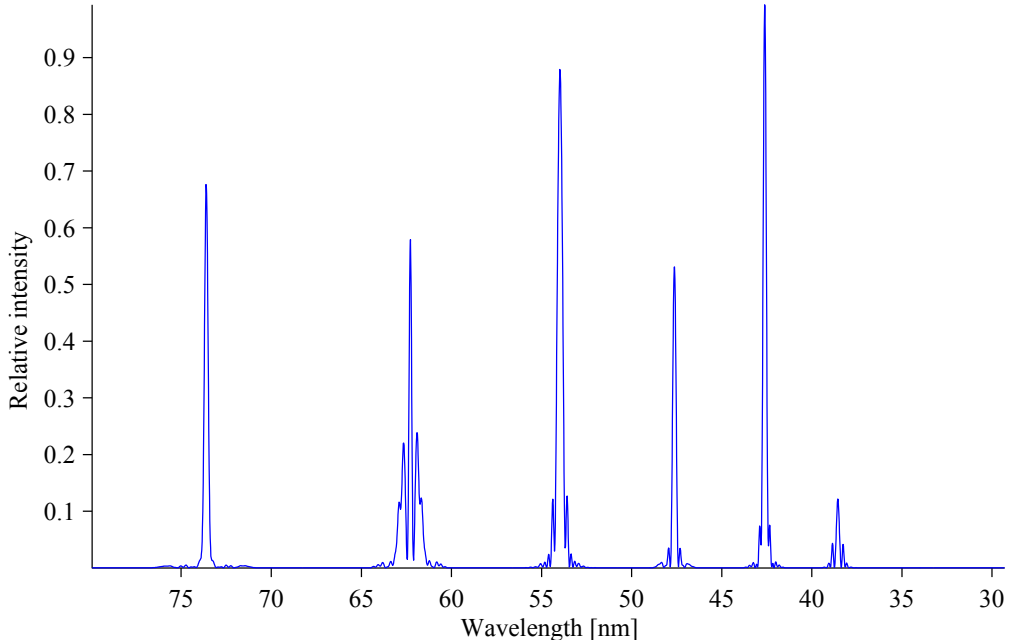

Figure 3.34 – Simulated XUV far-field spectrum on axis generated at 10^{14} W/cm^2. The medium is located 1 cm before focus.

3.36, 3.37 and 3.38. Note that we do not plot the whole 40 mm of MCPs, but only the central 20 mm part where the most of short path signal is concentrated.

The weak spectrally and spatially large ellipses disappeared and also the structures close

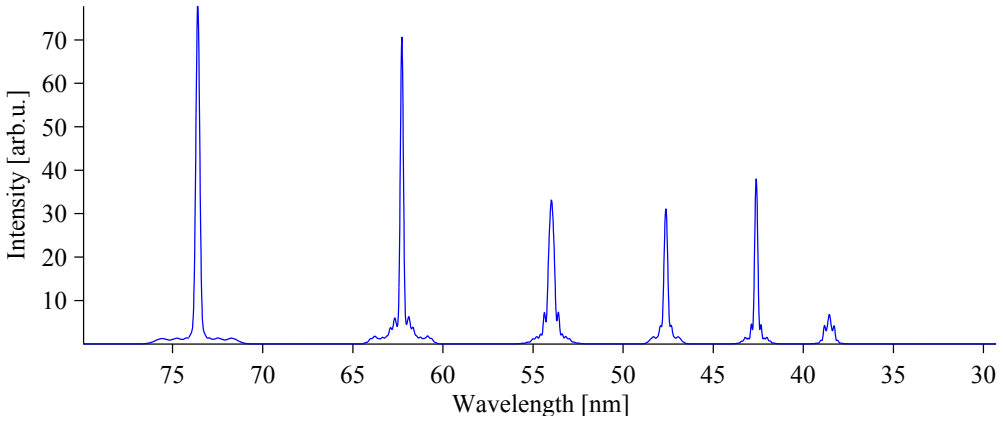

Figure 3.35 – Simulated spatially integrated XUV far-field spectrum generated at 10^{14} W/cm². The medium is located 1 cm before focus.

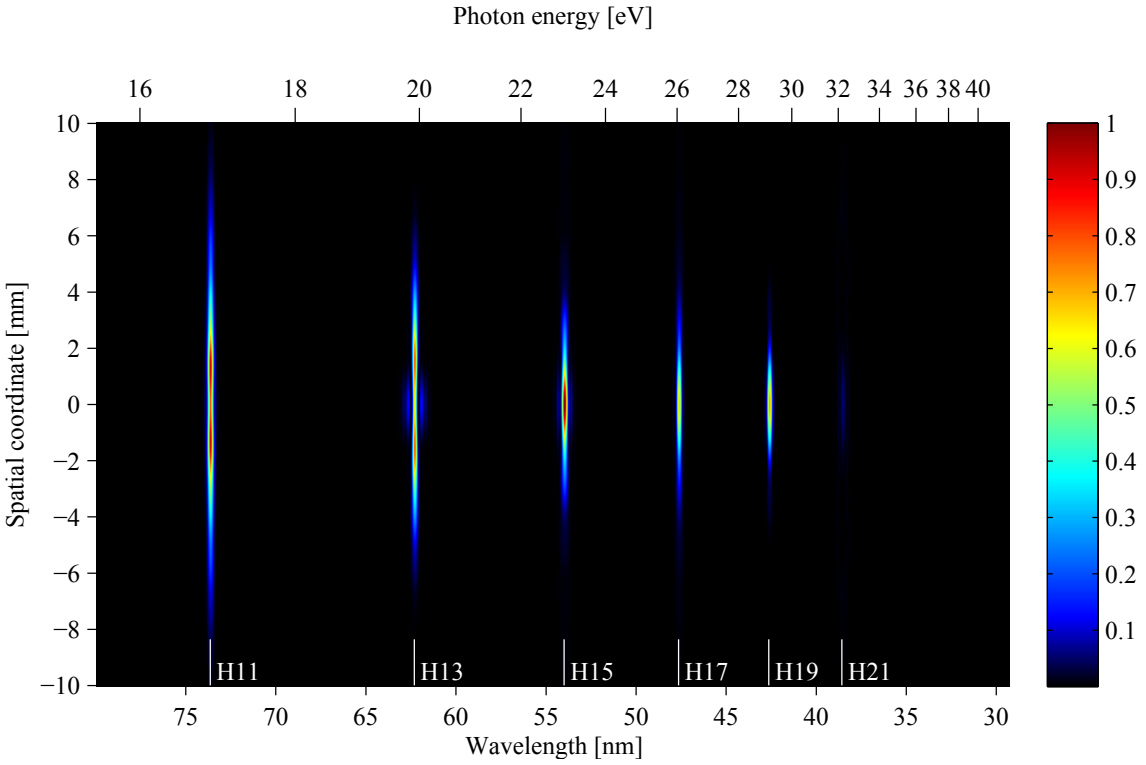

Figure 3.36 – (color) Simulated spatially resolved far-field harmonic spectra with no long path ($\alpha = 1$ or 13×10^{-14} cm²/W) generated in argon at 10^{14} W/cm² 1 cm before the focus.

to harmonic lines are weaker than before. Nevertheless, the general structure pattern is still present and also the relative on-axis amplitudes of harmonics stay almost unchanged. This is completely different from the near-field spectral profile, where most of the structures in short path were due to an interference with long path. To examine cutoff-plateau phase jumps, we plot the short path only on figures 3.39, 3.40 and 3.41.

The spectral structures completely disappeared except for fine inter-harmonic fringes

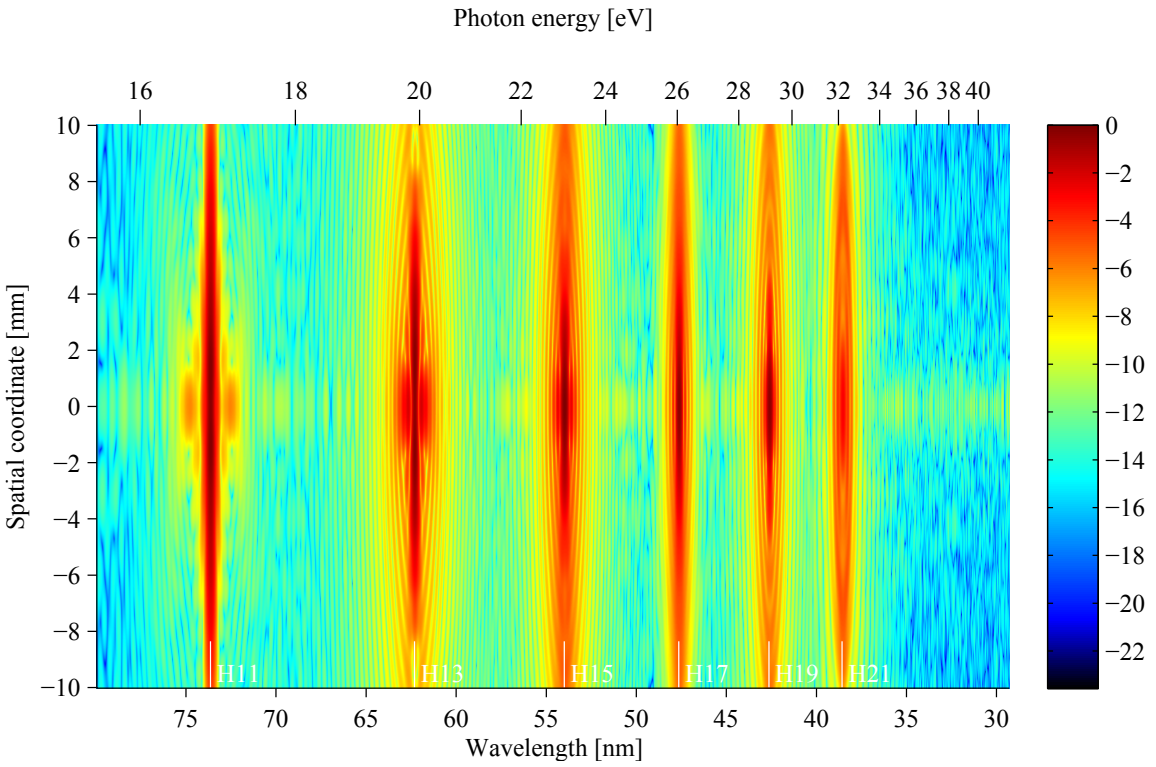

Figure 3.37 – (color) Simulated spatially resolved far-field harmonic spectra in log scale with no long path ($\alpha = 1$ or $13 \times 10^{-14}\,\mathrm{cm^2/W}$) generated in argon at $10^{14}\,\mathrm{W/cm^2}$ 1 cm before the focus.

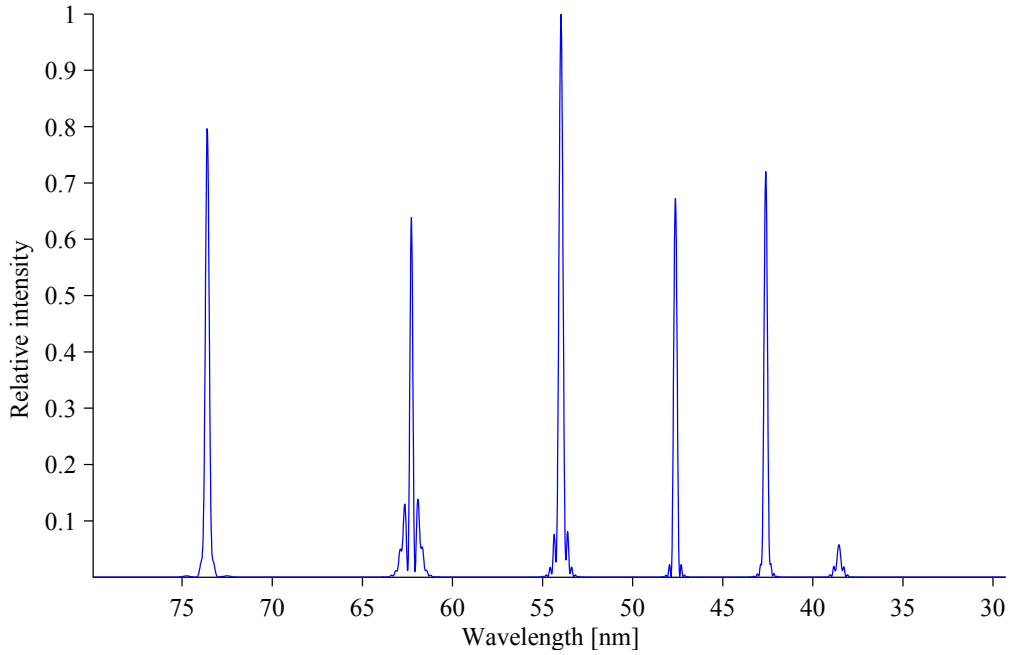

Figure 3.38 – Simulated XUV far-field spectrum on axis with no long path ($\alpha = 1$ or $13 \times 10^{-14}\,\mathrm{cm^2/W}$) generated at $10^{14}\,\mathrm{W/cm^2}$ 1 cm before focus.

whose intensity is, however, about 10 orders of magnitude lower than the signal peak and

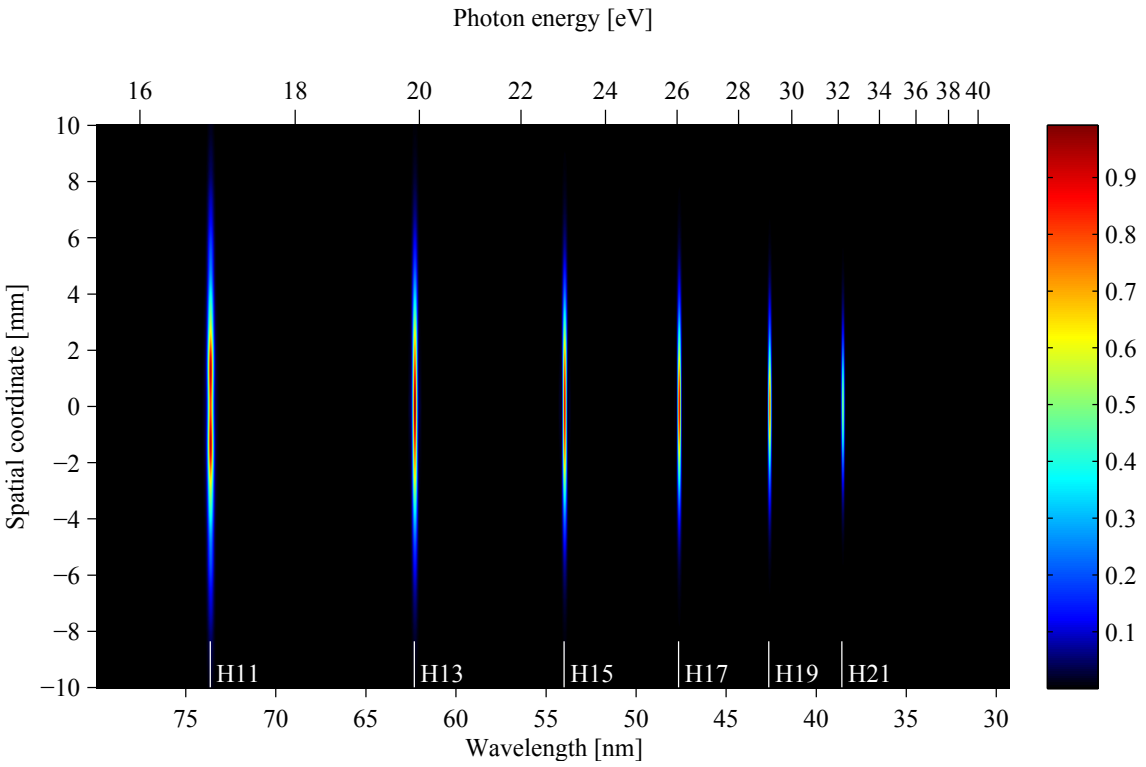

Figure 3.39 – (color) Simulated spatially resolved far-field harmonic spectra. Only the short path contributes ($\alpha = 1 \times 10^{-14}\,\mathrm{cm^2/W}$ independent on intensity). The spectrum was generated in argon at $10^{14}\,\mathrm{W/cm^2}$ 1 cm before the focus.

therefore those structures can be neglected (see figure 3.40).

The spatial modulations are still present. To see better the spatial modulations, we plotted harmonic 11 spatial profile on figure 3.42.

The figure 3.42 shows that even with an uniform dipole phase of $\alpha = 1 \times 10^{14}\,\mathrm{cm^2/W}$ the spatial profile of the harmonic 11 is modulated. To check if it is because of nonuniformity of the effective harmonic order q_{eff} we performed the simulation with constant $q_{eff} = 1.5$ even for intensities $I_{IR} < I_{cutoff}$. The spatially resolved harmonic spectra is on figure 3.43 and the spatial profile of harmonic 11 is on figure 3.44.

The spatial modulation has not disappeared, moreover its contrast increased from 12% to nearly 17% (saddle to peak).

It is known that diffracting a non-Gaussian beam to the far or intermediate field would lead to modulations of the profile. To check if our modulations are due to the size of the diffracting medium we put $q_{eff} = 1$ independently on intensity and harmonic order. Resulting spatially resolved spectra of the XUV radiation and spatial profile of harmonic 11 are on figures 3.45 and 3.46 respectively.

We observe that the spatial profiles of harmonics are more modulated than before. Compared to 12% with $q_{eff} = 1.5$ in the cutoff and $q_{eff} = 9/4$ in the plateau, the saddle-

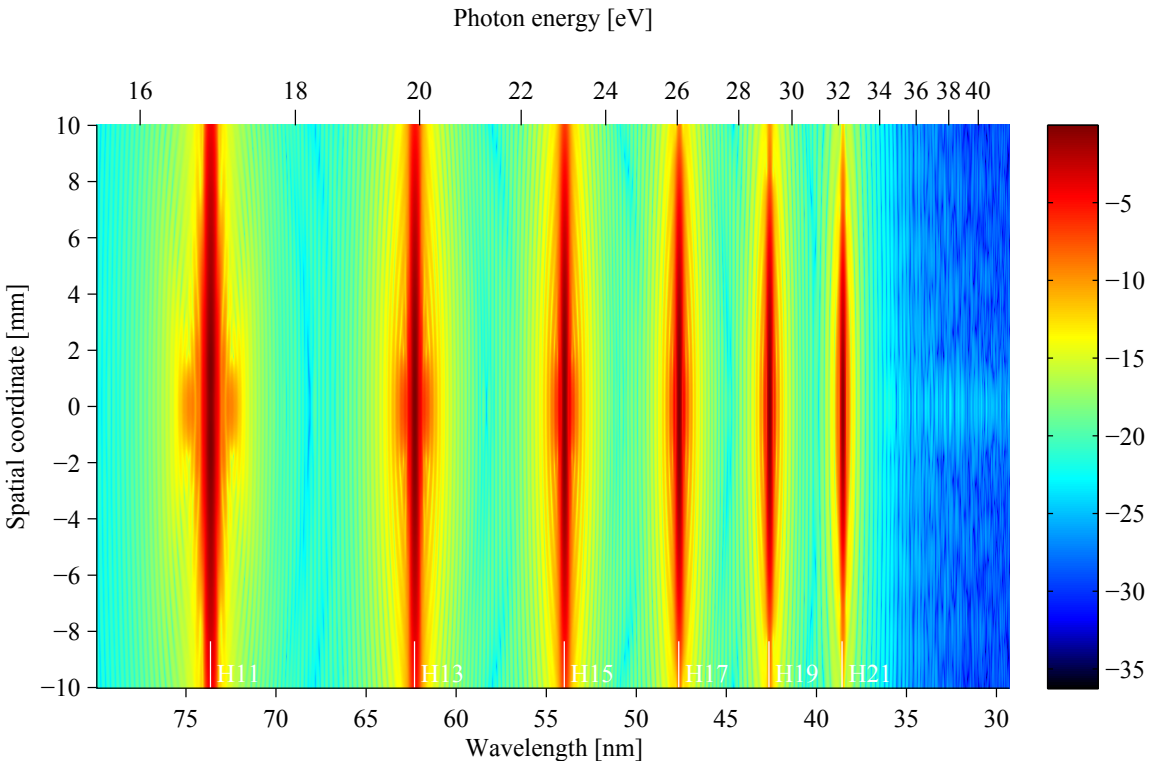

Figure 3.40 – (color) Simulated spatially resolved far-field harmonic spectra with short path only ($\alpha = 1 \times 10^{-14}\,\mathrm{cm^2/W}$ independent on intensity). The figure is in log scale and the spectrum was generated in argon at $10^{14}\,\mathrm{W/cm^2}$ 1 cm before the focus.

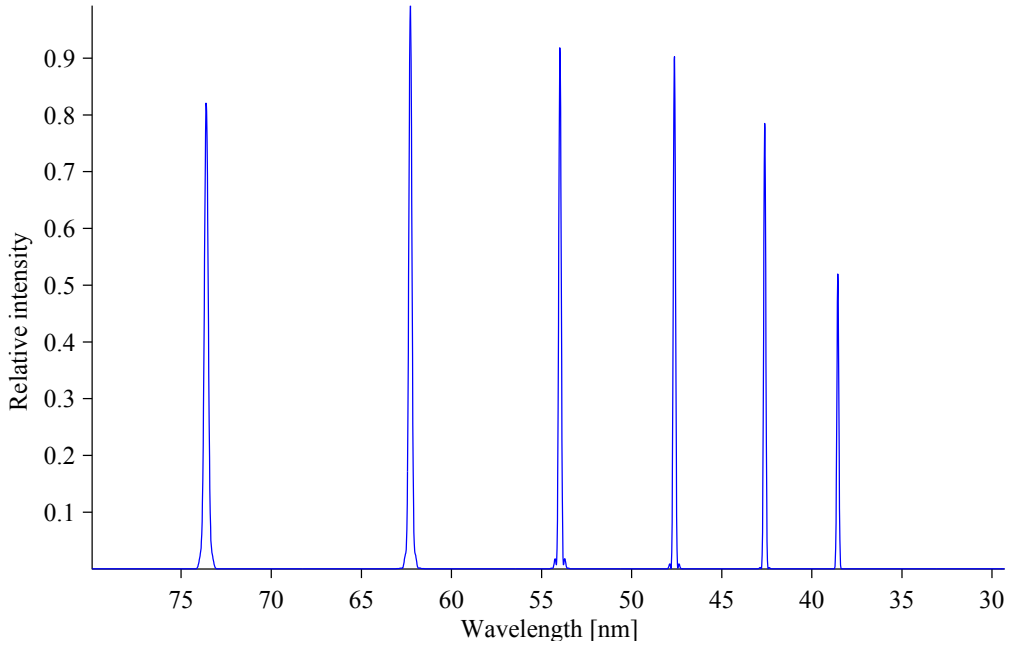

Figure 3.41 – Simulated XUV far-field spectrum on axis. Only short path is considered ($\alpha = 1 \times 10^{-14}\,\mathrm{cm^2/W}$ independent on intensity). The spectrum was generated in argon at $10^{14}\,\mathrm{W/cm^2}$ and the medium was located 1 cm before focus.

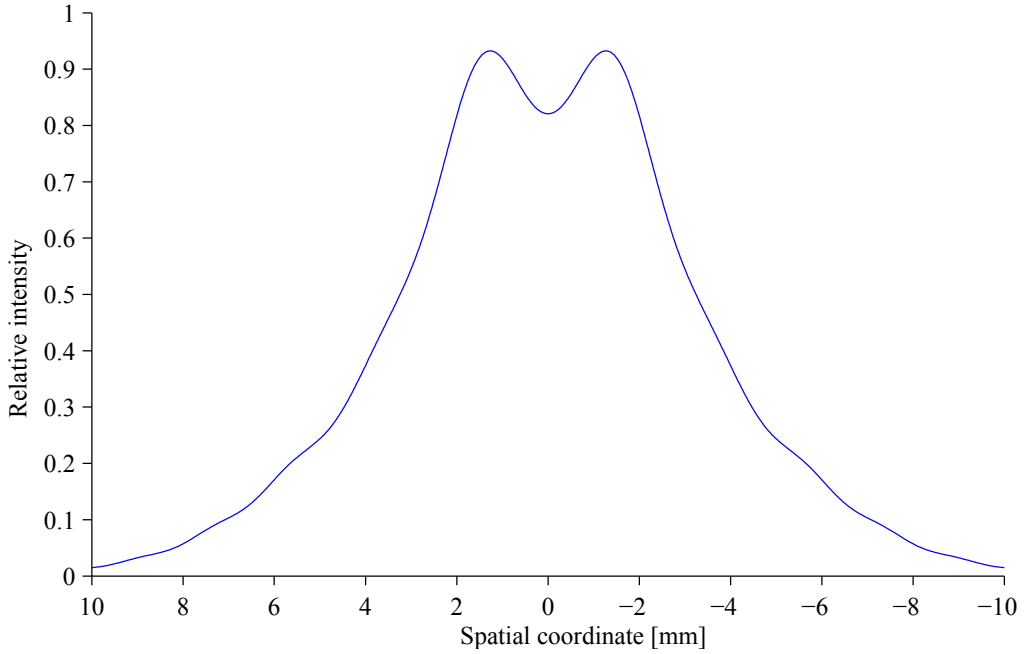

Figure 3.42 – Simulated far-field spatial profile of harmonic 11. Only short path is considered ($\alpha = 1 \times 10^{-14}\,\mathrm{cm^2/W}$ independent on intensity). The harmonic was generated in argon at $10^{14}\,\mathrm{W/cm^2}$ 1 cm before focus. The iris diameter was 30 mm and the collimated beam radium was 10 mm (at I_{max}/e^2).

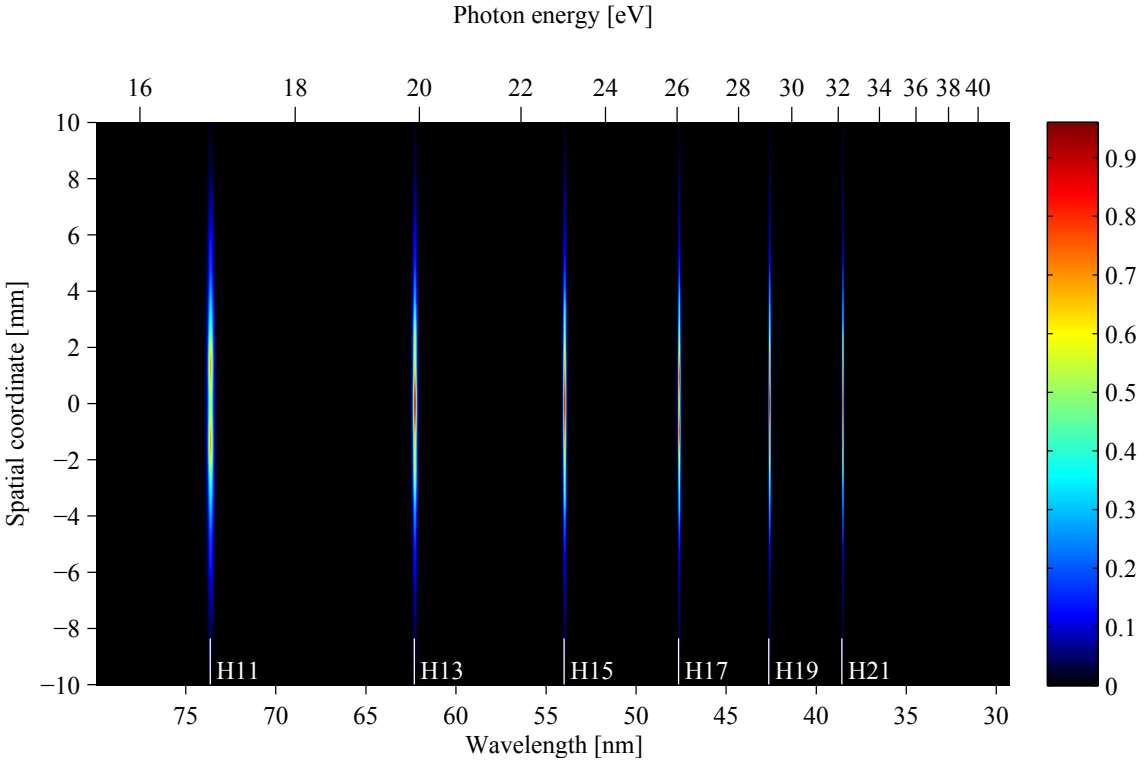

Figure 3.43 – (color) Simulated spatially resolved far-field harmonic spectra with short path only ($\alpha = 1 \times 10^{-14}\,\mathrm{cm^2/W}$ independent on intensity) and constant $q_{eff} = 1.5$ generated in argon at $10^{14}\,\mathrm{W/cm^2}$ 1 cm before the focus.

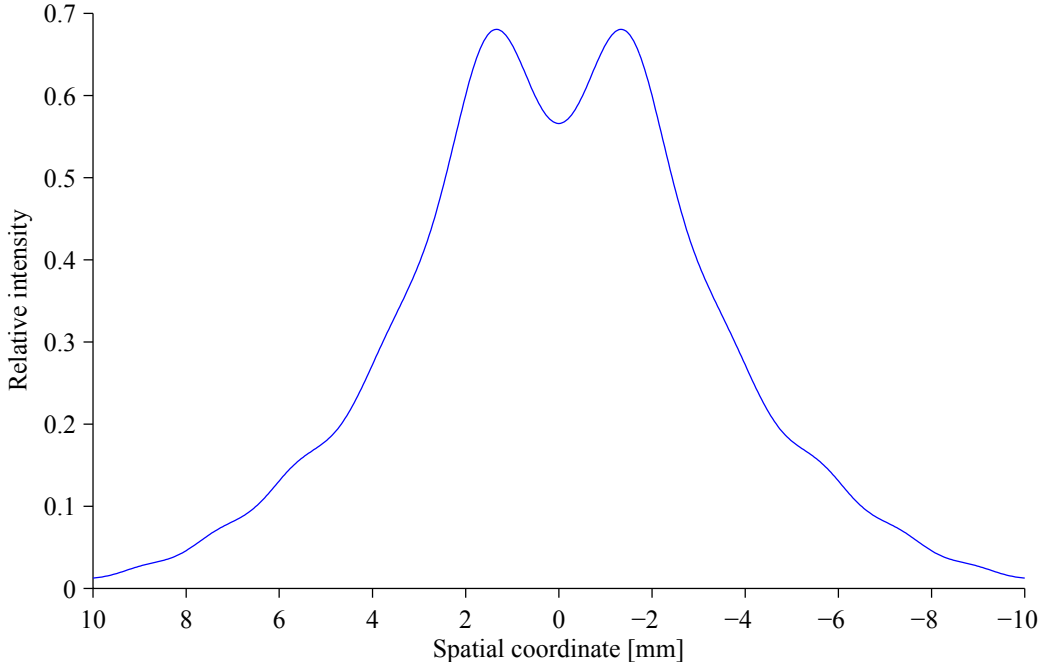

Figure 3.44 – Simulated far-field spatial profile of harmonic 11 short path only and constant $q_{eff} = 3$ generated in argon at 10^{14} W/cm² 1 cm before focus.

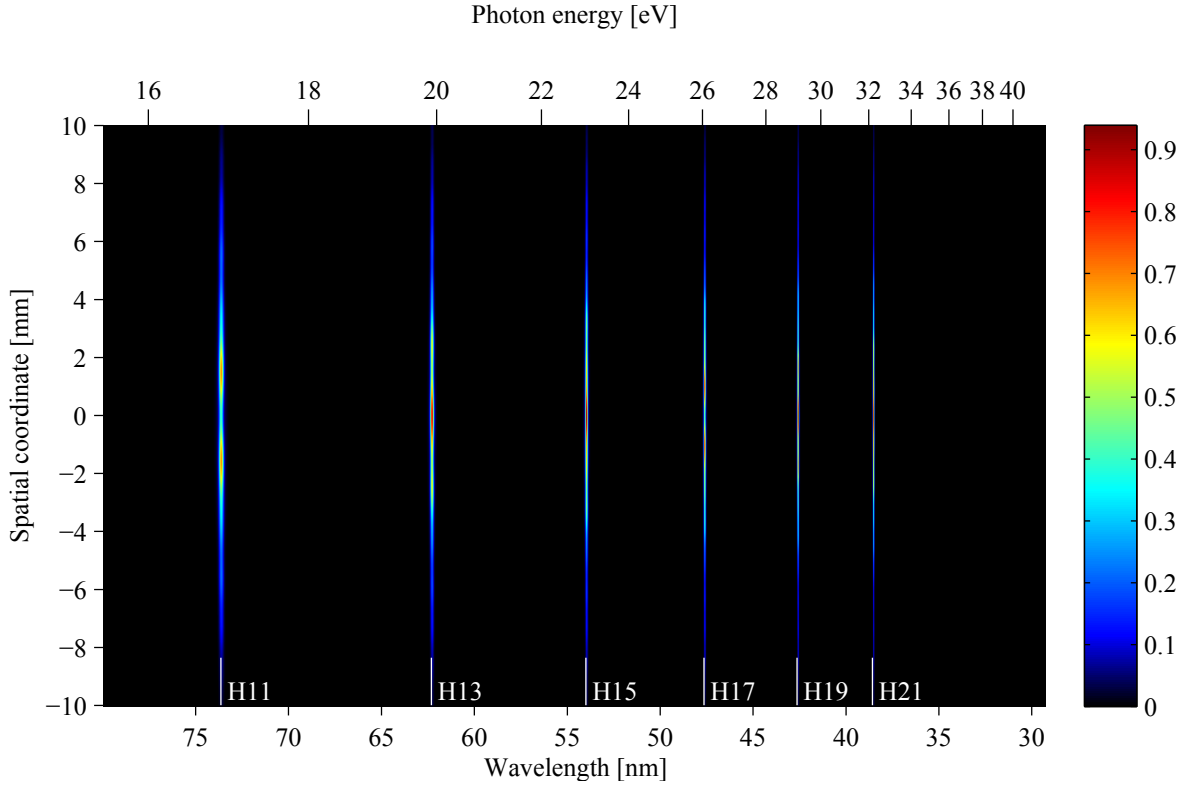

Figure 3.45 – (color) Simulated spatially resolved far-field harmonic spectra with short path only and constant $q_{eff} = 1$ generated in argon at 10^{14} W/cm² 1 cm before the focus.

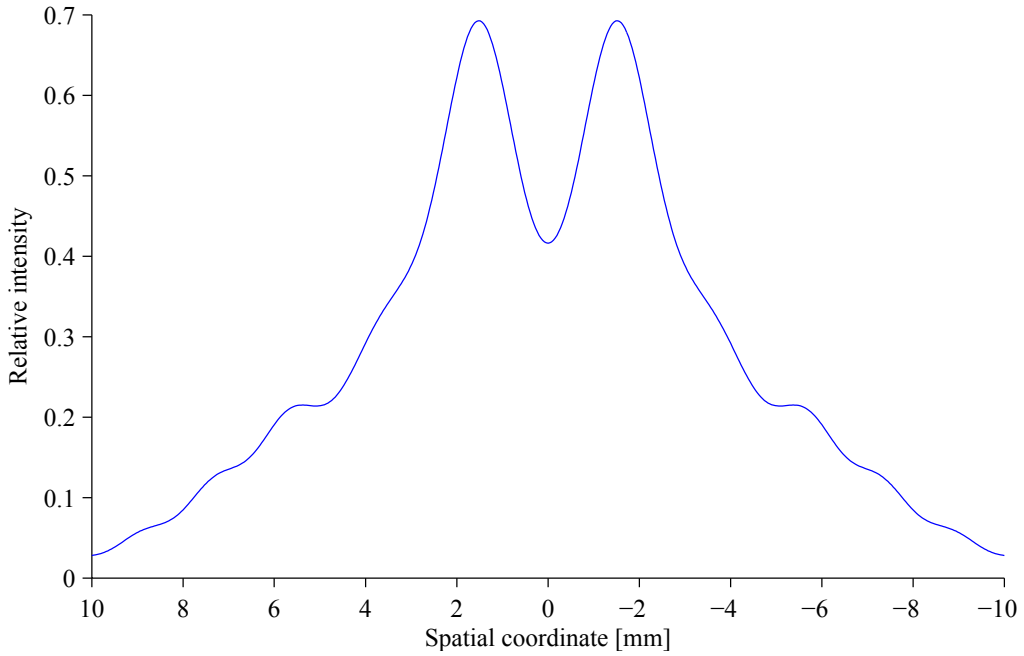

Figure 3.46 – Simulated far-field spatial profile of harmonic 11 short path only and constant $q_{eff} = 1$ generated in argon at 10^{14} W/cm² 1 cm before focus.

to-peak contrast reaches 40% with $q_{eff} = 1$ independently on the intensity. The size of the emitting source has therefore a strong impact on the structures in the spatial profile. Therefore another parameter left that can impact the far-field spatial profile is the harmonic dipole phase that depends on infrared intensity with α and that is as low as 1×10^{-14} cm²/W. We simulate the XUV profile under current conditions of $q_{eff} = 1$ and we put $\alpha = 0$. The resulting spectrogram is on figure 3.47 and the spatial profile of harmonic 11 on figure 3.48.

There are still modulations. One should note that the other harmonics may be modulated in another way. On figure 3.49 we plot the spatial profile of harmonic 21.

There is no minimum on axis but a three peak structure. In general the structures still exist and are different from one harmonic to the other.

As the structures are still present we have to check the beam profile in the gas jet before HHG. We check the infrared driving beam just after diffraction to the gas jet and plot it on figure 3.50.

We can see that the infrared spatial profile in the gas jet is nearly Gaussian. However, there are some small modulations at the wings. Those modulations are extremely weak - the second maximum represents only 0.02% of the main peak. Accordingly the phase is also slightly modulated.

Those modulations are due to an iris, that clips the driving beam before focusing to the gas jet (see figure 3.4). Until now the iris diameter was set to 30 mm that represents $3w_0$ where $w_0 = 10$ mm stands for beam radius at I_{max}/e^2. With that aperture it is commonly

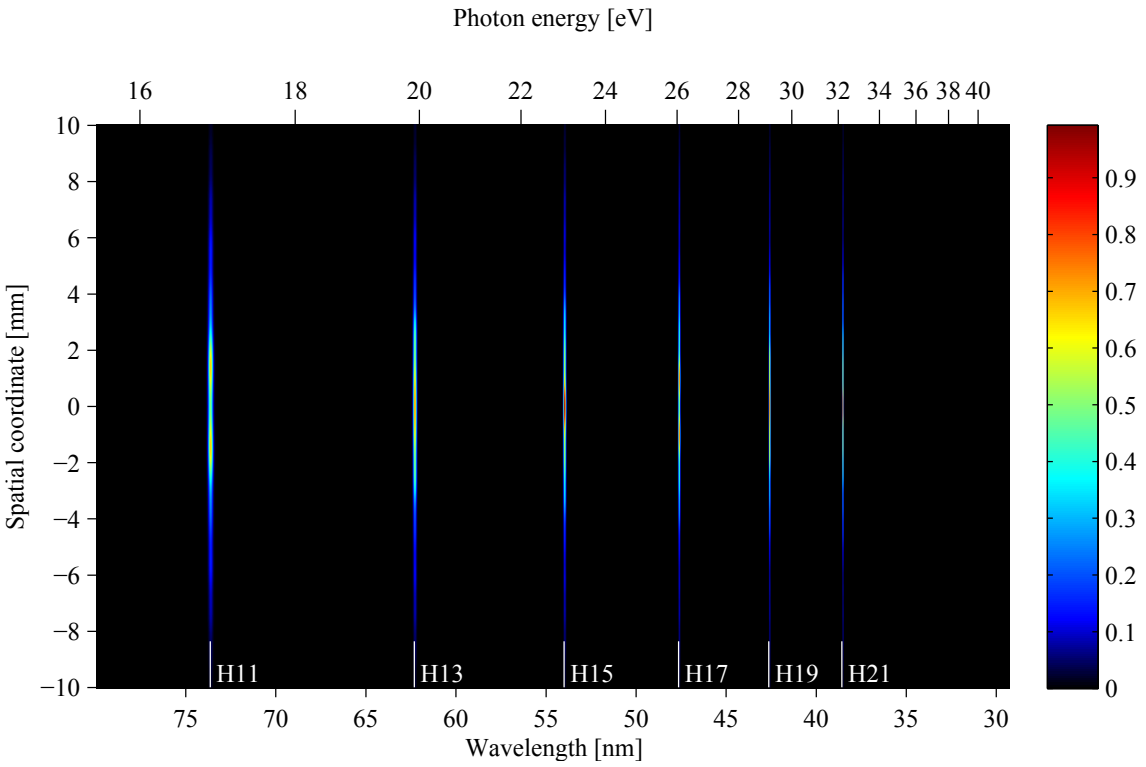

Figure 3.47 – (color) Simulated spatially resolved far-field harmonic spectra with constant $q_{eff} = 1$ and $\alpha = 0$ generated in argon at 10^{14} W/cm² 1 cm before the focus.

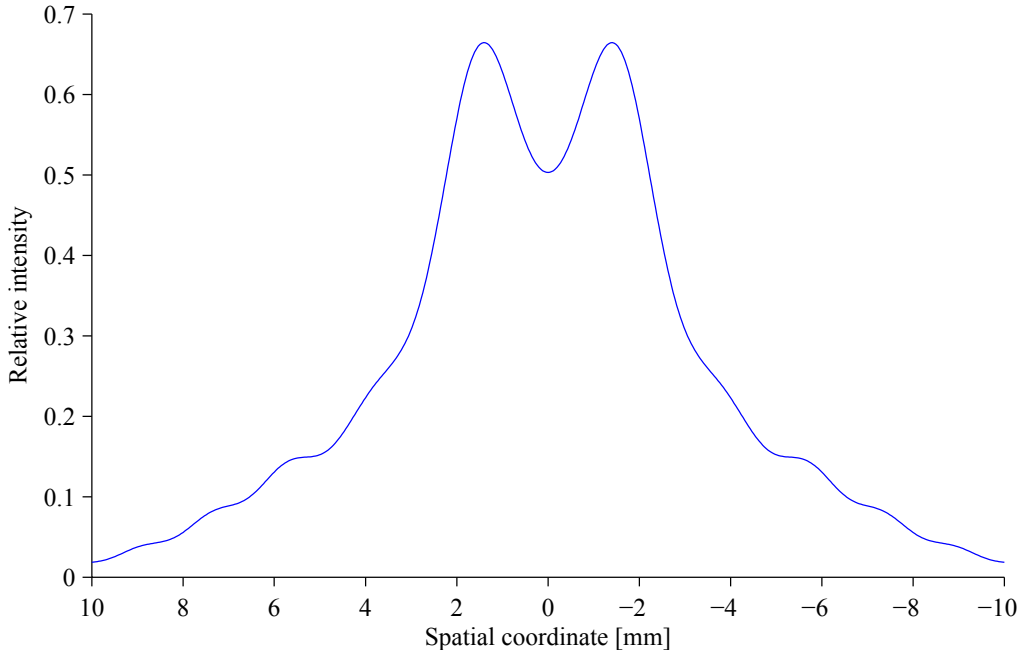

Figure 3.48 – Simulated far-field spatial profile of harmonic 11 with constant $q_{eff} = 1$ and $\alpha = 0$ generated in argon at 10^{14} W/cm² 1 cm before focus.

accepted that the 99% of the beam power is transmitted and this principle is accepted

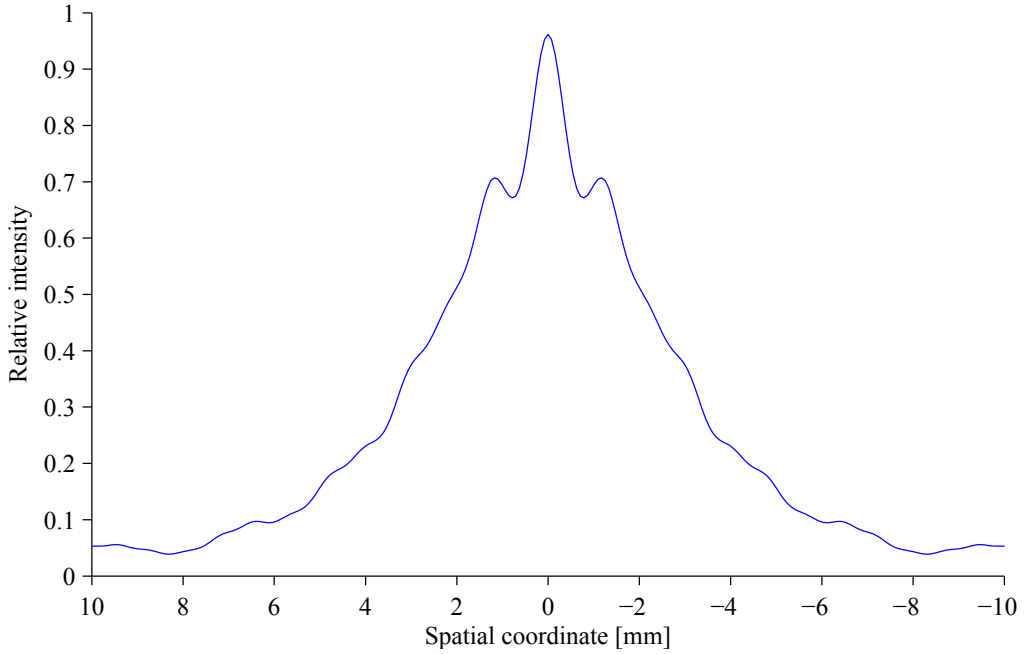

Figure 3.49 – Simulated far-field spatial profile of harmonic 21 with constant $q_{eff} = 1$ and $\alpha = 0$ generated in argon at 10^{14} W/cm² 1 cm before focus.

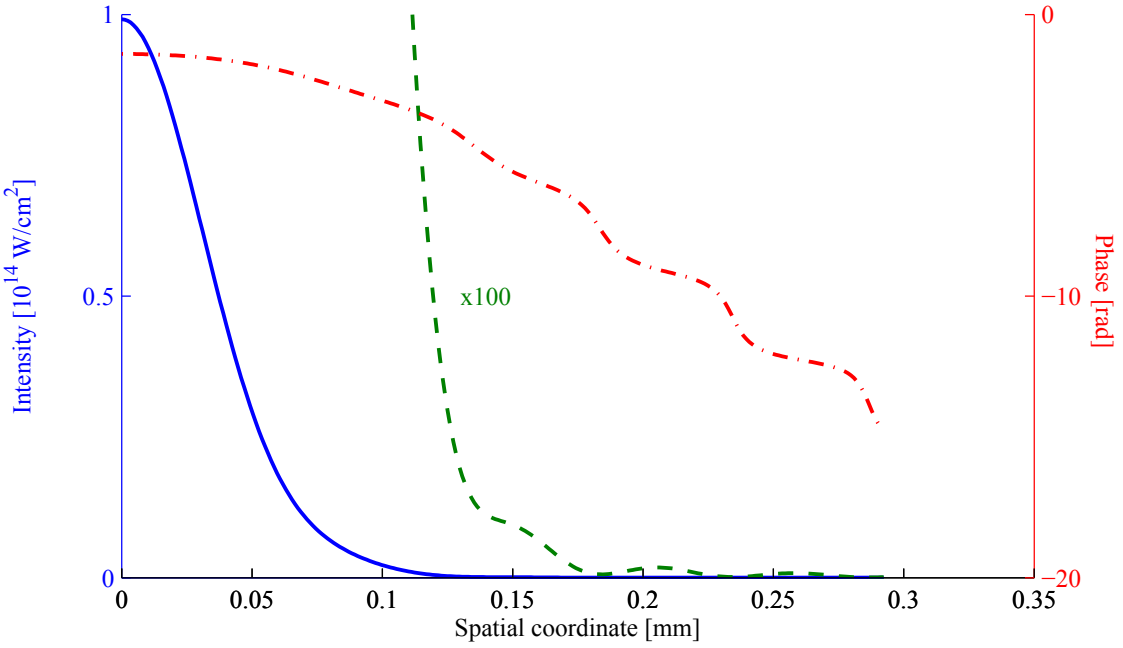

Figure 3.50 – Simulated infrared driving beam spatial profile in the gas jet (near-field) before HHG (blue solid) and a 100 multiplier (green dashed). Corresponding phase (red dot-dashed) is also shown. Before focusing the beam is clipped by iris of 30 mm diameter. The beam radius is 10 mm (at I_{max}/e^2).

also in designing an experimental setup to define the optics size needed to transmit the beam. Therefore the 30 mm iris diameter was present in our calculations to simulate the experimental optics aperture (2” optics).

In general those considerations are sound and sufficient (recall the second maximum of 0.02%).

In our case of high harmonic generation, however, all even extremely weak differences from the phase of the Gaussian beam will be amplified according to the harmonic order through the phase term $q\varphi_{IR}$. When considering also $q_{eff} > 1$ and $\alpha > 0$ then the resulting harmonic spatial profile would be even more modulated.

To be able to see harmonic with Gaussian spatial profile, we have to put $\alpha = 0$, $q_{eff} = 1$ and open the iris wider than $3w$. We can see the spectrum simulated with iris diameter of 50 mm on figure 3.51. To be sure that there are no more spatial modulations we will show whole MCP diameter i.e. 40 mm.

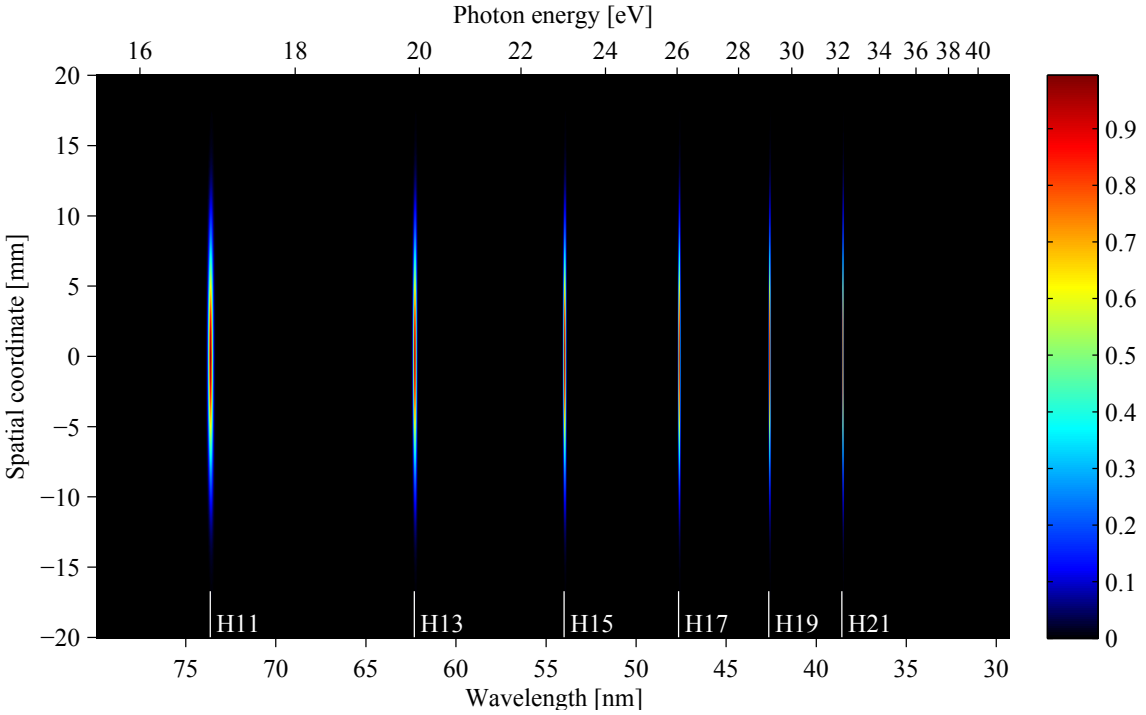

Figure 3.51 – (color) Simulated spatially resolved far-field harmonic spectra with constant $q_{eff} = 1$ and $\alpha = 0$ generated in argon at 10^{14} W/cm² 1 cm before the focus where the infrared beam was clipped with 50 mm diameter iris.

We can see that the spatial profile of harmonics is very close to Gaussian that means the iris diameter and afterward driving beam phase modulation was another responsible parameter that causes modulation of harmonic spatial profile.

The highest harmonic (same as H11) is a clean Gaussian as shown on figure 3.52.

One should not forget that in full simulation the significance of the driving beam wings decrease with effective harmonic order that equals $q/4$ where $I_{IR} < I_{cutoff}$. Also considering discontinued harmonic nonlinear phase and harmonic dipole amplitude, small modulations of infrared spatial profile would have very weak contribution to overall signal even for 30

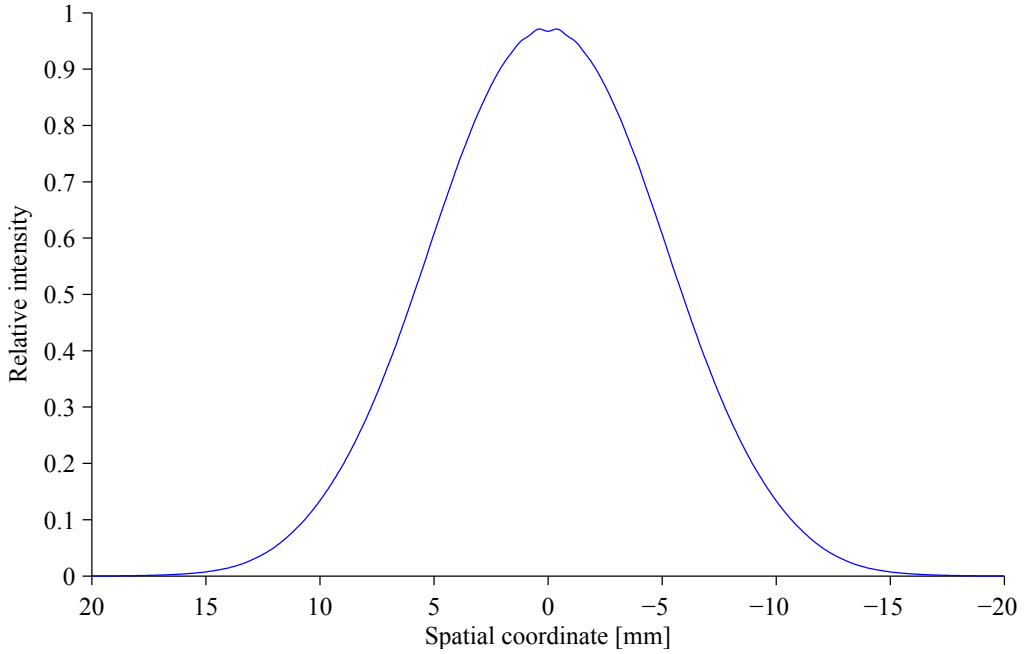

Figure 3.52 – Simulated far-field spatial profile of harmonic 21 with constant $q_{eff} = 1$ and $\alpha = 0$ generated in argon at 10^{14} W/cm² 1 cm before focus where the infrared beam was clipped with 50 mm diameter iris.

mm iris.

We reconsider all the phase and modulus components and simulate the far-field XUV profiles with iris diameter of 50 mm to compare with the figure 3.42. We show the spatial profile of harmonic 11 on figure 3.53.

We can see that in both cases with 50 mm diameter of iris the overall shape is close to Gaussian with only minor modulations. On the other hand the figure showing the H11 profile with iris diameter of 30 mm contains considerable modulation with a minimum on axis. Therefore the iris diameter should be considered when simulating the XUV profiles in the far field even if the infrared beam and phase modulation in the generating medium appear to be very small (as we have seen on figure 3.50).

3.3.3.3.2 Conclusion on short path structures in far field We observed that the short path on spatially resolved harmonic spectra in the far field contains some of the spatial structures. Those structures are qualitatively similar to structures seen in experimental spatially resolved XUV spectra. As the propagation in a generating medium is not included in our simulation, we attributed all the structures to interference and diffraction patterns of the harmonic spatio-spectral near-field.

There are no spectral structures in short path because the cutoff emission is not intense enough and the long path is spectrally very broad with major part of energy off the harmonic line. Therefore is concerns the short path structures only marginally. We will

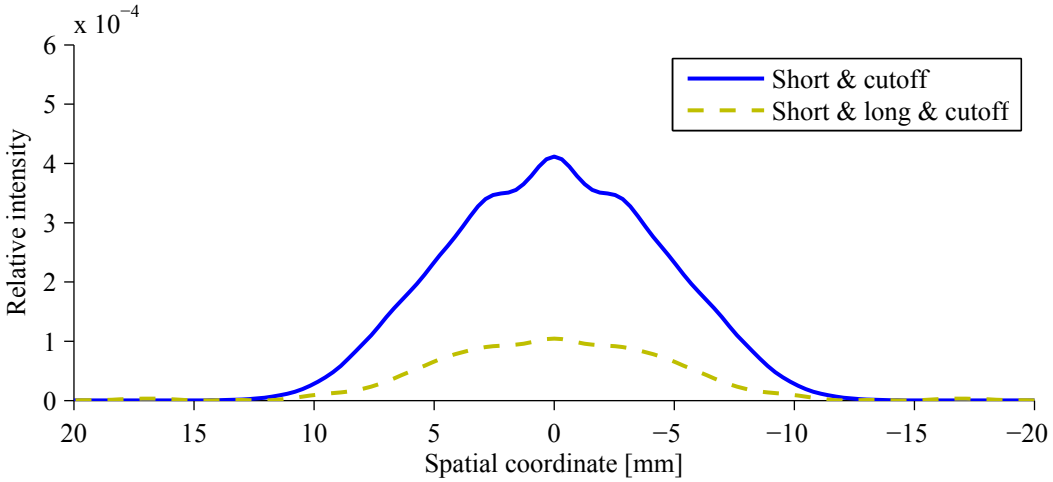

Figure 3.53 – Simulated far-field spatial profile of harmonic 11 generated in argon at 10^{14} W/cm² 1 cm before focus where the infrared beam was clipped with 50 mm diameter iris. Green dashed line denotes the case considering all the phase components while blue solid denotes the case without the long path ($\alpha = 1$ or 13×10^{-14} cm²/W).

devote next section to long path structures.

The spatial structures are made by harmonic dipole phase, dipole effective order and the presence of the driving beam intensity and phase profile that correspond to non-Gaussian beam due to iris. The IR phase profile is also very important because it is amplified by the dipole phase component $q\varphi_{IR}$. Note that the simulations were made 1 cm before the focus. HHG in the focus is a special case because the IR phase is zero (with additive constant) over whole beam so the $q\varphi_{IR}$ is also zero and the theoretical model is simpler.

All these features coherently sum together to create complex spatio-spectral XUV profile in the far field. For some part of some harmonics they can add constructively, somewhere they add destructively. Therefore the spatially integrated spectra are more regular and less structured than on-axis spectra.

3.3.3.3.3 Long path structures We have seen that the spectrally narrow short path is spatially modulated mainly by the dipole phase, effective order and the infrared driving beam phase and profile.

Because of α that is 25 times higher than the short path, the long path is spectrally much broader and contains more structures than the short path.

The most striking thing of the long path spatio-spectral profile are the so called multiple ellipses (see figure 3.33).

In [Heyl 11] authors explained similar structures as Maker fringes - the result of phase-matching controlled interference of the long path with itself. This approach, however, requires the propagation in the generating medium and thus it cannot be considered in our case where the generating medium is infinitesimally short i.e. the propagation is not

considered. Therefore the phase-matching conditions have no influence on the simulated XUV signal.

To check if the structures are due to quantum-paths-interference (QPI) [Zaïr 08, Holler 09, Schapper 10, Xu 08], we plot on figure 3.54 the spectra with long path only ($\alpha = 25 \times 10^{-14}\,\mathrm{cm^2/w}$ independent on intensity). The structures are still present in nearly the same

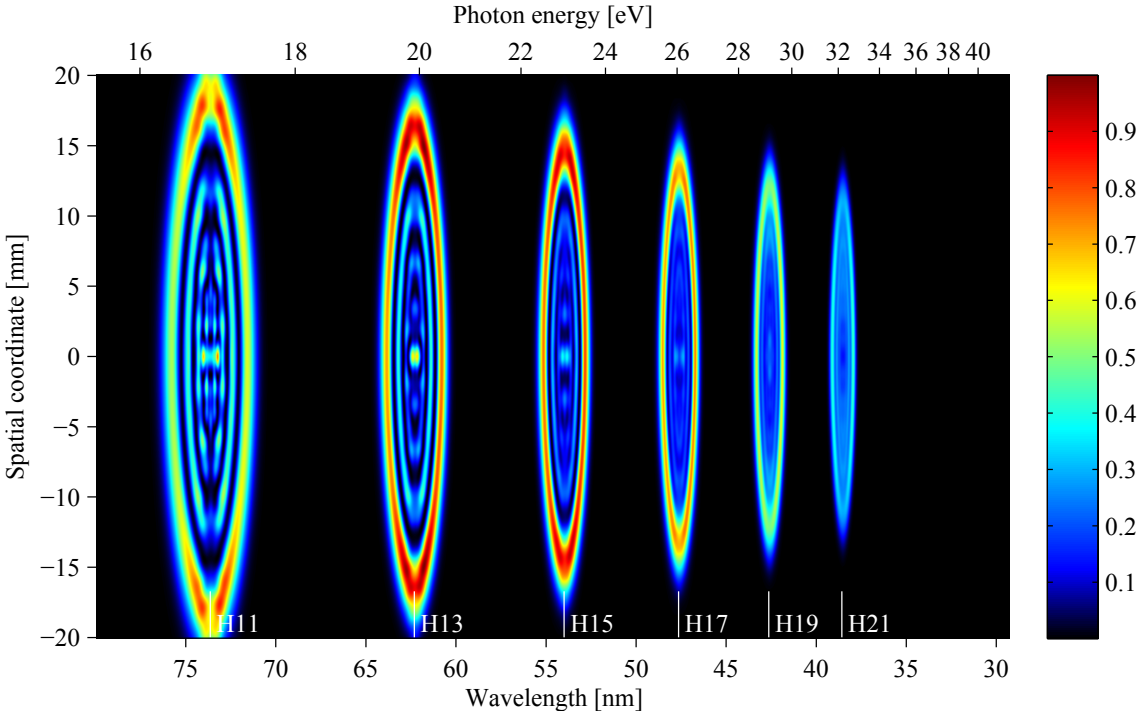

Figure 3.54 – (color) Simulated spatially and spectrally resolved XUV profiles in the far field. We consider only long path ($\alpha = 25 \times 10^{-14}\,\mathrm{cm^2/w}$ independent on intensity) and generation in argon at $10^{14}\,\mathrm{W/cm^2}$ 1 cm before the focus.

extent as in the case of both quantum paths. That excludes QPI as in [Zaïr 08] and also [Heyl 11] because there is no propagation in our simulation.

To test the influence of harmonics taking place in the plateau or in the cutoff, we set the generating intensity to $0.45 \times 10^{14}\,\mathrm{W/cm^2}$, putting harmonics 11, 13 and 15 in the plateau and harmonics 17, 19 and 21 to cutoff. The result is shown on figure 3.55, the on-axis spectra are on figure 3.56 and spatially integrated spectrum on figure 3.63 a).

The three harmonics H17, H19 and H21 in the cutoff still contain structures but they are spectrally more uniform than the three harmonics in the plateau. To have only Gaussian spatial profile of the harmonic dipole we put $q_{eff} = 1$ independently of the intensity for every harmonic. The resulting spectrum is on figure 3.57, the on-axis spectrum on figure 3.58 and the spatially integrated spectrum on figure 3.63 b).

The harmonic spatial profile structures are more pronounced as the structures are no more attenuated by high nonlinearity of the harmonic dipole.

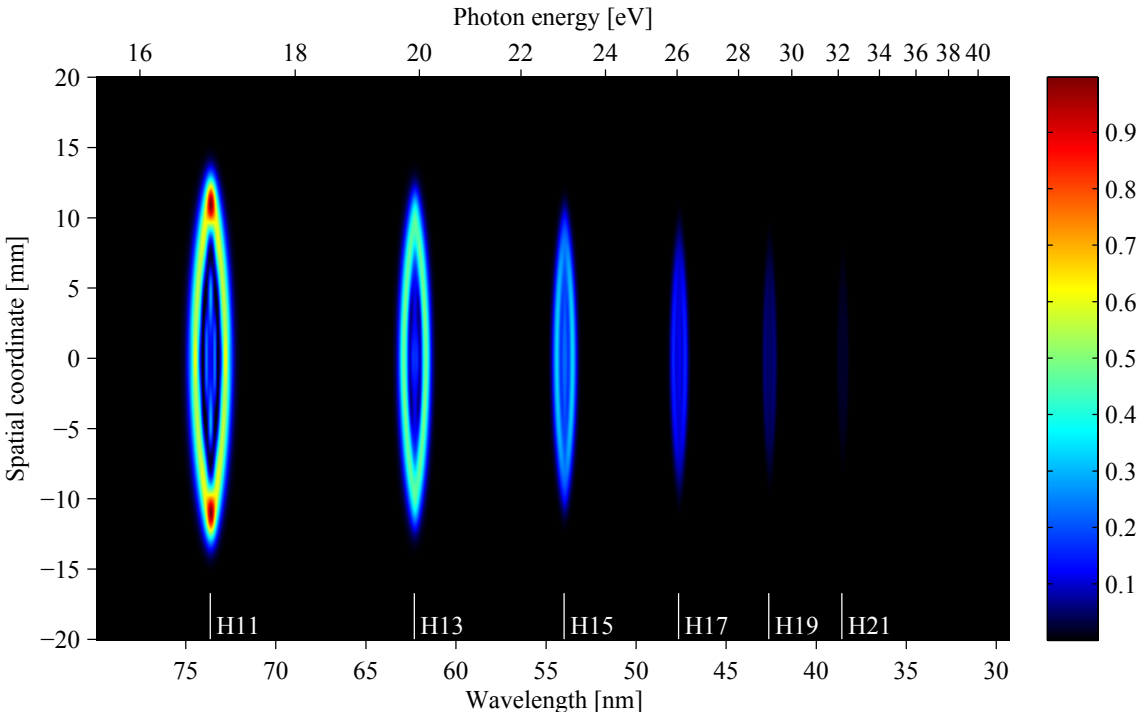

Figure 3.55 – (color) Simulated spatially and spectrally resolved XUV profiles in the far field. We consider only long path ($\alpha = 25\times10^{-14}\,\mathrm{cm^2/W}$ independent on intensity) and generation in argon at $0.45\times10^{14}\,\mathrm{W/cm^2}$ 1 cm before the focus.

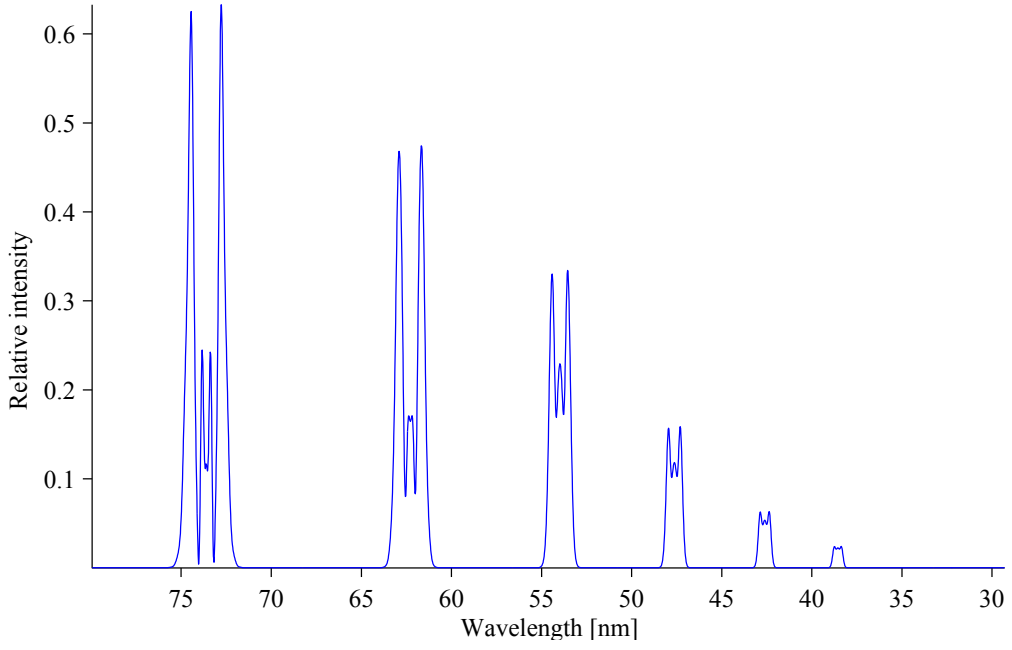

Figure 3.56 – Simulated on-axis XUV spectrum in the far field. The long path only ($\alpha = 25\times10^{-14}\,\mathrm{cm^2/W}$ independent on intensity) is considered and the peak infrared intensity is $0.45\times10^{14}\,\mathrm{W/cm^2}$ 1 cm before focus.

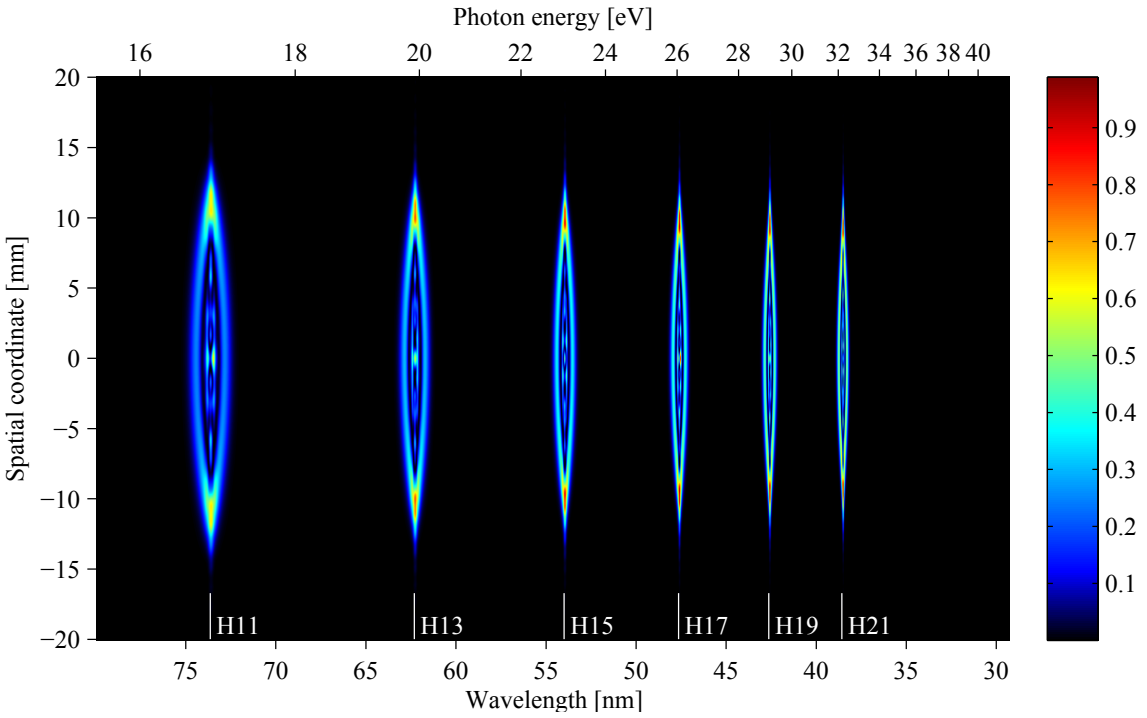

Figure 3.57 – (color) Simulated spatially and spectrally resolved XUV profiles in the far field. We consider only long path ($\alpha = 25 \times 10^{-14}\,\mathrm{cm^2/W}$ independent on intensity) and $q_{eff} = 1$ and generation in argon at $0.45 \times 10^{14}\,\mathrm{W/cm^2}$ 1 cm before the focus.

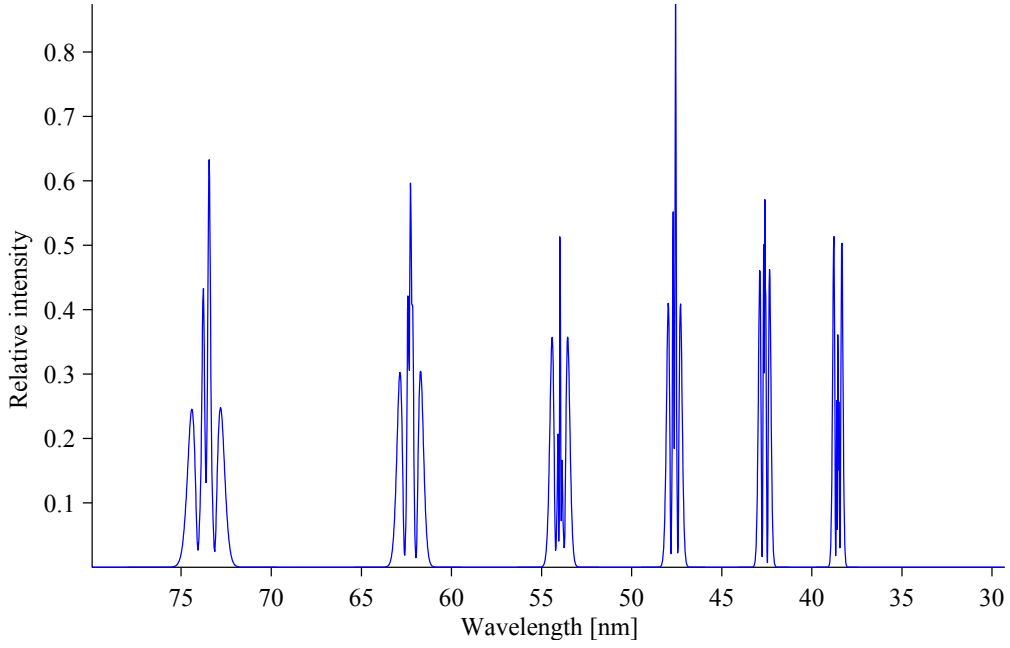

Figure 3.58 – Simulated spectral XUV far-field profile on axis with long path only($\alpha = 25 \times 10^{-14}\,\mathrm{cm^2/W}$ independent on intensity) and $q_{eff} = 1$ generated at $0.45 \times 10^{14}\,\mathrm{W/cm^2}$ 1 cm before focus.

Moreover the harmonic spatial profile (figure 3.59) became more structured.

The maxima are at around 10 mm off axis. As for the short path we simulated the

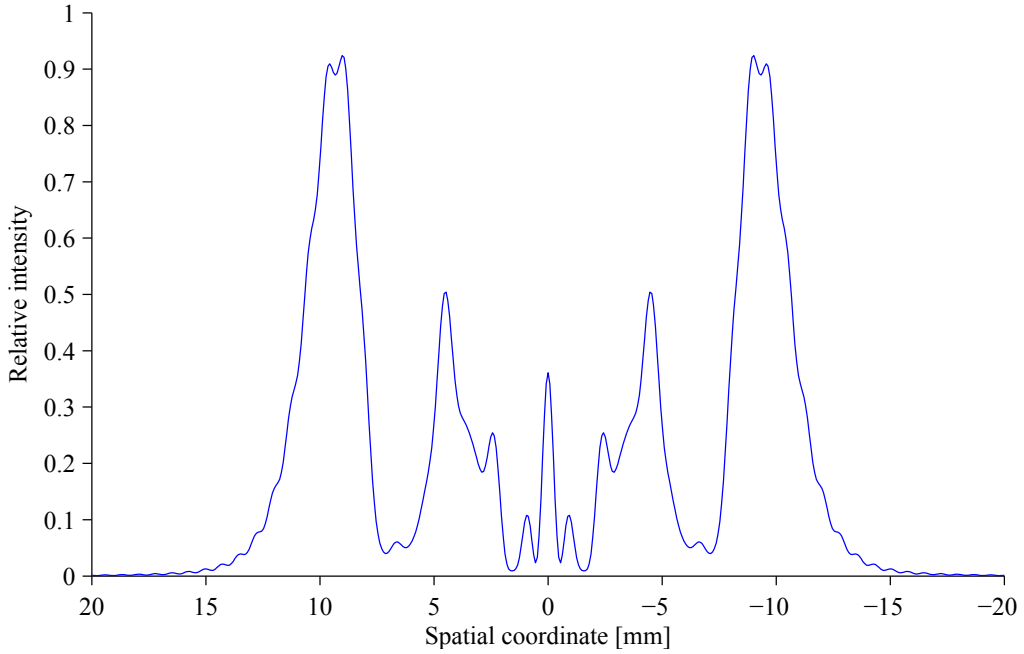

Figure 3.59 – Simulated far-field spatial profile of harmonic 21. We consider constant $q_{eff} = 1$ and long path only ($\alpha = 25 \times 10^{-14}\,\mathrm{cm^2/W}$ independent on intensity), generation in argon at peak intensity of $0.45 \times 10^{14}\,\mathrm{W/cm^2}$ 1 cm before focus. The infrared beam was clipped with 30 mm diameter iris before focusing.

long path only ($\alpha = 25 \times 10^{-14}\,\mathrm{cm^2/W}$ independent on intensity) and the $q_{eff} = 1$ with iris of 50 mm compared to 30 mm before. This would create more regular phase profile of the IR beam in the generating medium. The resulting spectrum is on figure 3.60, the on-axis spectral profile on figure 3.61, the harmonic 21 profile is on figure 3.62 and the spatially integrated spectra are on figure 3.63.

The spectral and spatial profiles are different from those with 30 mm diameter iris but they are still very structured. The 50 mm of iris diameter is large enough to avoid any spatial modulation in the harmonic signal as we saw on figure 3.52. That means that all the spatio-spectral structures that remain are due to long path interference with itself through the harmonic dipole phase component $\alpha_{long} I_{IR}$.

To quantitatively compare the spatially integrated XUV spectra we plot them on figure 3.63.

The figure 3.63 shows spatially integrated harmonic spectrum where we consider only the long path ($\alpha = 25 \times 10^{-14}\,\mathrm{cm^2/W}$ independent on intensity) and generation in argon at peak intensity of $0.45 \times 10^{14}\,\mathrm{W/cm^2}$ 1 cm before focus. The IR beam is clipped by a a), b) 30 mm or c) 50 mm diameter iris before focusing. The effective order q_{eff} equals 1.5 in the plateau and $q/4$ in cutoff in a), $q_{eff} = 1$ independently on intensity in b) and c). We can see that changing the iris diameter and the effective order changes the shape of the spectral structures, but not if they are present or not. This is in agreement with

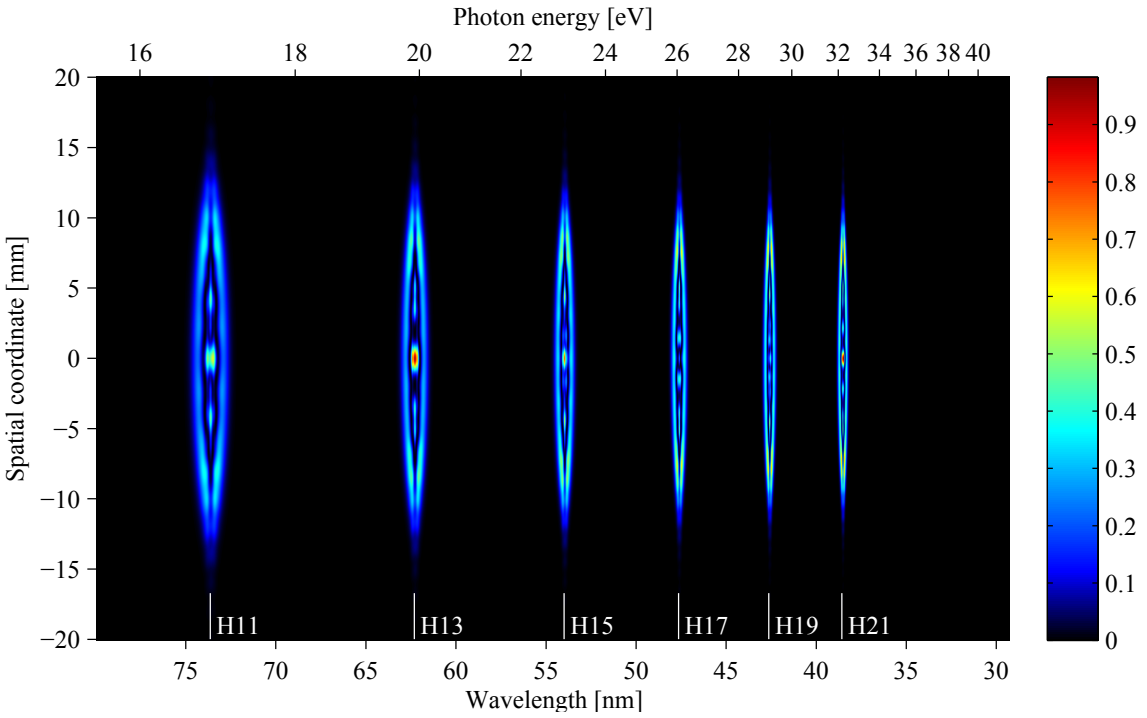

Figure 3.60 – (color) Simulated spatially and spectrally resolved XUV profile in the far field. We consider only long path ($\alpha = 25 \times 10^{-14}\,\mathrm{cm^2/W}$ independent on intensity) and $q_{eff} = 1$, generation in argon at $0.45 \times 10^{14}\,\mathrm{W/cm^2}$ 1 cm before the focus. The iris in the collimated IR beam is open to 50 mm.

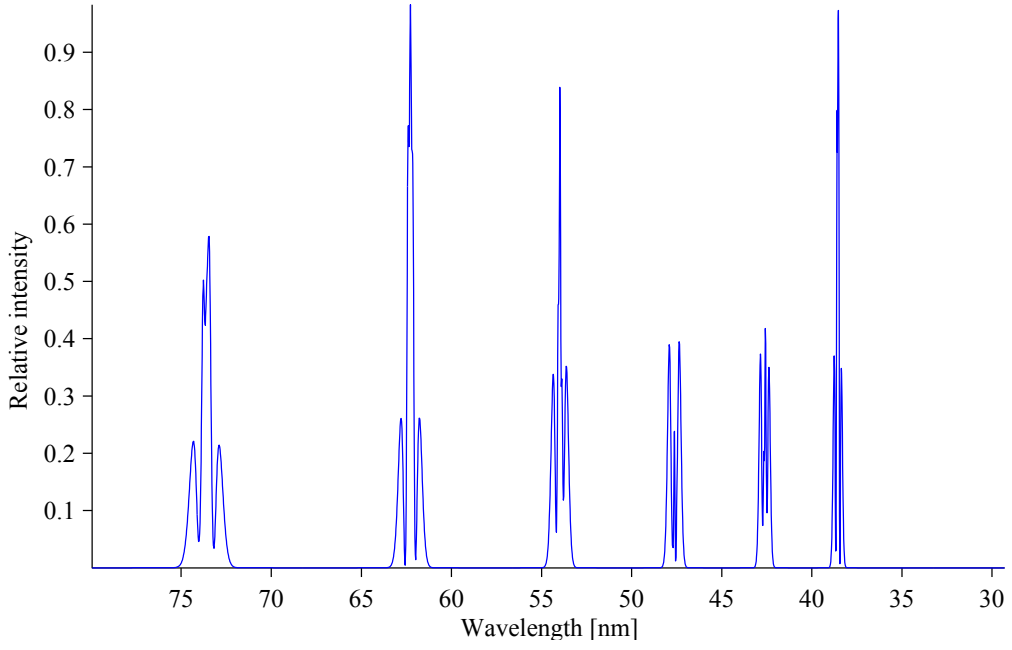

Figure 3.61 – Simulated XUV far-field spectrum on axis. We consider only the long path ($\alpha = 25 \times 10^{-14}\,\mathrm{cm^2/W}$ independent on intensity) and $q_{eff} = 1$ and generation in argon at $0.45 \times 10^{14}\,\mathrm{W/cm^2}$ 1 cm before focus. Before focusing the beam was clipped by 50 mm diameter iris.

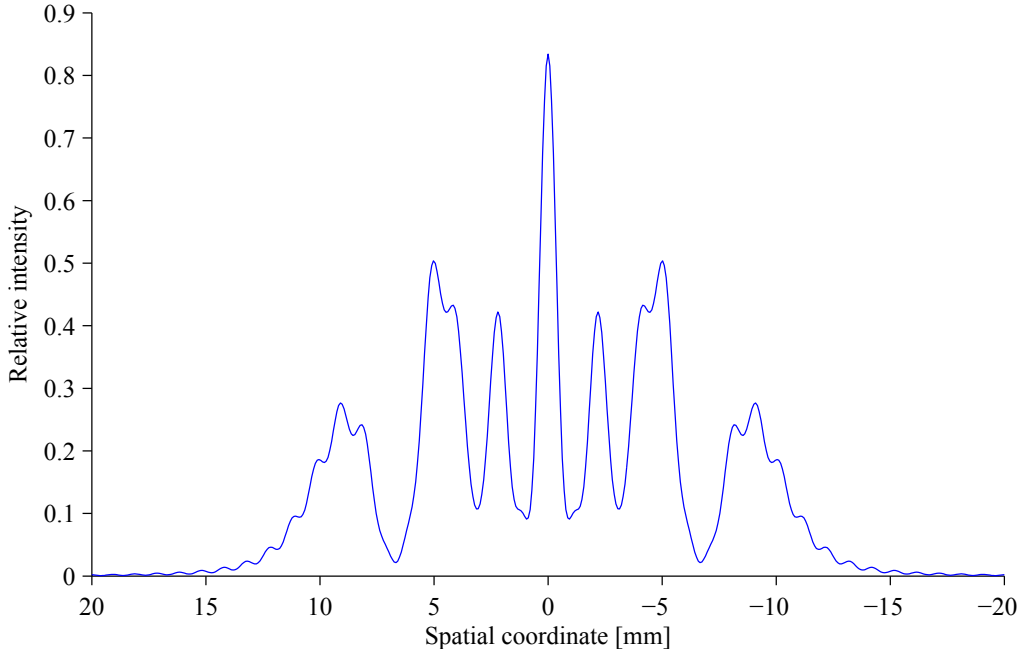

Figure 3.62 – Simulated far-field spatial profile of harmonic 21. We consider constant $q_{eff} = 1$ and long path only ($\alpha = 25 \times 10^{-14}\,\mathrm{cm^2/W}$ independent on intensity), generation in argon at $0.45 \times 10^{14}\,\mathrm{W/cm^2}$ 1 cm before focus. Before focusing the infrared beam was clipped with 50 mm diameter iris.

above paragraph where we identified the interferences between the long path with itself as a parameter that causes the spectral and spatial structures in the long path far-field spatially resolved spectra.

3.3.3.3.4 Conclusion on long path structures in far field

At low intensity driving field the long path is spectrally very large and promote a lot of substructures. Those structures both in frequency and space are mainly due to the interference of long path with itself via the nonlinear phase αI_{IR}.

Interference with the short path or with the cutoff XUV emission is reduced because there is much more long path signal off that lines than on the harmonic lines where the short path and cutoff emission take place.

The long path interference with itself is even stronger than iris influence on the far field harmonic spectra as shown with the short path.

3.3.3.4 Conclusion on HHG at low intensity driving pulses

We simulate HHG with low intensity driving pulses where the generating medium is practically not ionized. Propagation effects in the medium were not considered.

In the near field, we have seen separate harmonics and we distinguished spectrally narrow short path and spectrally large long path. There were spatial structures attributed

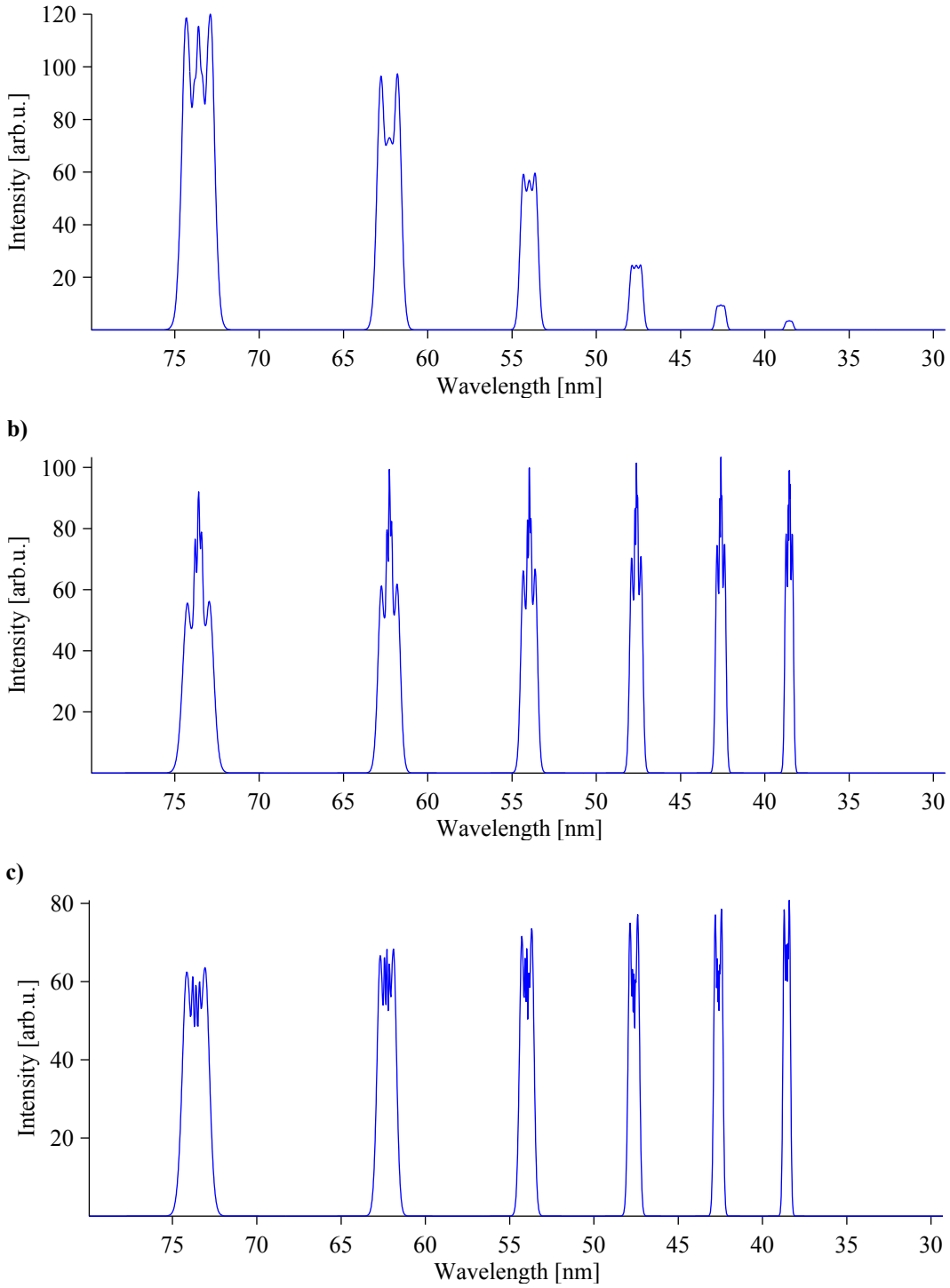

Figure 3.63 – Simulated spatially integrated harmonic spectrum. We consider only the long path ($\alpha = 25 \times 10^{-14}$ cm^2/w independent on intensity) and generation in argon at 0.45×10^{14} W/cm^2 1 cm before focus. The IR beam is clipped by a 30 mm diameter iris before focusing. Moreover the figure b) considers $q_{eff} = 1$ independently on intensity and the figure c) considers $q_{eff} = 1$ independently on intensity and the iris diameter of 50 mm.

to the quantum path interferences.

However, diffracting this harmonic emission to the far field changes a lot the causes of

the structures. As the long path is much more divergent from the short path, the quantum path interferences between the short and the long path can be neglected in the far field.

Spectrally narrow short path was spectrally modulated mostly because of an interference with cutoff harmonic emission. Spatial structures were attributed to interference with cutoff emission and modulation of the IR beam phase in the generation medium that are due to the iris that clips the infrared beam before focusing.

Spectrally large long path is much divergent than the short path. Interferences with itself result in structures in frequency and space visually reminding «ellipses».

In general in the far field, the structures in XUV spatially resolved spectra are due to harmonic phase that evolves in space and time. The origin of the evolution can be found in interferences (αI_{IR}) or in IR beam phase ($q\varphi_{IR}$). With higher q_{eff} the XUV beam is smaller, that lowers the contrast of the structures.

3.3.4 HHG at high intensity driving pulses

At low intensity we have seen structures in spatio-spectral XUV profile attributed to the spatial and temporal XUV phase profile. At high intensity the ionization gets important. In our simulation HHG in ions is omitted, thus ionizing an atom prevents it from generating harmonics. When the medium is 100% ionized the HHG can no more occur, changing importantly the HHG temporal and spatial distribution.

3.3.4.1 Near-field spatio-temporal XUV profile

To give a simple idea of what can happen at high intensity we can distinguish two major spatial regions:

On axis This region is completely ionized even before the temporal peak of the pulse. In this situation, the spatial distribution of emitters becomes asymmetric in time. It means that the emission takes place only in the rising edge of the driving pulse and so there is only a blue shift corresponding to $\alpha\frac{\mathrm{d}I_{IR}}{\mathrm{d}t}$ where the derivative is positive and no red shift is present.

Beam wings This region is characterized by infrared intensity that is not sufficient to ionize significantly the medium and then this case is similar to HHG at low intensity. The harmonic emission is symmetric or almost symmetric with both blue shift and red shift present.

There is no sharp border between these two regions. Certainly there are regions between them where the ionization is not 100% but high enough to asymmetrize temporally the

emission. Also there exist regions where the 100% of ionization is reached after the intensity peak.

All these regions interfere together in the far field contributing coherently to the overall detected signal.

We illustrate such generation conditions on figure 3.64. This spatio-temporal XUV

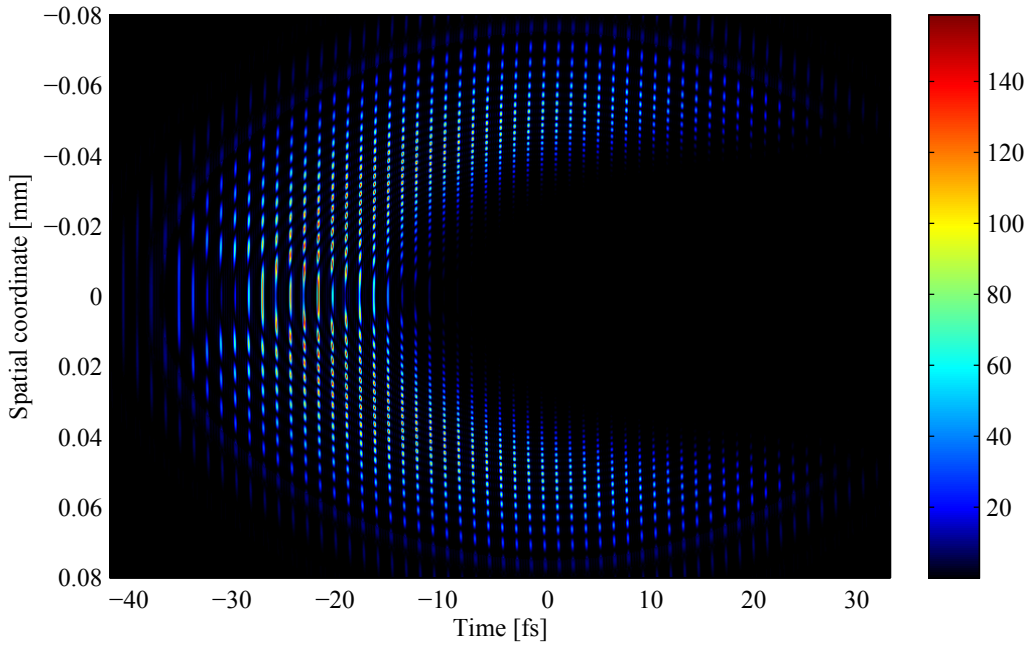

Figure 3.64 – (color) Simulated spatio-temporal XUV profile in the near field. HHG was simulated in argon at the peak intensity of 10^{15} W/cm² 1 cm before the cutoff for harmonics 11 to 21.

profile was simulated at ten times higher intensity than in the section 3.3.3.

We can observe that, on axis (where the intensity is maximal), the XUV emission occurs first. Then after around 15 attosecond pulses the emission on axis is terminated because of 100% ionization.

Slightly off axis, the infrared intensity is lower so the emission occurs later and finishes also later because of total ionization. In a time-spatial domain this creates a parabola-like emission pattern.

Far off axis the emission holds for entire duration of the infrared pulse but is attenuated in the falling edge because of high degree of ionization.

In the beam wings the emission is symmetric in time because of very low degree of ionization but is weaker than in former regions.

A striking thing appearing in the overall profile is that every attosecond pulse is spatially very modulated with a lot of fine structures. This is very different from the large spatial structures seen with low intensity pulses (figure 3.7).

To eliminate the influence of the harmonic dipole depletion we simulated the HHG without the depletion - considering the ionization degree equal to 0 everywhere. The resulting spatio-temporal profile is on the figure 3.65.

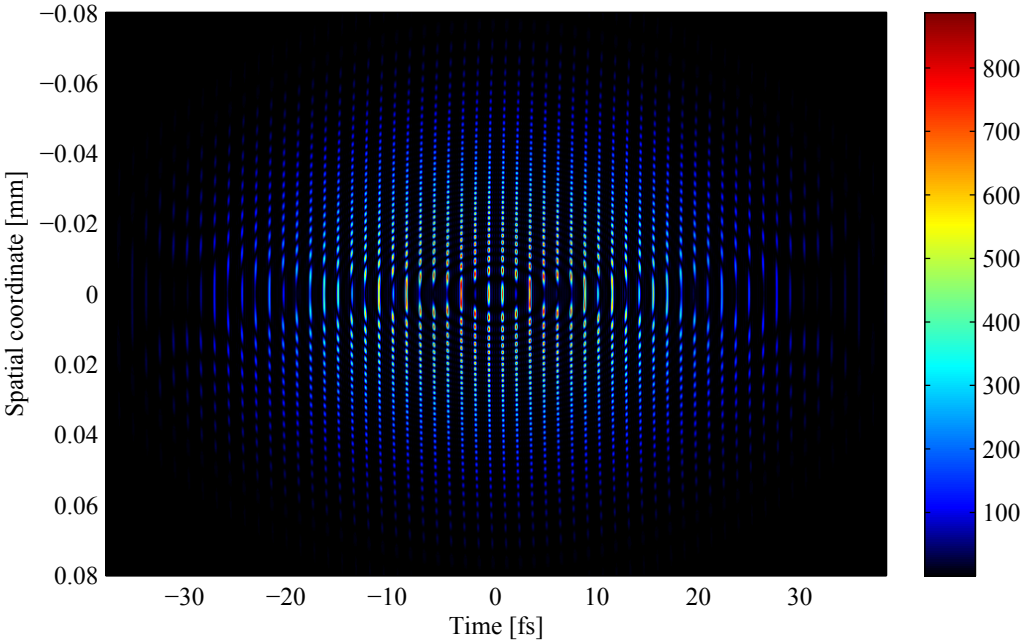

Figure 3.65 – (color) Simulated spatio-temporal XUV profile in the near field generated in argon at peak intensity of 10^{15} W/cm² 1 cm before the focus. The simulation is without ionization and without harmonic dipole depletion. We consider harmonics 11 - 21.

The parabolic overall profile of the emission became oval and symmetric but the fine spatial fringes inside attosecond pulses held unchanged.

At low intensity driving pulses, the major reasons for spatial modulations were the interference between the short and the long path $(\alpha_{long} - \alpha_{short})\, I_{IR}$. On figure 3.66 we can see the spatio-temporal profile without the long path. Now the attosecond pulses spatial profile is without any modulations.

Therefore the main reason for the spatial fringes is the interference between the short and the long path. XUV emission in the cutoff has practically no contribution at these intensity levels.

3.3.4.2 Near-field spatio-spectral XUV profile

The near-field spatio-spectral XUV profile with high intensity driving pulses is on figure 3.67.

The overall profile is completely different from that in the low intensity case on figure 3.17. However, with detailed examination one can find some similarities.

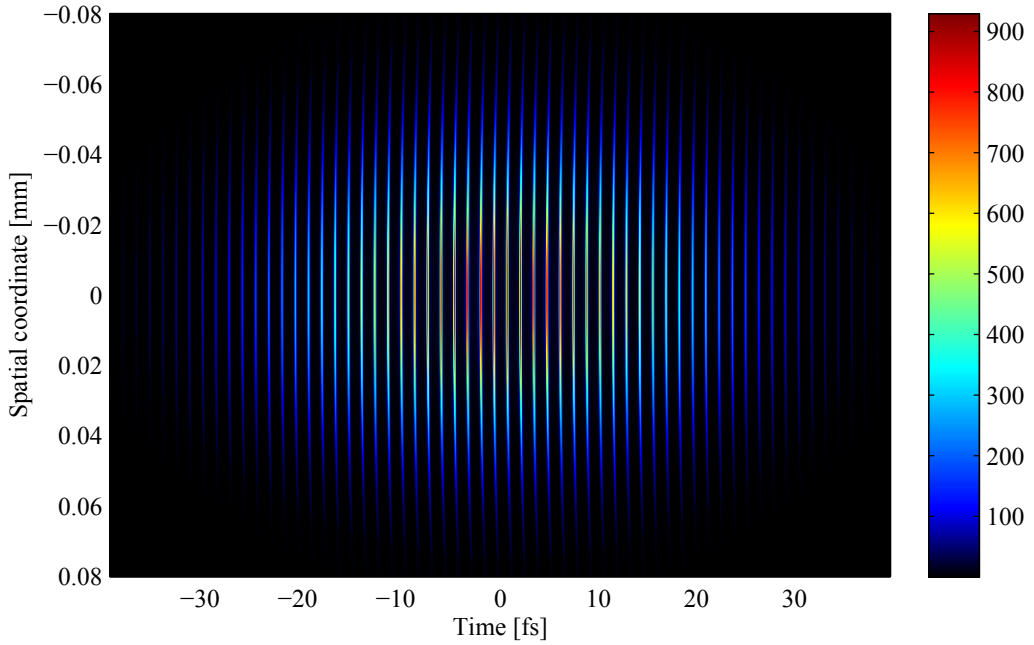

Figure 3.66 – (color) Simulated spatio-temporal XUV profile in the near field without long path generated in argon at 10^{15} W/cm² 1 cm before the cutoff. The simulation is without ionization and without harmonic dipole depletion. We consider harmonics 11 - 21.

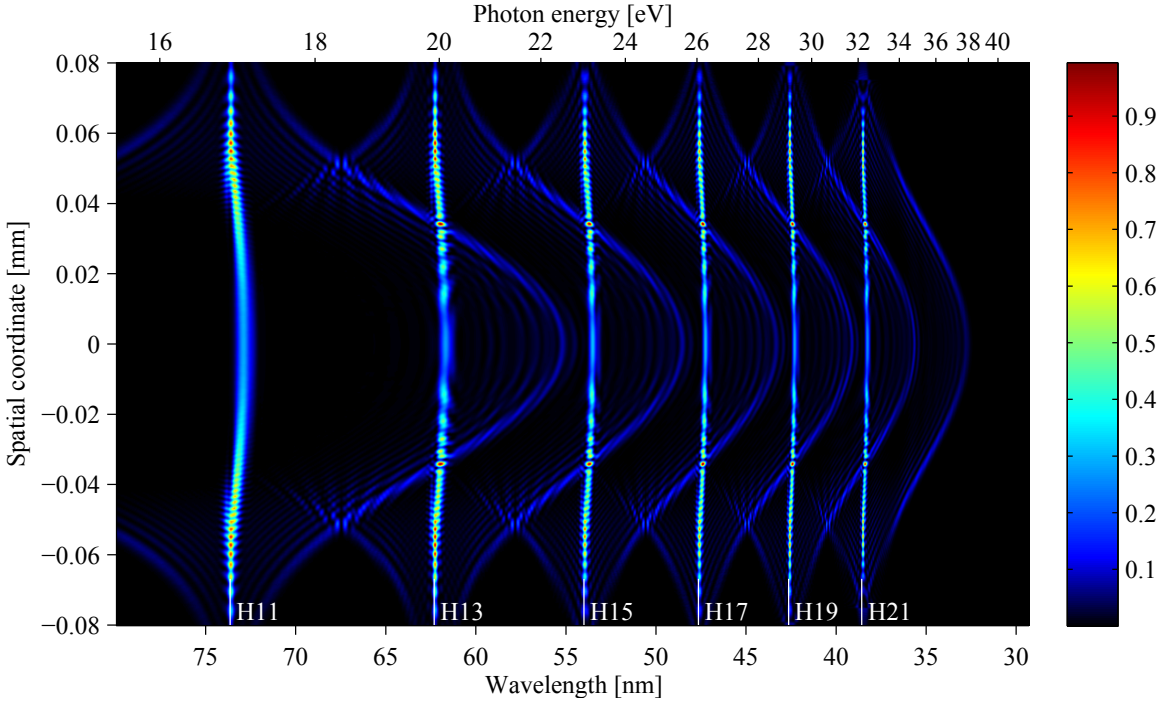

Figure 3.67 – (color) Simulated spatio-spectral near-field XUV profile generated in argon at peak intensity 10^{15} W/cm² 1 cm before the focus.

There are intense spectrally narrow lines on the harmonic frequency. Here at high intensity, they are curved to the shorter wavelength (blue-shifted) especially near axis and

highly modulated.

There are also multiple «bow» structures that are strongly blue-shifted on axis. The structures on axis are blue-shifted almost to the second higher harmonic. The structures of harmonic 15 interfere with structures of harmonic 11, 13, 17 and 19. That means that in general each harmonic interferes (at least partly) with 4 neighborhood harmonics.

To identify depletion effect we simulated the spatio-spectral profile without the ionization on figure 3.68.

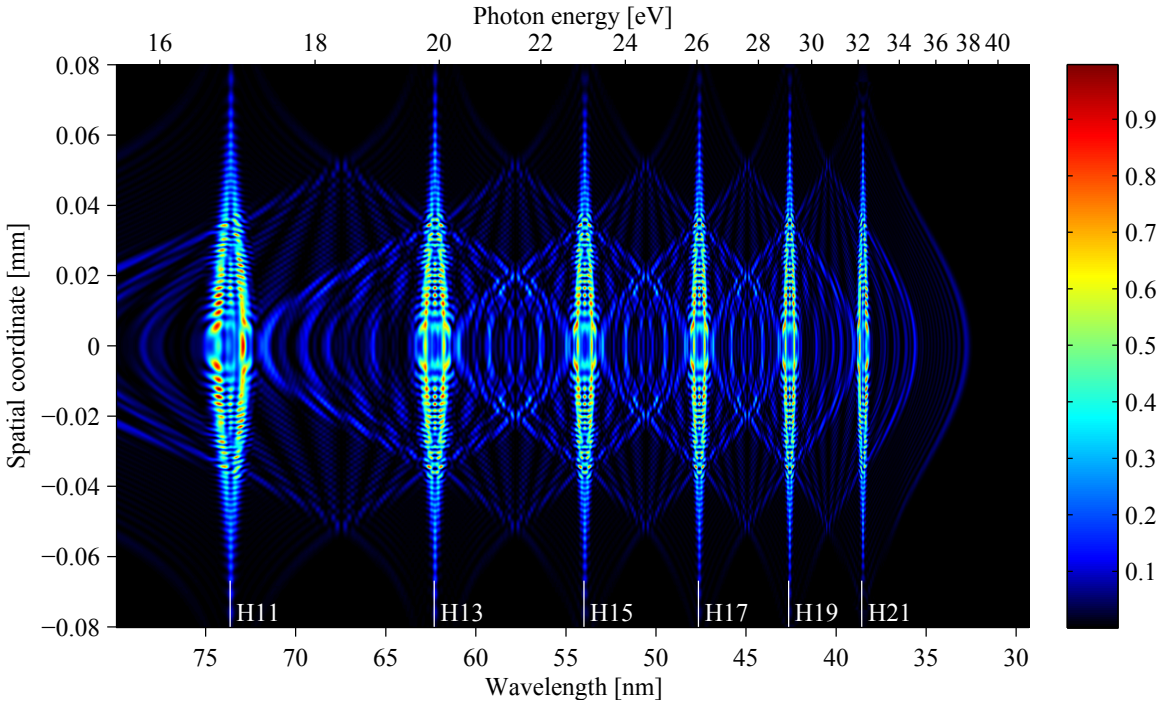

Figure 3.68 – (color) Simulated spatio-spectral near-field XUV profile generated in argon at $10^{15}\,\mathrm{W/cm^2}$ 1 cm before the focus without depletion.

The harmonic spectral profile became symmetric by adding the red-shifted part of each harmonic. This only adds more structures but their nature is the same as with depletion.

To identify long path influence we simulated the spatio-spectral profile without long path ($\alpha = 1$ or $13 \times 10^{-14}\,\mathrm{cm^2/w}$) on figure 3.69.

The spectra are less structured keeping only small spectral and spatial modulations.

The figure is almost the same as figure 3.29, where we simulated long path only for low intensity. In the low intensity case the long path structures were identified as long path interference with itself via harmonic nonlinear dipole intensity profile. In high intensity regime the frequency shift $\alpha\frac{\mathrm{d}I}{\mathrm{d}t}$ is important enough to that the structures can be observed also in the short path.

This spatial and spectral short path structures would change a lot when loosing the temporal symmetry i.e. when the depletion is considered. This case is illustrated on

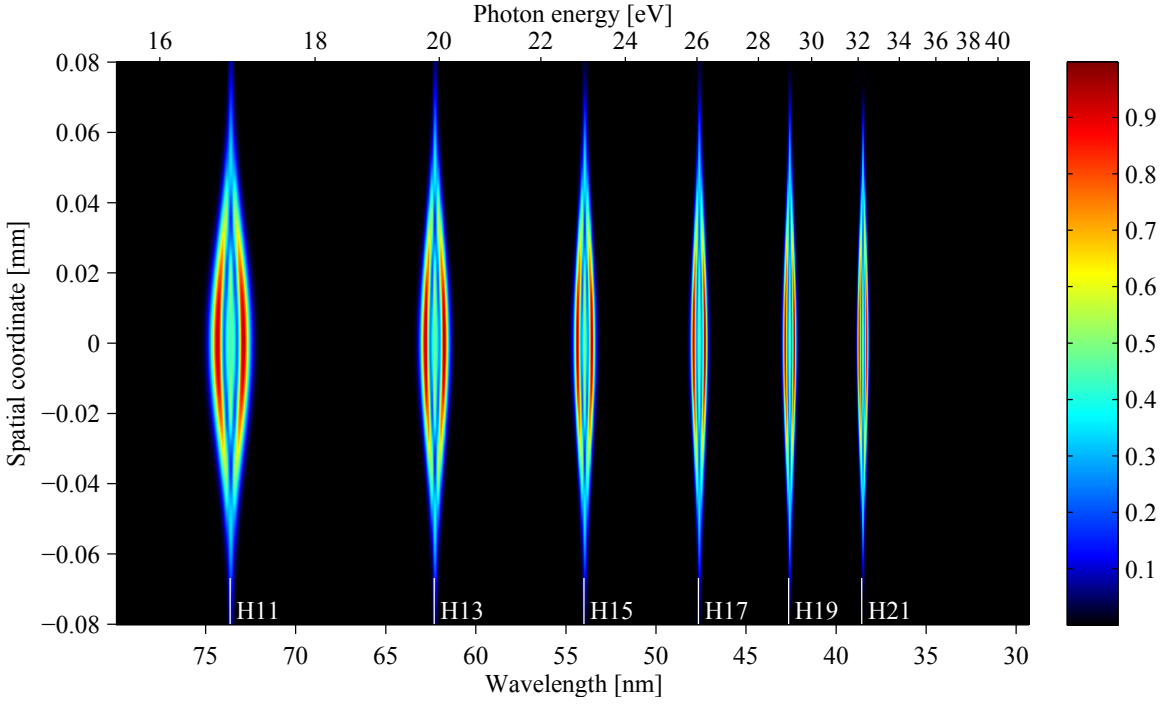

Figure 3.69 – (color) Simulated spatio-spectral near-field XUV profile generated in argon at 10^{15} W/cm² 1 cm before the focus without depletion and without the long path ($\alpha = 1$ or 13×10^{-14} cm²/W).

figure 3.70.

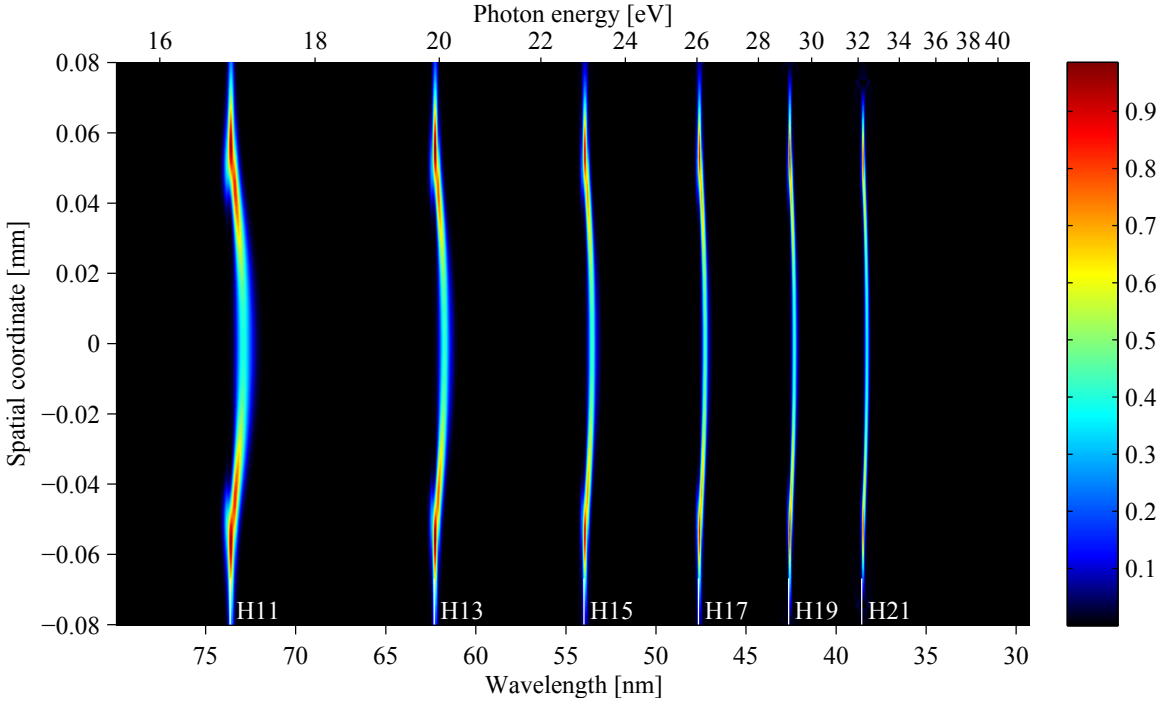

Figure 3.70 – (color) Simulated spatio-spectral near-field XUV profile generated in argon at 10^{15} W/cm² 1 cm before the focus without the long path ($\alpha = 1$ or 13×10^{-14} cm²/W).

We can see that without the long path the harmonic spectral profiles are without any modulations except the fact that on axis there is more blue shift than off axis.

The maximum of each harmonic is not placed on axis but off axis around 55 μm. This is because the zone where the spatial profile changes and the blue shift starts is off axis too. There are stationary conditions in the zone that allow accumulating the signal during the time. To quantify the zone we plot the ionization spatio-temporal profile on figure 3.71.

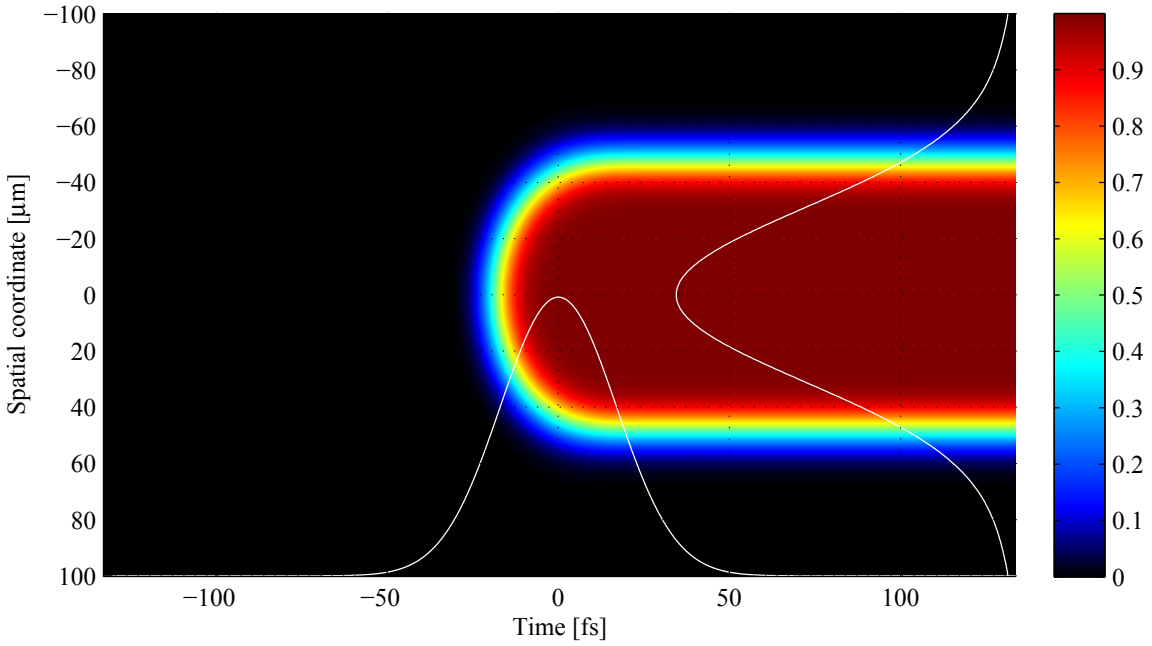

Figure 3.71 – (color) Simulated temporally and spatially resolved profile of the ionization degree in the generating medium. 0 stands for 0% and 1 for 100% of atoms ionized. The white Gaussian profiles give an idea about temporal and spatial profile of the infrared pulse intensity.

3.3.4.3 Far-field spatio-spectral XUV profile at high intensity

The near-field spatio-spectral profile was very structured because of the interference between the short and long path and because of interference of long path with itself and other harmonics. The depletion of the ground atomic state due to ionization reduces the structures.

The spatio-spectral profile of the XUV emission in on figure 3.72.

There are few things to notice:

- The harmonics are asymmetric and with blue-shifted and spectrally narrow bow-like overall profile.

- Those bow-like profiles are structured both in frequency and space.

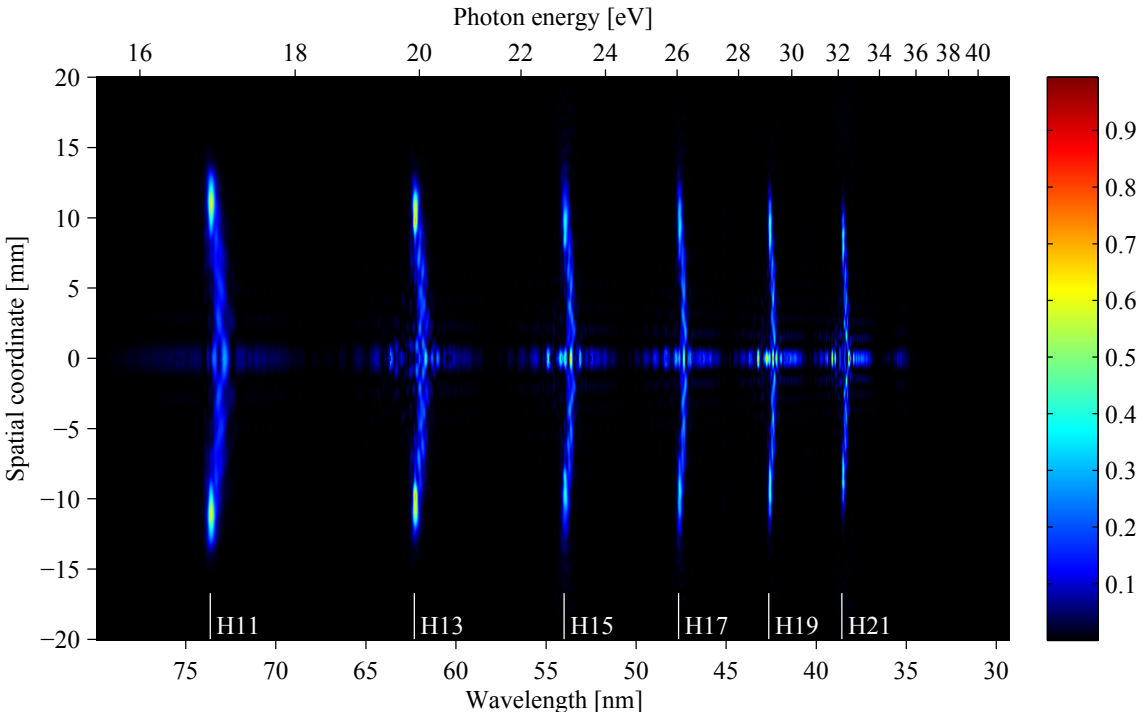

Figure 3.72 – (color) Simulated far-field spatially resolved XUV spectrum generated in argon at 10^{15} W/cm² 1 cm before the focus.

- There are no large spatio-spectral structures such as «ellipses» when generating with low intensity driving pulses.
- Maxima of the harmonics are not blue-shifted and are off axis in the distance of 10 mm for harmonic 11 and about 8 mm for harmonic 21.
- There are structures on axis.

As before, we will identify those aspects of XUV profile. To see better the structures we plot them in logarithmic scale on figure 3.73.

We still cannot see long path ellipses but there are a lot of inter-harmonic structures that are very regular. We simulated the generation without the long path ($\alpha = 1$ or 13×10^{-14} cm²/W) and the spectrum is presented on figure 3.74 and on figure 3.75 in log scale.

The long path creates the inter-harmonic regular diffraction pattern that has completely disappeared on figures 3.74 and 3.75. Also, the on-axis structure is almost completely gone, except for small red-shifted signal that can be seen on axis on figure 3.76. That means that even a highly divergent harmonic signal such as the long path has its contribution on axis in the far field.

To quantify the role of the depletion we plot the spatially resolved harmonics without the depletion on figure 3.77.

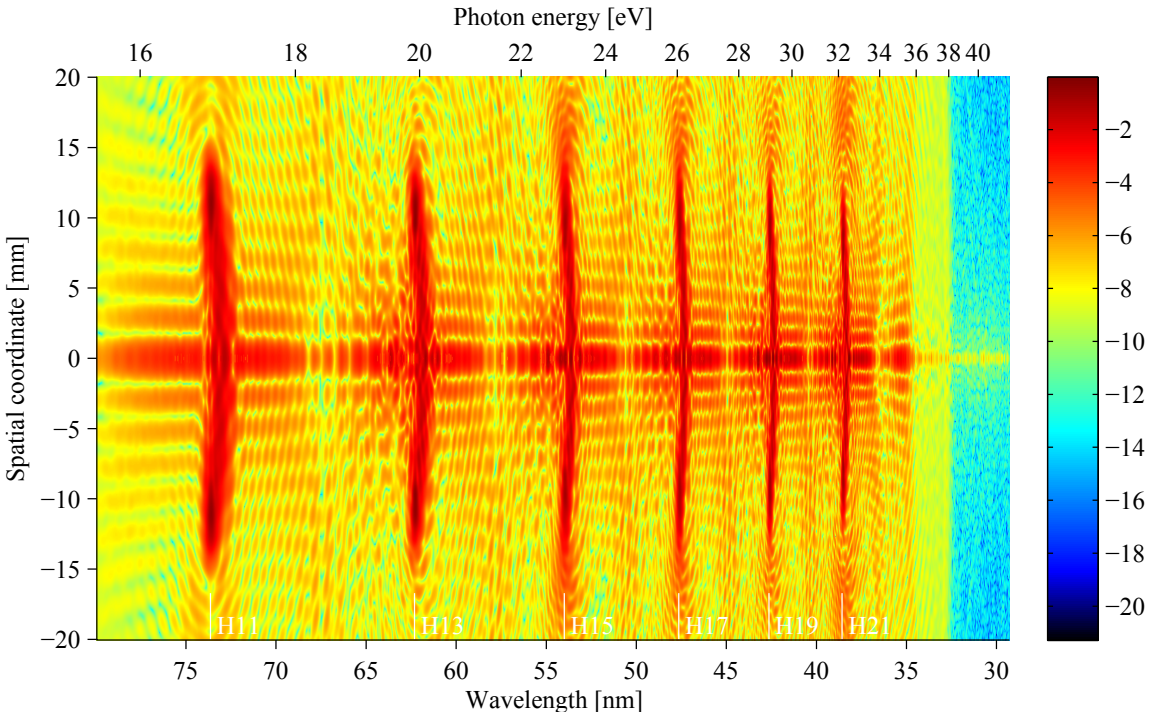

Figure 3.73 – (color) Simulated far-field spatially resolved XUV spectrum in logarithmic scale generated in argon at $10^{15}\,\mathrm{W/cm^2}$ 1 cm before the focus.

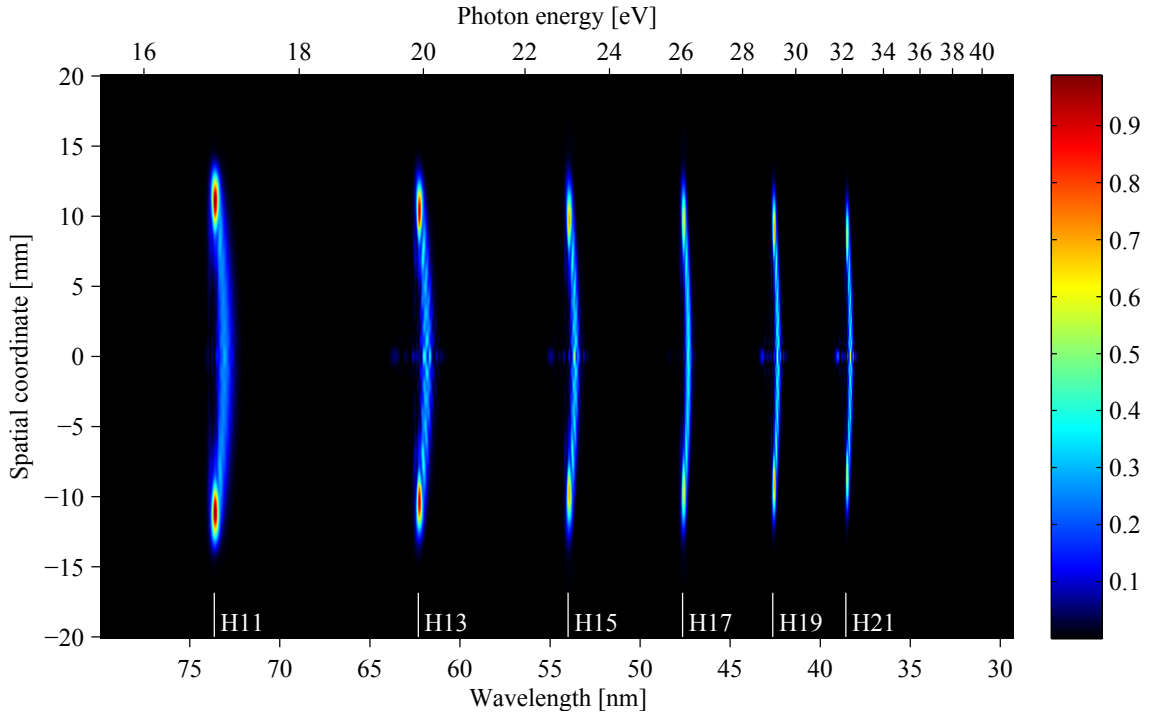

Figure 3.74 – (color) Simulated far-field spatially resolved XUV spectrum without the long path ($\alpha = 1$ or $13 \times 10^{-14}\,\mathrm{cm^2/W}$) generated in argon at $10^{15}\,\mathrm{W/cm^2}$ 1 cm before the focus.

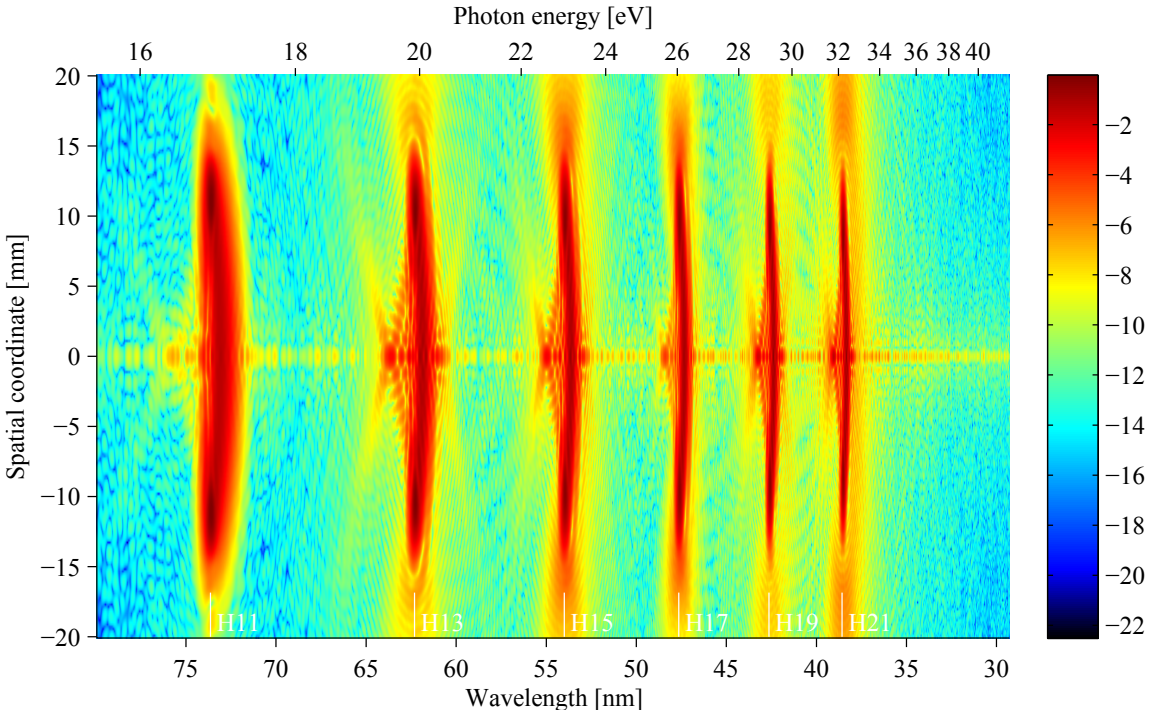

Figure 3.75 – (color) Simulated far-field spatially resolved XUV spectrum without the long path ($\alpha = 1$ or $13 \times 10^{-14}\,\mathrm{cm^2/W}$) generated in argon at $10^{15}\,\mathrm{W/cm^2}$ 1 cm before the focus.

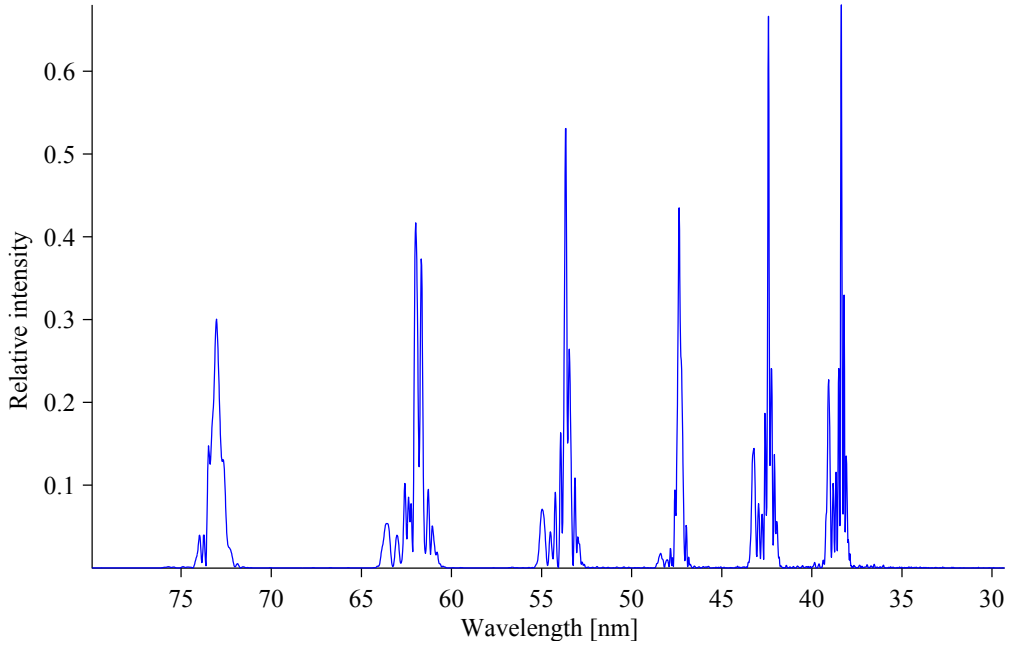

Figure 3.76 – Simulated on-axis spectral far-field XUV profile without the long path ($\alpha = 1$ or $13 \times 10^{-14}\,\mathrm{cm^2/W}$) generated in argon at $10^{15}\,\mathrm{W/cm^2}$ 1 cm before the focus.

Without the depletion the short path profile gains a «bow» also from the other side and blue-shifted structure and becomes symmetric. The main structures characteristics stay unchanged. The harmonic dipole depletion therefore does not create spectral structures.

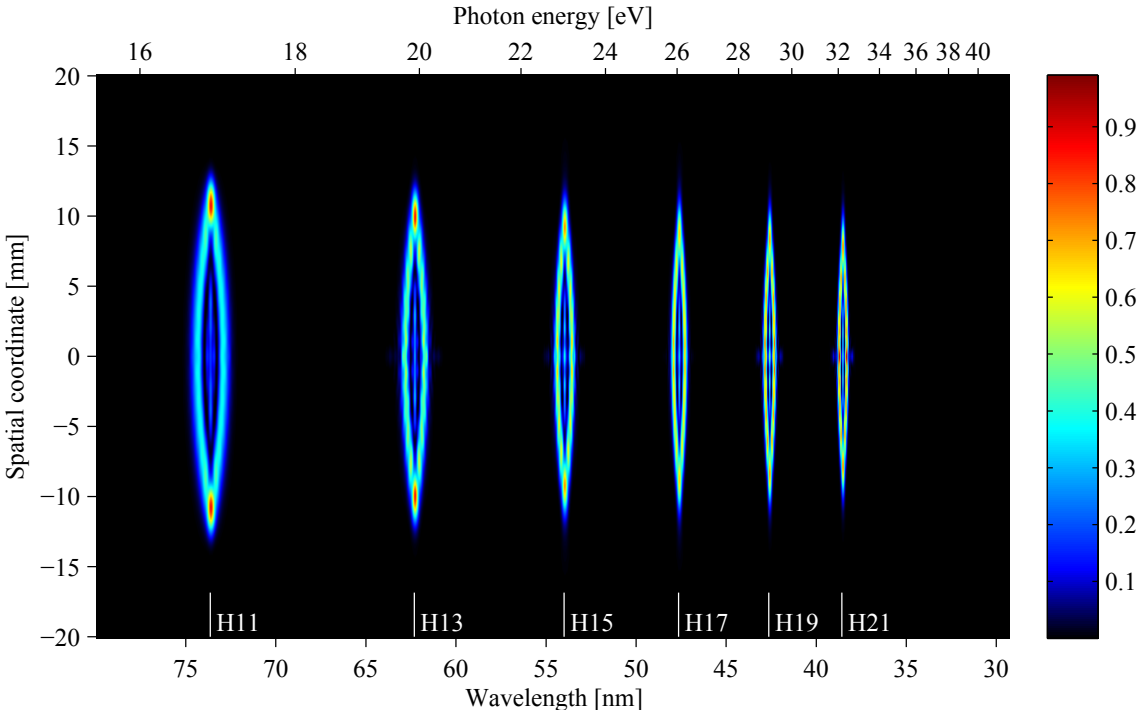

Figure 3.77 – (color) Simulated far-field spatially resolved XUV spectrum without the long path ($\alpha = 1$ or $13 \times 10^{-14}\,\mathrm{cm^2/W}$) and without the depletion generated in argon at $10^{15}\,\mathrm{W/cm^2}$ 1 cm before the focus.

We have already noted that near-field off-axis signal can have large contribution on axis in the far field. Thus we plot the XUV profile with short path only on figure 3.78.

It seems that the on axis spatially small red and blue-shifted structures disappeared. To validate this we plotted the short path only with depletion on figure 3.79 and on 3.80 in logarithmic scale.

We can see that either the structures disappeared or the relative weight of the short path lines decreased significantly. To see more in detail, we plotted the on-axis spectral profile on figure 3.81. The inter-harmonic structures completely disappeared (compared to figure 3.76) and there are only small and narrow modulations on the red side of the harmonics.

To check the impact of q_{eff} we omitted it on figures 3.82, 3.83 and 3.84. Note that there is still only the short path $\alpha = 1 \times 10^{-14}\,\mathrm{cm^2/W}$.

The inter-harmonic space is completely without any structure and the only modulations left are within the short path bow-like structures. Those structures seem keeping the original profile where the most blue-shifted part is on axis and is of low intensity and the brightest part is located in the wings of about 11 mm far from axis. This is little different from previous cases. A careful look on the figures show that with constant $q_{eff} = 1$, those harmonic wing maxima are located at the same position (11 mm off axis). This value is determined by the infrared spatial profile in the gas jet, the diffraction distance and the

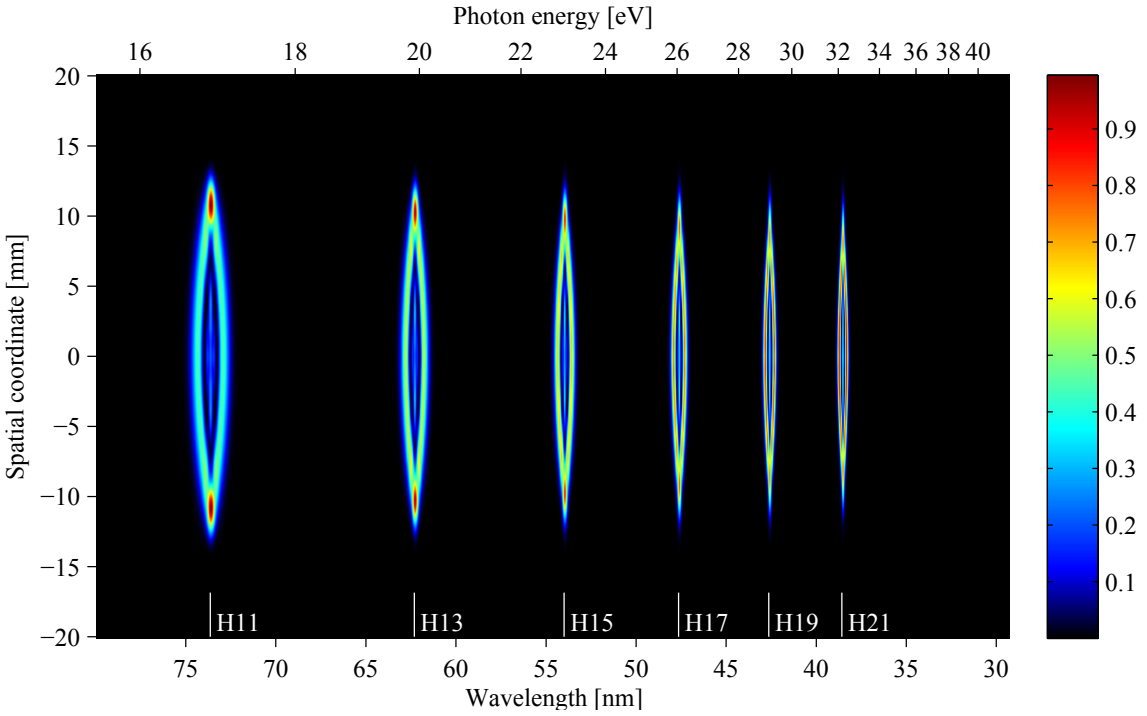

Figure 3.78 – (color) Simulated far-field spatially resolved XUV spectrum with short path only ($\alpha = 1 \times 10^{-14}\,\mathrm{cm^2/W}$ independently on the intensity) and no depletion generated in argon at $10^{15}\,\mathrm{W/cm^2}$ 1 cm before the focus.

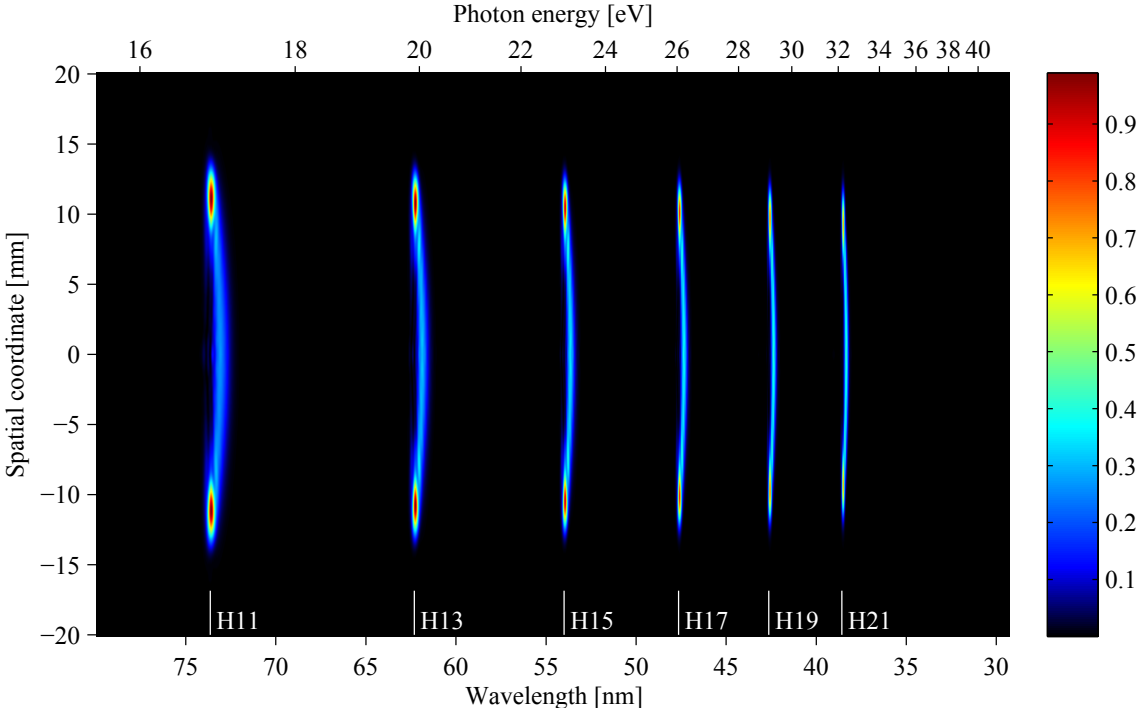

Figure 3.79 – (color) Simulated far-field spatially resolved XUV spectrum with short path only ($\alpha = 1 \times 10^{-14}\,\mathrm{cm^2/W}$ independently on the intensity) generated in argon at $10^{15}\,\mathrm{W/cm^2}$ 1 cm before the focus.

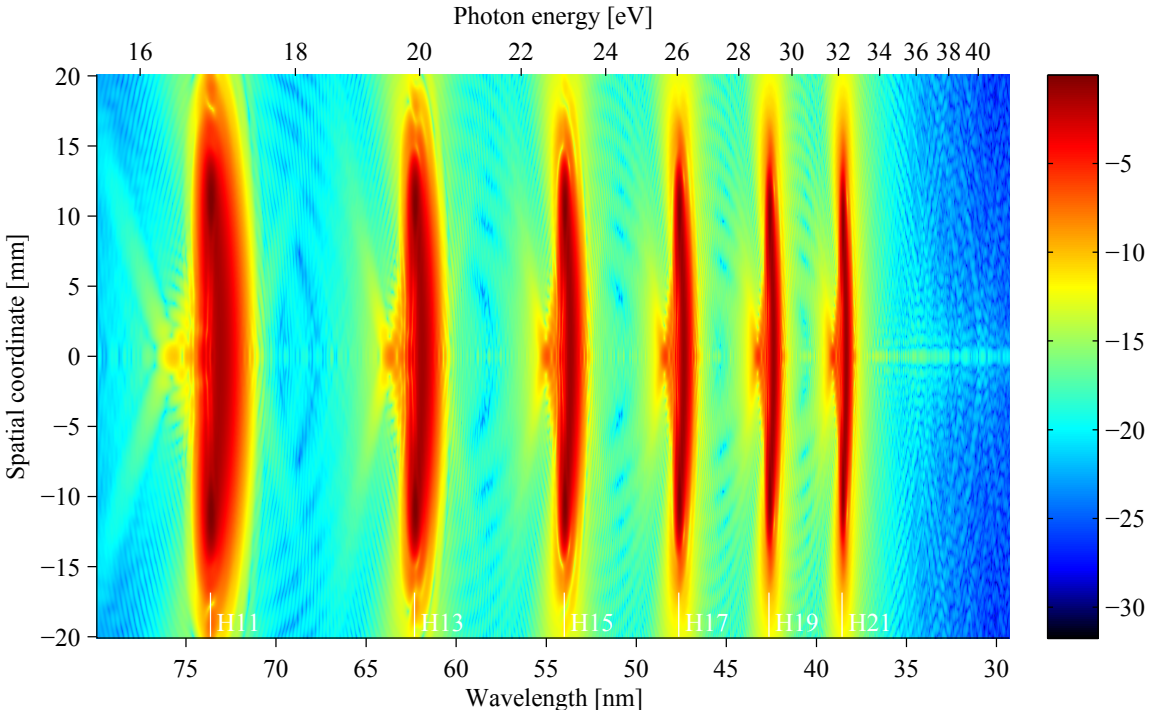

Figure 3.80 – (color) Simulated far-field spatially resolved XUV spectrum with short path only ($\alpha = 1 \times 10^{-14}\,\mathrm{cm^2/W}$ independently on the intensity) in logarithmic scale generated in argon at $10^{15}\,\mathrm{W/cm^2}$ 1 cm before the focus.

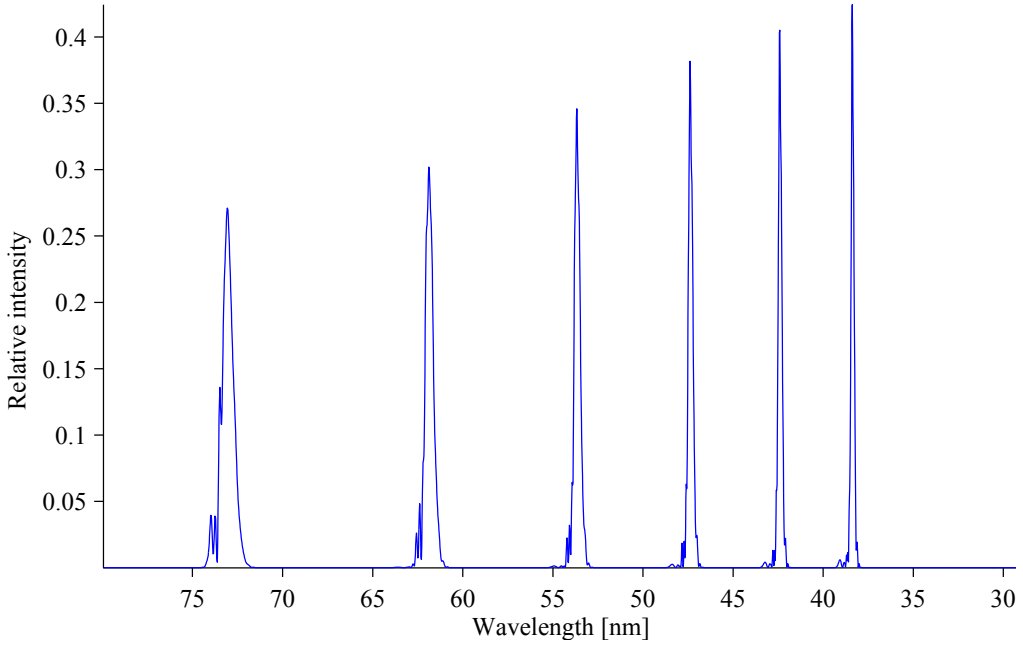

Figure 3.81 – Simulated far-field on-axis spectral XUV profile with short path only ($\alpha = 1 \times 10^{-14}\,\mathrm{cm^2/W}$ independently on the intensity) generated in argon at $10^{15}\,\mathrm{W/cm^2}$ 1 cm before the focus.

value of harmonic dipole phase.

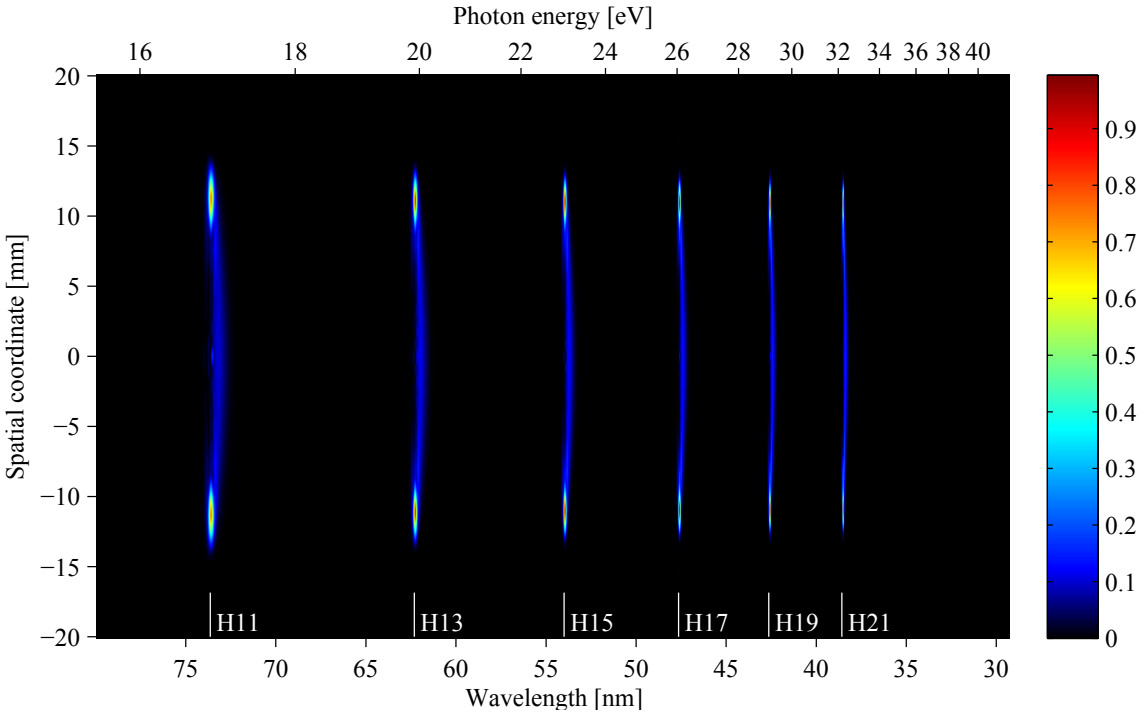

Figure 3.82 – (color) Simulated far-field spatially resolved XUV spectrum with short path only ($\alpha = 1 \times 10^{-14}\,\mathrm{cm^2/W}$ independently on the intensity) and $q_{eff} = 1$ generated in argon at $10^{15}\,\mathrm{W/cm^2}$ 1 cm before the focus.

3.3.4.3.1 The case for the gas jet position of 1 cm after the focus (diverging IR beam) We have seen that the driving beam phase profile influences a lot the resulting spectrum via the harmonic dipole phase $q\varphi_{IR} + \alpha I_{IR}$. Until now, we have investigated only spectra generated in the gas jet placed before the focus i.e. in the converging driving beam.

To estimate the influence of the driving beam phase on the HHG, we simulated also the generation in the same conditions except for medium position that is now 1 cm behind the focus. The near-field spectra are similar to the case of 1 cm before the focus. However the far-field spectra are very different and we show them on figure 3.85.

There are still well distinguishable harmonics that are structured both spectrally and spatially but the overall shape of the signal is completely different from the case of 1 cm before the focus as seen on figure 3.72. Compared to the latter case the most striking characteristic is the divergence that is very reduced compared to the case before the focus.

To identify the short path and long path, we plot the spectrum without the long path on figure 3.86.

With or without the long path, the spatio-spectral XUV profile is almost the same. That means that the long path can be only barely seen even when considered in the simulation.

To quantitatively see the influence of the cutoff emission and the harmonic beam size we simulated only short path and the effective order will be put $q_{eff} = 1$ independently of

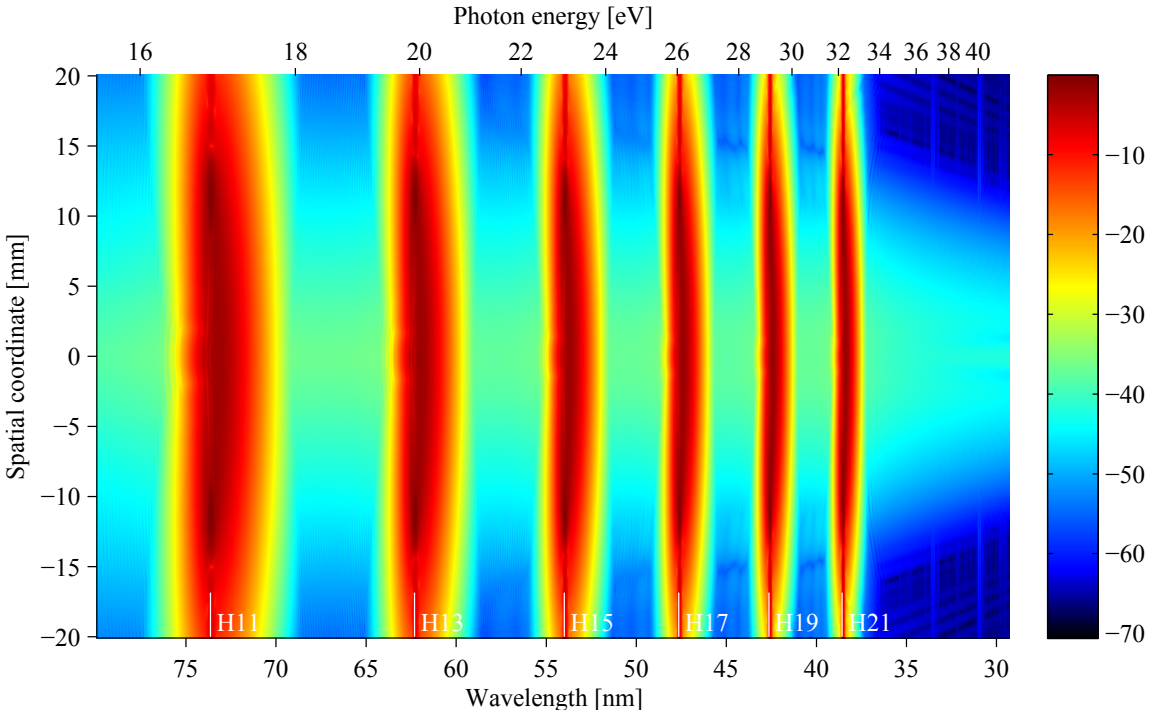

Figure 3.83 – (color) Simulated far-field spatio-spectral XUV profile with short path only ($\alpha = 1 \times 10^{-14}\,\mathrm{cm^2/W}$ independently on the intensity) and $q_{eff} = 1$ in logarithmic scale generated in argon at $10^{15}\,\mathrm{W/cm^2}$ 1 cm before the focus.

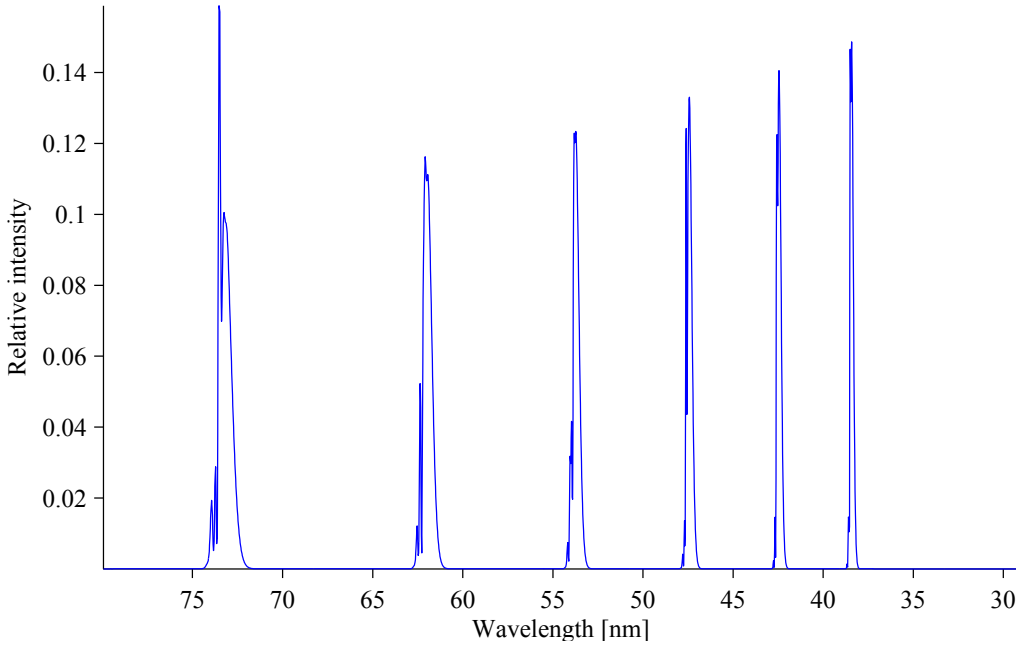

Figure 3.84 – Simulated far-field on-axis spectral XUV profile with short path only ($\alpha = 1 \times 10^{-14}\,\mathrm{cm^2/W}$ independently on the intensity) and $q_{eff} = 1$ generated in argon at $10^{15}\,\mathrm{W/cm^2}$ 1 cm before the focus.

intensity. The resulting spectrum and the on-axis spectral profile are on figures 3.87 and 3.88.

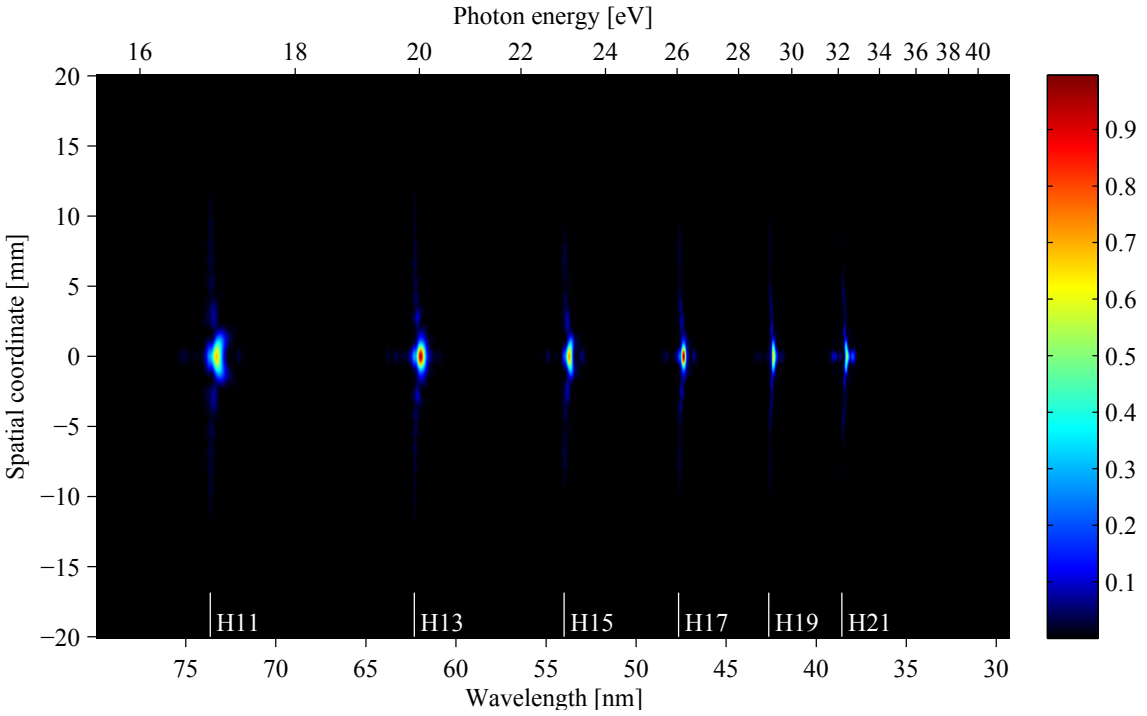

Figure 3.85 – (color) Simulated far-field spatio-spectral XUV profile generated in argon at 10^{15} W/cm² 1 cm after the focus.

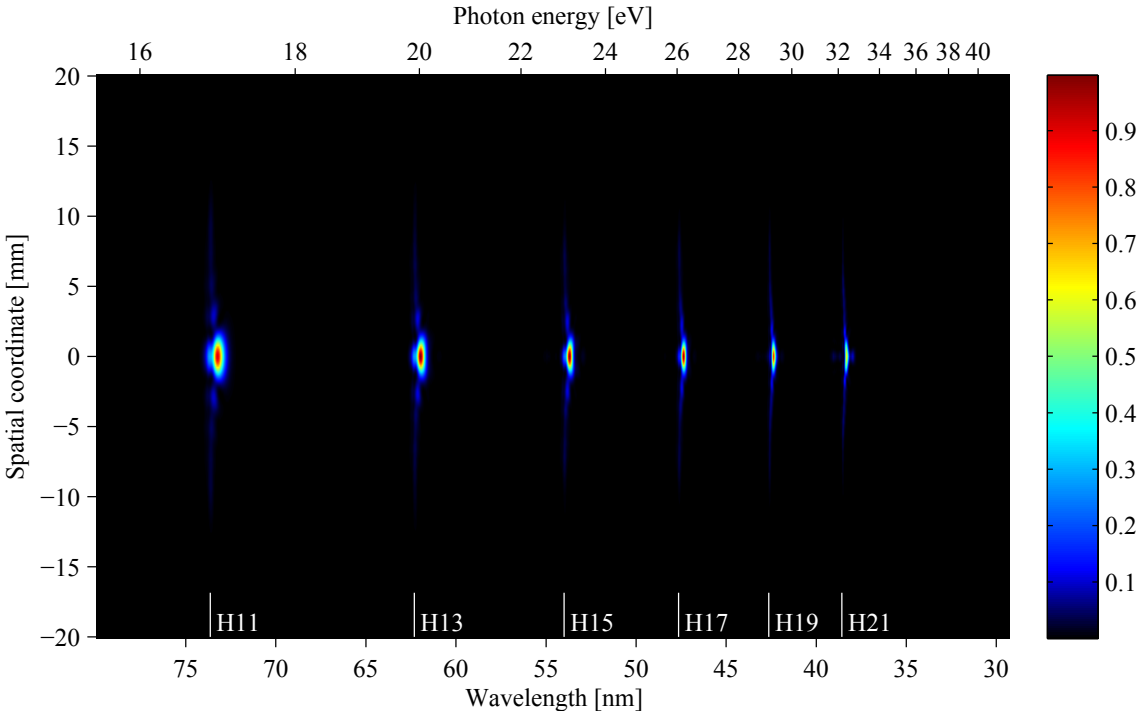

Figure 3.86 – (color) Simulated far-field spatio-spectral XUV profile without the long path generated in argon at 10^{15} W/cm² 1 cm after the focus.

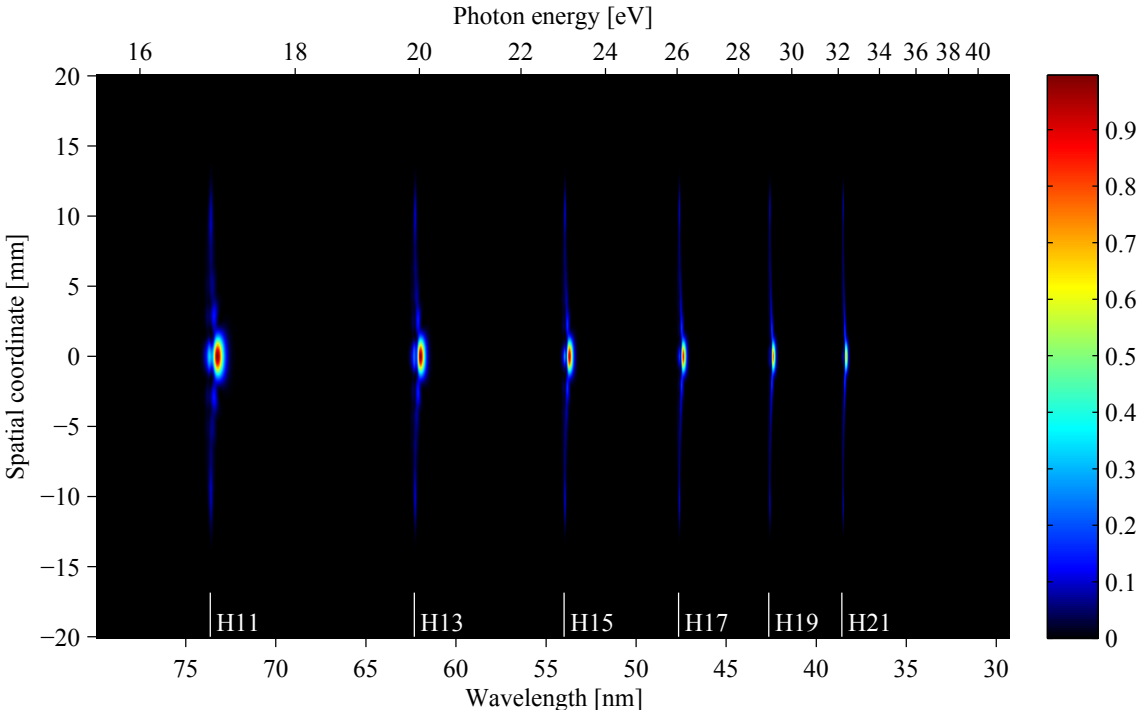

Figure 3.87 – (color) Simulated far-field spatio-spectral XUV profile with short path only ($\alpha = 1 \times 10^{-14}\,\mathrm{cm^2/W}$ independently on the intensity) generated in argon at $10^{15}\,\mathrm{W/cm^2}$ 1 cm after the focus.

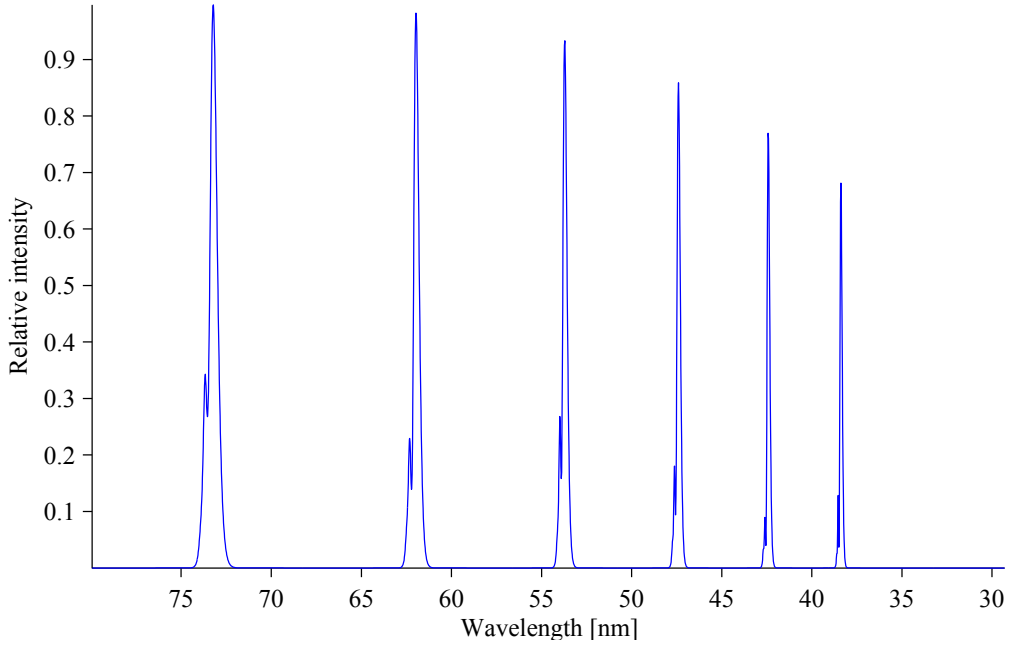

Figure 3.88 – (color) Simulated far-field on-axis XUV profile with short path only ($\alpha = 1 \times 10^{-14}\,\mathrm{cm^2/W}$ independently on the intensity) and constant $q_{eff} = 1$ generated in argon at peak intensity of $10^{15}\,\mathrm{W/cm^2}$ 1 cm after the focus.

The overall harmonic shape did not change. That means that the maximum for each harmonic is still on axis and slightly blue-shifted. Those small modulations are therefore

identified as short path interference with itself.

3.3.4.4 Conclusion on HHG at high intensity driving pulses

At high intensity driving pulses, the harmonic dipole phase αI_{IR} gains a lot of importance limiting the observation of the long path, that gets spatially and spectrally distributed everywhere.

Short path depends strongly on the infrared phase spatial shape. In our cases of the gas jet position of 1 cm before and after the focus the short path shape was completely different. Before the focus the driving beam phase is convex so in the far field the intense signal is located off axis. However, behind the focus the signal is typically concentrated on axis. Inside the short path signal, there are spatio-spectral structures that we identified as interference of short path with itself and this case is very similar to the long path one at low energy.

The XUV emission that is generated with infrared intensity lower than the cutoff intensity has significant contribution only in the case of the gas jet before the focus. Then it contributes on axis creating a red-shifted structure. In the case when the gas jet is behind the focus the contribution of such emission can be neglected.

3.3.5 Conclusion of the simulations

From simulated pictures, it is clear that spatially, spectrally (and therefore also temporally) the harmonic spectra are highly structured even with Gaussian driving beam and Gaussian pulses.

Moreover the structures are present even with lower intensity than the cutoff. One should not forget that the simulation cannot give a quantitative idea of the contrast because of quantum paths ratio dependence on the intensity that is not included in present calculations (for more details about numerical methods see section 3.3.2 on page 55).

The high intensity regime is characterized by depletion of the harmonic dipole due to the ionization. This causes that the harmonic emission is not uniform in time and space therefore making blueshifted and red-shifted structures both in time and space. Their relative weight and contribution depend on the generation geometry.

The high intensity also gives more importance to the infrared beam spatial profile of intensity and phase through the αI_{IR}. This leads to diffraction of the long path out of the MCP where the driving beam spatial phase is convex.

One should note that concrete conclusions made in sections above are valid only for our case of the gas jet position, iris diameter and focal length. In another configuration, the spatial profile of intensity and phase of the driving beam may be completely different

making the XUV profile also different.

An important point is that usual phase-matching due to in-the-medium-propagation is not taken into account as the generating medium is very thin, and both spectral and spatial structures appear.

Our simple simulations gives us an insight into the creation of the coupled structures both in frequency and space and links them in the HHG mechanisms. This is possible numerically with the option to arbitrary omit phenomenon in the simulation.

To conclude the theoretical observations, we observe that HHG with Gaussian pulses in driving Gaussian beams are far away from being Gaussian and exhibit many structures that are well explained by coherence and interferences arising with complex distribution of emitters. The structures in simulated XUV profiles shown in this section are visible also experimentally. We will discuss them in the next section.

3.4 HHG in the gas jet: Structures

Numerically we have seen a lot of different structures in the far-field spatially resolved XUV spectra. In this section we will show and describe the most current structures observed experimentally.

3.4.1 Long path ellipses

One of the most common spatio-spectral structures in spatially resolved XUV spectra are the ellipses (rings) around bright spots on harmonic lines. We can see evolution of such structures on iris diameter on figure 3.89. The spectrogram acquisition was single-shot and generated in argon gas jet with backing pressure of 3.03 Bar, 250 μm nozzle diameter, placed in the focus. The energy before iris was estimated to be about 20 mJ. The iris diameter was a) 8 mm, b) 9 mm, c) 10 mm and d) 11 mm.

The iris diameter influences both focal spot size and the intensity. In the conditions of placing the gas jet in the focus, the focal spot spatial profile is Gaussian and the intensity rises with rising iris diameter.

For iris diameter of 8 mm, we can see only harmonic 21 and 23. This is because of the low driving beam intensity that is not high enough to generate higher harmonics effectively. With the table of cutoff intensities (table 2.2 on page 30), we can estimate the intensity in the gas jet between 1×10^{14} W/cm^2 and 1.16×10^{14} W/cm^2. Both harmonic have circular regular shape with no structures. The horizontal dimmed line above harmonics is diffusion of the lower harmonics in the bellow that connect MCP and detection chamber (see figure 2.8 on page 38).

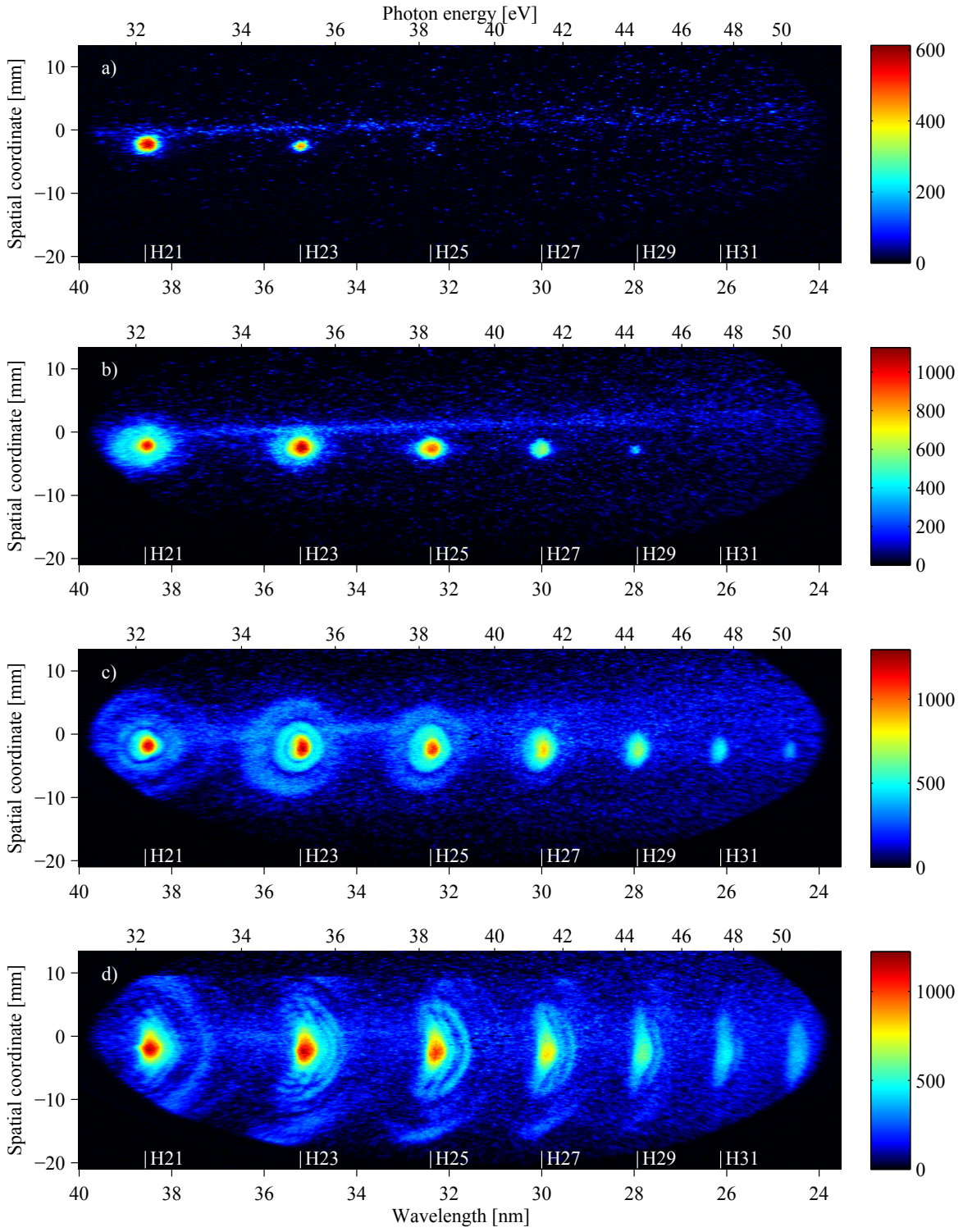

Figure 3.89 – (color) Experimental single-shot far-field spatially resolved XUV spectra generated in argon gas jet with backing pressure of 3.03 Bar, 250 μm nozzle diameter, placed in the focus. The energy before iris was estimated to be about 20 mJ. The driving beam radius before focusing was 10 mm (at I_{max}/e^2). The iris diameter and estimated driving intensity in the jet was a) 8 mm, 1.2×10^{14} W/cm^2, b) 9 mm, 1.6×10^{14} W/cm^2 c) 10 mm, 1.8×10^{14} W/cm^2 and d) 11 mm, 2.1×10^{14} W/cm^2.

For iris diameter of 9 mm, there are three new harmonics 25, 27 and 29. However, we still cannot see the harmonic 31. That corresponds to the intensity between 1.48×10^{14} W/cm² and 1.63×10^{14} W/cm².

All the harmonics are circular and we can distinguish ellipses in the harmonics 21 and 23.

For iris diameter of 10 mm, we can see 7 harmonics from 21 to 33. Our spectral window does not allow us to see more harmonics but, thanks to the relative intensity of single harmonics, we can estimate that the intensity is only a little higher than necessary for seeing harmonic 33 i.e. 1.79×10^{14} W/cm².

At this intensity we can clearly distinguish multiple ellipse structures around the harmonics 21 - 27. As discussed in the simulation section (paragraph 3.3.3.3.3 on page 86), those ellipses are identified as the long path and multiple circle structure as the long path interference with itself. For low harmonics, the short path is represented by the bright spectrally narrow and spatially collimated signal.

We can also see that the ellipse diameter decreases with increasing harmonic order. From the figures a) and b) one can see that the highest three visible harmonics do not contain such ellipse structures. This is coherent with theory as the short and the long path merge together in the cutoff.

Also, high intensity creates a small blue shift of all harmonics causing spectral asymmetry of the XUV signal.

For the highest iris diameter of 11 mm (figure d) there are a lot of changes. The short and the long path are still distinguishable, but the shape of both short and long path is different.

Short path signal is only a little more blue-shifted than before but its shape became spectrally asymmetric. There are also spatio-spectral structures that appear at high intensity.

The long path became also asymmetric and much more divergent. For lower harmonic it even exits the observable spatial window. This fact suggests that long path is so divergent at very high intensities that it can be detected only under stationary conditions i.e. on axis. This also agrees with our theoretical conclusion.

3.4.2 Second order of the XUV grating

Under certain experimental conditions one can see a structure that reminds like if there were 2 «new» harmonics generated between regular ones. A series of those spectra is presented on figure 3.90.

The figure presents four experimental spatially-resolved single-shot XUV spectra gen-

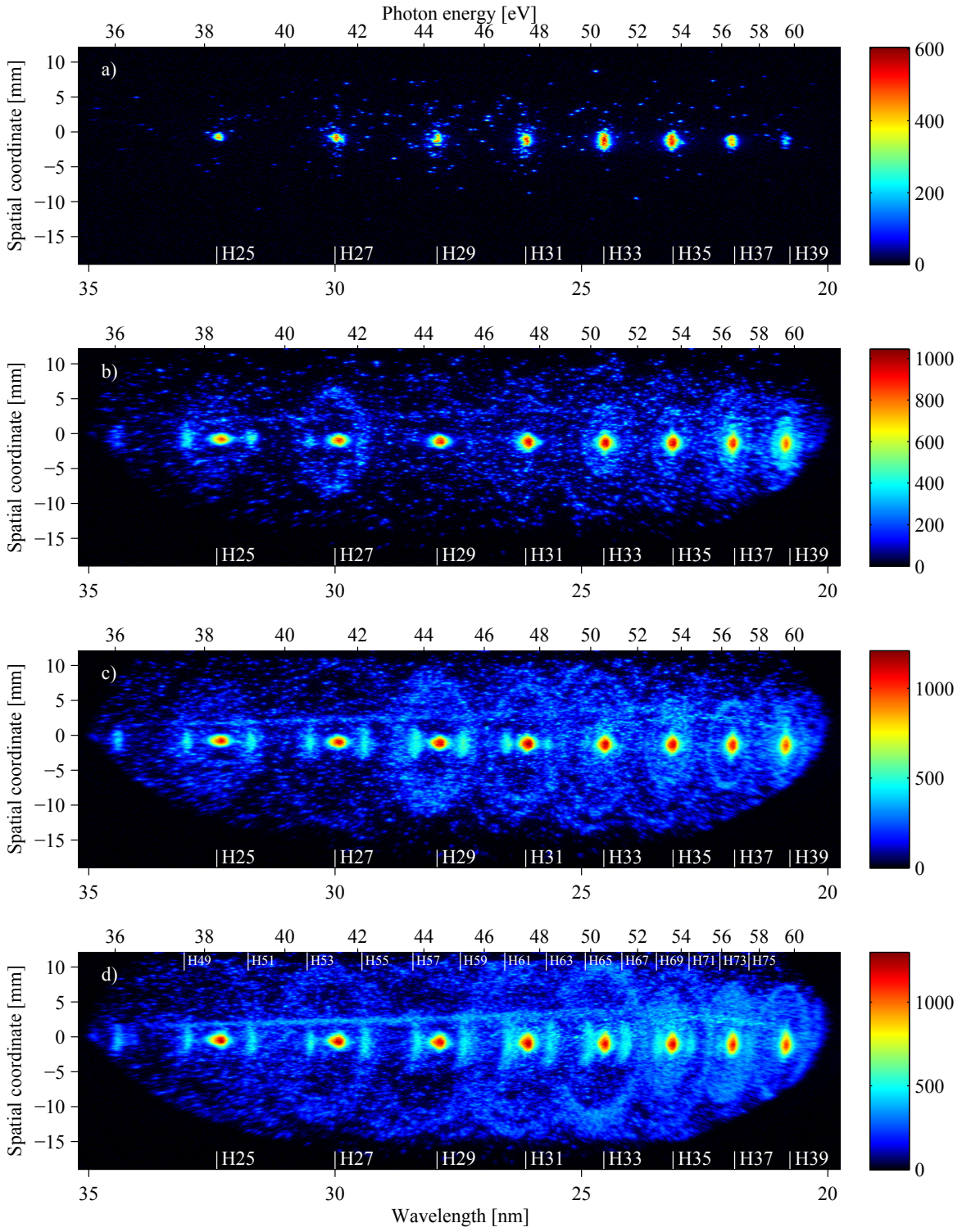

Figure 3.90 – (color) Experimental far-field spatially-resolved single-shot XUV spectra generated in Neon gas jet located 28.7 mm before the focus with the backing pressure of 3.18 bar, pulses of 25 mJ before iris that was open to a) 8 mm, b) 9 mm, c) 10 mm and d) 11 mm. We can distinguish short path, long path ellipses and short path second order of the XUV grating.

erated in neon gas jet located 28.7 mm before the focus with the backing pressure of 3.18 bar, pulses of 25 mJ before iris that was open to a) 8 mm, b) 9 mm, c) 10 mm and d) 11 mm.

The 8 mm case (a) shows harmonics near the cutoff intensity.

When the iris is open to 9 mm (figure b) there are 2 new structures in the spectrum: spatio-spectral rings associated to the long path (already discussed in sections 3.3.3.3.3 and 3.4.1) and few on-axis regular structures. Those are the higher harmonics diffracted by the second order of the XUV grating so they can be detected in the same window as low harmonics. Around a harmonic of order n there are two second order harmonics of order $2n-1$ and $2n+1$ appearing at the position of the harmonics $n-1/2$ and $n+1/2$. As we generate only odd-order harmonics, the first and second grating orders are separated spectrally.

Though the highest detectable harmonic is identified as the order of 53 estimating the peak intensity in the gas jet more than $3.07 \times 10^{14}\ \mathrm{W/cm^2}$.

With iris open to 10 mm (figure c) the highest harmonic is 63. The long path rings are larger and one can clearly distinguish the different position of those rings and grating second order harmonics.

For 11 mm of iris diameter (figure d) the long path ellipses are so divergent that they cannot fit to the spatial observable window for harmonics lower than 29. One should note that the long path (that overlaps for several harmonics) has not disappeared, it is just everywhere in the spectrogram and one could take it as noise. The highest observable harmonic is the 75.

In conclusion, the second order of the grating provides extra signal that can be easily distinguished from the first-order signal. While with spectrally larger harmonics it can contribute to overall complexity of a spectrum, it should not be forgotten that its origin is purely technical and not connected to underlying physics.

For argon and gases with lower ionization potential the second order of diffraction of the grating is typically not detected. For instance, considering the classically predicted highest harmonic in argon of 39 would raise the second order harmonic around the harmonic 19.

3.4.3 Spatial structures

Spatial structures are also very common type of structure observed with our experimental setup and can be seen in many different conditions. Three different structures in far-field spatially resolved XUV spectra generated in krypton are on figure 3.91.

We can see a lot of spatial structures in the krypton spectra. One can observe many spatially thin fringes as seen on figure 3.91 a), or only two intense signals off axis on figure

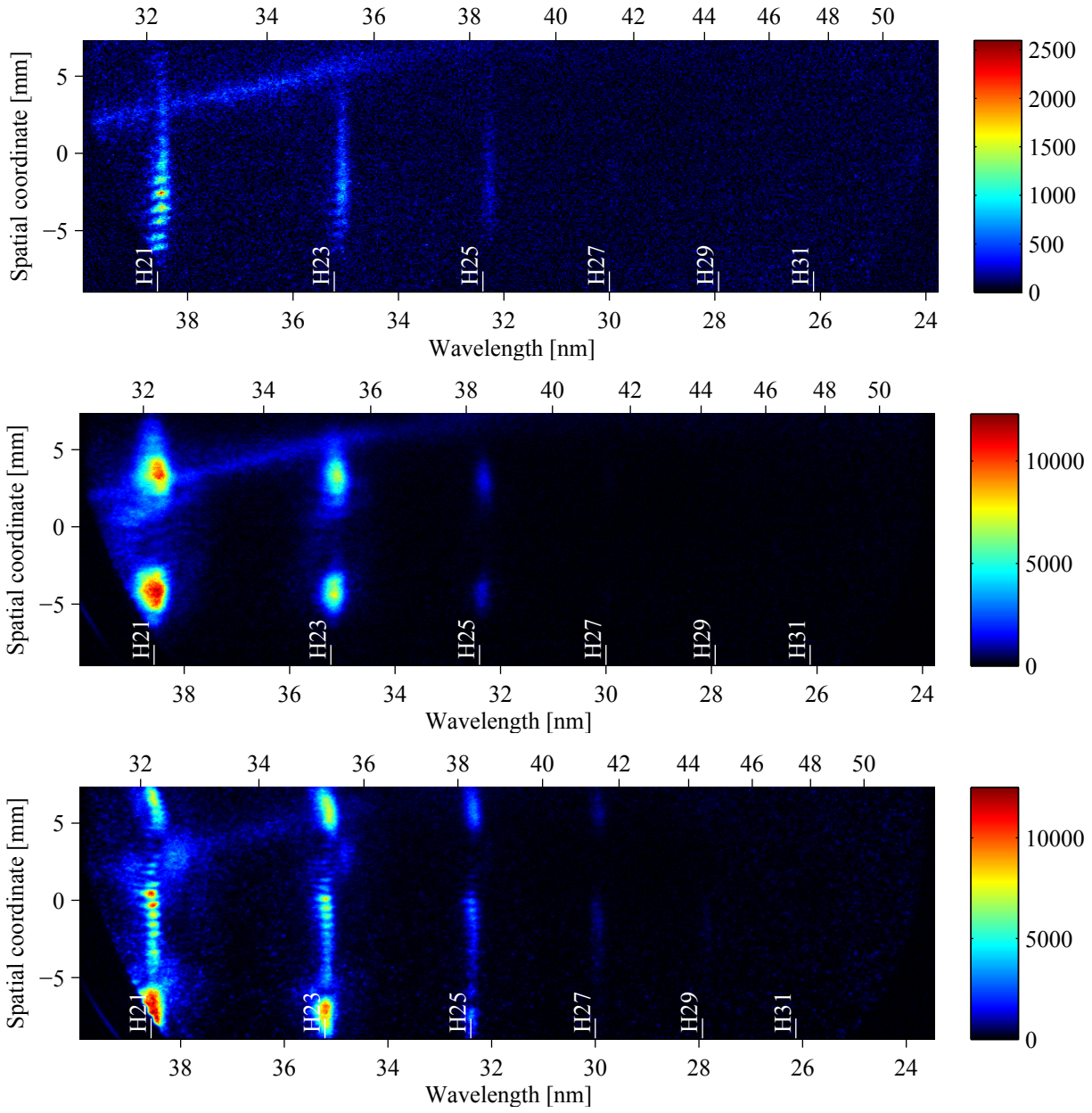

Figure 3.91 – (color) Experimental single-shot far-field spatially resolved XUV spectra generated in krypton jet. 50 mJ pulses before the iris and 1.2 cm after the focus. The spectra was generated with a) 5 bar of backing pressure, beam-jet distance of 0.5 mm, 22 mm of iris diameter, b) 5 bar of backing pressure, beam-jet distance of 0.5 mm, 12 mm of iris diameter c) 6 bar of backing pressure, beam-jet distance of 2 mm, and iris diameter of 16 mm.

b) or both structures together as on figure c). As discussed earlier in the simulation part of the chapter, we attribute the spatial structures mainly to the $q\varphi_{IR} + \alpha I_{IR}$. As the spectra were not generated in the focus, clipping the driving beam before focusing results in strong modulation of the phase and intensity of the infrared driving beam.

In the near field, the very high driving beam intensity would cause rapid depletion of the atomic ground state, favoring XUV emission in the regions where the generation

conditions are stationary.

Therefore the major part of the XUV emission in the near field would take place off axis making the harmonic dipole distribution annular. The two locations of emission in the near field result in the far-field on-axis signal with spatial fringes as on figure 3.91 a).

If their phase-fronts point in different directions in the near field, they will be detected off axis in the far field such as on figure 3.91 b).

If the driving beam spatial profile and phase are more complicated in the generating medium, one can find a combination of both structures in the far field as on figure 3.91 c).

The structures are robust and can be generated not only in krypton. We detect them also when performing HHG in other gases as shown on figure 3.92.

On figure 3.92 we present spatial structures in XUV spectra generated in a) helium and b), c) neon. Comparing with previous figure 3.91 we can find similar structures to that in spectra generated in krypton. Two distinguished off-axis maxima were detected both in helium (figure 3.92 a), neon 3.92 b) and in krypton (figure 3.91 b). Two off-axis maxima with spatial fringes between them were observed in neon (figure 3.92 c) and krypton (figure 3.91 c).

Figures 3.92 a) and b) show the spectra generated under the same conditions except the generating gas is either helium or neon. The structure is qualitatively identical for the two gases. Quantitatively we observe that the distance of the two off-axis maxima is slightly higher in the case of helium (about 10 mm in helium and 8 mm in neon). This corresponds to the different wave-front due to the different ionization rate that corresponds to slightly different ionization potential of helium compared to neon.

Note the appearance of the second order of the XUV grating in each of the three figures presented on 3.92.

The spatial structures are also robust against different geometries of the HHG. On figure 3.93, we present a XUV spatially resolved experimental spectrum generated in Argon (3.2 bar of backing pressure) with the focusing mirror focal length of 75 cm (compared to 2 m), iris diameter of 11 mm and the jet gas 17.4 mm before the focus and 55 fs pulses.

Harmonics are spectrally symmetric and narrow, that corresponds to low intensity driving pulses. Spatially they are large and very divergent compared to the results with 2 m focal length mirror. All the harmonics are modulated with small spatial fringes and contain 2 off-axis maxima as seen on figures 3.91 and 3.92. The noise signal «lines» are attributed to the diffusion of the lower harmonics in the inner surface of the bellow that connects the MCP to the detection chamber.

In conclusion the spatial structures are very robust and can be generated with high intensity driving pulses under various geometries and with various gases. They are due to the spatial coherence of the source and the harmonic phase that is modulated in time and

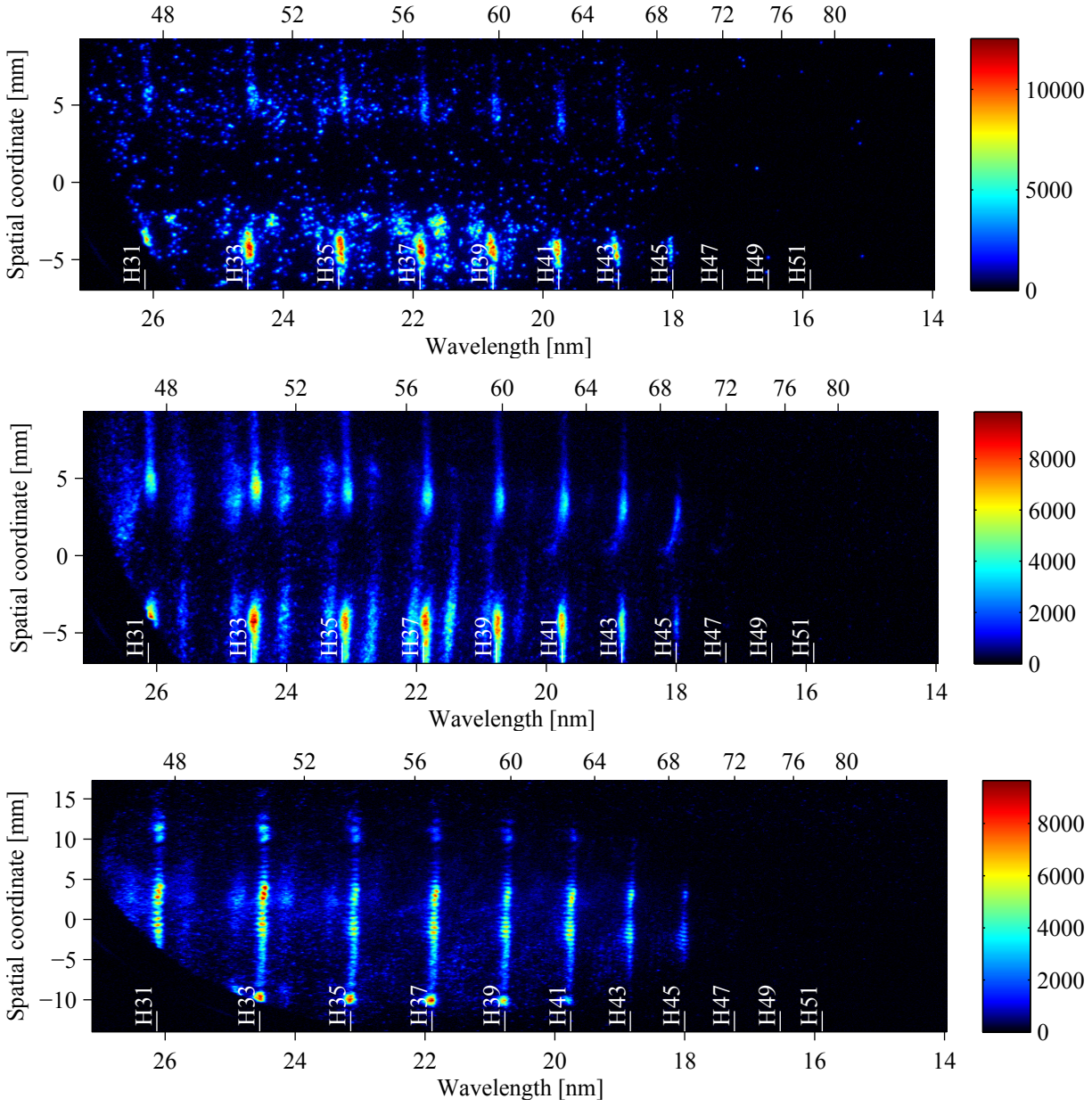

Figure 3.92 – (color) Experimental single-shot far-field spatially resolved XUV spectra. 60 mJ pulses before the iris and beam-jet distance of 0.5 mm located 4 cm before the focus. The spectra was generated with a) 5.8 bar of backing pressure of helium, 19 mm of iris diameter, b) 6 bar of backing pressure of neon, 19 mm of iris diameter c) 6 bar of backing pressure of neon and iris diameter of 22 mm.

space [Tosa 09, Gaarde 08] due to $q\varphi_{IR} + \alpha I_{IR}$.

3.4.4 Spectral structures on the red side of harmonic line

One of the typical spatio-spectral structures in XUV signal generated at high energy driving pulses is so called «Red-Shifted Structure» (RSS). It is a spectrally narrow structure that appears on the red side of each harmonic for high generating intensities. It is a ro-

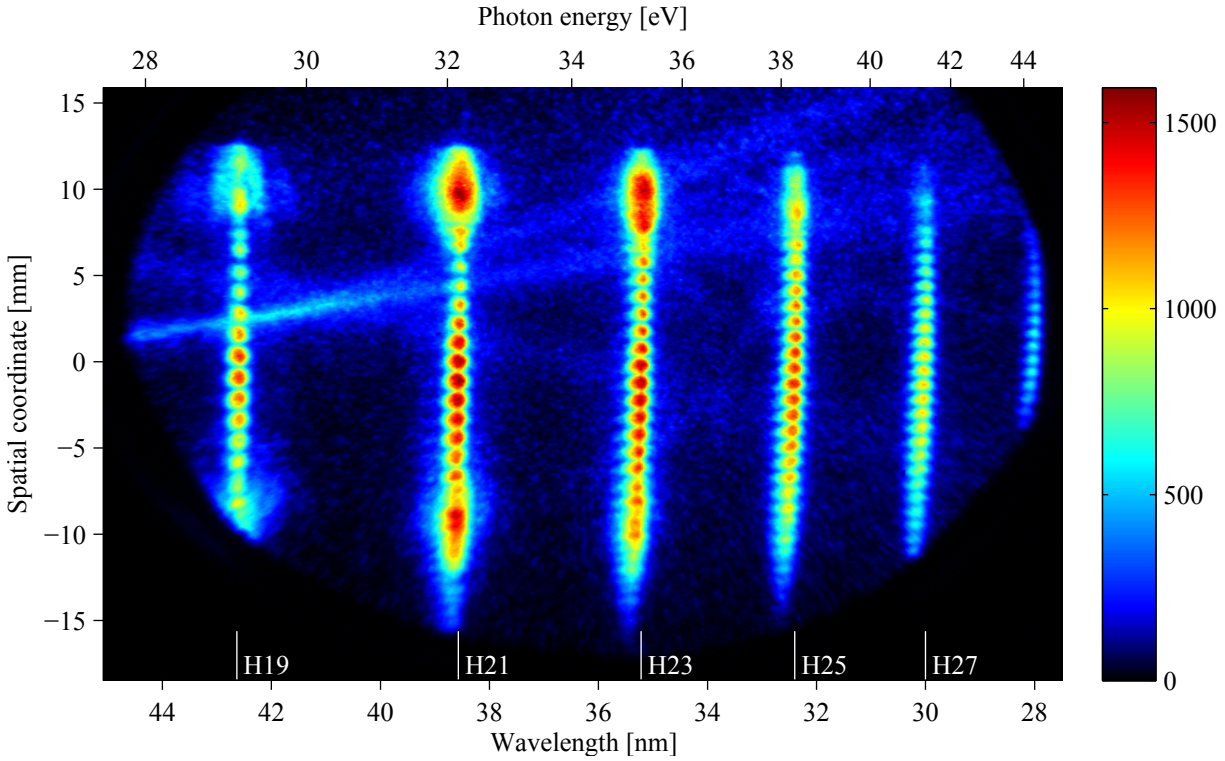

Figure 3.93 – (color) Experimental single-shot far-field spatially-resolved XUV spectrum generated in Argon (3.2 bar of backing pressure) with the focusing mirror focal length of 75 cm, iris diameter of 11 mm and the jet gas 17.4 mm before the focus.

bust structure that can be seen under many generating conditions. It was described in [Brunetti 08, Cao 12], where it was attributed to the long path.

3.4.4.1 Experimental results

3.4.4.1.1 Red-Shifted Structures overview A typical RSS evolution in krypton on driving pulse peak intensity can be seen on figure 3.94.

The figure 3.94 presents XUV spatio-spectral profile generated in krypton jet of 3 bar backing pressure placed 11 mm after the focus. Each image is averaged of 10 shots. The focal length used was 2 m, iris diameter 22 mm and the pulse energy before iris was a) 0.7 mJ, b) 3.8 mJ, c) 5.8 mJ and d) 11.1 mJ. Estimating the beam size (radius at I_{max}/e^2) as 74 μm we can derive a peak infrared intensity in the generating medium of a) 1.3×10^{14} W/cm², b) 7×10^{14} W/cm², c) 1.1×10^{15} W/cm² and d) 2×10^{15} W/cm². Note that in cases b), c) and d) the generation occurs largely above barrier suppression intensity that is 1.54×10^{14} W/cm².

On figure 3.94 a) one can see harmonics 17, 19 and 21 that are asymmetric and slightly blue-shifted on axis. This was already discussed in the section on simulations.

The figure b) shows harmonics generated at 4.5 times higher intensity than the barrier

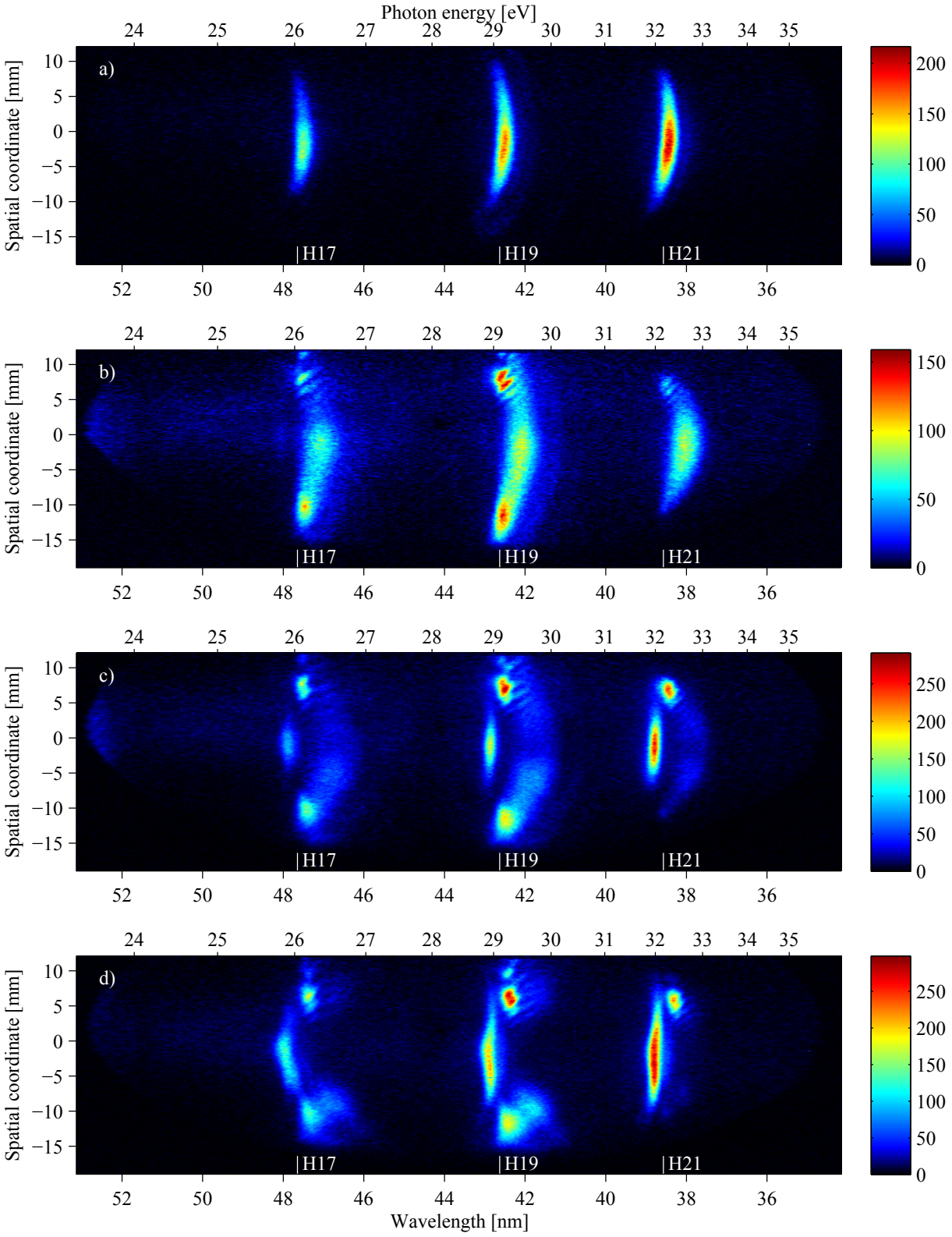

Figure 3.94 – (color) Experimental far-field spatio-spectral XUV profile generated in krypton jet placed 11 mm after the focus. The focal distance was 2 m and iris diameter 22 mm. Estimated peak driving intensity in the gas jet was a) 1.3×10^{14} W/cm², b) 7×10^{14} W/cm², c) 1.1×10^{15} W/cm² and d) 2×10^{15} W/cm².

suppression intensity. On axis the harmonics are very blue-shifted and form a spatio-spectral «bow» shape. Off axis there are two bright spots that are much less blue-shifted than the on-axis part. These characteristics have been observed theoretically at high intensity (see figure 3.72 on page 101).

The figure c) firstly introduces red-shifted structures. It appears as spectrally narrow clean spectral line on the red side of initial harmonic frequency position. The red-shifted structure is spatially centered on axis and narrow. The peak intensity is comparable to the peak intensity of the off-axis harmonic structures. Also the harmonics change, the bow structure is spectrally larger and the blue shift is stronger. This can be explained simply by higher generating intensity. It is interesting to note that the on-axis part has a reduced amplitude so the relative weight of the on-axis and off-axis harmonics signal changes a lot compared to figure b).

Higher driving intensity (figure d) weakly raises only the RSS divergence. However the original harmonic signal that was completely on axis disappeared letting RSS being the only signal on axis. Despite the very high intensity used here, the RSS have still a regular and centered shape. In here the higher harmonic orders show brighter RSS.

To quantitatively determine the RSS spectral shift we plot the spatially integrated (1 mm over the axis) XUV spectrum on figure 3.95.

On figure 3.95 a) and b) we cannot see the RSS, only harmonics that are very blue-shifted. On figure 3.95 c) and d) we can determine that the corresponding central wavelength of the driving pulses of the RSS is 815 nm (compare with 810 nm of the regular harmonics).

3.4.4.1.2 Red-shifted structures maximal order To illustrate the typical dependence of RSS on the generating intensity, we show spectra on figure 3.96.

The figure 3.96 present single-shot XUV spatio-spectral profile generated in an argon jet (3.1 bar backing pressure) placed at focus. The focal length used was 2 m, iris diameter 22 mm and the pulse energy in the gas jet was a) 2.1 mJ, b) 2.5 mJ, c) 2.8 mJ and d) 3.2 mJ. Estimating the beam size (radius at I_{max}/e^2) as 73 μm we can derive a peak infrared intensity in the generating medium to a) 4.4×10^{14} W/cm^2, b) 5.3×10^{14} W/cm^2, c) 5.9×10^{14} W/cm^2 and d) 6.7×10^{14} W/cm^2. Note that in every case the peak intensity is largely above barrier suppression intensity that is 2.47×10^{14} W/cm^2.

To better compare the relative intensities between the harmonics and the structures we plot spatially integrated spectra (1 mm over the optical axis) on figure 3.97.

On figure a) the intensity is not high enough to generate RSS. However the intensity is high enough to make the harmonics asymmetric, blue-shifted and to broaden them spectrally.

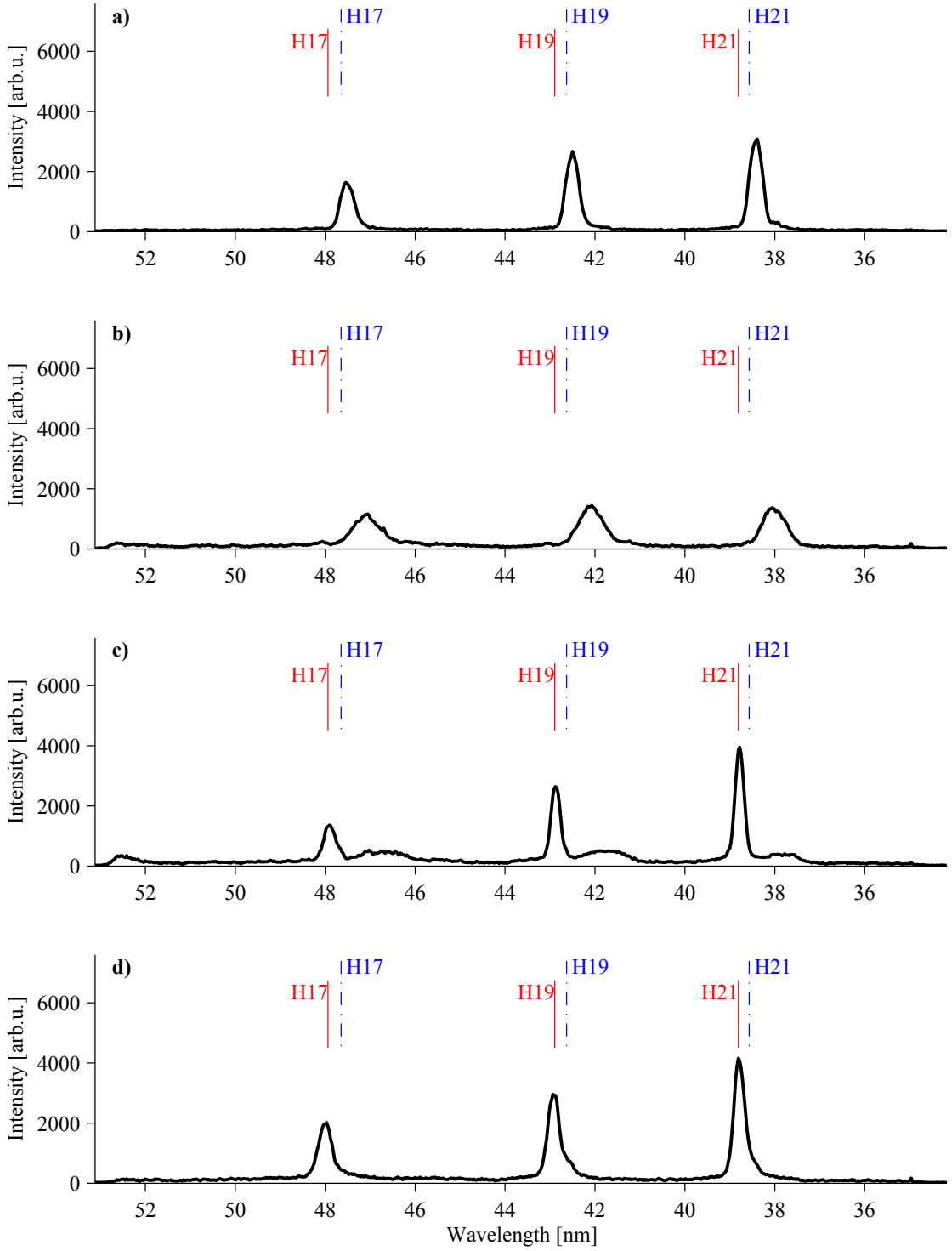

Figure 3.95 – Experimental far-field spatially integrated (1 mm over the axis) XUV spectra generated in krypton jet placed 11 mm after the focus. The focal distance was 2 m and iris diameter 22 mm. Estimated peak driving intensity in the gas jet was a) 1.3×10^{14} W/cm², b) 7×10^{14} W/cm², c) 1.1×10^{15} W/cm² and d) 2×10^{15} W/cm². The blue lines show position of harmonics generated with 810 nm, The red solid lines the RSS that corresponds to 815 nm.

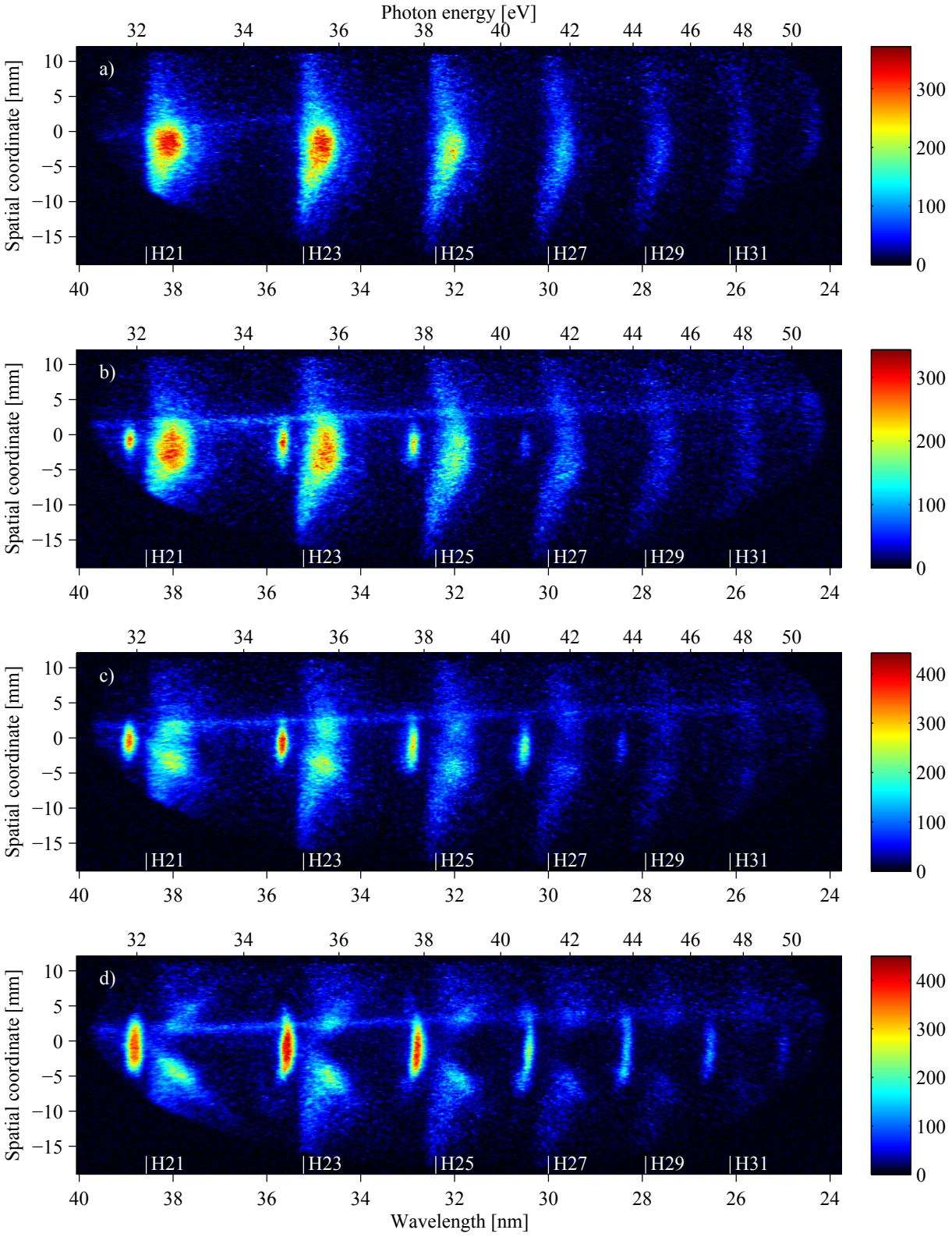

Figure 3.96 – (color) Experimental far-field single-shot spatio-spectral XUV profile generated in argon jet of 3.1 bar backing pressure placed in the focus. The focal length used was 2 m, iris diameter 22 mm and the pulse energy in the gas jet was a) 2.1 mJ, b) 2.5 mJ, c) 2.8 mJ and d) 3.2 mJ.

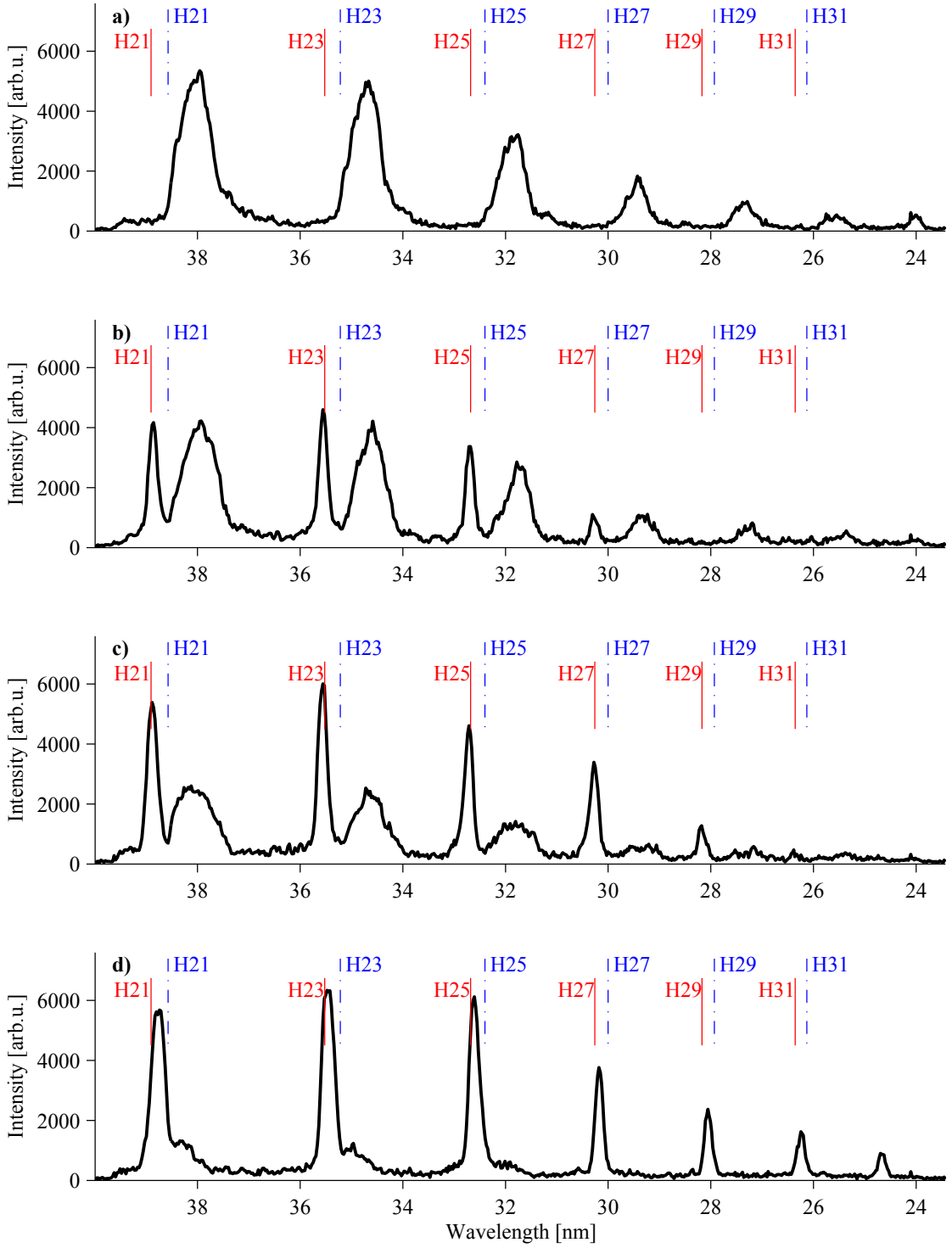

Figure 3.97 – Experimental far-field single-shot XUV spectrum integrated over 1 mm over the axis generated in argon jet of 3.1 bar backing pressure placed in the focus. The focal length used was 2 m, iris diameter 22 mm and the pulse energy in the gas jet was a) 2.1 mJ, b) 2.5 mJ, c) 2.8 mJ and d) 3.2 mJ. The figure corresponds to figure 3.96. The blue lines correspond to driving central wavelength of 810 nm (regular harmonics) and the solid red lines to driving central wavelength of 817 nm (RSS).

Figure b) shows RSS on the red side of harmonics 21- 27. All harmonics lost their high brightness. We observe here that RSS are brighter with low order harmonics.

The RSS «cutoff» on figure c) is at harmonic 31 and the harmonics start to be spatially modulated.

Figure d) shows RSS at every harmonic which are present only off axis. Note that RSS spatial profile is larger with intensity.

In general, on axis, high intensity blue-shifts the regular harmonics, but the RSS spectral position is constant for every value of intensity. The RSS appears first on low order harmonics. We can determine that the corresponding central wavelength of the driving pulses of the RSS is 817 nm (compare with 810 nm of the regular harmonics).

3.4.4.1.3 Red-shifted structures generated in pulsed gas cell We performed HHG in a gas cell that was fixed on a pulse valve that we normally used as a gas jet. Thus we obtained a pulsed gas cell. The gas cell length was 2.6 mm and the entrance and exit holes were drilled by the driving laser beam. The gas cell was placed in the focus. The XUV spatio-spectral profile generated in the gas cell filled with helium is on figure 3.98.

The figure 3.98 shows RSS dependence on helium pressure in a 2.6 mm long pulsed gas cell placed in a focus.

The estimated beam size (radius at I_{max}/e^2) is 67 μm; we can derive a peak infrared intensity in the generating medium to 8.5×10^{15} W/cm^2. The figure is an average of 10 shots.

In contrast to the case of krypton and argon, the harmonics generated in helium are spectrally narrow, symmetric and spatially centered on axis and convergent. To observe quantitatively the structures, we plot the spatially integrated signal over 1 mm over the axis on figure 3.99.

The frequency gap between harmonics and RSS is much higher than in the case of krypton and argon. We can determine that the corresponding central wavelength of the driving pulses of the RSS is 840 nm (compare with 810 nm of the regular harmonics).

There is no sign of dependence of the RSS on helium pressure in the gas cell. The only parameter that changes with pressure is the intensity of RSS as the ordinary harmonics do too.

To conclude, we have seen the RSS in helium cell, argon jet and krypton jet. The corresponding driving wavelength was 840 nm in the case of helium cell, 817 nm in the case of argon jet and 815 nm in krypton jet. In every case the RSS were spectrally narrow, spatially uniform and centered over the optical axis. Their spectral position is not dependent on the infrared intensity nor on the pressure in the generating medium.

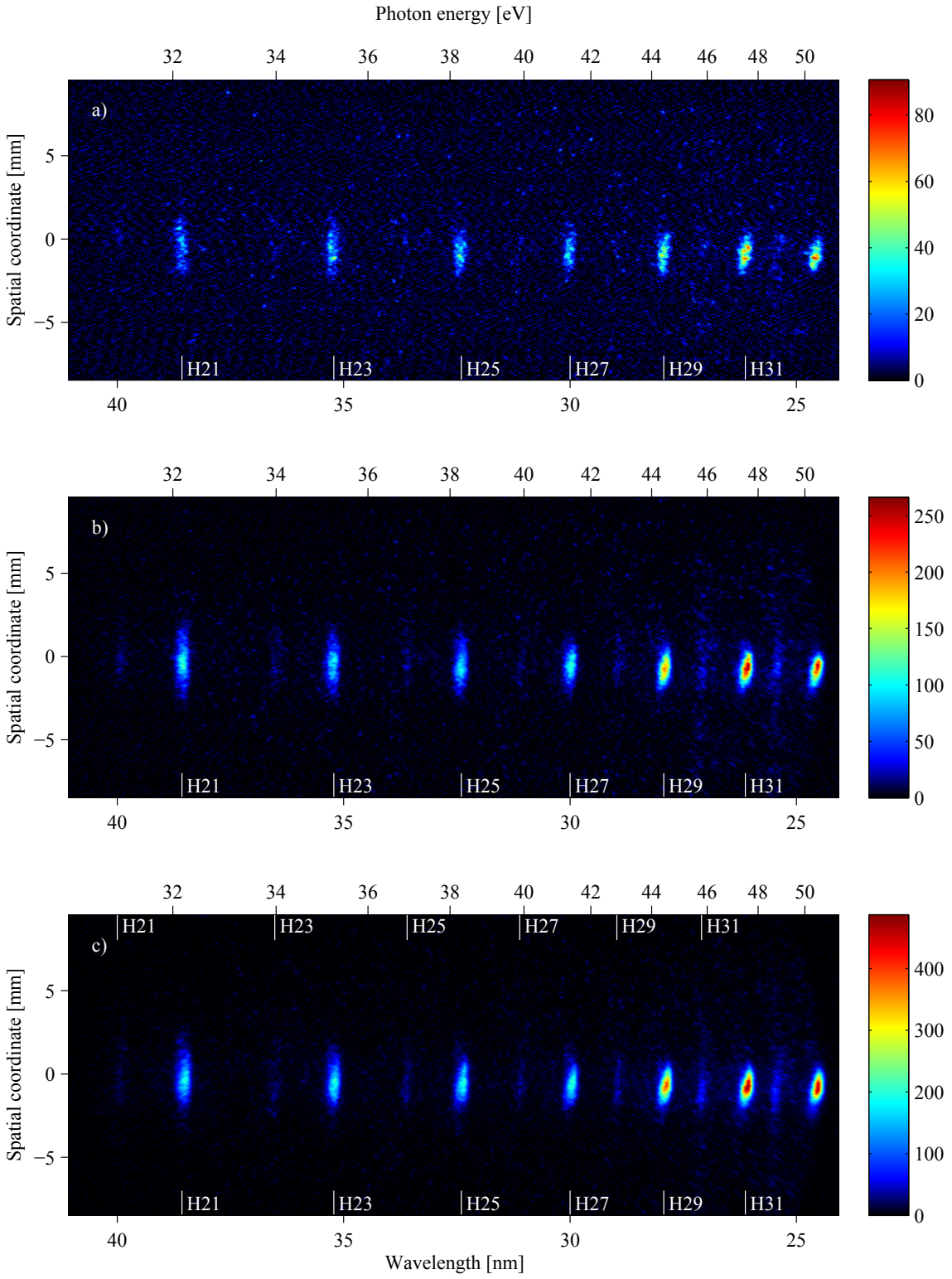

Figure 3.98 – (color) Experimental far-field spatio-spectral XUV profile generated in helium filled pulsed cell. Pulse valve backing pressure was a) 0.8 bar, b) 1.5 bar and c) 2 bar. The iris diameter was 25 mm and estimated peak intensity 8.5×10^{15} W/cm^2.

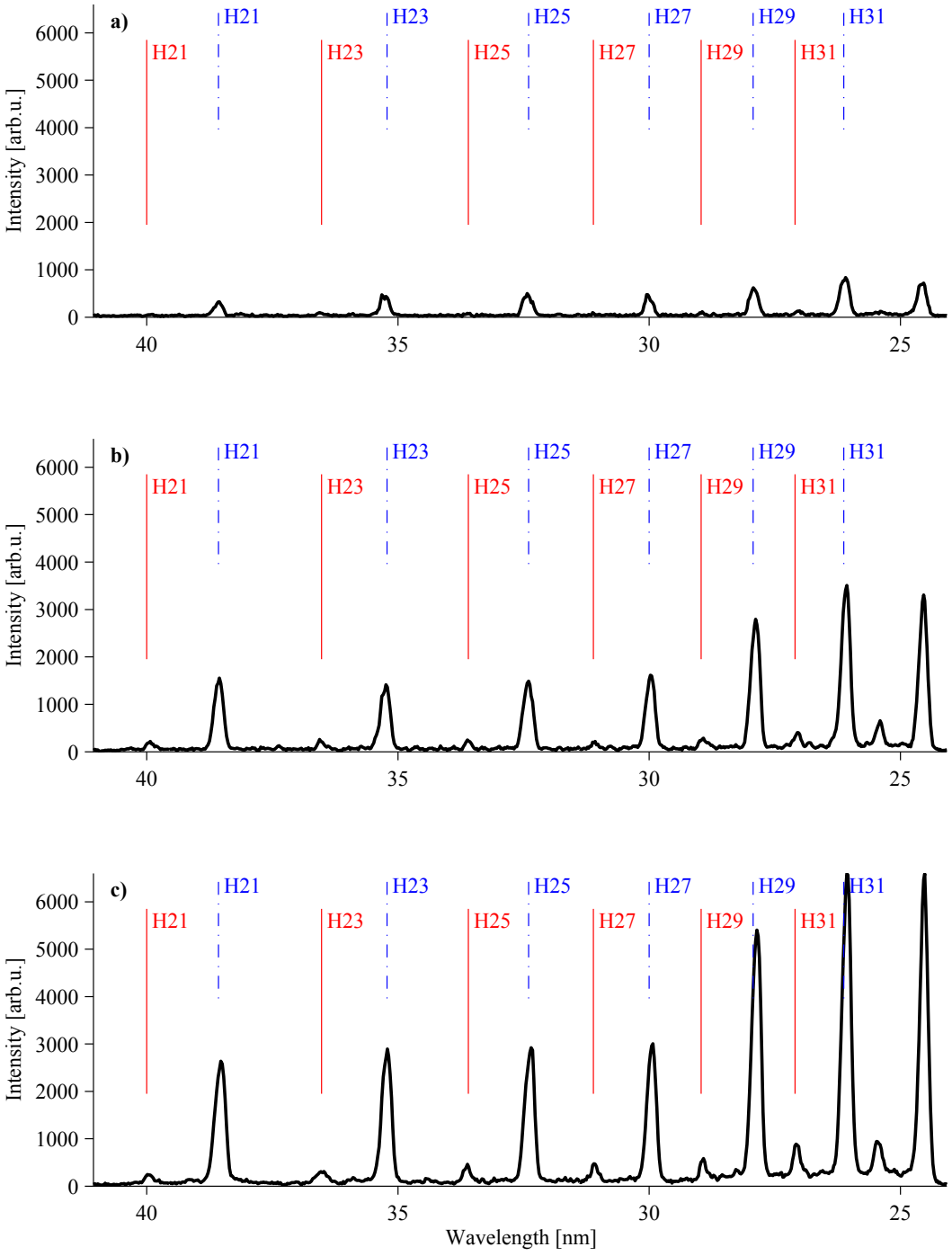

Figure 3.99 – Experimental far-field XUV spectra integrated over 1 mm over the axis generated in helium filled pulsed cell. Pulse valve backing pressure was a) 0.8 bar, b) 1.5 bar and c) 2 bar. The iris diameter was 25 mm and estimated peak intensity 8.5×10^{15} W/cm^2. The figure corresponds to figure 3.98. The blue lines correspond to driving central wavelength of 810 nm (regular harmonics) and the solid red lines to driving central wavelength of 840 nm (RSS).

3.4.4.1.4 Comparison of XUV and driving IR spectra We carried an measurement of XUV signal and the corresponding IR spectra after the HHG performed in argon

jet. We performed a study for different gas pressures that was realized by timing the trigger signal of the pulsed valve. The generated single-shot spatially and spectrally resolved XUV profiles are on figure 3.100.

The trigger signal is provided by the masterclock of the driving Ti:Sapphire laser chain. We control the delay of this signal with a Stanford pulse generator. Simply by tuning the time delay between the gas jet and the laser one can control the time when the laser interacts with the gas. In this way, this method is equivalent to controlling the interaction zone gas pressure.

We observed that the RSS are not affected by the pressure except their amplitude. The fact that the overall signal (harmonic and RSS intensity) grows with pressure can be simply viewed as a direct result of rising the number of emitters (atoms) in the laser beam and this confirms that the pressure changes.

To see if the driving pulse stayed also unchanged with the delay we studied the driving laser spectra after the HHG. Spectra were taken at the entrance of the XUV spectrometer - the diffusion of the slit and are shown on figure 3.101.

The figure shows the infrared driving beam spectrum after HHG in argon jet for different interaction pressures in the gas jet. The investigated delays extent was nearly 1 ms. Note that the driving laser repetition rate is 10 Hz giving 100 ms of time interval between two consecutive shots. Therefore the influence of two pulses is avoided. The 1 ms was also long enough compared to pulsed valve opening time of 400 μs. The border cases of high delays corresponds to the case where there is no interaction of the gas with the laser.

The laser peak intensity is high enough to ionize 100 % of atoms in the medium. The high ionization causes large spectral changes of the driving pulse [Altucci 96, Tosa 05] as seen on figure 3.101.

The striking thing is that between -50 and 150 μs the spectral width of infrared pulse nearly doubles its width but the corresponding XUV spectra do not change. That means that the large spectral broadening observed in the IR spectra does not transfer to XUV spectra.

3.4.4.2 Analysis and discussion

After a careful look on precedent figures 3.94, 3.96, 3.98, 3.100 and 3.101 and considering additional results we can summarize general characteristics of red-shifted structures (RSS):

1. RSS were observed for high intensity and there is no maximum intensity for generation of RSS.

2. RSS were generated in all tested gaseous media: helium, neon, argon, krypton, xenon and air (RSS in neon, xenon and air were also observed but not presented in here).

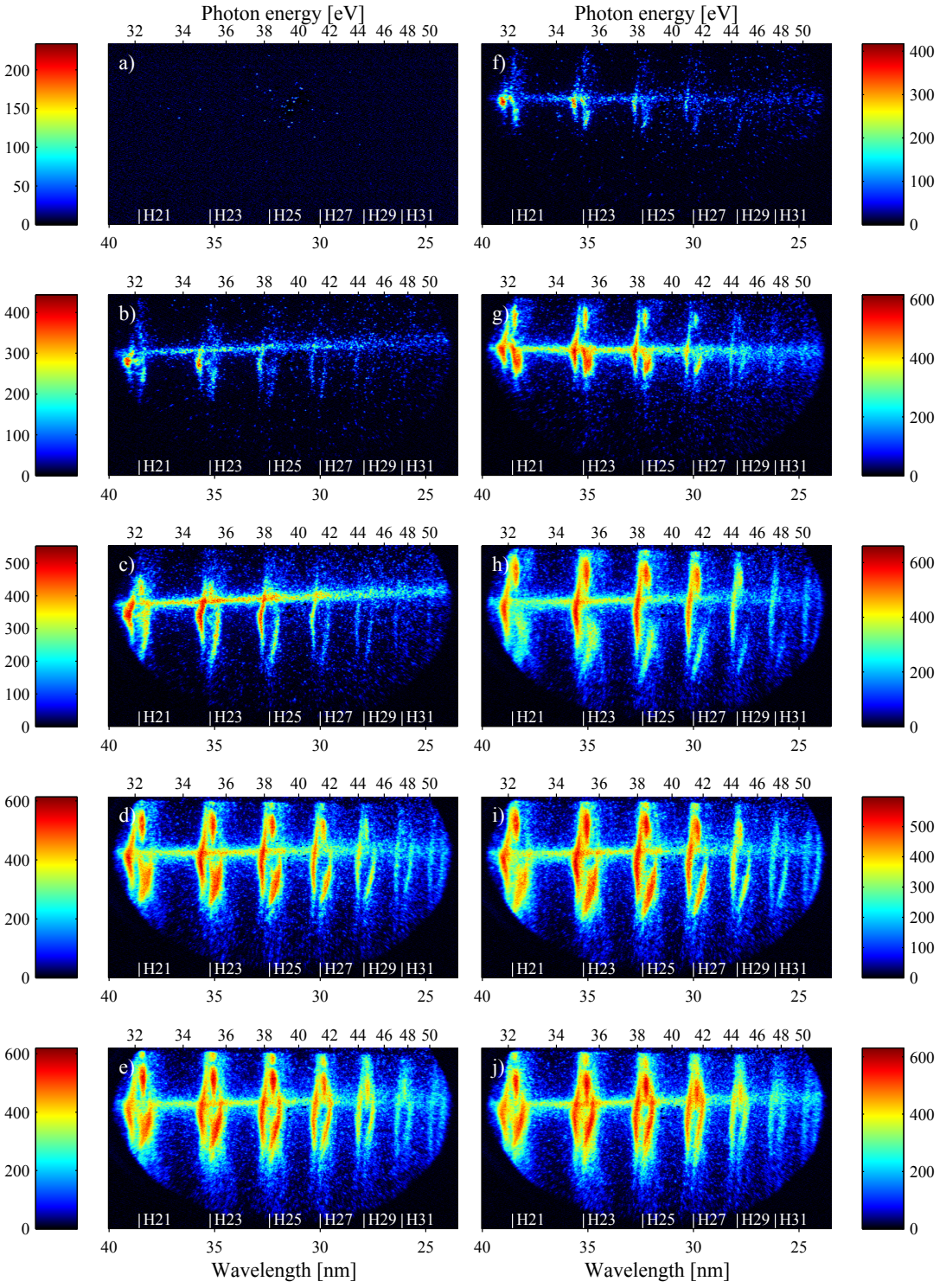

Figure 3.100 – (color) Experimental far-field single-shot spatio-spectral XUV profile generated in argon gas jet placed at the focus with the delay of a) $-500\,\mu$s, b) $-250\,\mu$s, c) $-150\,\mu$s, d) $-50\,\mu$s, e) $0\,\mu$s, f) $300\,\mu$s, g) $250\,\mu$s, h) $150\,\mu$s, i) $100\,\mu$s and j) $50\,\mu$s. The gas jet backing pressure was 3 bar. The iris diameter was 25 mm and estimated peak intensity 1.2×10^{16} W/cm^2.

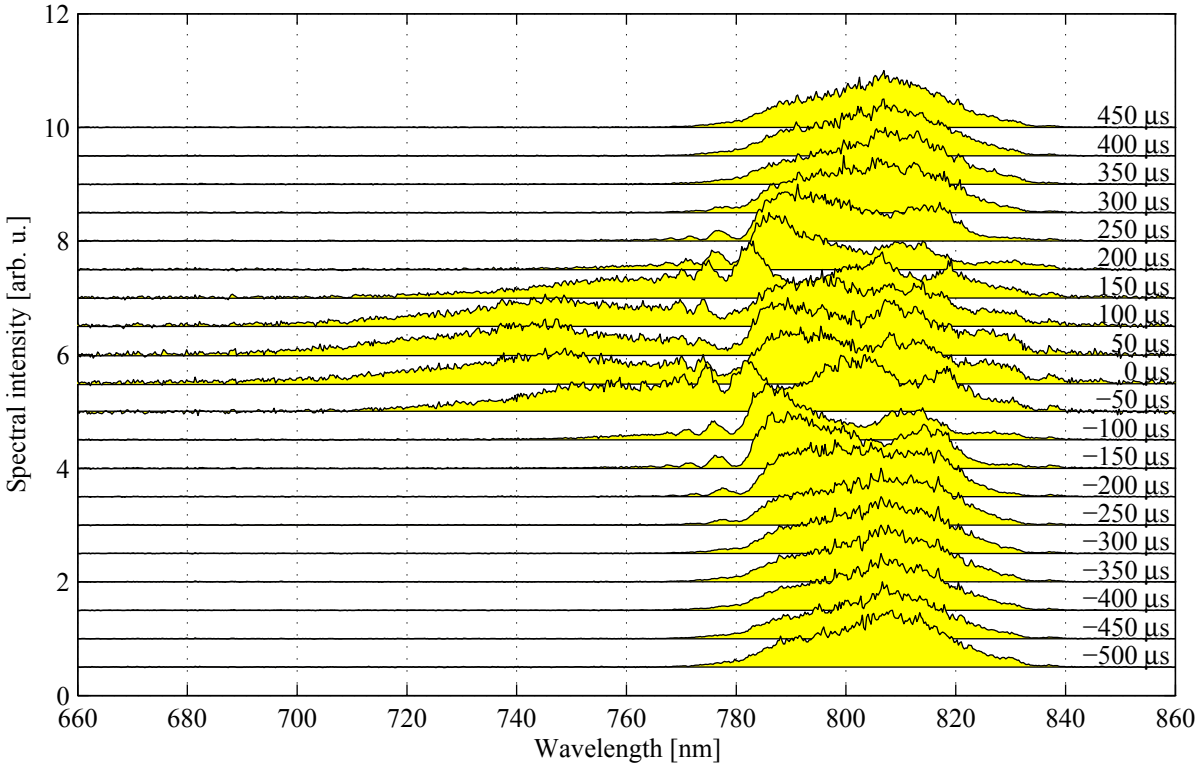

Figure 3.101 – Experimental far-field single-shot infrared spectra after HHG in argon gas jet placed in the focus with the delay. The noted delay is between the gas jet and the driving pulse. The zero delay is the delay where the highest signal is generated in most conditions. The gas jet backing pressure was 3 bar. The iris diameter was 25 mm and estimated peak intensity 1.2×10^{16} W/cm^2. The spectra were collected at the entrance of the XUV spectrometer.

3. RSS were generated in geometries: gas jet with f = 2 m, gas jet with f = 75 cm, and pulsed gas cell. RSS were not observed in gas filled capillary.

4. The spectral extension of RSS and corresponding harmonics is the same or lower.

5. The «cutoff» RSS rises with driving intensity

6. Typically RSS are spatially clean and spectrally narrow on the same wavelength for the whole spatial profile.

7. The RSS shape and position is not dependent on pressure of the generating medium

8. Spectral gap between the RSS and corresponding harmonic raises with frequency, i.e. for higher harmonics the RSS is approaching the precedent harmonic. In other words RSS can be assigned to a driving central wavelength different from the central wavelength of regular harmonics.

9. RSS were observed for iris diameters higher than 14 mm.

10. RSS were observed for large interval of position of the gas jet along optical axis - at least 40 mm centered at focus

In general RSS are very robust against many parameters and their observation is very reproducible.

There are many possible candidate phenomena to cause the red-shifted structures. We will present them one-by-one and discuss the observation that can exclude them:

3.4.4.2.1 Driving pulse spectral changes due to Kerr effect self phase modulation When a high intensity pulse propagates in the medium, the refractive index of the medium can vary significantly during the pulse propagation. This can be achieved via Kerr effect. In Kerr effect induced SPM the red shift is generated in the rising front of the pulse but has to be pressure dependent. In our XUV spectra we do not observe any dependence of the spectral position of the RSS with the pressure therefore the driving pulse self phase modulation cannot cause RSS due to characteristic 7.

3.4.4.2.2 Phase-matching The influence of phase-matching can be neglected according to the RSS robustness against macroscopic parameters as the gas pressure (characteristic 7), iris diameter (char. 9) and gas jet position (char. 10).

3.4.4.2.3 Long quantum trajectory We have seen theoretically on figures 3.72 and 3.73 that the long path signal can be strong on axis. However, the spectral structures should appear. Experimentally we do not see any spectral structure in the RSS violating the characteristic 6.

3.4.4.2.4 XUV grating aberrations The XUV grating used in the flat-field XUV interferometer is cylindrical and can cause aberrations. However, with such small XUV beam as generated in helium-filled pulsed cell (see figure 3.98) there should not be any aberrations.

3.4.4.2.5 Second recollision In the simple-man model (more in section 2.1.1 on page 24) the third step lies in recombination of accelerated electron with the ion. However the electron may not recombine and continue its trajectory in the continuum. Then it can recombine the next cycle. When there is a success, such an event is called «second recollision». Experimentally it would create «second cutoff» in form of additional harmonic peaks. Theoretically it was predicted in [Balcou 93] and experimentally it was reported in [Brunetti 08].

The second recollision can be viewed as some sort of «long long path». Because of its long time spent in continuum its harmonic dipole phase parameter α has to be much higher that the one of long path [Brunetti 08]. This implies large spectral extent and spectral structures. We do not observe such characteristics in the XUV spectra. That means that the second recollision cannot be the reason for RSS violating the characteristics 6 and 7.

3.4.4.2.6 HHG in two-atom dimers When considering a molecule that consists of two atoms, one can slightly adapt the simple-man model. There is only the second step (acceleration) that has to be changed in the way that the liberated electron is not stopped after acceleration in the continuum by the field of opposite sign. Instead of that the electron after ionization is accelerated and recombine with the second ion even without being slowed down. Compared to «long long path» of the second-recollision case the two-atom molecules present contrast with «shorter than short path».

This hypothesis is rather complex and difficult to evaluate taking account of all the parameters. However, to exclude dimers from the candidate list for RSS, considering the helium case is sufficient and no further investigation is necessary. The main issue of helium is a very low energy of such He-He bond that is lower than the thermodynamical energy $k_B T = 0.026\,\mathrm{eV}$ under standard conditions. That means that no He_2 molecules exists with room temperature and there is no reason that the temperature of helium in the gas cell is significantly lower.

Also the presence of dimers should be highly pressure dependent.

Therefore the RSS generated by shorter than short path are violating the characteristic 2.

3.4.4.2.7 Second diffraction order of the XUV grating We have seen on figure 3.90 that under certain conditions we can detect high harmonics via the second order of diffraction of the XUV grating. The second order of diffraction appears as two new harmonics between each of two original (first order) harmonics.

However, the RSS always appear as only one structure between two original harmonics.

Moreover, with our XUV spectrometer we cannot detect second diffraction order of the XUV grating when generating in krypton and xenon.

3.4.4.2.8 Generation in ions When using driving pulses of a very high peak intensity one could imagine to ionize the medium with the rising edge of the pulse and to generate in the falling edge in ions making them red-shifted via $\alpha \frac{\mathrm{d}I_{IR}}{\mathrm{d}t}$. However, there are two simple counterarguments:

1. The RSS cutoff will be higher as much higher harmonics can be generated in ions. This violates characteristic 4.

2. RSS would be also bow-like as the regular harmonics violating characteristic 6.

3.4.4.2.9 Cutoff-plateau transition In our model we considered the shift of the frequency as $\alpha\frac{\mathrm{d}I_{IR}}{\mathrm{d}t}$. That gives a blue shift in the front edge of the driving pulse and a red shift in the trailing edge. When considering $\frac{\mathrm{d}(\alpha I_{IR})}{\mathrm{d}t}$ one can obtain a red shift even on the front edge.

At a cutoff intensity I_c, a given harmonic will go from the cutoff ($\alpha = 13 \times 10^{-14}\,\mathrm{cm^2/w}$) to the plateau ($\alpha = 1 \times 10^{-14}\,\mathrm{cm^2/w}$). The instantaneous frequency change can be written as

$$\delta\omega = \frac{\mathrm{d}\varphi}{\mathrm{d}t} = \frac{\mathrm{d}\left(\alpha I_{IR}\right)}{\mathrm{d}t} = \alpha\frac{\mathrm{d}I_{IR}}{\mathrm{d}t} + I_{IR}\frac{\mathrm{d}\alpha}{\mathrm{d}t}$$

We can develop

$$\frac{\mathrm{d}\alpha}{\mathrm{d}t} = \frac{\mathrm{d}\alpha}{\mathrm{d}I_{IR}}\frac{\mathrm{d}I_{IR}}{\mathrm{d}t}$$

therefore the instantaneous frequency become

$$\delta\omega = \frac{\mathrm{d}I_{IR}}{\mathrm{d}t}\left(\alpha + I_{cutoff}\frac{\mathrm{d}\alpha}{\mathrm{d}I_{IR}}\right)$$

We can assume that the transition from cutoff to plateau occurs between the intensity I_{cutoff} and $1.2I_{cutoff}$ [Zaïr 08] therefore

$$\frac{\mathrm{d}\alpha}{\mathrm{d}I_{IR}} = \frac{\delta\alpha}{1.2I_{cutoff} - I_{cutoff}} = -5\frac{\alpha_{cutoff}}{I_{cutoff}}$$

where we have approximated $\delta\alpha = (\alpha_{short} - \alpha_{cutoff}) = \alpha_{cutoff}$. Therefore around this transition the instantaneous frequency equals

$$\delta\omega = \frac{\mathrm{d}I_{IR}}{\mathrm{d}t}\left(\alpha_{cutoff} - 5\alpha_{cutoff}\right) = -4\alpha_{cutoff}\frac{\mathrm{d}I_{IR}}{\mathrm{d}t}$$

and this gives a red shift. This red shift is smaller than the blue shift associated to the long path since the equivalent α value is quite large ($4 \times 13 \times 10^{-14}\,\mathrm{cm^2/w}$) but it occurs at low intensity and where $\frac{\mathrm{d}I_{IR}}{\mathrm{d}t}$ is low.

Those considerations predict the RSS generation in very typical HHG conditions, so that the RSS should appear in other experiments too. This is not the case.

Also the intensity distribution in the focus would make the term $\frac{\mathrm{d}I_{IR}}{\mathrm{d}t}$ different on axis and off axis, and this should spectrally smear the RSS.

For those reasons the RSS are not caused by the transition from the cutoff to the plateau.

3.4.4.3 Phenomenon explanation

To this point we failed to explain the red-shifted structures with various phenomena listed above. None of them is robust enough to exist under such high number of different constraints parameters.

It is also hard to combine them together as each of them has some special characteristics that are not compatible with others.

We propose to investigate the possibility of combination of ionization-induced self phase modulation of the driving pulses together with depletion of the ground state of atoms. We therefore divide the argumentation to three parts: driving pulse spectral shaping before HHG due to propagation of the driving pulse in the medium, HHG and checking the overall characteristics.

3.4.4.3.1 Driving beam spectral & temporal shaping The spectral shaping of high intensity infrared femtosecond pulses during the propagation in the medium was published in [Kim 02, Gaarde 08]. The spectral shaping was explained by the self-phase-modulation by ionization.

With high intensity pulses the phenomenon is strong enough to significantly shape the pulses even in such a short medium as a gas jet. The spectrum and the temporal profile of the pulse are then strongly modulated and the pulse becomes positively chirped even when the original pulse is a perfect Gaussian with flat spectral phase.

A real laser pulse is typically longer than its Fourier limit (even when compressed to a minimal duration) due to the chirp of higher orders. Considering such pulse induced self-phase-modulation by ionization one obtains even more complicated temporal profile after the propagation in the medium. Such modulation can be strong enough to split the pulse. The first pulse (prepulse) would be red-shifted due to the positive chirp.

3.4.4.3.2 HHG with the shaped driving pulses In the previous section we assumed to dispose of the driving infrared pulses with red-shifted prepulse. The prepulse interacts with the gas jet before the main pulse.

Assuming low peak intensity of the driving pulse before interaction with the generating medium, the ionization-induced SPM would not have strong effect and the harmonics would be generated with the original central wavelength.

However, assuming high peak intensity of driving pulses would dramatically change the situation. As we have seen earlier in this chapter, the high intensity can cause 100%

ionization of the medium on axis. After the complete ionization there is no more HHG in this on-axis region.

The red-shifted prepulse generates harmonics with the red-shifted central frequency. Then the main pulse generates harmonics centered on the original wavelength (corresponding to figure 3.94 c). If the red prepulse is strong enough to deplete the medium, the main pulse would not generate high harmonics. Therefore there would be only RSS on axis, where the peak intensity is high enough to deplete completely the ground state of atoms (corresponding to figure 3.94 d).

Off axis the ionization is not so strong so the spectrum of the driving pulse is not changed, the pulse is not chirped and harmonic signal appears on the harmonic line.

3.4.4.3.3 Experimental signatures The transition from «ordinary» harmonics to RSS is well shown on figures 3.94 and 3.96. With low intensity one can see only ordinary harmonics. With more intensity the RSS appears on axis and simultaneously the on-axis signal of ordinary harmonics declines. This process continues with more intensity to the point where the RSS that are on axis are spectrally brighter than ordinary harmonics and there is no ordinary harmonics signal on axis. As a result, the different parts of temporal pulse were detected on different spatial places on the detector. It means that with proper spatial filtering in the far field one can choose the time of HHG.

We have to check our hypothesis for the characteristics listed above. Characteristics are written in *italic*, argumentation in upright style.

1. *RSS were observed for high intensity and there is no maximum intensity for generation of RSS.* The high intensity is necessary for ionization-induced self phase modulation. The higher intensity is demanded for the red-shifted part of the driving pulse is intense enough to generate harmonics.

2. *RSS were generated in all tested gaseous media: helium, neon, argon, krypton, xenon and air.* The ionization induced self phase modulation can take place in all gases.

3. *RSS were generated in various geometries: gas jet with $f = 2$ m, gas jet with $f = 75$ cm and pulsed gas cell. It was not observed in gas filled capillary.* There is no problem for ionization induced self phase modulation to occur with various geometries because the only parameters needed are high intensity laser pulse and enough of gas pressure. On the other hand a long medium such as capillary can destroy the spectrally separated prepulse mixing the simple spectral shaping also with those induced by capillary (guiding, re-focusing, mode beating...).

4. *The spectral extension of RSS and corresponding harmonics is the same or lower.* As RSS are the same harmonics but generated with slightly different central wavelength

the maximal cutoff has to be equal in both cases. Under certain lower intensity levels the intensity contained in the red-shifted part of the driving pulse is not high enough to generate RSS for higher harmonics. Therefore the cutoff of RSS can be either equal or lower than the cutoff of ordinary harmonics.

5. *The «cutoff» of RSS rises with driving intensity.* This was answered in precedent point.

6. *Typically RSS are spatially clean and spectrally narrow, centered on the same wavelength for the whole spatial profile.* RSS are typically harmonics in the plateau and the red-shifted part of the driving pulse is spectrally narrow. RSS is the XUV signal generated with red-shifted driving pulse, it is not red-shifted XUV signal. Therefore the spectral position of RSS with our levels of intensity does not depend on driving pulse intensity.

7. *The RSS shape and position is not dependent on pressure of the generating medium.* This is not intuitive unless we consider the creation of the red-shifted part of the driving pulse. This is based on self-phase-modulation by ionization. In high intensity regime the medium becomes completely ionized in every case. Thus the temporal and spectral shaping are present in nearly same way making the RSS shape and position not sensitive to pressure of the generating medium.

8. *Spectral gap between the RSS and corresponding harmonic raises with intensity i.e. for higher harmonics the RSS is approaching the precedent harmonic.* This apparent «gap increasing» is direct result of seeing harmonics generated with 2 different central wavelengths.

9. *RSS were observed for iris diameters higher than 14 mm.* This is explained by the need of high intensity and power characteristics of our driving laser.

10. *RSS were observed for large interval of position of the gas jet along optical axis - at least 40 mm.* The same as precedent point.

As we look on figure 3.98 where we observed RSS in helium-filled cell it is evident that the RSS spectral position is in excellent agreement with harmonics generated with central wavelength of 840 nm. RSS generated in argon jet and krypton jet corresponds to 817 nm and 815 nm respectively. That can be also explained as the RSS are generated with the prepulse that is spectrally centered on different wavelength compared to the main pulse. As the ionization potential of different gases used is different, the SPM would shape the IR spectrum differently resulting in different central wavelengths.

Note that the prepulse cannot be delivered already by the laser chain, in such case the infrared spectrum before the HHG has to be modulated (for femtosecond time difference) or it has to be seen on figure 5.11 on page 195, which is not the case (see large delays in figure 3.101).

3.4.4.4 Discussion

The spectra of infrared driving beam after HHG in argon jet are on figure 3.101. As the RSS are much closer to original harmonics than in the case of helium we can also expect that the featured red-shifted signal in the driving pulse spectra would be much closer to the original central wavelength. Unfortunately it is hard to find a well spectrally separated signal in rather continuous spectra.

To conclude, we observed unprecedented red-shifted structures when performing HHG at very high intensities. Those spectral features are very robust against most of experimental parameters - both microscopic and macroscopic. This robustness excluded many phenomena from consideration of origin of RSS. Those excluded phenomena included phase-matching, long quantum trajectory only and many others.

Even if this study can not be fully conclusive, we propose to explain such structures as due to HHG with a red-shifted prepulse. This prepulse is made by ionization-induced self phase modulation of the fundamental laser pulses in the generating medium. The RSS are then generated with this prepulse while the regular harmonic signal is generated with the main pulse. This explanation is coherent with all the characteristics of experimentally observed RSS. Note that we have acquired XUV spatially resolved spectra with RSS in over 900 different experimental conditions.

The red-shifted structures are robust and were observed in gas jet and pulsed gas cell in helium, neon, argon, krypton, xenon and air.

An important fact is also a well designed XUV characterization technique. If using a XUV spectrometer with a detector of only 1 cm diameter (not 4 cm as we have) one would not see the regular harmonics on figure 3.94 d) and thus, one would consider the RSS to be regular harmonics.

3.5 HHG in gas filled capillaries

At the very beginning of this chapter we compared different generation techniques such as gas jet, gas cell and gas filled capillary. In our work the most of effort was devoted to experimental exploitation of gas jet and gas filled capillary. In the table 2.3 we show that in our experimental conditions the most of XUV photons can be obtained with gas jet.

The gas jet with its small medium length is, as we believe, simpler to understand than the capillary due to the medium length. Also the number of experimentally controllable parameters are much higher in the case of jet, e.g., the x-y-z position in space of a capillary is completely defined by the focal spot position. Due to very short medium the experimental conditions in the gas jet are close to our simulations where the medium length equals 0 (the propagation in the medium is not considered). Therefore we devoted much more space in this manuscript to the gas jet than to the capillary.

However, the harmonic spectra of the XUV emission produced in the capillary are very interesting in the main frame of this work as they provide additional phenomena.

There is also a motivation for HHG in a gas-filled capillary.

3.5.1 Motivation

In the introduction of this work, we mention one special application of high harmonic generation: a seeding of soft x-ray lasers [Zeitoun 04, Wang 08, Lambert 08]. With seeding one can overcome spontaneous emission amplification (ASE) that is behind poor stability and coherence of non-seeded x-ray lasers. With the advantage of harmonic seeding of spectrally and spatially coherent stable beam one can keep those characteristics under amplification. For that to work the harmonics has to be of high energy to overcome ASE in the amplifier. The spectral region of interest concerns the wavelengths below 20 nm (above 60 eV).

Neutral argon cannot be used as a generating gas because the maximum harmonic order generated with 800 nm laser is 39 [Gibson 04] as will be discussed later in this section. Typically neon is used to generate XUV radiation below 20 nm, but the conversion efficiency is very low and so there were some efforts to boost the signal from neon e.g. with two-color fields [Watanabe 94] or combining the fundamental and low order harmonics [Brizuela 13]. A different approach is to generate high harmonics in Argon ions [Gaudiosi 06]. To avoid issues of high intensity with tight focusing one can enjoy the multimode beating resulting into spots of very high intensity in an argon filled capillary.

Experimental results presented in this section were made in collaboration with the group of Sophie Kazamias (Sameh Daboussi, Kevin Cassou and Olivier Guilbaud) from LPGP (Paris, France), who are interested in seeding an X-ray laser and proposed this work.

3.5.2 Experimental setup

The experimental setup (figure 3.102) is very similar as the one for HHG in the gas jet with 2 m of focal length mirror (figure 3.4 on page 52).

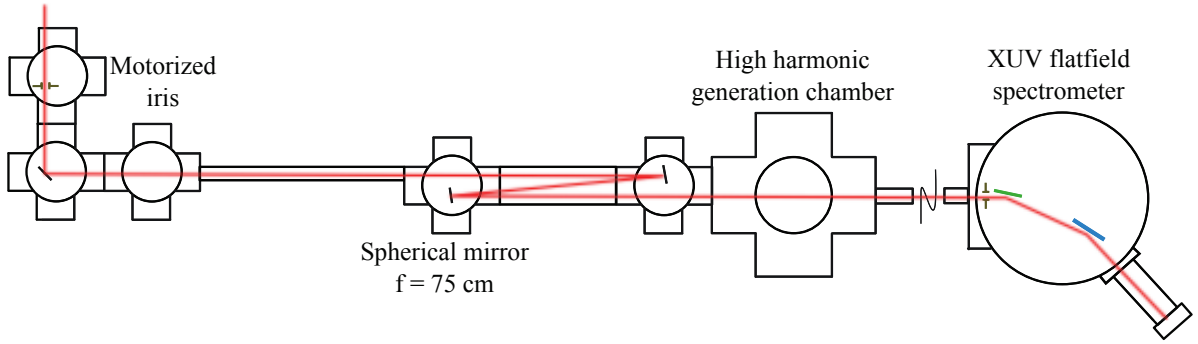

Figure 3.102 – Experimental setup for HHG in the gas-filled capillary in detail

The only difference is that now the focusing mirror has the focal length of 75 cm and is the last one before the beam interacts with the gas jet.

The focal length was changed to provide similar injection characteristics as in [Zepf 07]. In this paper the authors claimed to obtain XUV emission up to 360 eV from an argon-filled capillary thanks to the quasi-phase-matching obtained by multi-mode coupling.

We used hollow core glass capillaries. Their length was of 30 and 50 mm and the core inner diameter was 101 or 150 μm.

As the flat and the spherical mirrors, in the Z-shape beamline, were already equipped with motorization controlled from outside the vacuum, we decided to install the capillary in a fixed support with the possibility of z-axis tuning only. The capillary support was designed for best stability and is shown on figure 3.103.

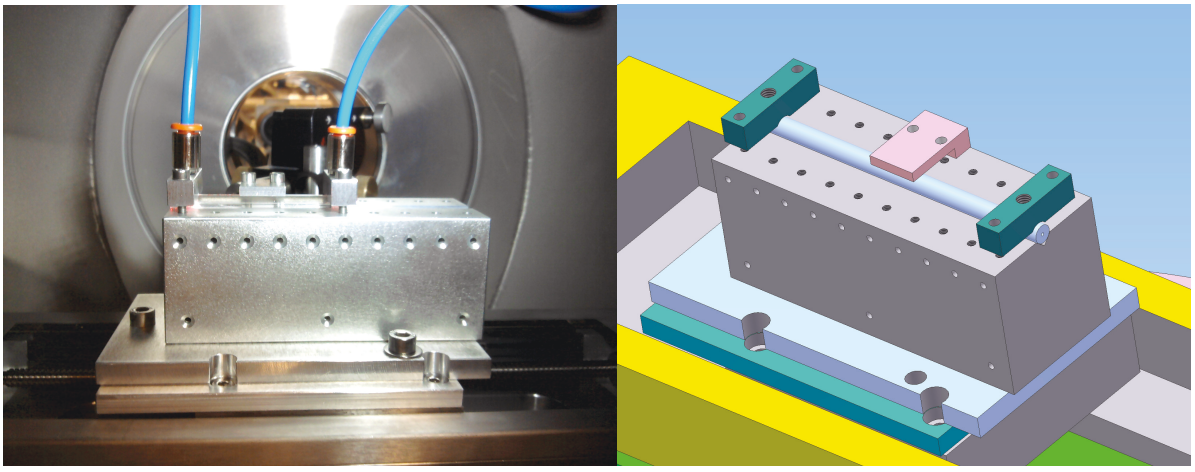

Figure 3.103 – (color) Photograph and drawing of the capillary with its support installed on a translation stage (yellow) along the optical axis in the HHG chamber.

We can see that the support is strong enough to avoid any capillary vibration or shape change. The capillary is fixed in the position by two high clamps at both ends of the capillary and one clamp in the middle.

The two high clamps at capillary ends are also used for gas injection. There are two holes drilled in the cladding of the capillary perpendicularly to the core at the distance of 3 mm from the capillary edge. There are small pieces of Teflon squeezed between the capillary and the clamps to avoid gas leaking. The gas is brought by two plastic tubes (blue on the image) under controlled pressure. The number and position of gas injection holes were chosen to have the constant gas pressure inside the capillary.

The capillary supports were designed to be fixed on a translation stage along the optical axis. We can see the operating screw of the translation stage on the image. The transversal position of the beam focus can be tuned via the two mirrors before the focus. In that way, the focus can be placed arbitrarily in the x-y-z space.

Note that the focal length of 75 cm is about two orders of magnitude higher than the capillary length. With the iris diameter of 30 mm (fully open) the Rayleigh distance is 1 cm (compare to 3 and 5 cm of capillary length).

3.5.3 Experimental results

3.5.3.1 Reference gas jet spectrum

To better understand the following spectra generated in the gas filled capillary we first show spectra generated in the gas jet in similar conditions except the focal length of 2 m. The spectrum in on figure 3.104.

The spectrum was generated with pulses of 45 fs and 22 mJ after the iris giving $7 \times 10^{14}\,\mathrm{W/cm^2}$ peak intensity in the gas jet.

The spectrograms present clean short path harmonics both spatially and spectrally. However, they are not symmetric spectrally because of high intensity.

The long path is barely detected and is visible only off axis as very thin and weak vertical lines on the right side of the short path strong signal.

The noise on the right side of the image is caused by diffusion of low harmonic orders in the bellow that connects MCP and detection chamber.

The highest harmonic detected is of order 39. The harmonic 41 is too close to the barrier suppression limit (see table 2.1 on page 28 for barrier suppression and 2.2 on page 30 for cutoff intensity). That means that in neutral argon the highest harmonic order we can detect is the order 39.

3.5.3.2 HHG in the capillary

We performed HHG in argon filled capillary of length of 30 mm and 101 μm core inner diameter. The series of single-shot spatially and spectrally resolved spectra as a function of argon pressure is presented on figure 3.105. The focusing mirror has a focal length of 75

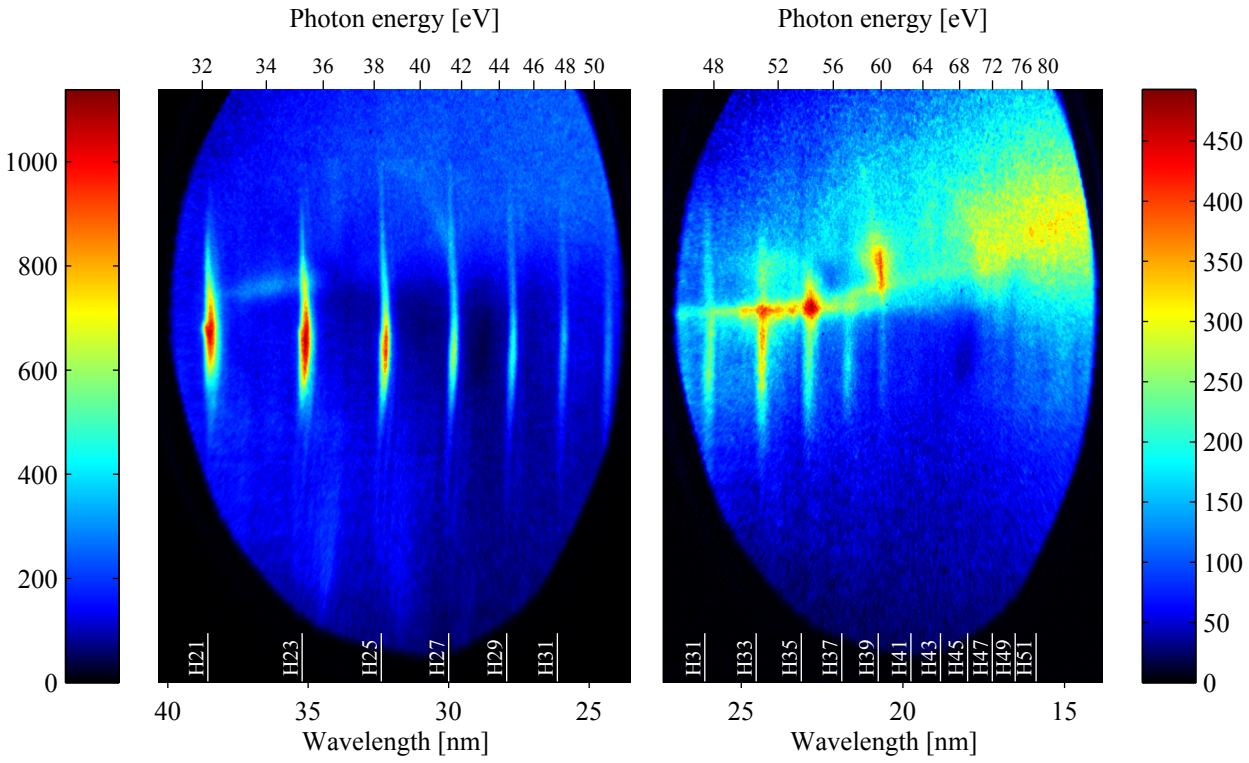

Figure 3.104 – (color) Experimental spatially-resolved XUV spectrum generated in Argon (2.6 bar of backing pressure) with the focusing mirror focal length of 2 m, iris diameter of 13 mm and the jet gas at focus.

cm, iris diameter was 7.5 mm giving a beam focal spot of $w_0 = 42\,\mu$m (radius at I_{max}/e^2). The pulses duration was 45 fs with an energy of 6.5 mJ before the iris giving 6.7×10^{14} W/cm^2 at focus.

The coupling parameter was chosen to be $\frac{w_0}{r_{cap}} = 0.82$ to favor the monomode coupling. One should note that the optimal parameter for the maximum coupled energy to the fundamental mode is around 0.65 [Marcatili 64], but the higher parameter favors the coupling to fundamental mode to the expense of energy that will not be injected into the capillary.

For the lowest pressure of 5 mbar of argon in the capillary, the harmonics are similar to the gas jet case on figure 3.104. However, they are slightly blue-shifted (as also seen in [Schnürer 98]) and there are more of them. The HHG in gas jet produced harmonics up to order of 39 that is the classical limit of neutral argon harmonics [Gibson 04].

With 5 mbar in the capillary we detect harmonics up to order of 53. According to high brightness of such high harmonic orders, this is likely to be attributed to the HHG in argon ions [Christov 96, Gaudiosi 06, Zepf 07]. Comparing the peak intensities of the XUV signal for low (figure a) and high (figure f) one can say that under these conditions the harmonics from ions are more than half intense than the low order harmonics (that is in agreement with [Covington 11]).

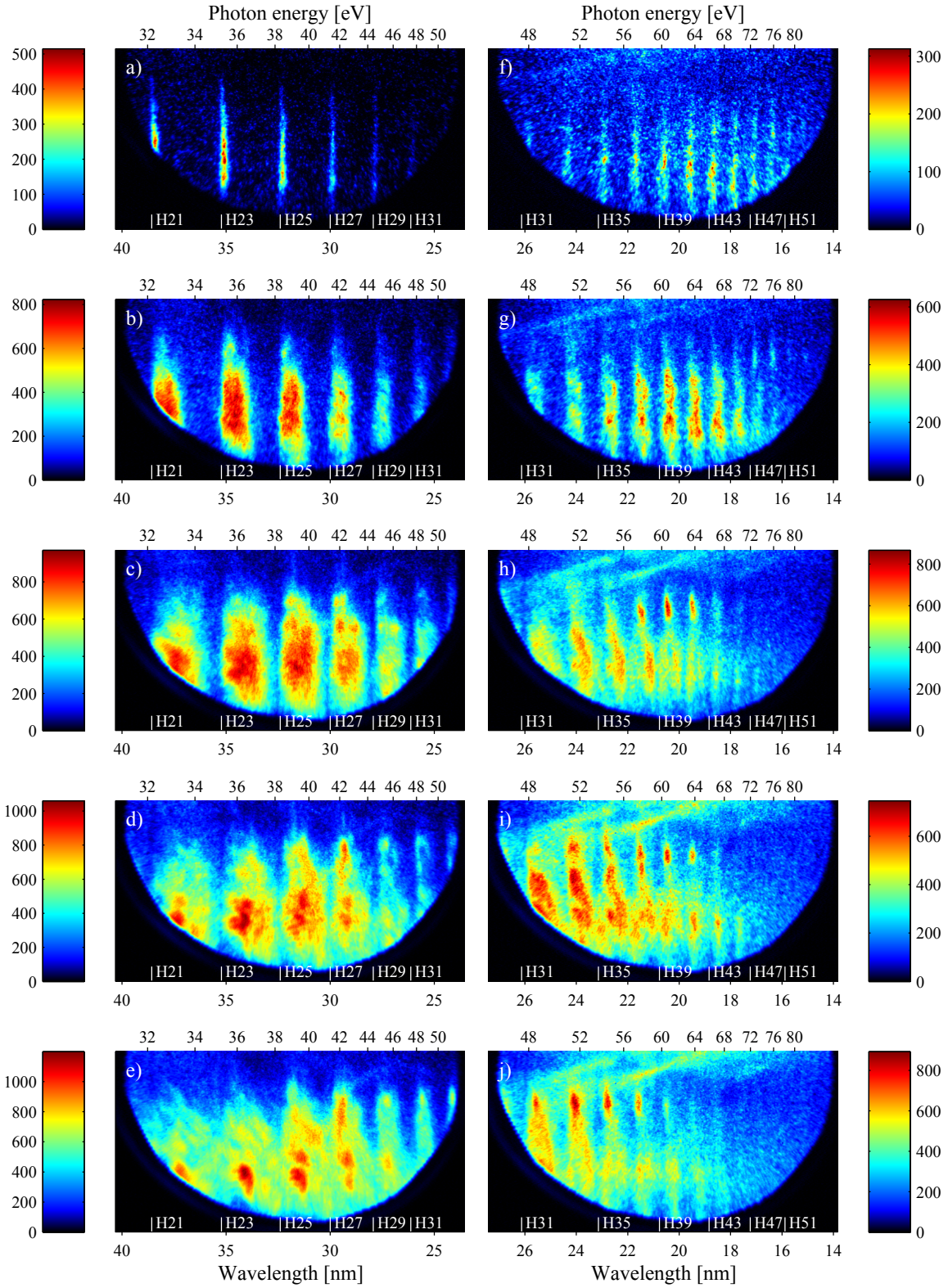

Figure 3.105 – (color) Experimental spatially-resolved XUV spectra generated in Argon filled capillary of 101 μm core inner diameter and the length of 30 mm. The argon pressure in the capillary was a), f) 5 mbar, b), g) 12 mbar, c), h) 25 mbar, d), i) 35 mbar and e), j) 50 mbar. Other parameters in text.

With 12 mbar of argon in the capillary the spectral width of the harmonics changes dramatically. The low harmonics are several times larger than with 5 mbar and high harmonics are also larger than before. The harmonics are also even more blue-shifted. Spatially, however, they do not differ from the 5 mbar case. We cannot distinguish any regular structures easily discriminable above the noise. One can also notice that harmonics 51 and 53 can now be only barely seen.

25 mbar in the capillary brings spectrally larger harmonics with more blue shift. Harmonics start to be spectrally so large that they touch each other. Some interferences between neighbors harmonics can be seen on harmonics 37-43. There is also spatial modulation on high harmonics with distinguishable maximum off axis. The highest visible harmonic is the 47.

With 35 mbar the harmonics start to loose their spectral and spatial homogeneity. They form a quasi-continuum on some spatial coordinates and the highest visible harmonic is the 45.

50 mbar of argon destroys the low harmonic spatial and spectral profile. Also high harmonics contain a lot of irregular spatial and spectral structures. Highest visible harmonic is 43 therefore the intensity has to be still high enough to generate in ions.

To see the following evolution of harmonic spectra we plot spatio-spectral harmonic profiles for high argon pressures in the capillary on figure 3.106.

The harmonics are still distinguishable and so large that they interfere with each other. Strong blue shift is still present. There is also a very special phenomenon: the evolution of the brightest harmonic in the spectra.

On image a) (90 mbar) the most intense harmonic is the harmonic 23. Then with 100 mbar (b) the harmonic 23 and 25 are of maximum and almost equal intensity. With 110 mbar (c) this maximum shifts to harmonics 25 and 27. 120 mbar prefers only harmonic 27 and 140 mbar (e) puts clearly the most of intensity on harmonic 29.

On figure 3.106 we see that the brightest harmonic position depends on the pressure. In the pressure interval between 90 to 140 mbar the brightest harmonic shifted from H23 to H29.

While all these harmonics are in the plateau, the effect cannot be explained by simple decrease of intensity due to gas density.

The absorption length is shown on figure 3.107. Therefore in this case the brightest harmonics should be still the highest ones.

The figure 3.107 show the absorption length of different harmonic orders with different pressures. We can see that the higher harmonics (H31 and H33) are absorbed in the medium more than 10 times longer than the lower harmonics (H21 and H23). This trend is true also for different gas pressures.

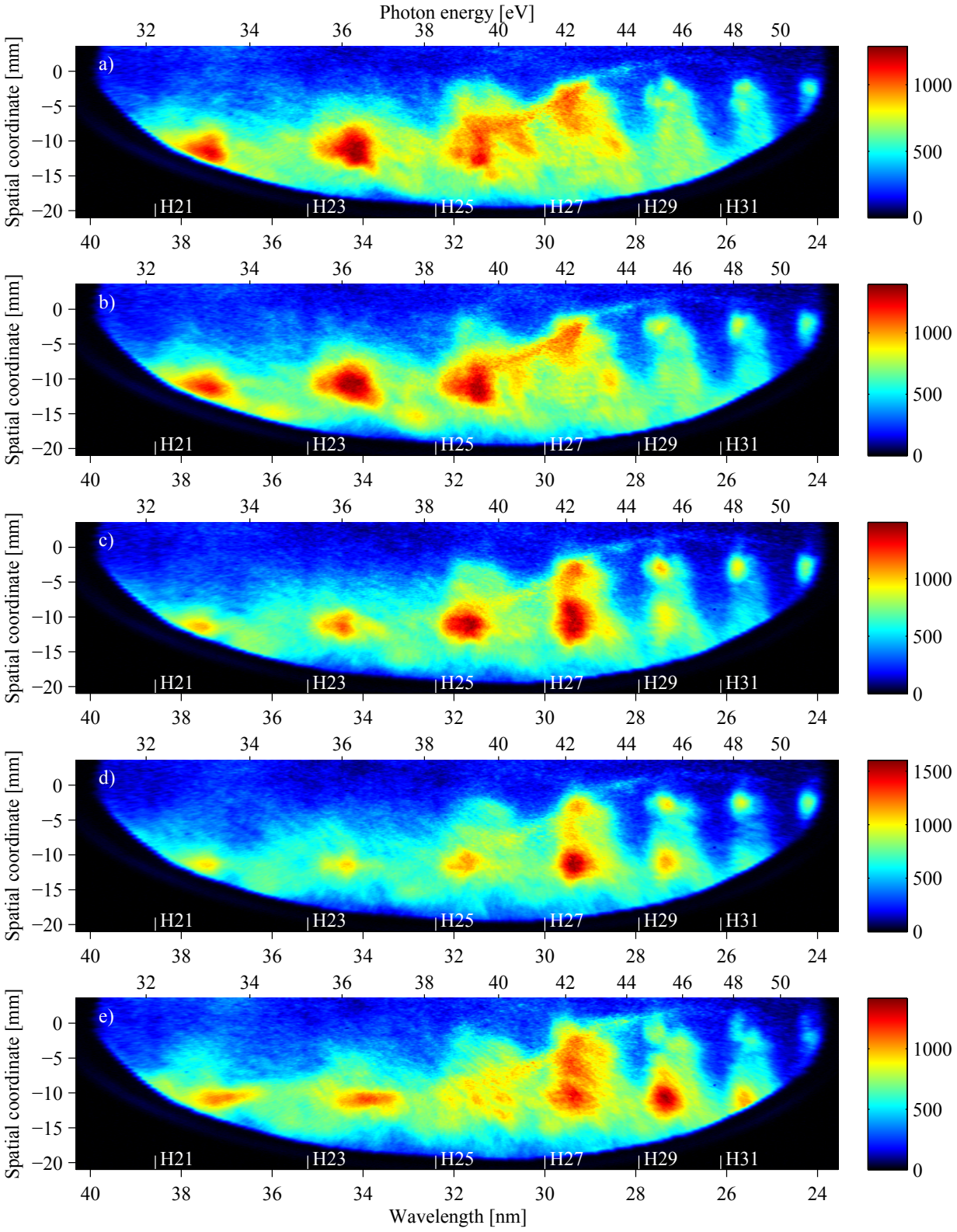

Figure 3.106 – (color) Experimental spatially-resolved XUV spectrum generated in Argon filled capillary of 101 μm core inner diameter and the length of 30 mm. The argon pressure in the capillary was a) 90 mbar, b) 100 mbar, c) 110 mbar, d) 120 mbar and e) 140 mbar. Other parameters in text.

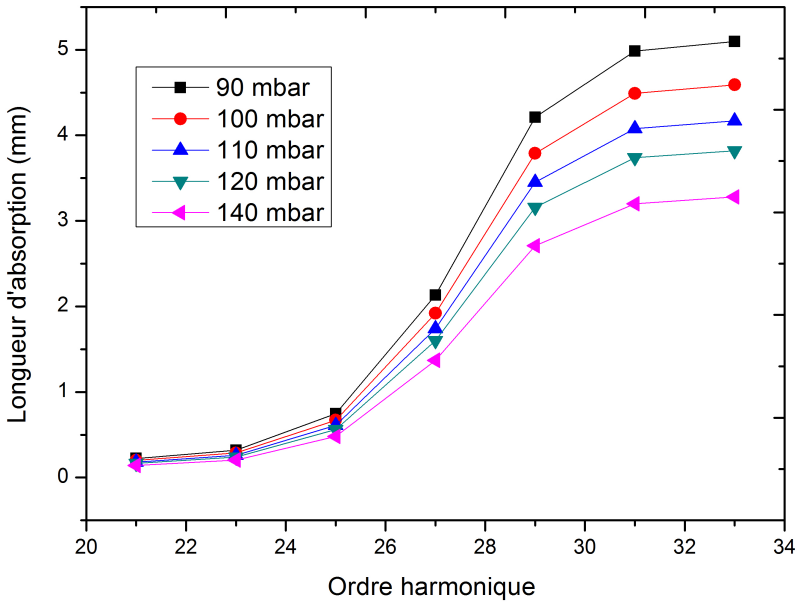

Figure 3.107 – Calculated absorption length for different pressures and harmonic orders. Adopted from [Daboussi 13].

The peak intensity doubles the barrier suppression intensity in argon, but during the propagation in the capillary the driving pulse intensity is likely to decrease at the end of the capillary. Due to the neutral gas absorption length that is much shorter (few mm) than the capillary length, one can estimate that changing the pressure would change the ionization degree at the end of the capillary. Then the brightest harmonic is defined by the balance between the propagation efficiency and the generation efficiency as the intensity drops to low levels at the capillary end. This also explains why high order harmonics disappear with the pressure.

3.5.4 Analysis and discussion

To conclude on the major differences between the XUV spectra generated in gas jet and in capillary at comparable intensities, we have observed that the spectral bandwidth of harmonics increased to the extent where the harmonics create a XUV continuum. Also the number of detectable harmonic orders was much higher in the case of capillary due to the generation in ions [Christov 96, Gaudiosi 06, Zepf 07].

3.5.4.1 Number of observable harmonics

To give an additional image of the number of observable harmonics we can compare three typical cases on figure 3.108: HHG in argon gas jet, HHG in neon gas jet and HHG in argon filled capillary.

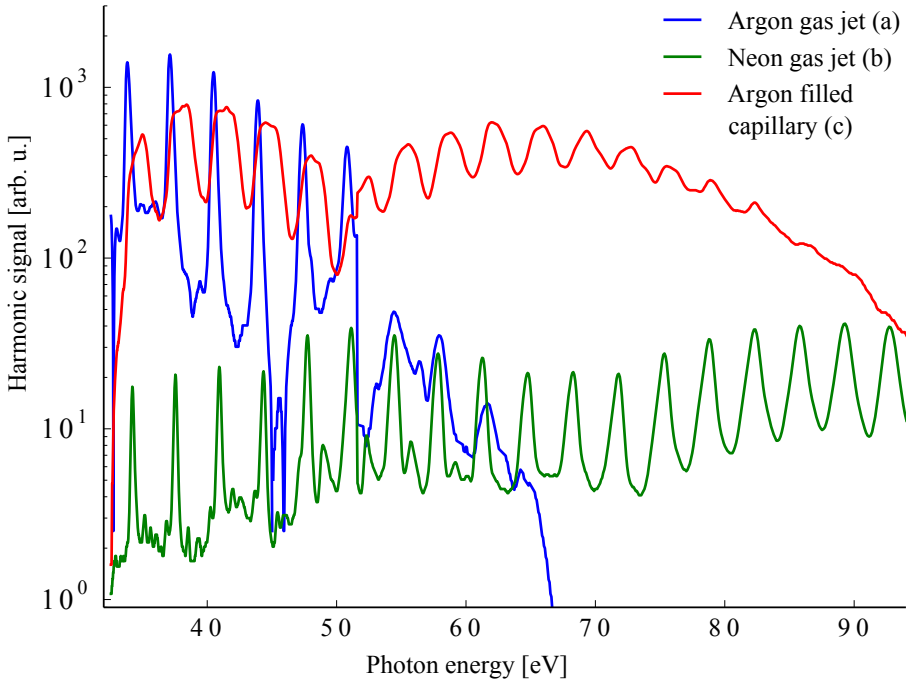

Figure 3.108 – (color) Experimental on-axis spectral profile comparison for different generation geometries and different gases. a) (blue) optimized XUV signal obtained in argon gas jet with a driving pulse peak intensity of 8×10^{14} W/cm², b) (green) optimized XUV signal obtained in Neon gas jet with a driving pulse peak intensity of 9×10^{15} W/cm², c) (red) optimized XUV signal obtained in argon filled capillary at pressure of 15 mbar with a driving pulse peak intensity at capillary face of 7×10^{14} W/cm². Adopted from [Daboussi 13]

The spectrum a) was generated in argon gas jet with backing pressure of 2.6 bar. The driving beam was clipped by an iris of 13 mm diameter and the pulse energy was 21 mJ before clipping. The resulting intensity in the gas jet was 8×10^{14} W/cm².

The spectrum b) was generated in neon gas jet with backing pressure of 3 bar. The driving beam was clipped by an iris of 20 mm diameter and the pulse energy was 72 mJ before clipping. The resulting intensity in the gas jet was 9×10^{15} W/cm².

The argon jet spectrum finishes at harmonic 39 that corresponds to the maximum in the neutral argon gas (in the classical model [Corkum 93]). In the argon filled capillary we can see the second plateau up to harmonic 53 that we identified as due to the generation in argon ions [Christov 96, Gaudiosi 06, Zepf 07]. This is different from the single plateau of neon.

The HHG in ions is weaker than in neutral atoms. In our conditions they were both of comparable intensity, so either the HHG in neutral atoms is suppressed or HHG in ions is

enhanced or the HHG in neutral atoms is very enhanced only for higher harmonics.

The first two reasons are probably acting together. First, the generation intensity is almost 3 times higher than the barrier suppression intensity. Therefore the medium is ionized very quickly even before the peak of the pulse giving not so much time for HHG in neutral atoms. Second, HHG in ions may be enhanced as shorter wavelengths propagate better in ionized gas.

3.5.4.2 Harmonic spectral width and blue shift

Figures 3.105, 3.106 and 3.108 suggest that harmonics generated in argon filled capillary are spectrally much broader than harmonics generated in gas jet. Also their blue shift is very important. The important thing is that the the harmonics are symmetric in the plateau that can be seen very well e.g. on figure 3.105 b) and c). So we cannot explain such a blue shift and spectral broadening by αI component of the harmonic dipole phase.

The probable cause of the phenomena lies in self phase modulation (SPM) of the driving pulses. The phase then becomes time dependent and can be expressed as

$$\varphi(t) = \varphi_0 + \frac{2\pi}{\lambda_0} \int_0^L n(t,z)\,\mathrm{d}z$$

where L, n and φ_0 stands for the length of the medium, refractive index of the plasma/gas and input pulse phase. Note that the integral $\int_0^L n(t,z)\,\mathrm{d}z$ represents time-dependent optical medium length.

The instantaneous angular frequency $\omega(t)$ can be found by deriving $\varphi(t)$ leading to

$$\omega(t) = -\frac{d\varphi(t)}{dt} = \omega_0 - \frac{\omega_0}{c} \int_0^L \frac{dn(t,z)}{dt}\mathrm{d}z$$

where the blue shift is represented by the second term. The blue shift and spectral broadening are due to the refractive index changes during the pulse propagation in the generating medium. The origin of such important refractive index dynamics can be attributed to two types of SPM:

- Kerr effect induced SPM
- Ionization induced SPM

3.5.4.2.1 Kerr effect induced SPM Kerr effect lies in the dependence of the refractive index n of a material on applied field of intensity I. For centro-symmetric medium this dependence can be expressed as:

$$n(t,z) = n_0 + n_2 I(t,z)$$

where $n_0 = \sqrt{1+\chi_{lin}}$ is the linear refractive index and $n_2(I)$ is a second-order nonlinear coefficient of refractive index. For gases, this nonlinear refractive index rises with pressure. For argon the $n_2 = p \times 9.8 \times 10^{-20}\,\mathrm{bar{\cdot}cm^2/W}$ [Nisoli 96].

With Kerr effect SPM, the spectra are broadened symmetrically and both the blue shift and red shift are present.

3.5.4.2.2 Ionization induced SPM Ionization induced SPM lies in nonlinear dependence of a gas refraction index on the degree of ionization of the medium expressed as:

$$n(t,z) = \sqrt{1 - \frac{n_e(t,z)}{n_c}} \tag{3.3}$$

$n_e(t,z)$ denoting time and space dependent free-electron density and n_c the critical electron density ($n_c = 1.7 \times 10^{21}\,\mathrm{e^-/cm^3}$ at 800 nm). The critical electron density does depend only on laser angular frequency. Note that the refraction index of neutral gas is considered to be 1 which derives directly from equation 3.3 putting $n_e = 0$.

We would like to stress here that the ionization induced SPM induces a blue shift.

3.5.4.2.3 Comparison of Kerr effect and ionization contribution As seen on figures 3.105 and 3.108 the red shift is not present. This suggests that the blue shift and spectral broadening are mainly due to the ionization self phase modulation.

To compare both effects on the final blue shift and spectral broadening we use the characteristic value of the Kerr effect - the critical power P_{crit} expresses as

$$P_{crit} = \frac{\lambda^2}{2\pi n n_2(p)}$$

The critical power P_{crit} stands for power level at which the beam collapses due to the self-focusing.

We will review and detail more issues of Kerr effect and ionization induced SPM in chapter 5.

Now we plot on figure 3.109 the spatially and spectrally integrated XUV signal that depends on ratio of the driving power P to the critical power P_{crit}.

The figure shows a rapid increase of the XUV integrated signal for values of the power up to $0.6 \cdot P_{crit}$ and a linear only slowly increasing tendency in the power region above. Those are typical characteristic for HHG without any SPM.

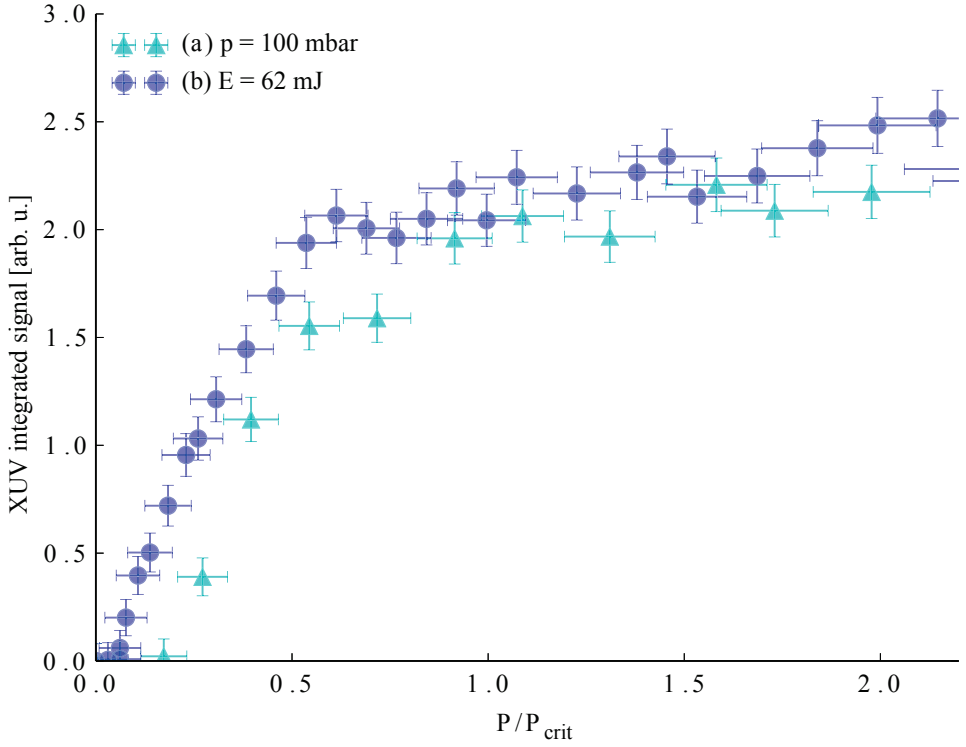

Figure 3.109 – (color) Experimental integrated signal of harmonics 21-31 as function of the ratio of the driving power P and the critical power P_{crit} a) (green) with a constant pressure of 100 mbar, b) (blue) with a constant driving pulse energy 62mJ. Adopted from [Daboussi 13]

Therefore the spectrally large harmonics with blue-shifted spectra (figure 3.105) are likely to be generated with driving pulses that are already spectrally large and blue-shifted due to the propagation in the gas with ionization induced SPM.

3.5.4.3 Spatial structures

HHG in a capillary with low intensity pulses is shown on figure 3.110.

The figure 3.110 shows XUV spectra in the far field and spatial profile of the harmonic 23. The XUV is generated in the capillary of 3 cm length and 300 μm core inner diameter filled with 84 mbar of argon. The pulse energy before iris is 38 mJ and the iris diameter is 5 mm giving an incident energy on the capillary to 2.6×10^{14} W/cm^2.

Such conditions are not favorable for SPM and propagation of shaped IR pulses in the capillary. Therefore only low intensity driving pulses generate harmonics at the end of the capillary. That explains the spectrally symmetric and narrow harmonics. The XUV source becomes also coherent and due to the diffraction to the far field we can observe spatial structures.

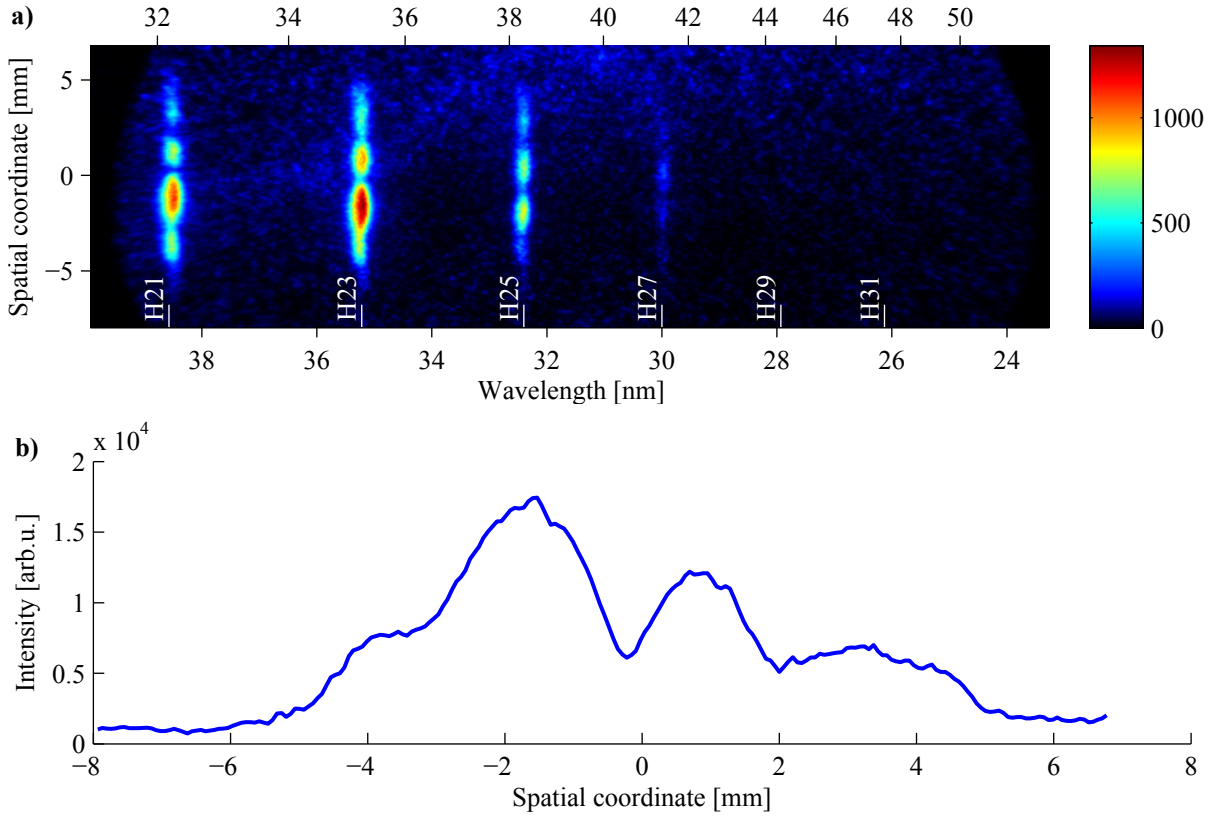

Figure 3.110 – (color) Experimental a) spatially resolved XUV spectra in the far field and b) spatial profile of the harmonic 23. The XUV is generated in the capillary of 3 cm length and 300 μm core inner diameter filled with 84 mbar of argon. The pulse energy before iris is 38 mJ and the iris diameter is 5 mm giving an incident energy on the capillary to 2.6×10^{14} W/cm^2.

3.5.5 Conclusion on HHG in argon filled capillary

The presented HHG at high intensity driving pulses in argon filled capillary is an efficient way to generate harmonics up to order 49 (74 eV). The corresponding XUV signal is more than one order of magnitude higher than the maximum signal from neon gas jet in the same spectral range. Such high photon energies are attributed to the HHG in argon ions.

Increasing the argon pressure in the capillary blue-shifts significantly the harmonics, creating them spectrally very broad while keeping the brightness at the same level. This is explained considering the blue shift and spectral broadening of driving infrared pulses that propagates in the gas during ionization. Those rapid changes of free-electron density result in ionization induced self phase modulation.

At high argon pressure between 90 and 140 mbar the interplay between harmonic generation efficiency, plasma transmission and absorption results in local harmonic intensity maximum that shifts from harmonic 23 to harmonic 29 as the argon pressure in the capillary increases.

In general, at high intensity the harmonics are spectrally very large and create quasi

continuum. Such broad spectra are attributed to ionization induced self-phase-modulation of the driving pulses. At low intensity the harmonics are spectrally narrow and contains spatial structures. The intensity is not high enough to induce significant SPM and due to absorption the detected XUV signal is generated at the end of the capillary making the case similar to gas jet.

The presented characteristics of the XUV emission at high intensity (spectrally broad, high photon flux) make it a good candidate for seeding a soft X laser amplifier.

3.6 Conclusion on HHG with high energy long femtosecond pulses

In this chapter we investigated theoretically and experimentally the high harmonic generation with high energy long femtosecond pulses of 50 fs. We compared HHG in different geometries and we developed a simple simulation that does not consider propagation of the XUV in the generating medium. This simulation allowed us reproducing and explaining many structures observed in spatially and spectrally resolved XUV spectra in the far field. The structures are more pronounced at high driving pulse energy and are mainly due to the infrared beam modulated phase $q\varphi_{IR}$ and the harmonic phase term αI_{IR}.

Similar structures were presented also in experimental spatially and spectrally resolved XUV profiles. One kind of structure, called red-shifted structure, was tentatively explained considering the presence of a red-shifted driving prepulse.

Finally we described HHG in an argon filled capillary and found large and blue-shifted bright harmonics. We found this kind of XUV source well adapted for soft X ray lasers amplifiers seed.

Chapter 4

HHG with high energy long femtosecond pulses and driving beam spatial shaping

In previous chapter we have explained various spatial and spectral features in harmonic spectrograms by spatial coherence of XUV radiations and the diffraction toward a detector (MCP). The nonlinearity of the harmonic dipole and dipole phase was identified as the major effect. Other effects such as XUV propagation in the medium play only minor role. We have seen that even with Gaussian driving beam and Gaussian pulses, the XUV radiation could easily be not emitted in Gaussian beam.

As we already discussed in section 3.2, the IR beam delivered by the CPA laser chain has quasi-flattop (saturated) beam profile of Strehl ratio around 60%.

For certain cases we filtered spatially the beam with a capillary and we obtained beam profile very close to Gaussian.

In the next section we will present another possibility to clean the driving beam wavefront that gives moreover access to advanced features as focusing optics astigmatism precompensation.

Note that the IR wavefront is very important for HHG [Salières 95] because of the dipole phase term $q\varphi_{IR}$. Obtaining regular phase of the driving beam out of the focus could be an alternative approach to obtain huge generating medium as compared to HHG at focus with large focal distance mirrors.

4.1 Deformable mirror

4.1.1 Introduction to adaptive optics

In here we will use the term «adaptive optics» for the technology designed to measure and control the phase-front of the fundamental beam. The control of the phase-front usually

differs according to application.

4.1.1.1 Applications

In the second half of the last century four major application domains were born

- astronomy
- medicine and biology
- military
- lasers

In astronomy telescopes adaptive optics allows to discriminate the influence of air density fluctuations in the Earth atmosphere giving an image close to what could be seen if the telescope took place at Earths orbit such as the Hubble. The main issues are speed of fluctuations that are very high and low photon flux coming to the telescope.

In medicine and biology adaptive optics can discriminate a biological tissue that covers the tissue of interest making microscopes really «seeing through». Moreover microscopes intrinsic aberrations can be compensated.

Military applications use adaptive optics to lengthen the observation distance.

In laser domain adaptive optics helps to clean laser beams to gain smaller and brighter focal spots and specific beam shapes on demand.

4.1.1.2 Principle

The principle of adaptive optics (figure 4.1) consists of three separate blocks (our system is indicated in parenthesis):

- Wavefront analyzer (HASO HA v3)
- Wavefront modulator (deformable mirror HIPAO standing for HIgh Power Adaptive Optics)
- Computing & commanding unit (CASAO)

Those blocks work together in several steps:

1. The beam reflected by the wavefront modulator (in the following we will call it «deformable mirror» as this is our case) goes though a beam-splitter where only a small part is transmitted to wavefront analyzer.

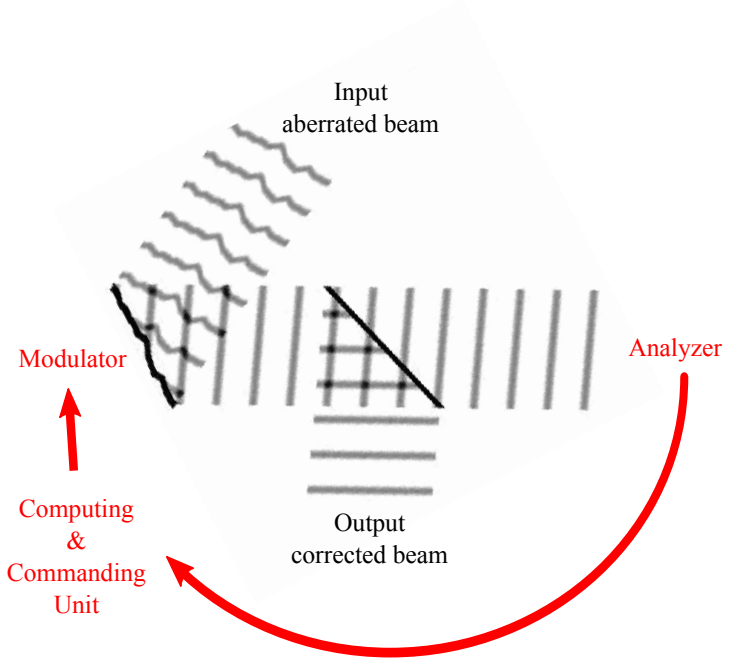

Figure 4.1 – Schematic principle of adaptive optics wavefront correction using deformable mirror.

2. The wavefront characteristics are then sent to a computer equipped with necessary software that calculates the changes to be taken by the modulator and sends the command for compensation to the wavefront modulator.

3. The deformable mirror performs the requested deformation.

These three steps are iteratively repeated until the wavefront meets requested shape.

In the first step, the wavefront analyzer gains information about wavefront and intensity profile. This is sufficient to determine the beam profile anywhere on axis. For this there is also one fundamental principle to be fulfilled - a modulator-analyzer conjugation. It means that for proper measurement of the phase front the deformable mirror has to be imaged on the analyzer and proper magnification has to be assured. Only in this case the intensity profile detected by analyzer does not depend on the deformable mirror shape and thus the wavefront shape information can be easily and precisely extracted.

In the second step, the needed correction is calculated. Note that laser beam can be expressed as linear combination of aberrations. Those aberrations are mathematically expressed as Zernike polynomials.

First, all motors are put to zero (the middle) position. Then one by one each motor is asked to go to one positive and the same but negative position and the resulting beam wavefront and intensity profile are acquired. In that way the impact of every motor is known and a linear combination of aberrations is assigned to every motor. Collection of aberration combination for all the motors is called «interaction matrix».

Inverting the interaction matrix leads to «command matrix», that represents assignment of linear combination of motors to every type of aberration.

When the real beam is analyzed, the amount of each aberration is calculated same as for target beam[1]. The needed displacement for every motor is then calculated as a linear sum of all single aberration differences between the real beam and the target beam with well defined direction and focusing distance.

4.1.2 Experimental setup

4.1.2.1 Implementation

Experimental setup is shown on figure 4.2.

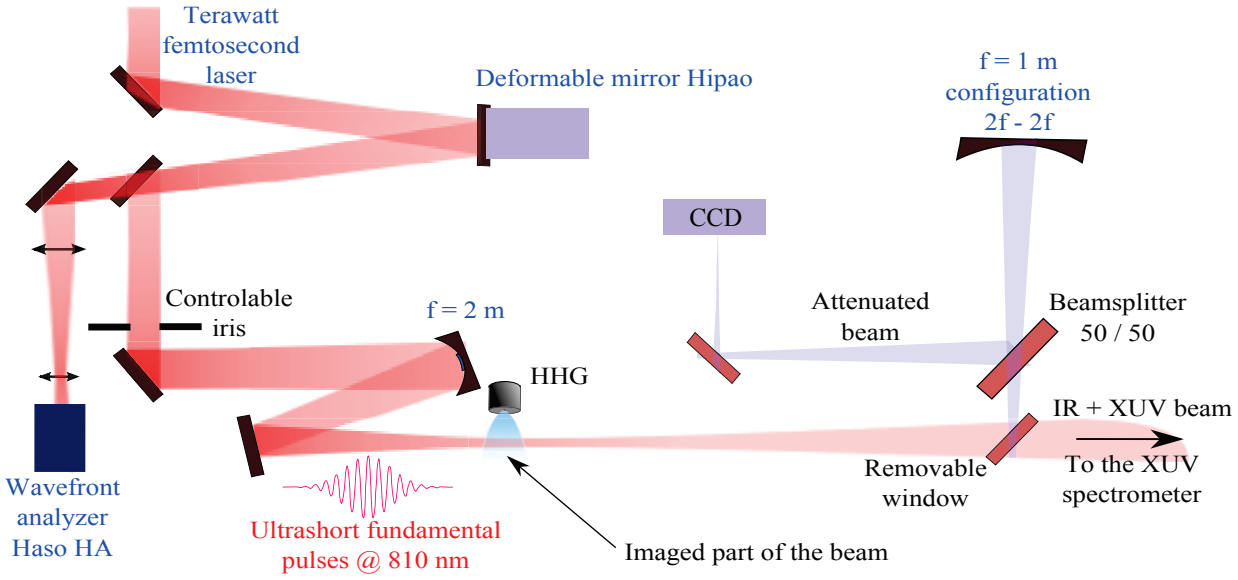

Figure 4.2 – Experimental setup including adaptive optics

The beam is reflected by the deformable mirror and then reflected by a 100% mirror to the iris. The 100% mirror second face is also polished and coated for 100% of transmission. The substrate of the mirror is also optical quality and plane parallel. In that way only a mirror leak is sent to be analyzed by HASO. In our experimental conditions of high intensity laser pulses this is necessary because of nonlinear effects caused in the material and to avoid damage.

[1]Typically «perfect Gaussian beam» is wanted in the interaction zone. But, actually in reality, one wants to have a perfect beam with defined direction, defined focal spot position and e.g. focal mirror astigmatism precompensation. So at the end the «target beam» is also well aberrant correspondingly to optical system and together they produce demanded «perfect beam».

4.1.2.2 Wavefront modulator HIPAO

The HIPAO (HIgh Power Adaptive Optics) is a deformable mirror developed in collaboration with Imagine Optics and ISP Systems. The main goal of the project was to develop an adaptive optics system of high stability and compatibility with high energy femtosecond pulses e.g. high damage threshold, large spectral bandwidth and large diameter (minimum 3 inches) [Canova 07, Lefaudeux 12]. As most of high energy ultrafast laser sources are of low repetition rate, the mirror was adapted for fast corrections of aberration and few shots were sufficient. On the other hand, the HIPAO is not adapted for corrections at high repetition rate.

Photos of the membrane and the motors and of the final covered mirror are on figure 4.3.

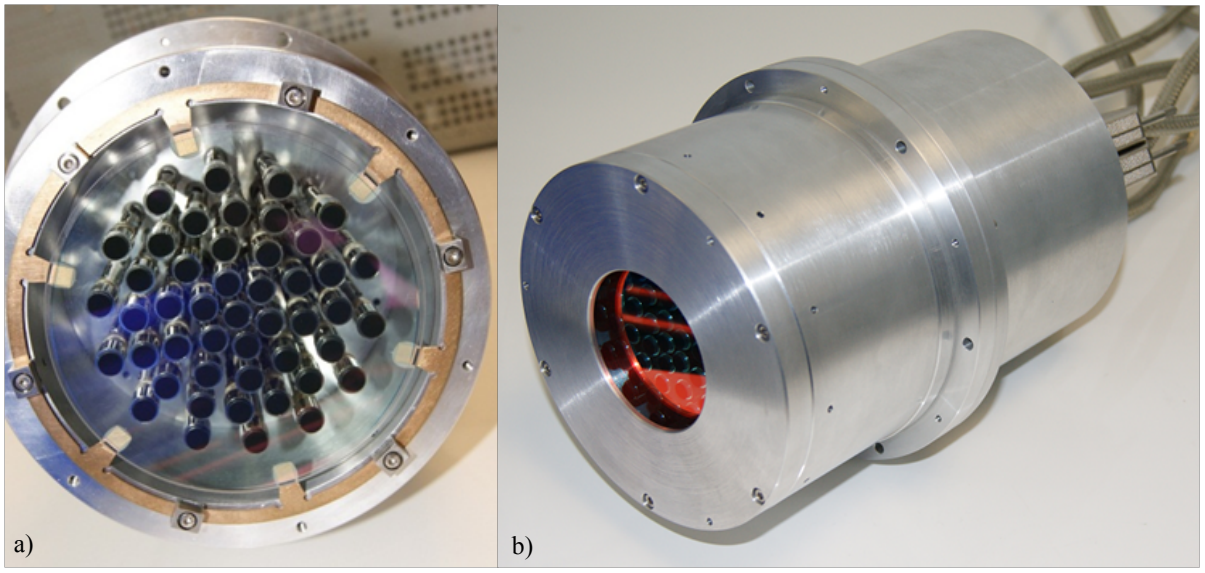

Figure 4.3 – (color) a) Front view of the membrane and step motors and b) front-side view of finished HIPAO mirror.

The prototype we tested consists of 1 mm thick dielectric membrane and 47 step motors.

4.1.2.2.1 Membrane testing We performed tests of damage threshold of 7 different commercially available ultrafast coatings. The results can be found in table 4.1 on the following page.

The toughest mirror was provided by manufacturer C. Its coating holds 320 $^{mJ}/_{cm^2}$ but provided limited bandwidth of only 160 nm. On the other side the largest bandwidth of 240 nm was offered by manufacturer SO but the mirror was the most fragile among the queried group.

The mirror of LO with its 170 $^{mJ}/_{cm^2}$ and 215 nm of spectral bandwidth was chosen as a compromise. Note that EO with its promising numbers was denied because of poor reproducibility of mechanical deformations.

Manufacturer	Bandwidth [nm]	Threshold [$^{mJ}/_{cm^2}$]
SO	670 - 910	90
FT	670 - 900	140
LC	690 - 910	140
LO	705 - 920	170
EO	695 - 930	200
O	45° design	200
C	720 - 880	320

Table 4.1 – Damage threshold of different commercially available coatings for ultrafast mirrors

4.1.2.2.2 Motors characteristics To provide demanded high level stability the membrane is deformed by 47 step motors instead of piezo actuators as usual. The main advantage is that the position of step motor holds even when the power is off. Second advantage is the high ratio strength/size of step motors among piezos. Each motor in HIPAO can apply force up to 7 N giving 14 N between two motors set to opposite directions. If put vertically the HIPAO deformable mirror can raise up to 32.9 kg. Therefore the mirror is compatible with thick dielectric membranes.

Major disadvantage of such motors is their linearity that results in reduced speed of possible correction that can reach up to one second for one iteration. Moreover the demanded shape of the membrane is not achieved simultaneously by all the motors at the same time in the way that the requested beam shape appears linearly from the previous shape. Instead of that, one motor is operated after another so the beam shape is not controlled between the starting and finish shape of the mirror. This includes not only aberrations but also beam direction and focal spot position drastic changes that can be dangerous when operating with high power lasers. One solution is to shutter the beam when performing iterations.

4.1.2.3 Wavefront analyzer HASO HA v3

The HASO HA wavefront analyzer is based on Shack-Hartmann technique.

German astronomer Johannes Franz Hartmann in late 19th century used a plaque with regularly placed holes in front of a telescope to study of a wavefront of a star. American physician Roland Shack in 1970 replaced the holes with lenses to gain more signal. The function of the Shack-Hartmann technique is illustrated on figure 4.4.

The HASO analyzer consist of a microlenses array (Shack-Hartmann grating) and a CCD. The focal distance of the microlenses equals the microlenses-CCD distance. The microlens diameter is 150 μm and the focal distance 5 mm.

An incoming arbitrary beam samples itself on the microlenses. If the wavefront of the sample arrives at an angle, the focal spot position on the CCD will move accordingly.

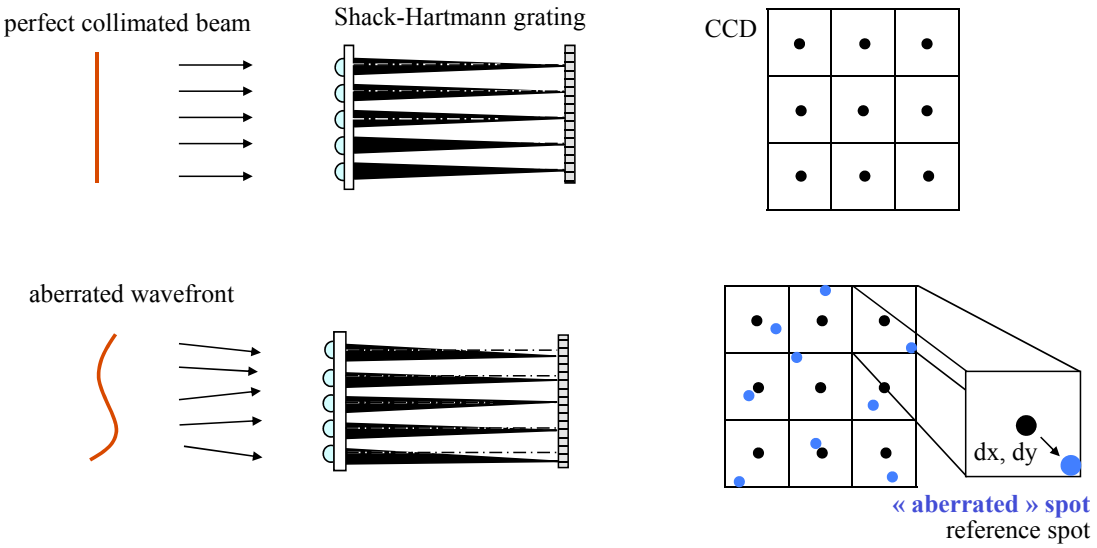

Figure 4.4 – (color) Shack-Hartmann technique principle

With a perfectly plane wave the focal spots form a regular grid of spots on the CCD. This fundamental grid is calibrated in the factory. An arbitrary beam would make a non-uniform grid of spots. With the distance between the new spots and the fundamental ones the computing & commanding unit (CASAO) can calculate the shape of the wavefront.

This manner of wavefront measurement is relatively fast, sensitive and broadband. The technique is also completely achromatic. Different wavelengths of light are focused either in front of the CCD, or behind making the spots of different size but still at the same position on the chip. Only limit is represented by CCD spectral acceptance. With our HASO one can even measure a wavefront of a white light of 350 - 1100 nm.

However, accordingly, Shack-Hartmann technique cannot determine chromatic aberrations directly. One possible way around is using spectral filters to measure different spectral regions one by one.

4.1.3 Experimental results & interpretation

4.1.3.1 Phase correction

The HASO wavefront analyzer provides us of direct measurement of the beam phase. The original and a corrected phase profile is on figure 4.5.

The figure 4.5 shows spatial phase profile of original beam with the phase error of 98 nm RMS. Such a value is typical for a beam delivered by CPA laser chains where the beam gets saturated in the last amplification stage. When focusing the beam one obtains only 59% of energy in the central spot.

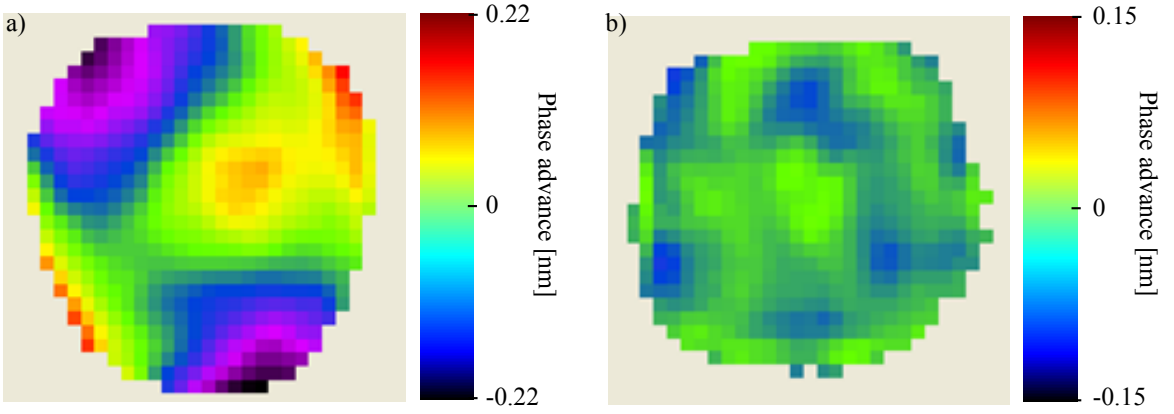

Figure 4.5 – (color) Measured phase profiles of the driving beam a) before and b) after phase correction via deformable mirror (3 iterations). The phase error and corresponding Strehl ratio of the beam was a) 98 nm RMS, 59% and b) 14 nm RMS and 93%.

After correction of the phase with the deformable mirror we obtained a beam with 14 nm RMS phase error only and thus the central spot of the focused beam contains 93% of the overall energy.

Note that more perfect correction is difficult to obtain with CPA laser chain because of laser fluctuation, intensity spatial profile and limited number of motors in the interaction zone (miniaturization of step motors is a challenge in itself).

4.1.3.2 HHG with corrected pulses

We performed a study of HHG dependance on iris diameter far from focus. The integrated signal of single harmonics is plotted vs. the iris diameter on figure 4.6.

The signal is unprecedentedly modulated and contains 8 local maxima and 7 minima with high contrast.The modulations are similar for all harmonics. Note that typically the XUV integrated signal dependance on iris has only one maximum as shown on figure 4.7 and already reported in [Kazamias 03b].

To give an insight in the XUV spectra that are integrated on figure 4.6 we plot the spatially resolved XUV spectra for several iris diameters on figure 4.8.

We can see that the spatial profile of harmonics depends on the iris diameter and for some values of iris diameter there are strong spatial structures. Moreover, the highest generated harmonics vary with iris diameter. Those facts suggest that the intensity spatial distribution of the driving beam varies significantly with iris. We performed a simulation and show it on figure 4.9.

The driving pulse beam profile (figure 4.9) varies a lot with iris diameter. There is an intensity maximum on axis for up to 8 mm of iris diameter. With larger diameter the spatial profile becomes annular for around 11 mm of iris diameter. Opening more the iris, the spatial profile becomes more modulated with local maxima and minima. To compare

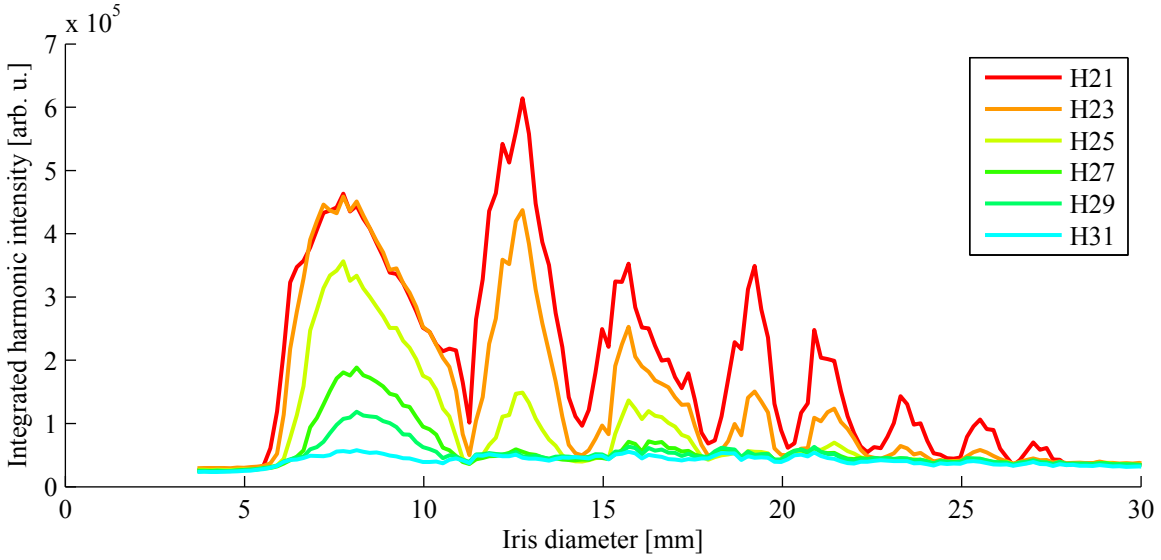

Figure 4.6 – (color) Experimental spatially integrated signal of single harmonics vs. the iris diameter. The HHG was performed in krypton jet 18 cm before the focus with 54 mJ before the iris. The phase-front was corrected via deformable mirror.

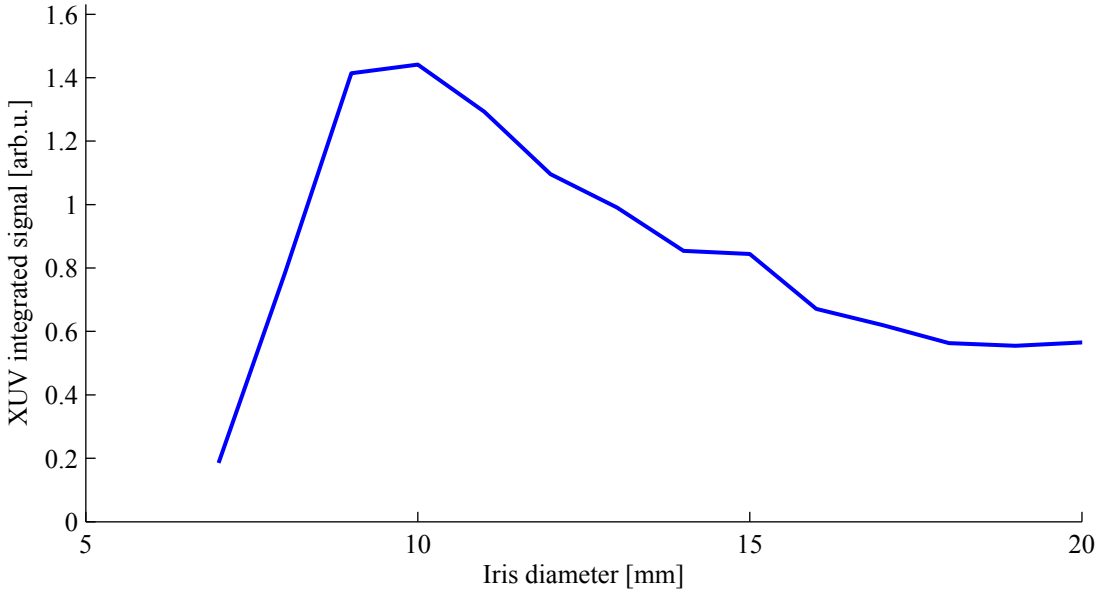

Figure 4.7 – Experimental spatially integrated signal of harmonics 21-29 vs. the iris diameter. The HHG was performed in krypton jet with 54 mJ before the iris. There is no wavefront correction.

the relative intensity quantitatively we plot the on-axis intensity and maximal intensity on figure 4.10.

The on-axis driving beam intensity oscillates with the iris diameter with a very high contrast for low iris diameters. The contrast is lower for oscillation of maximum intensity with given iris diameters that corresponds to annular spatial profiles. Such modulated driving beam would modulate the overall XUV signal. On figure 4.11 we plot simulated

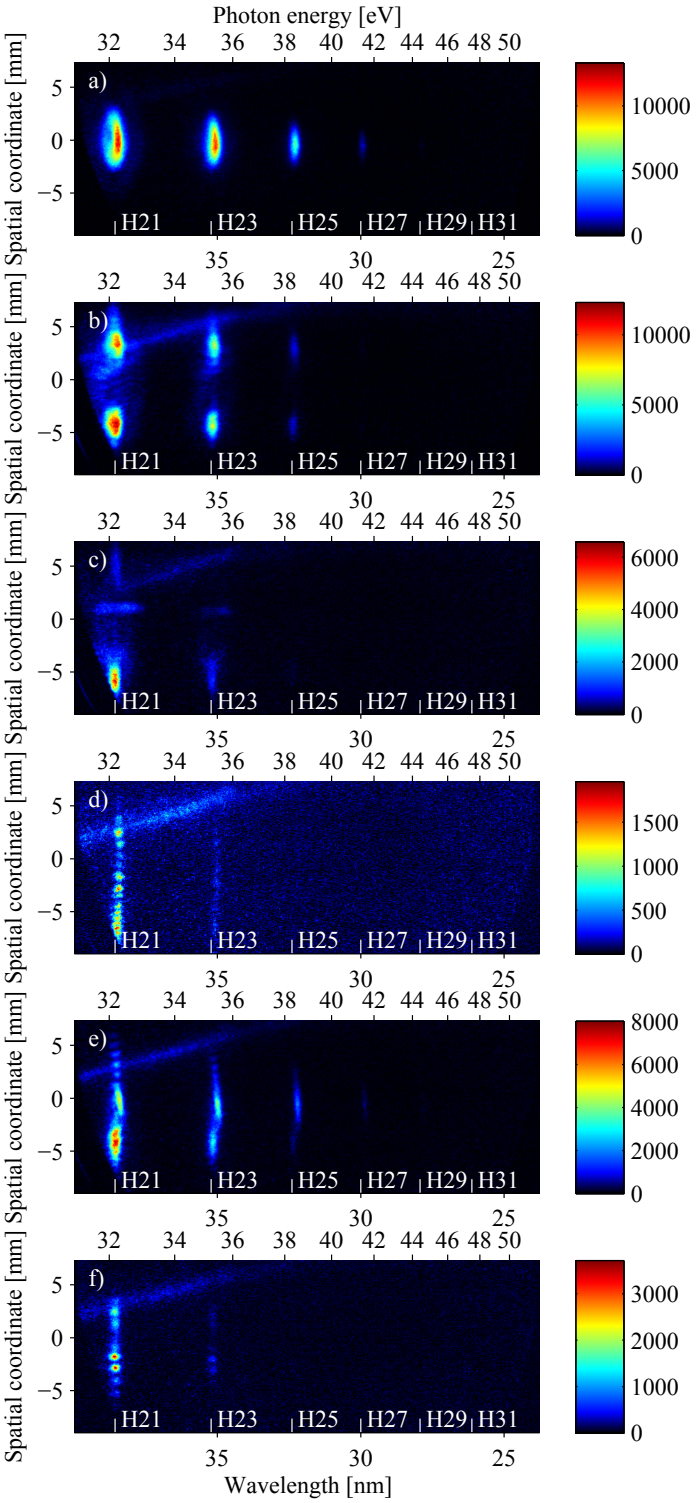

Figure 4.8 – (color) Experimental spatially resolved XUV spectra. The HHG was performed in krypton jet 18 cm after the focus with 54 mJ before the iris. The phase-front was corrected via deformable mirror. The iris diameter was a) 7 mm, b) 12 mm, c) 15 mm, d) 18 mm, e) 21 mm and f) 27 mm.

spatially integrated signal of single harmonics against the iris diameter.

The figure shows the integrated signal dependence on iris diameter that contains many

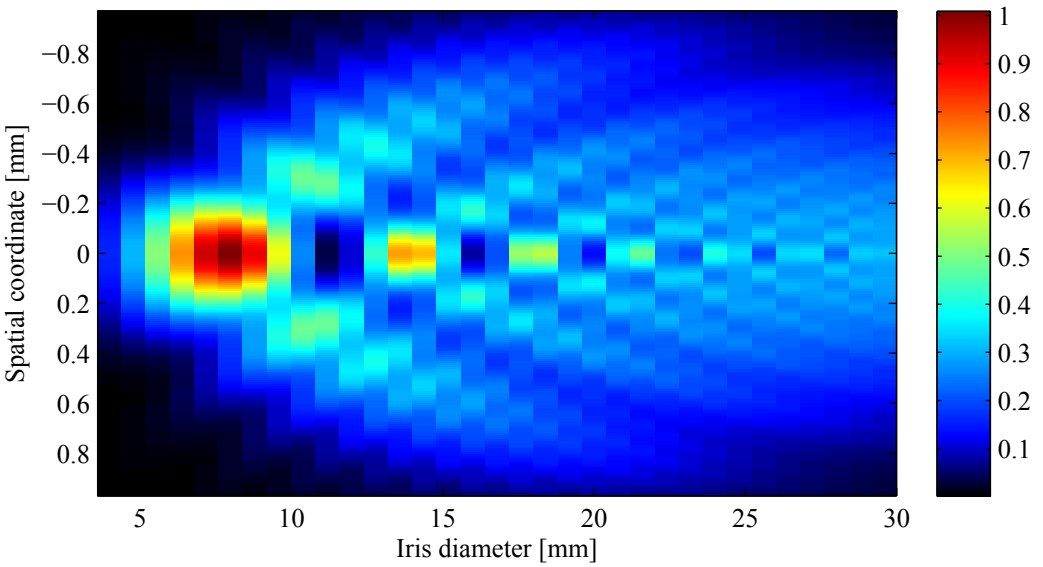

Figure 4.9 – (color) Simulated driving beam spatial profile (peak intensity) in the generating medium. The medium is located 18 cm before the focus. The spatial profile varies with iris diameter.

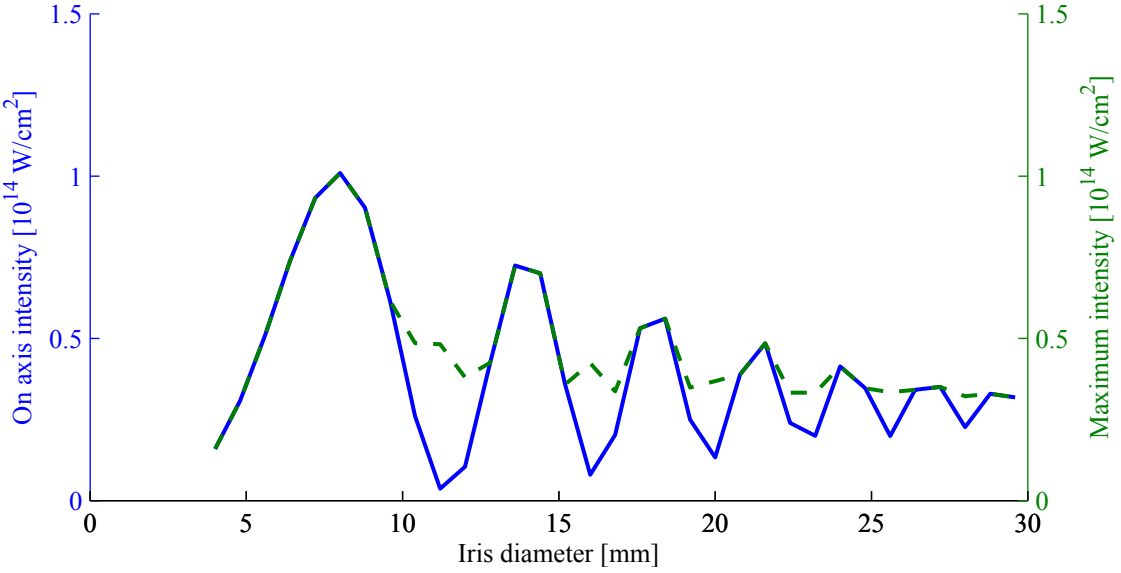

Figure 4.10 – (color) Simulated driving beam spatial profile (peak intensity) in the generating medium. The medium is located 18 cm before the focus. The spatial profile varies with iris diameter.

maxima and minima. Although quantitatively the modulation is not the same as in the experimental case, qualitatively the simulation is in good agreement. The XUV signal is modulated and in general decreases with iris diameter. In our simulation we used less energy of driving pulses in order to approach the conditions to higher harmonics observed experimentally (H15 - 21 in simulation and H21-29 observed experimentally).

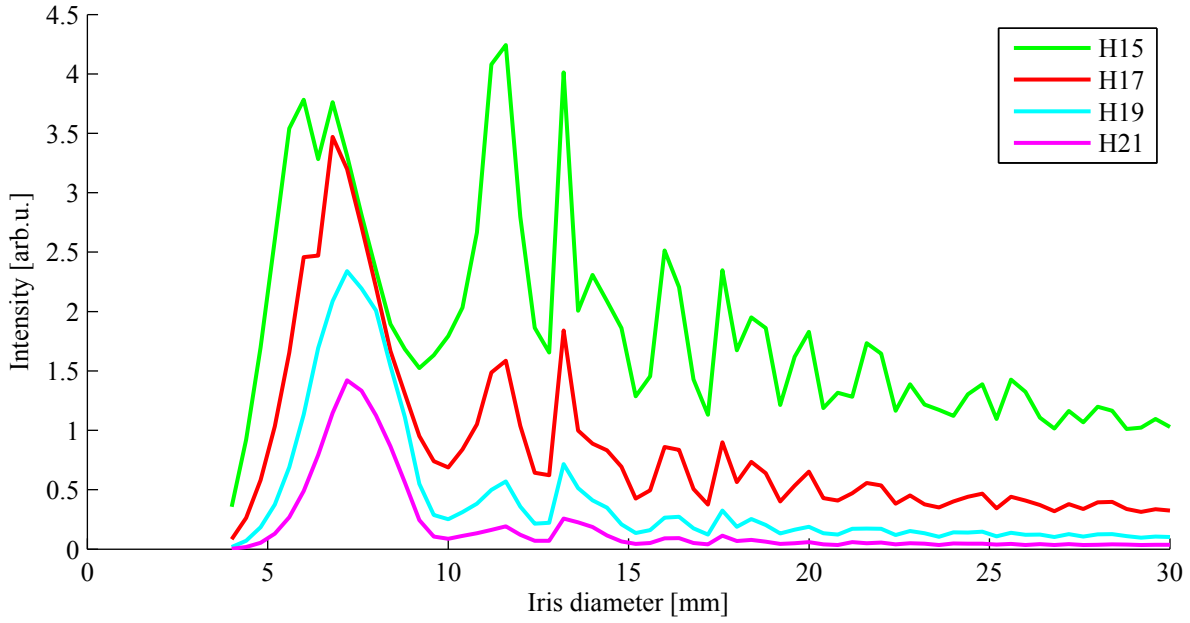

Figure 4.11 – (color) Simulated spatially integrated signal of single harmonics vs. the iris diameter. The HHG was performed in krypton jet 18 cm after the focus with 20 mJ before the iris.

4.1.3.3 HHG with driving beam with aberrations

We studied influence of strong aberration of the driving beam on HHG. The aberrations were added to the driving beam in a controlled way using the Hipao deformable mirror. On figure 4.12 we present measured driving beam spatial profile and corresponding spatially resolved XUV spectra.

We introduced a spherical aberration, an astigmatism and a trefoil via deformable mirror. We can observe spatially large and structured harmonics and a second order of the XUV grating. The spatial structures of the harmonics depend strongly on the driving beam spatial profile and phase as already discussed in previous chapter. With spherical aberration we observe fine spatial fringes in the spatially resolved XUV spectra. With astigmatism we observe more regular harmonic spatial profiles and with trefoil the harmonic spatial profile is divided into 3 zones with zero signal in between them.

4.1.3.4 Conclusion on beam shaping via deformable mirror and HHG control

We observed that correcting the phase-front of the driving beam has a strong impact on the HHG. Adding aberrations to the driving beam in a controlled way changes directly the spatial XUV profiles in the far field. In general, as the driving beam phase influences the shape and creates structures in harmonics, its control via wavefront modulator such as deformable mirror is a convenient way to control and modulate the XUV emission. Moreover, the adaptive optics used was compatible with high energy femtosecond pulses.

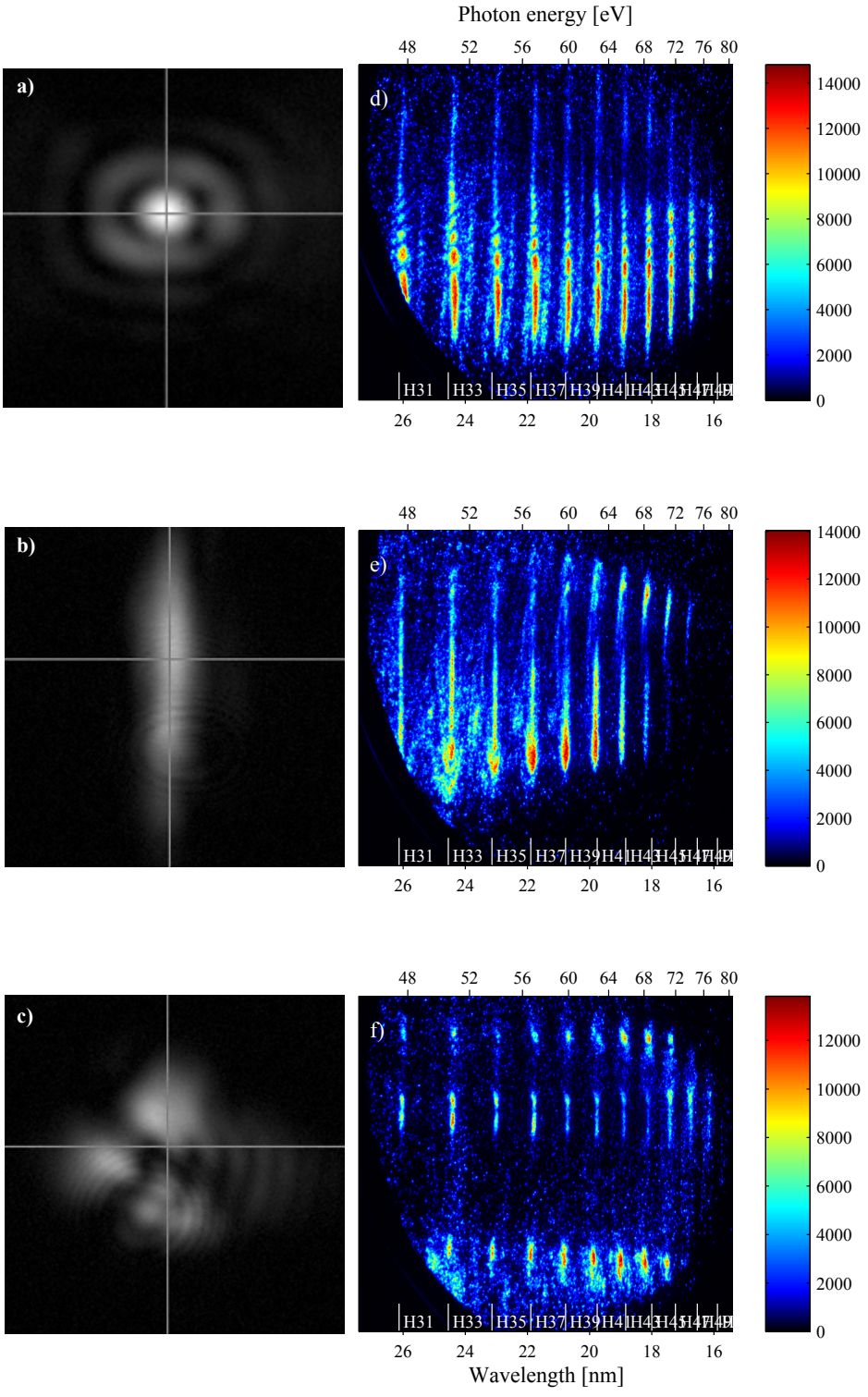

Figure 4.12 – (color) Experimentally measured driving beam spatial profiles in the generating medium and corresponding spatially resolved XUV spectra. The HHG was performed in neon jet with 19.5 mJ before the iris. The deformable mirror was set to correct the phase-front and to introduce a) spherical aberration, b) astigmatism and c) trefoil. The corresponding XUV spectra are on images d), e) and f).

4.2 Reflective phase mask

In previous section we explored a sophisticated method to correct an arbitrary beam phase close to phase of a Gaussian beam.

In this section we will present a technique of an opposite kind. Instead of cleaning the beam we will explore the influence of adding a nonuniformity - a constant phase in the center of the beam. This is to circumvent the fact that the spatially dependent driving pulse intensity generated time-dependent XUV emission (see figure 3.64 on page 95). Therefore with a flat-top (spatially independent) driving pulse intensity and constant phase the XUV emission would be temporally concentrated.

4.2.1 Motivation & Introduction

Effort on generation of high energy isolated attosecond pulses suffers from the fact that for Gaussian driving pulse in a Gaussian beam, the intensity rises first on axis and after that also off axis. This leads to the XUV generation at first on axis and off axis after. Therefore even if - using various techniques - we would generate only one attosecond pulse in time at a given spatial position, in the far field we would detect all of these pulses on axis and also off axis resulting in a train of attosecond pulses.

One proposed technique to circumvent this issue was theoretically investigated in [Strelkov 08, Strelkov 09]. Authors considered a flat-top spatial profile of the driving beam that generates XUV at the same time over the whole beam profile. Authors calculated that 20 fs pulses in the flat-top spatial profile would generate isolated attosecond pulses independently of CEP.

The main technical challenge is to obtain the flat-top spatial profile in the focus where the intensity is the highest. The flat-top profile also has to be maintained along the optical axis for a longer distance than the XUV generating medium. The technique has also to be polychromatic enough to support a very short femtosecond pulses with very large bandwidth. The first efforts led to a phase mask [De Saint Denis 06, Boutu 11].

The concept was to add a π phase to the central part of the beam through a plate transmission. In the focus this would lead to destructive interferences in the beam center flattening the spatial profile.

The main issue of the technique was low damage threshold of such optics that cannot withstand high fluence lasers.

An advanced approach is to use a reflective mask to dephase the beam center through the two optical path mirror (TOP mirror) developed in [Dubrouil 11a]. Then the technique is all-reflective and thus compatible with high energy femtosecond pulses.

In here, we push the work further and present additional characteristics of the technique.

4.2.2 TOP mirror

The TOP mirror replaces the focusing mirror so the experimental setup is the same as presented on figure 3.4 on page 52.

The top mirror is presented schematically and on a photograph on figure 4.13.

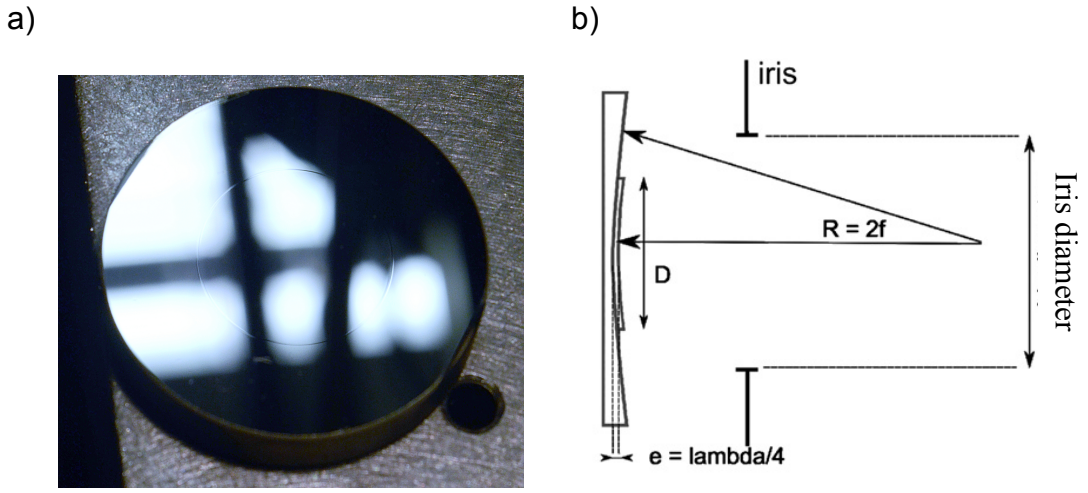

Figure 4.13 – a) Photograph and b) schematic side view of the TOP mirror with the corresponding iris.

The TOP mirror is a focusing silver mirror with a circular central part where the substrate is 200 nm thicker than in the outer part. The two parts have the same curvature. The mirror was fabricated by Fichou company.

The interference of the beam part reflected by the inner and the outer part of the mirror depends on multiple parameters:

- the dephasing between two parts of the reflected beam (central and annular part) controlled by the height difference between them
- the diameter of the central zone
- the incoming beam size on the TOP mirror
- the focal length of the TOP mirror
- the position of the gas jet compared to the focus

Under vacuum the beam size is efficiently controlled by a motorized iris as shown on figure 4.13. Closing the iris to smaller diameter than the central zone diameter cancels the shaping effects. On the other way, opening the iris is a precise approach to tune the spatial profile in a precise controlled and robust manner.

As there are a lot of parameters to control the spatial profile of the driving beam, we performed simulations to identify optimal conditions for HHG. The beam diffraction from the iris to the focus was performed using Hankel transform detailed in appendix A.

4.2.3 Spatial profile simulations

4.2.3.1 Dephasing effects

To demonstrate the dephasing effects on the beam near focus, we plot on figure 4.14 the spatial profile for several positions along the optical axis.

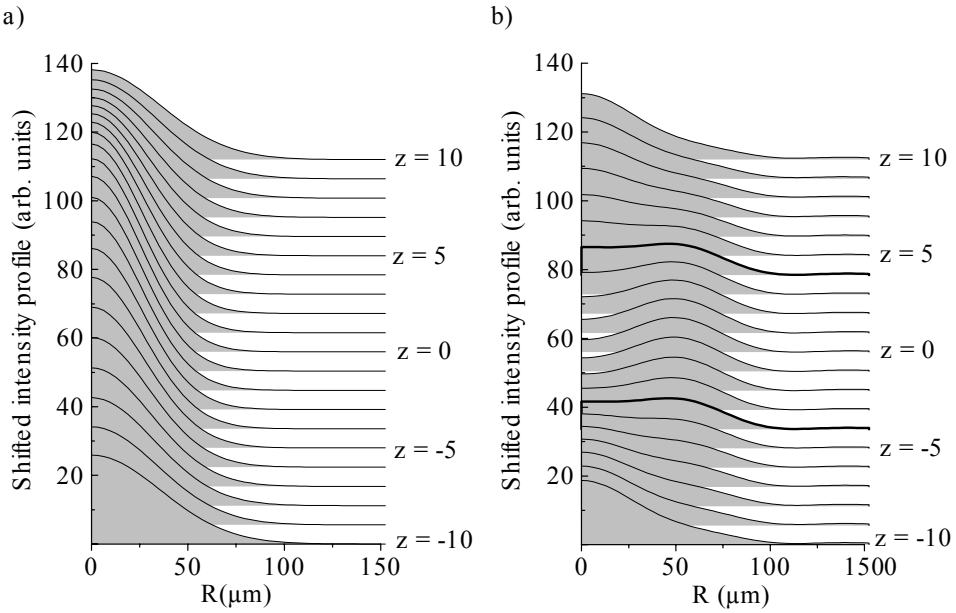

Figure 4.14 – Simulated driving pulse intensity spatial profiles for different position z along the optical axis and central TOP mirror part giving the dephasing of a) 0 and b) π. The laser central wavelength is 800 nm, the beam size radius was 10 mm (at I_{max}/e^2) and the mirror central zone diameter was 20 mm. The iris is wide open i.e. does not affect the beam. Adapted from [Constant 12].

The laser central wavelength is 800 nm, the input Gaussian beam size radius was 10 mm (at I_{max}/e^2) and the mirror central zone diameter was 20 mm. The corresponding energy reflected from the inner part of the TOP mirror represents 86 % of the total energy, the remaining 14% are reflected by the outer part. The iris is wide open i.e. does not affect the beam.

With zero dephasing the TOP mirror become a simple focusing mirror and the spatial profile in and around the focus is Gaussian for every longitudinal position with the highest peak intensity in the focus due to the smallest beam size of 60 μm FWHM.

With the dephasing equal to π the spatial profile overall evolution became different. For on-axis position far from focus where $|z| > 10$ mm the spatial profile is close to Gaussian but of lower intensity than in the case of zero dephasing. When approaching the focus the

central part of the beam lowers its intensity while there is a maximum emerging around 50 μm far from axis. In the focus the evolution finishes with an intensity minimum on axis.

The total maximum of intensity of the beam is located at the position of ± 25 mm (not shown in the graph). The beam becomes also very large close to the focus. For instance at $z = \pm 4$ mm the beam size is very wide reaching 154 μm and promoting a quasi flat-top spatial shape. Note using such technique one can never obtain a really sharp flat-top shape but a super-Gaussian one that has wide flat part. Therefore such shape would be called a «flat-top» in the following.

For the flat-top beam intensity does not exceed 10% of variation inside a beam size of 120 μm. To compare, the Gaussian beam keeps its intensity between 100% and 90% inside a diameter of 24 μm only. Also the peak intensity is approximately six times smaller in the case of flat-top beam than that of the Gaussian beam that is ideal when using too high intensity.

Note that the spatial profiles are symmetric with the center in the focus only for dephasing of zero or π. To illustrate the case of different dephasing we plot dephasing of 1.2π and 0.8π on figure 4.15.

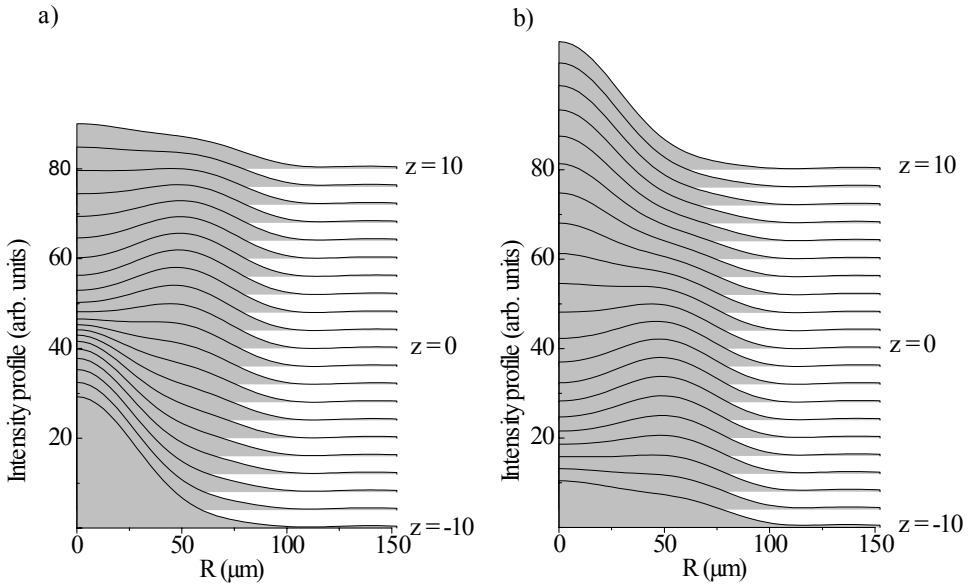

Figure 4.15 – Simulated driving pulse intensity spatial profiles for different position z along the optical axis and central TOP mirror part giving the dephasing of a) 1.2π and b) 0.8π. The laser central wavelength is 800 nm, the beam size radius was 10 mm (at I_{max}/e^2) and the mirror central zone diameter was 20 mm. The iris is wide open i.e. does not affect the beam. Adapted from [Constant 12].

We can see that the point of minimal intensity on axis (the widest beam) is now displaced by few millimeters. It is a consequence of the interference origin of the beam shaping. That means that changing the dephasing would change the position of the interference structures. Therefore, the exact dephasing near π does not practically affect the shape of the flat-top beam, it only shifts the flat-top profile along the axis.

We show that the dephasing is not the necessary parameter to be controlled in order to obtain a controllable flat-top beam (provided dephasing close to π).

In the light of such findings we have chosen the fixed dephasing of π for our experiments and used this dephasing afterward.

4.2.3.2 Central zone diameter effects

To find out the optimal central zone diameter we performed a study shown on figure 4.16.

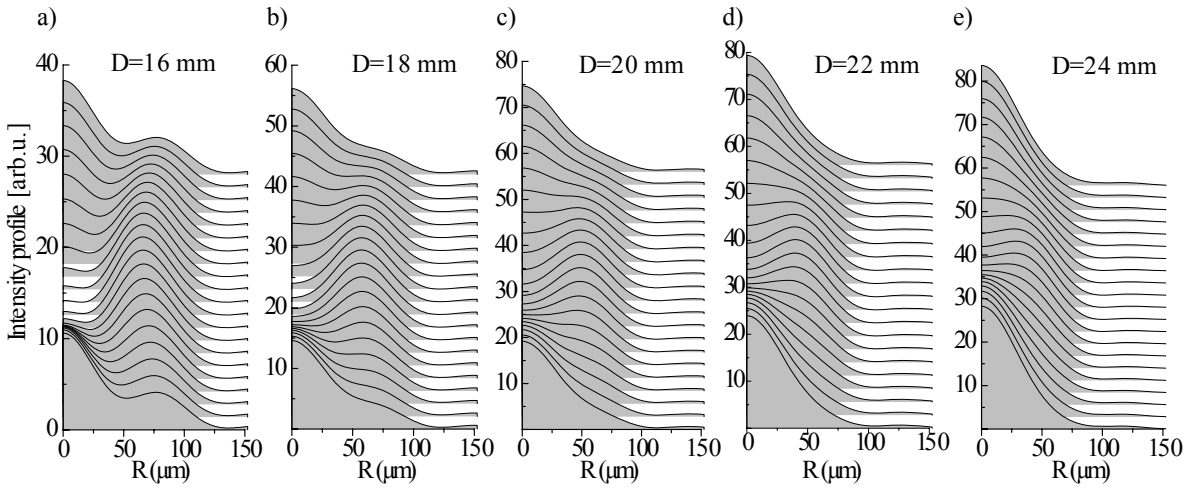

Figure 4.16 – Simulated driving pulse intensity spatial profiles near focus (each line stands for 1 mm) and different diameters D of central TOP mirror part of a) 16 mm, b) 18 mm, c) 20 mm, d) 22 mm and e) 24 mm. The laser central wavelength is 800 nm, the beam size radius was 10 mm (at I_{max}/e^2). The iris is wide open i.e. does not affect the beam. Adopted from [Constant 12].

The figure shows simulated driving pulse intensity spatial profiles near focus and different diameter of central TOP mirror part of a) 16 mm, b) 18 mm, c) 20 mm, d) 22 mm and e) 24 mm. The laser central wavelength is 800 nm, the Gaussian beam size radius was 10 mm (at I_{max}/e^2). The iris is wide open i.e. does not affect the beam.

We can see that the central zone diameter strongly affects the beam spatial profile near the focus. Even changing the central diameter of only few mm results in drastic shaping of the beam that can vary in the focus from doughnut (annular) shape for the diameters of 16 and 18 mm to narrow flat-top for diameter of 24 mm. Also for small diameters of 16 and 18 mm few mm far from focus the beam is very modulated.

The main issue of such strong dependence of the spatial profile on the axis position is the persistence of the flat-top beam. The 16 and 18 mm central zone diameters do not create a flat-top profile in the simulated range of parameters. With the diameter of 20 mm there are two places where the flat-top occurs but they do not hold for more than 1 mm along the optical axis. The situation becomes better with larger diameter and finally with 24 mm the flat-top holds for about 5 mm around the focus. Widening more the central

zone diameter would finally destroy the flat-top shape and the beam becomes Gaussian.

Experimentally one needs to maintain the flat-top shape over the whole generating medium thus from this point of view under discussed conditions the zone diameter of 24 mm is preferable. However in this case the iris was fully open and closing it would immediately result in transforming the flat-top profile back to Gaussian leaving no experimental control. As we will see later in this section, it is possible to maintain the flat-top over long distances even with the central zone diameter of 20 mm by closing a little the iris. This approach would keep a tuning parameter to further control of the beam. Therefore we have chosen an internal diameter of 20 mm.

4.2.3.3 Iris diameter influence

As we determined optimal dephasing of π and optimal central zone diameter of 20 mm we still have to determine the iris diameter for which the flat-top occurs in the focus. On figure 4.17 we present a study of the iris diameter influence.

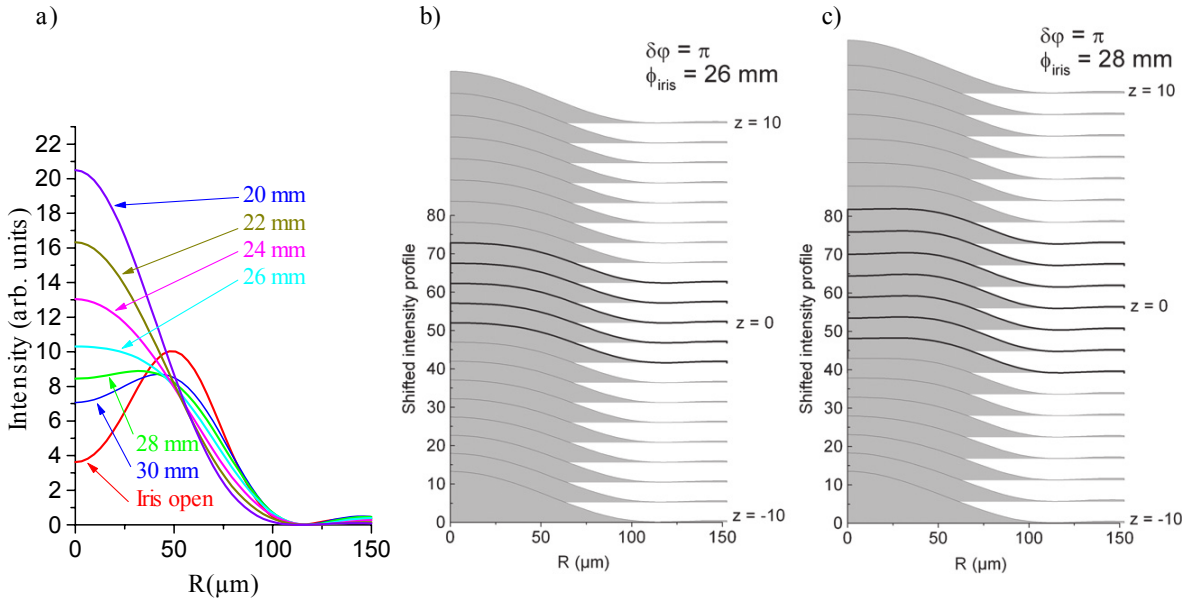

Figure 4.17 – Simulated driving pulse intensity spatial profiles for different position z along the optical axis and different diameter of iris. a) shows the influence of several iris diameters on the spatial profile in the focus. The spatial profiles along the optical axis are shown on for iris diameter of 26 mm on b) and for 28 mm on c). The laser central wavelength is 800 nm, the beam size radius was 10 mm (at I_{max}/e^2). Adopted from [Constant 12].

The figure 4.17 a) shows simulated driving pulse intensity spatial profiles in the focus for different diameters of iris. The spatial profile in the focus has a significant minimum on axis for iris diameter above 28 mm and the profile is Gaussian-like for iris diameter under 26 mm. Therefore the flat-top can be obtained in the focus only for iris diameters between 26 and 28 mm. The spatial profile evolution along the optical axis for such iris diameters

is shown on b) and c) respectively.

We can see that for 26 mm of iris diameter the flat-top is maintained for about 4 mm around the focus while for iris diameter of 28 mm the flat-top holds for up to 7 mm.

Under this conditions the beam size in the focus reaches 140 μm FWHM compared to 60 μm in the case of Gaussian beam.

Also note that such wide open iris does not cause significant power losses.

In conclusion, for an incident beam of a radius of 10 mm (at I_{max}/e^2), the optimal experimental conditions to obtain a robust flat-top beam profile is dephasing of π in the diameter of 20 mm. Then the flat-top can be effectively tuned with an iris before the TOP mirror.

4.2.3.4 Chromaticism investigation

To check if the TOP mirror is also suitable for short pulses of large spectral bandwidth, we studied the flat-top robustness against different wavelength on figure 4.18.

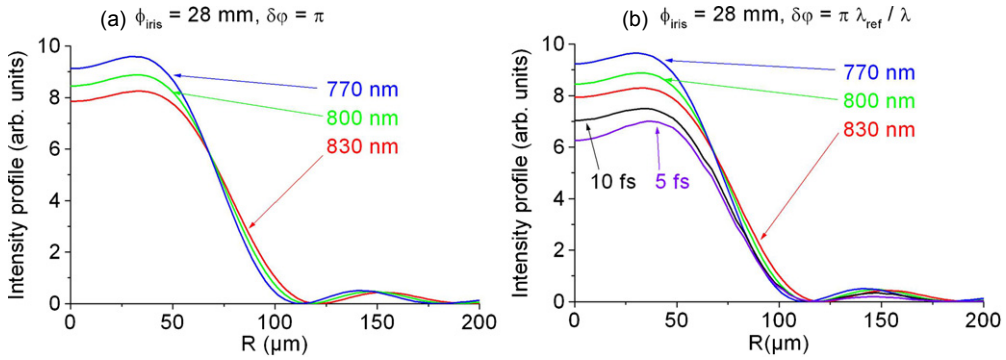

Figure 4.18 – (color) Simulated driving pulse intensity spatial profiles in the focus for different wavelength with a dephasing of a) π for all the wavelengths, b) 200 nm giving the dephasing of π only for 800 nm. The inner zone diameter is 20 mm, the iris diameter was 28 mm and the beam size radius was 10 mm (at I_{max}/e^2). Adopted from [Constant 12].

To check if a constant dephasing of π for every spectral component would change the results we simulate on figure 4.18 a) the flat-top profiles where the height of the step is different and wavelength dependent. One can see that the flat top profiles are also maintained.

On the figure 4.18 b), we can see the flat-top spatial profiles in the focus with a step of 200 nm giving the dephasing of π only for 800 nm. All three investigated wavelengths of 770, 800 and 830 nm show very similar flat-top profile in the focus so the technique can support also very short pulses. This case corresponds to our experimental conditions of fixed mirror with silver coating.

In conclusion we have chosen a TOP mirror with a central zone of 20 mm diameter providing a fixed dephasing of π for 800 nm. This mirror is well adapted for high energy

femtosecond pulses with a very short duration and even if the flat top is only super-Gaussian, the parameters are not critical and are compatible with experimental use.

4.2.4 Experimental results

Experimental spatial profile of the beam with the iris diameter of 27 mm is presented on figure 4.19.

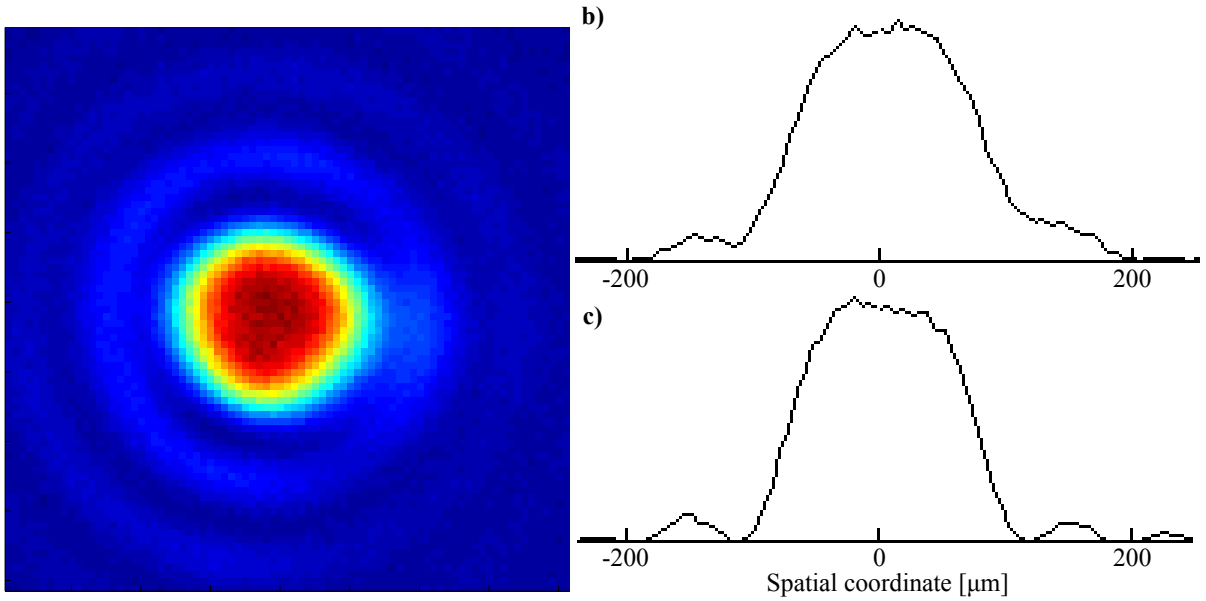

Figure 4.19 – (color) Experimental intensity spatial profile (a) with horizontal (b) and vertical (c) profile. The iris diameter was 27 mm and the profile was acquired in the focus.

The spatial profile is circular with a flat top shape.

With such a beam, we performed HHG and we present a study of iris influence on figure 4.20.

On the figure, we can see experimental single-shot spatially and spectrally resolved XUV profiles in the far field generated in neon jet for different iris diameters. The neon jet was placed 4 mm after the focus and the pulse energy was 54 mJ before the iris.

The figure presents harmonics in plateau. We can see efficient HHG with iris diameter of 15 mm (figure 4.20 a) where the intensity is already high enough to blue-shift and bend the harmonics. Opening the iris to 20 mm (figure b) drastically diminishes the overall signal because the beam size in the medium is smaller than with smaller iris diameter so is the number of emitters.

With the iris diameter of 24 mm the beam spatial profile in the jet broadens, increasing the number of emitters thus increasing the overall signal. At 27 mm of the iris diameter the flat-top beam profile generates collimated harmonics as shown on figure 4.20 d).

The result is in perfect agreement with experimental results published in [Dubrouil 11b].

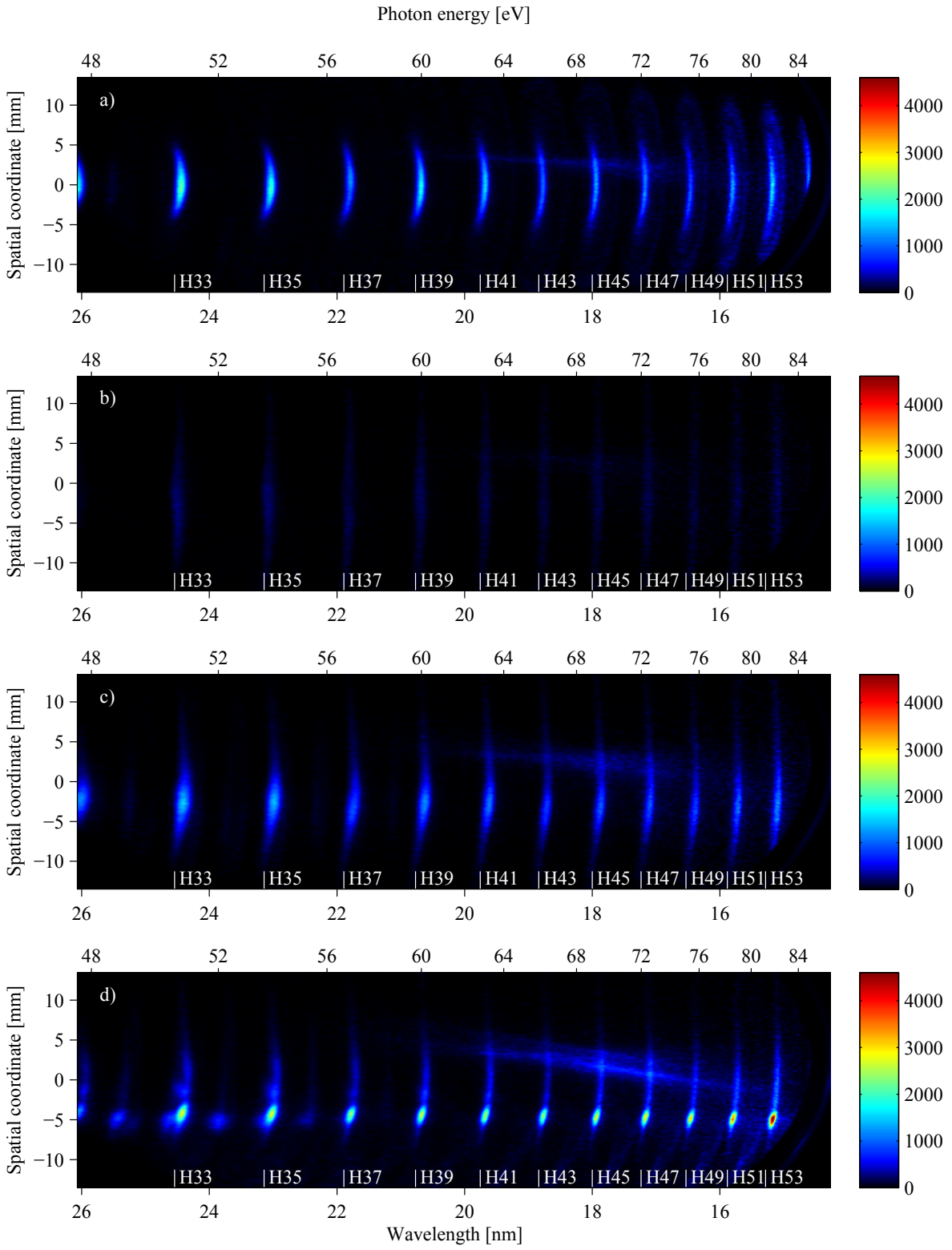

Figure 4.20 – (color) Experimental single-shot spatially and spectrally resolved XUV profiles in the far field generated in neon jet with iris diameter of a) 15 mm, b) 20 mm, c) 24 mm and d) 27 mm. The neon jet was placed 4 mm after the focus and the pulse energy was 54 mJ before the iris. On c) and d) we can also observe blue-shifted second order of diffraction of the XUV grating.

Note that the signal between the harmonics corresponds to blue-shifted harmonics diffracted in the second order of diffraction of the XUV grating in the XUV spectrometer.

4.2.4.1 XUV photon flux

To better compare the photon flux obtained for different diameters of iris we plot an integrated XUV signal as a function of the iris diameter on figure 4.21.

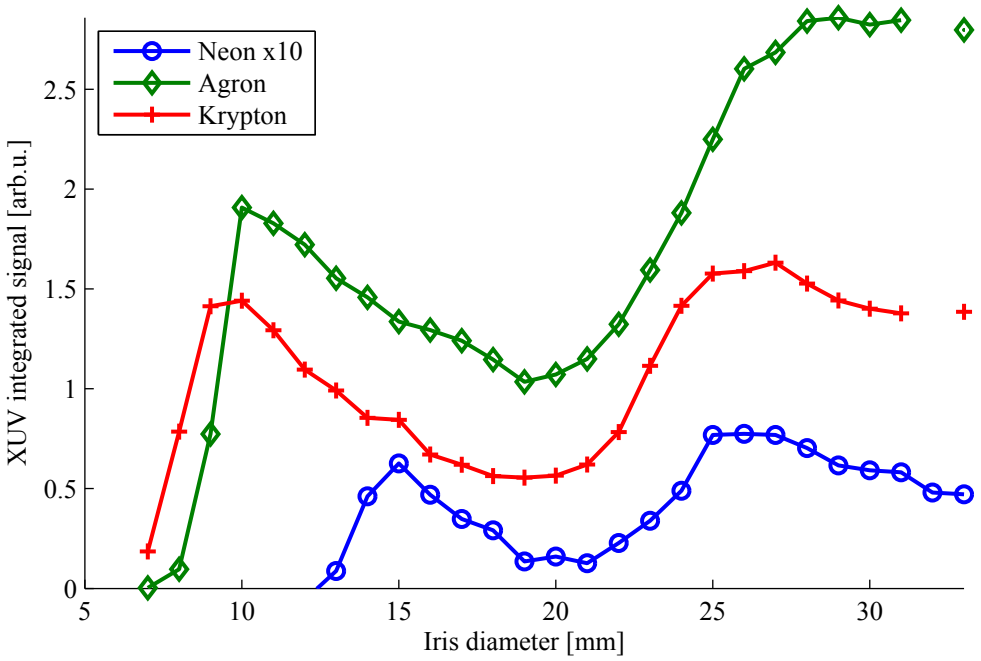

Figure 4.21 – (color) Experimental spatially and spectrally integrated XUV signal in the far field generated in neon (blue circles), argon (green diamonds) and krypton (red crosses) with the pulse energy of 54 mJ before the iris. For neon the integrated signal consists of harmonics 31 - 53, for argon and krypton the considered orders of harmonics are 21-29. The signal is integrated after the transmission of the entrance slit of the XUV spectrometer.

The figure shows experimental spatially and spectrally integrated XUV signal in the far field generated in neon, argon and krypton and the pulse energy was 60 mJ before the iris. For neon the integrated signal consists of harmonics 31 - 53; for argon and krypton the considered orders of harmonics are 21-29. The curve for neon corresponds to spatially and spectrally resolved spectra on figure 4.20.

In general independently on gas type the iris diameter has a very strong influence on the integrated signal and contains one minimum and two maxima.

4.2.4.1.1 First maximum The first maximum depends on gas type and is induced by the balance of the intensity and the beam size. When the iris is very closed and the intensity

is low, the harmonics are poorly generated. Consequently increasing intensity by opening iris increases the XUV signal. After reaching saturation intensity, further increasing the iris diameter decreases the beam size and thus the volume where the harmonics can be emitted while the density of HHG remains nearly the same (saturation). Therefore the XUV signal decreases.

As the ionization and saturation are dependent on ionization potential of the gas, the HHG occurs for each gas at specific intensity level. The same principle applies for saturation intensities. That is why the first detectable XUV signal occurs with the iris diameter of about 13 mm for neon, 7 mm for argon and even before for krypton.

The XUV signal maximum also varies on gas and is reached for larger iris diameter for gases with higher ionization potential. The first maximum occurs for iris diameter of 15 mm for neon, 10 mm for argon and 9 mm for krypton.

4.2.4.1.2 Second maximum While increasing the intensity in the gas jet via iris diameter lead to minimum of the integrated XUV signal at about 20 mm equally for each of investigated gas. Then the TOP mirror starts to influence the beam spatial profile by widening it and reducing the peak intensity.

The second maximum of the XUV photon flux is then placed for iris diameter of 25-27 mm for neon, 28-31 mm for argon and 25-27 mm for krypton. As the second maximum is found for similar iris diameters for each gas one can conclude that this maximum is mainly controlled by the spatial shaping effects on the beam rather than by other possible phenomena (e.g. microscopic effects).

The experimental value of the iris diameter of the second maximum corresponds to the value found theoretically.

4.2.4.1.3 Maxima photon flux comparison From the figure 4.21 we can clearly see that the photon flux of optimized HHG with Gaussian beam (first maximum) is nearly the same as the photon flux of optimized HHG generated with flat-top beam profile. In the case of argon the flat-top generates even approximately one quarter more.

This is a very important finding that the HHG with flat-top driving beam profile produces more or comparable XUV photons than the common HHG using a Gaussian beam.

Moreover an examination of the figure 4.20 shows that the generating intensity in the gas medium while using flat-top spatial profile is slightly higher than with optimized Gaussian. The peak intensity can be estimated as a cutoff intensity comparing the highest generated harmonic in both cases.

Thanks to the second order of the grating we observe a harmonic 63 generated with Gaussian beam with iris diameter of 15 mm (figure 4.20 a). While using flat-top beam

profile with iris diameter of 27 we observe harmonics of the order up to 75. That corresponds to peak intensity between 3.86 and 3.94 $\times$ 10^{14} W/cm^2 for Gaussian beam and between 4.81 and 4.88 $\times$ 10^{14} W/cm^2 for flat top. Note that the barrier suppression intensity is 8.65 $\times$ 10^{14} W/cm^2 for neon (see table 2.1 on page 28).

Two direct conclusions can be derived:

1. The driving pulse energy in the medium is approximately 1.36 times higher in the case of flat-top iris open to 27 mm compare to 15 mm of iris diameter for Gaussian harmonics. As the resulting photon flux is comparable for both the Gaussian and flat-top driven HHG we can conclude that the HHG efficiency is lower with the flat-top driving beam.

2. With the same incident energy on the iris the flat-top driving beam shape allows us generating high harmonics at higher intensities resulting in higher order of harmonics.

One should also note that with the same level of integrated signal, the harmonics are much less divergent when generated with flat-top driving beam than Gaussian one (see figure 4.20). Therefore the XUV brightness is higher when generated with flat-top.

4.2.5 Perspectives for isolated attosecond pulse generation

We simulated the HHG with 10 fs pulses and the flat-top driving beam profile in the focus. It is illustrated on figure 4.22.

The figure 4.22 shows the spatially resolved temporal profile of the ionization degree in the generating medium. The ionization rises very quickly with the increasing intensity on axis and about 0.1 mm over the axis (flat top effect).

To see quantitatively the ionization dynamics we plot the on-axis ionization temporal profile on figure 4.23.

One can see that the ionization increases from 10% to 90% during only 2 optical cycles and the complete ionization is reached even before the driving pulse intensity maximum.

We have discussed the possibility of a generation of isolated attosecond pulses. On figure 4.24 we show the XUV spatio-temporal profile in the near field.

We can see few attosecond pulses whose temporal profile depends on time. However the maximum of the signal is on axis. To investigate quantitatively the XUV emission we plot on figure 4.25 a) integrated signal (1 mm over the axis). This could correspond to experimental spatial filtering in the far field [Gaarde 06].

On figure 4.25 a) we can see that there are only few attosecond pulses generated with the flattop driving beam. Only two pulses are more than twice more intense than the others. The brightest pulse (generated at -7.2 fs) duration is 220 as (FWHM). The most

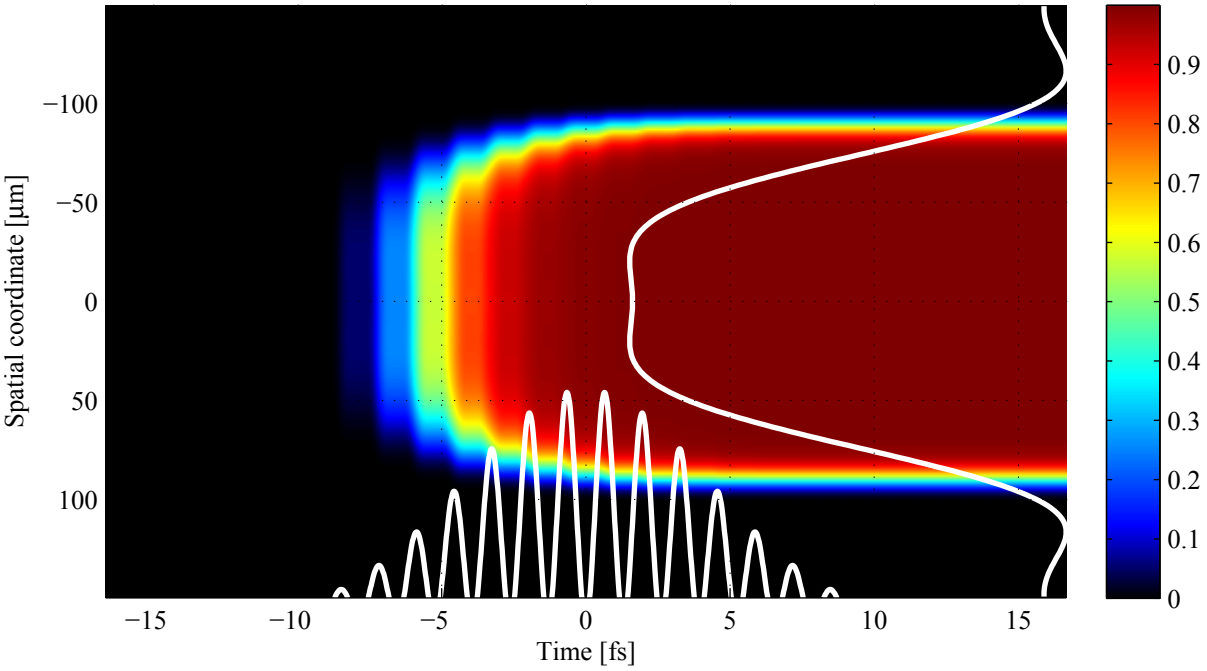

Figure 4.22 – (color) Simulated temporally and spatially resolved profile of the ionization degree in the generating medium. 0 stands for 0% and 1 for 100% of atoms ionized. The white Gaussian profiles give an idea about temporal and spatial profile of the infrared pulse intensity. The HHG was numerically performed in krypton in the focus with the iris diameter of 27 mm and an peak intensity of 1.7×10^{15} W/cm^2.

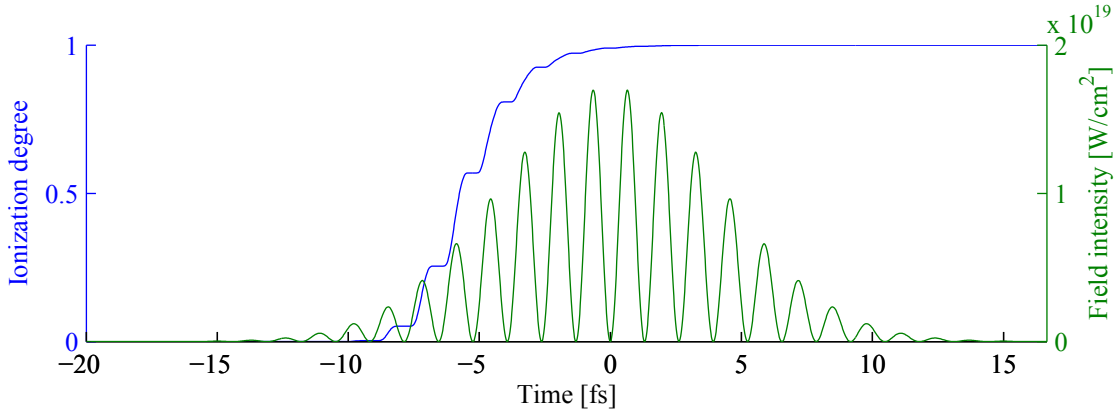

Figure 4.23 – Simulated temporal profile of the ionization degree in the generating medium on axis. 0 stands for 0% and 1 for 100% of atoms ionized. The ionization was numerically performed in krypton in the focus with the iris diameter of 27 mm and a peak intensity of 1.7×10^{15} W/cm^2.

of the XUV signal is generated when the ionization is low and there is practically no HHG after -1.7 fs.

A single attosecond pulse would be generated when considering longer medium as discussed in [Strelkov 09, Strelkov 08].

On figure 4.25 b) we show reference case of the generation with Gaussian beam. We obtain 4 pulses that are brighter than 50% of the maximum and there are many other

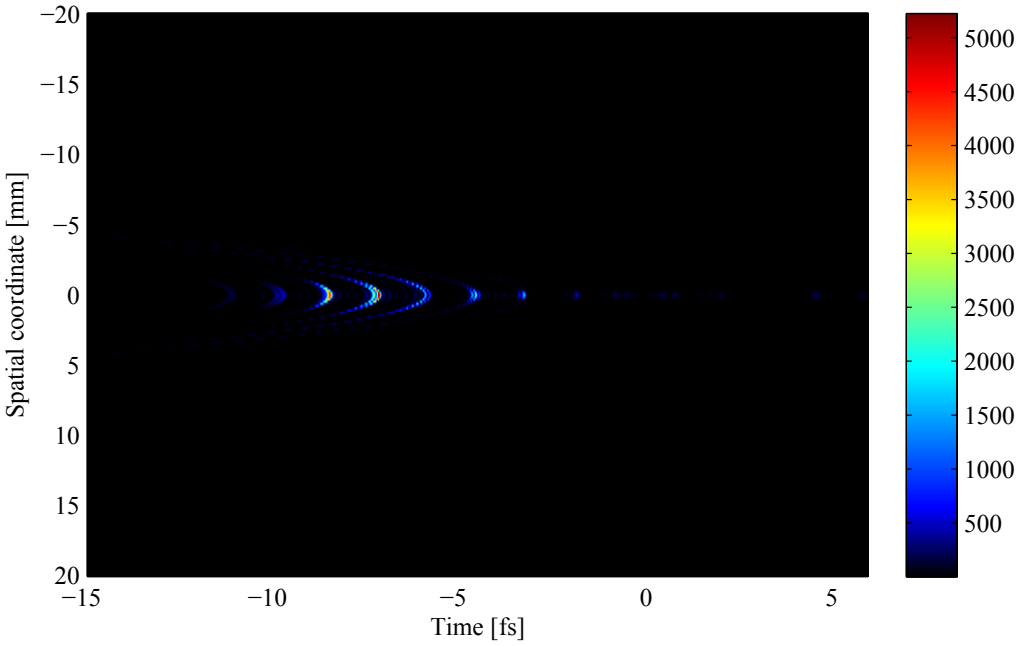

Figure 4.24 – (color) Simulated temporally and spatially resolved profile of attosecond pulses in the far field. The HHG was numerically performed in krypton in the focus with the iris diameter of 27 mm and a peak intensity of 1.7×10^{15} W/cm^2. We considered harmonics 11 - 21.

pulses of lower intensity. Moreover the most intense attosecond pulse is about 10 times weaker than the attosecond pulse generated using the flat-top driving beam.

4.2.6 Conclusion on flat-top driving beam shaping

The spatial shaping technique via TOP mirror works well with high energy short femtosecond pulses. The technique is robust, achromatic and the main control parameter is an iris diameter that can be controlled under vacuum. Experimentally we demonstrated much lower divergence of harmonics using the flat-top beam.

The flat-top driving beam shaping could be coupled with deformable mirror.

Using simple simulations the flat-top driving beam generates 2 attosecond pulses but

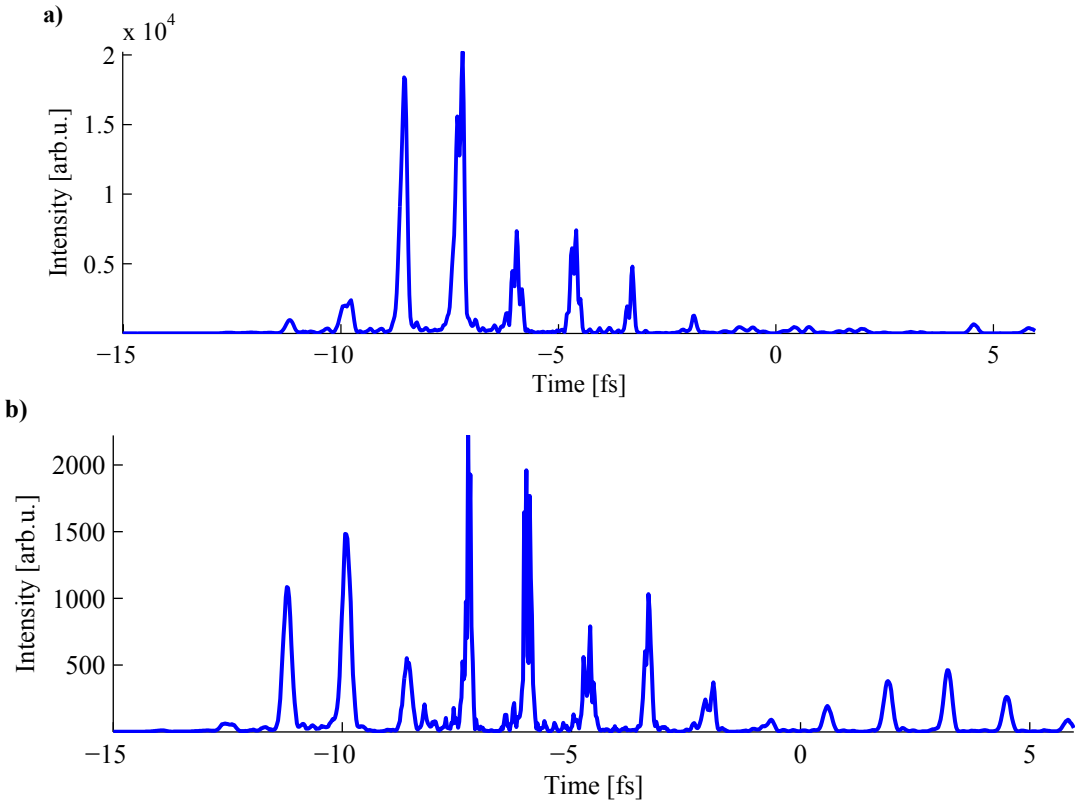

Figure 4.25 – Simulated temporal profile of attosecond pulses in the far field. The signal was integrated over 1 mm over the axis. The HHG was numerically performed in krypton in the focus with the iris diameter of 27 mm and an peak intensity of 1.7×10^{15} W/cm^2. We considered harmonics 11 - 21. The phase difference induced by the TOP mirror is a) π and b) 0 (no step on the mirror - HHG with Gaussian beam)

considering the propagation in the medium only one pulse would be generated.

Chapter 5

Infrared source development: High energy TW post-compression

In previous chapters the high harmonic generation (HHG) with high energy femtosecond pulses was investigated in detail. We have shown that using TW-level 50 fs pulses for HHG results in a lot of unprecedented structures in XUV spectra rising from complex spatio-temporal dependance of the harmonic dipole. We investigated different generating geometries as gas jet, cell and capillary (more in chapter 3) and driving beam spatial shaping via deformable mirror and a phase mask (chapter 4).

In the next chapter, we will focus on HHG with much shorter pulses. We will use 10 fs 10 mJ pulses as they would reduce significantly the XUV generating time and under some conditions may even finish only with one, i.e., single attosecond pulse as already demonstrated via generalized double optical gating (GDOG) technique (28 fs is the recent record for single attosecond pulse generation [Feng 09]), which however is not suitable for high energy pulses or proposed using spatial shaping [Strelkov 09] that is compatible with high energy pulses.

However, such a laser source delivering TW level 10 fs pulses is not common and we devote this chapter to its development.

5.1 State-of-the-art

There are two families of few-cycle[1] TW laser sources: optical parametric chirped-pulse amplification (OPCPA) based laser chains and post-compression techniques.

[1]Often in literature "few-cycle pulses" denotes 2 optical cycles (giving 5.4 fs pulses centered at 800 nm). In this work we use this term to denote "very short" femtosecond pulses meaning the pulse duration up to 10 fs corresponding to slightly less than 4 cycles.

Optical parametric chirped-pulse amplification arises from the fusion of chirped pulse amplification (CPA) [Strickland 85] and optical parametric amplifier (OPA) [Baumgartner 79]. A signal pulse is stretched to match the pump pulse duration (typically few picoseconds) and then amplified in a suitable nonlinear crystal. Compared to the CPA based on laser medium the OPCPA typically promotes much higher single pass gain, much lower thermal load on the crystal and high contrast because of weaker amplified spontaneous emission (ASE). The main drawback is a poor beam spatial profile and phase, as any imperfection of the pump beam is directly transferred to the signal beam. OPCPA laser chains can generate very short pulses with extremely high energy per pulse (16 TW in 10 fs [Tavella 07]) but because of poor spatial characteristics only one high energy OPCPA chain was used for HHG to date [Heissler 12].

Conventional post-compression technique can be installed at the end of any conventional (commercial) CPA laser chain (while OPCPA *is* a laser chain) of reasonable pulse energy level. The spectrum of femtosecond pulse is broadened in a gas using Kerr effect induced self phase-modulation (SPM) and using chirped mirrors. The pulse is then compressed to few times lower duration than before post-compression. Moreover, using a gas filled waveguide [Nisoli 96, Tempea 98] results in a quasi-perfect spatial phase and profile which makes such a nonlinear process as the post-compression technique a perfect candidate for HHG. Other schemes were also presented e.g. filamentation [Hauri 05] but they are also based on the Kerr effect induced SPM. As the nonlinear refraction index is small (Kerr effect is weak) for gases, high pressure (few bars) and long medium (few meters) are necessary for efficient spectral broadening. These are the major disadvantages of the Kerr effect based post-compression technique. The necessary medium length makes the technique incompatible with some experimental rooms and the high gas pressure implies also low critical power P_{crit} expressed as

$$P_{crit} = \frac{\lambda^2}{2\pi n n_2(P)} \tag{5.1}$$

where $n_2(P)$ denotes pressure dependent nonlinear index of the gas and critical power P_{crit} stands for power level at which the beam collapses due to the self-focusing[2]. For $\lambda = 810\,\text{nm}$ and helium ($n_2(P) = 3.48 \times 10^{-21} \frac{\text{cm}^2}{\text{W}} \cdot P\,[\text{Bar}]$) the equation 5.1 simplifies

[2]Note that the critical power does not depend on the beam size. This is because of the balance between the strength of the Kerr effect that decreases with beam diameter and a beam sensitivity to lensing that increases with beam diameter canceling each other.

to

$$P_{crit} = \frac{3 \times 10^{11}}{P\,[\text{bar}]}$$

giving $P_{crit} = 0.3\,\text{TW}$ for 1 bar of helium corresponding, e.g. for 3 mJ 10 fs pulses. Therefore maximum output power allowed with conventional (based on Kerr effect) post-compression techniques is limited by the self-focusing making the maximum output pulse energy also limited to few mJ [Tempea 98]. Optimizing parameters led to the record generation of 5 mJ in 5 fs (1 TW) using a 2.2 m long capillary filled with 1.8 bar of helium [Bohman 10]. One should also consider that this technique requires 4.5 m focal length mirror for injection and a dispersion line of -540 fs^2.

The conventional post-compression technique based on Kerr effect is therefore not compatible with our laser delivering 130 mJ in 50 fs. Our goal is to develop a new post-compression technique compatible with multi-TW CPA laser chains and delivering stable 10 mJ 10 fs pulses in reliable way.

5.2 Principe of the high energy post-compression

We developed a post-compression technique that is based on ionization-induced self-phase-modulation in a gas filled capillary [Fourcade-Dutin 10]. As the plasma is highly dispersive, the refractive index modulation due to ionization is larger than Kerr effect nonlinear index contribution $n_2 I$. So the process of ionization-induced spectral broadening requires only few millibars of gas pressure and few tens of centimeters of propagation are needed to obtain desired spectral bandwidth (compare to few bars and few meters needed for Kerr effect based techniques).

5.2.1 Theory of the ionization-induced spectral broadening

The ionization-induced spectral broadening originates from rapid[3] ionization dynamics of gas. As more gas atoms get ionized during the pulse propagation, the temporal phase of the pulse at the output of the capillary becomes time dependent. In 1D approach[4] it can

[3] In this case "rapid" means that helium gets ionized from 0 to $\approx$ 100 % during a time interval that is shorter or comparable to the original femtosecond pulse duration.

[4] Here we present 1D approach that is sufficient to explain the principle and to explore qualitatively major characteristics of the ionization post-compression. For complex evaluation and understanding of underlying physics one need to perform a 3D simulation that includes also propagation in the medium. Such simulations were already performed and results published in [Auguste 12, Auguste 13].

be expressed as

$$\varphi(t) = \varphi_0(t) + \frac{2\pi}{\lambda_0}\int_0^L n(t,z)\,\mathrm{d}z \tag{5.2}$$

where L, n and φ_0 stands for the length of the medium, refractive index of the plasma/gas and input pulse phase. Note that the integral $\int_0^L n(t,z)\,\mathrm{d}z$ represents time-dependent optical medium length.

The instantaneous angular frequency $\omega(t)$ can be found by deriving $\varphi(t)$ (5.2) leading to

$$\omega(t) = \frac{d\varphi(t)}{dt} = \omega_0 + \frac{\omega_0}{c}\int_0^L \frac{dn(t,z)}{dt}\mathrm{d}z \tag{5.3}$$

where

$$n(t,z) = \sqrt{1 - \frac{n_e(t,z)}{n_c}} \tag{5.4}$$

$n_e(t,z)$ denoting time and space dependent free-electron density and n_c the critical electron density[5] ($n_c = 1.7 \times 10^{21}\ \mathrm{e^-/cm^3}$ at 800 nm). Note that the refraction index of neutral gas is considered to be 1 which derives directly from equation 5.4 putting $n_e = 0$.

To estimate the experimental parameter values, we rewrite the equation 5.3 to

$$\Delta\omega \cong \frac{\omega_0}{c}\frac{\Delta n L}{T} \tag{5.5}$$

that shows the maximal blue shift that can be acquired while propagating in the medium of length L that changes the refraction index of Δn during the time T.

We can make an estimate of medium length L necessary for the blue shift of e.g. $\frac{\Delta\omega}{\omega_0} = \frac{1}{5}$ and $T = \frac{1}{5}\tau$ where τ is the pulse duration. The equation 5.5 will then read

$$25\Delta n L = c\tau \tag{5.6}$$

with the unknown parameter of refractive index change Δn. Recalling the equation 5.4 developed into Taylor series[6]

$$n = \sqrt{1 - \frac{n_e}{n_c}} \backsimeq 1 - \frac{1}{2}\frac{n_e}{n_c} - \frac{1}{8}\left(\frac{n_e}{n_c}\right)^2 - \frac{1}{16}\left(\frac{n_e}{n_c}\right)^3 - \frac{1}{128}\left(\frac{n_e}{n_c}\right)^4 - \dots$$

[5] Critical electron density (also critical plasma density) is a fundamental characteristics of laser-matter interaction. Defined as $n_c = \frac{m\varepsilon_0\omega^2}{e^2}$ where m, ε_0, ω and e stands for electron mass, vacuum permittivity, laser angular frequency and electron charge, it is the maximal electron density of the plasma in which a laser of the angular frequency ω can propagate. [Mulser 10]

[6] As we look for maximal blue shift the refraction index is no more time and space dependent so $n(t,z)$ will read as n.

will lead after neglection of small terms to

$$n = 1 - \frac{1}{2}\frac{n_e}{n_c}$$

$$\Delta n = 1 - n = \frac{n_e}{2n_c}$$

where the electron density $n_e(t, z)$ was considered to be much smaller than the critical density n_c.

In order to estimate the value of $\frac{n_e}{2n_c}$ it will be comfortable to find an equivalent critical pressure P_c of the gas whose complete ionization will result in electron density of the same value as n_c. Than we can use the state equation for ideal gases

$$PV = n_{as}RT \tag{5.7}$$

where the variables stand from left to right for pressure, volume, amount of substance, universal gas constant and thermodynamic temperature. The amount of substance n_{as} can be expressed as $\frac{Vn_c}{N_A}$ where N_A is the Avogadro's constant. The ideal gas constant equals to Avogadro's constant multiplied by Boltzmann constant

$$R = N_A k_B$$

so the state equation 5.7 gives the critical pressure P_c (for 800 nm) of

$$P_c = n_c k_B T = 4.14 \times 10^{-21} n_c = 7.04\,\text{MPa} = 70.4\,\text{bar} \tag{5.8}$$

So the equation 5.6 gives

$$0.18 n_e L = c\tau$$

where n_e is now alternatively expressed in bars (in normal conditions). Taking 55 fs of the pulse duration finishes the equation to the form of

$$n_e L = 9.2 \times 10^{-4}\,\text{bar} \cdot \text{m}$$

One can easily calculate that a length of 9.2 mm will be sufficient while using 10 mbar of gas that is 3 orders of magnitude lower than the critical pressure P_c.

This result depends on multiple parameters that can be found in equations 5.3 and 5.4 that show the general spectral broadening caused by blue-shifting the instantaneous frequency (the second term in equation 5.3). The blue shift can be theoretically controlled via several parameters:

Laser wavelength (angular frequency ω_0) Shorter wavelength leads to more blue shift. In our case the laser wavelength cannot be tuned so we cannot control the blue shift via this parameter.

Medium length L The longer the medium the more the blue shift and thus also the wider the output spectrum. We have chosen 40 cm that was enough to reach our goal of 10 mJ 10 fs.

Free-electron density n_e is the only parameter that is tuned in this work. Intuitively it is dependent on

Gas type We used exclusively helium for its high ionization potential of 24,6 eV (the highest among atomic elements) that is necessary for high energy laser pulses. The technique was also functional with neon and argon giving little worse results than the case of helium [Fourcade-Dutin 10, Auguste 13].

Gas pressure The helium pressure is an easy way to tune the free-electron density and thus the spectral broadening simply by controlling a valve. This can be used since the required pressure is small compared to critical pressure $P \ll P_c$.

Laser intensity and pulse energy in the capillary The laser intensity has to be high enough to ionize an atom via tunneling and the pulse energy has to be high enough to provide enough photons to ionize enough of helium atoms in the capillary. Those two parameters are coupled as the input pulse duration is fixed close to the Fourier limit and cannot be easily tuned without changing too much the pulse spectral phase.

One should note that those parameters are often coupled and this coupling could be nonlinear and even not monotonous so it is not straightforward to increase the spectral broadening with tuning only one parameter. Nevertheless these parameters can be used to optimize the characteristic of the post-compressed pulses.

5.2.2 Theory of broadened spectra recompressibility

Post-compression technique consists of two parts: the spectral broadening and a recompression. In previous section we showed that ionization induced spectral broadening of femtosecond pulses is possible. Pulses at the output of the capillary are therefore spectrally larger than before the capillary and of the same duration approximately because a self-phase-modulation does not change the temporal profile, only the phase. With capillary inner diameter of 420 μm and the low pressure used here, the capillary dispersion and neutral gas dispersion can be neglected. Therefore the output pulses are chirped. The

recompressibility of the pulses to low duration will be investigated in detail in the next section.

As one plots the helium ionization dynamics and the resulting spectral broadening (figure 5.1), it is clear that the instantaneous frequency blue shift is followed by a return to the original frequency.

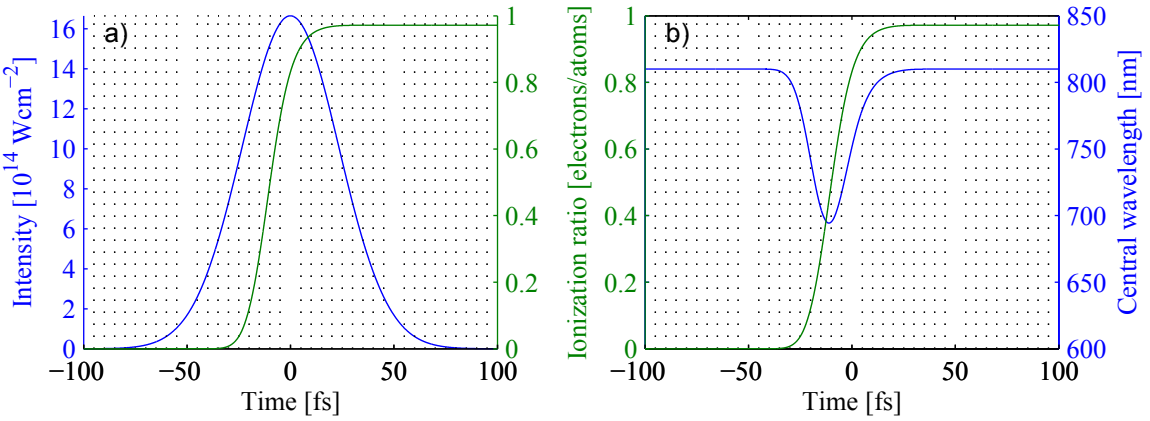

Figure 5.1 – Calculated a) Ionization dynamics of helium and b) resulting blue shift of the instantaneous wavelength. The code is 1D ADK for propagation of 55 fs pulses in 8 mbar of helium for 2 cm. The intensity is 1.67×10^{15} W/cm².

Note that we have chosen 2 cm of pulse propagation for the simulation although the real capillary is 40 cm long. The ADK 1D code quantitatively extremely overestimates the amount of blue shift. Moreover, the central wavelength of 810 nm and high intensity of 1.67×10^{15} W/cm² present conditions close to the validity limit of ADK. In addition, the high ionization level is not achieved everywhere in the capillary. Therefore the 2 cm of the capillary length is the effective length of the process. A complete 3D model with modal structure and capillary guiding is necessary to retrieve the results with more realistic parameters. Complex 3D model of intensity and plasma distribution in the capillary can be found in [Auguste 12].

The frequency return is necessary as the frequency has to stay unchanged when the ionizing pulse is over. This is a simple result of the law of energy conservation.

Fourier-transforming the original Gaussian pulse in the temporal domain

$$E(t) = E_0 e^{-2\ln 2 \frac{t^2}{\tau^2}} e^{i\varphi(t)}$$

where τ denotes the pulse length (FWHM) and the nonlinear phase $\varphi(t)$ is described by equation 5.2 and discussed in previous section. This will finally lead to the infrared intensity frequency profile

$$I(\omega) = |\mathcal{F}(E(t))|^2$$

that is shown on figure 5.2.

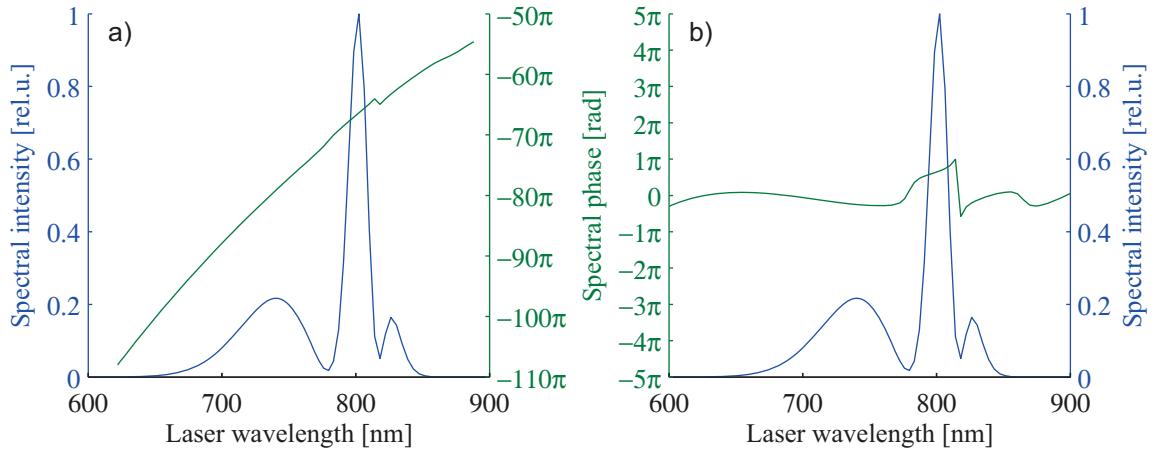

Figure 5.2 – Simulated spectra of post-compressed pulses. (a) shows the total accumulated phase while (b) shows a residual phase that stays after quadratic phase subtraction. The conditions are the same as in 5.1.

The figure shows largely broadened spectral profile and a total phase (fig. 5.2 a) and a residual phase after subtraction of quadratic phase fit (fig. 5.2 b). This is the first approximation of chirp compensation in practice. In other words, the figure b shows the best phase that can be obtained considering common chirp compensation techniques (chirped mirrors, prisms, ...).

We can also see intensity modulations and phase jumps that are due to 2 instants of generation of the same blue shift (the same wavelength).

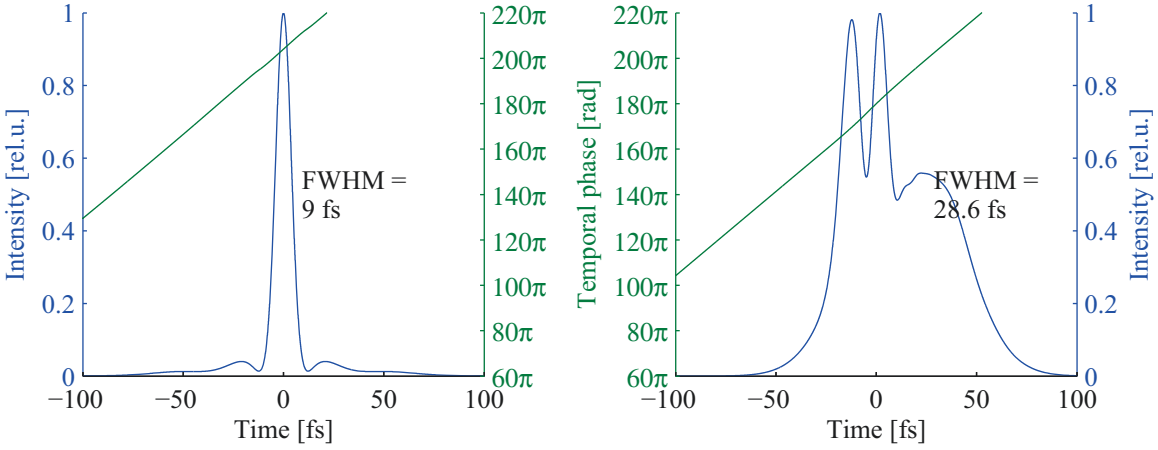

Figure 5.3 – Simulated temporal profile of post-compressed pulses. The conditions are the same as in previous two figures. (a) and (b) show the Fourier-transformed spectrum of fig. 5.2 (a) and (b) without any residual phase (a) and with residual phase.

The spectrum is large and can support sub 10 fs pulses as shown on figure 5.3 (a) assuming completely flat (or linear) phase. The temporal profile resulting from the spectrum

with phase jumps as shown on fig. 5.2 (b) is much longer (fig. 5.3 (b). Moreover there is a significant pulse splitting and pedestal that is not taken into account by considering only the FWHM value.

Such phase jumps are inevitable in the simple simulation. Also the return to original frequency create a frequency chirp with an opposite sign compared to the blue shift and experimentally it is not possible to compensate both chirps. When compensating average value of the chirp one can not get an ultrashort profile.

On one hand the fact is that the phase jumps are inevitable. On the other hand we can give much more importance (weight) to the blue shift by suppressing the energy in the time interval where the return to original frequency occurs. The phase jumps will be preserved, however their amplitude will be strongly reduced. Energy in that part of the pulse can be controlled e.g. via nonlinear processes such as losses.

The intensity under the part of the pulse where the frequency returns to origin is reduced naturally via refraction losses: as the gas is first ionized on axis a plasma density gradient is created over the capillary diameter. This plasma density gradient projects directly to refraction index gradient via equation 5.4 on page 184. As the refraction index is smaller on axis than in the outer part the divergent lens is instantly created. The lens directs the light to the core wall of the capillary and part of energy is transmitted to the glass cladding and therefore lost. Similar losses occur also by coupling in higher modes that are afterward filtered naturally because of their higher divergence.

To take this effect into account we considered the transmission as a function of the degree of ionization giving $T = 1$ for neutral gas and $T = 0$ for complete ionization. The resulting spectra simulation with dynamic transmission implemented are presented on figure 5.4.

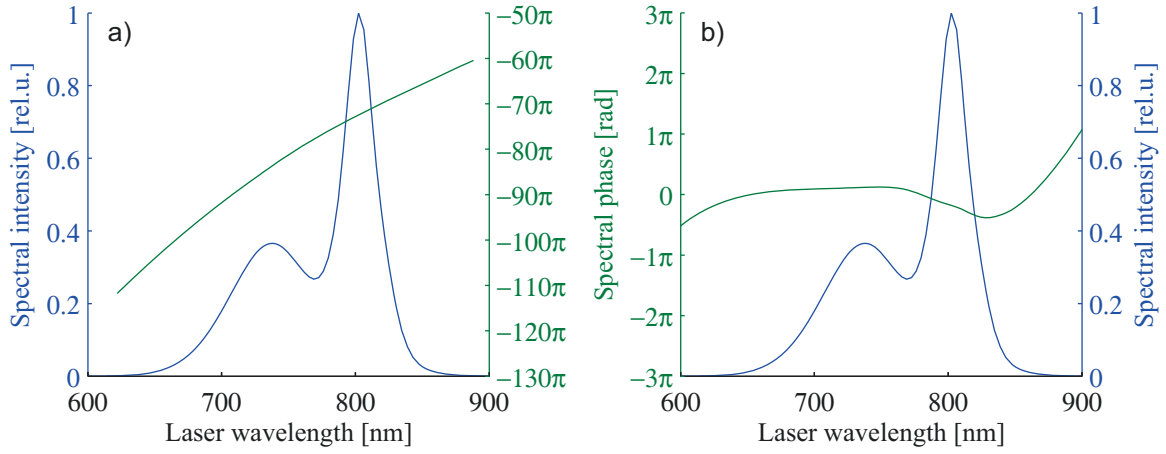

Figure 5.4 – Simulated spectra of post-compressed pulses with dynamic capillary transmission. (a) shows the total accumulated phase while (b) shows a residual phase that stays after quadratic phase subtraction. The conditions are the same as for previous figures.

We observe that the spectra are more smooth, regular and the phase remaining after quadratic compensation is much smoother than in the case before (fig. 5.2). Important observation is that the bandwidth is not reduced.

The corresponding temporal profiles (fig. 5.5) show similar duration considering flat phase as on fig. 5.3 (a). Much shorter pulses with quadratic chirp compensation with a significantly reduced pedestal compared to fig. 5.3 (b). Despite the asymmetry, we obtain a pulse that is only 15% above the Fourier limit.

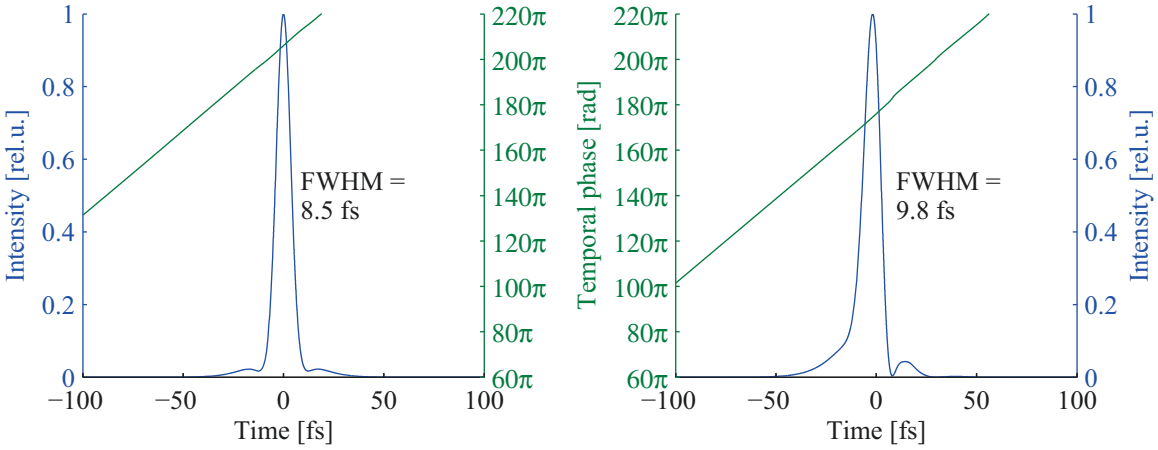

Figure 5.5 – Simulated temporal profile of post-compressed pulses with dynamic capillary transmission corresponding to spectra on 5.4 (a) Fourier-limited and (b) with residual nonlinear nonquadratic phase.

5.2.3 Parameters dependence

We have seen that theoretical simulations showed significant spectral broadening and resulting pulse duration reduction were from original 55 fs to less than 10 fs, which can be achieved by proper compensation of quadratic phase (linear chirp). We used simple simulations based on ADK and showed that both microscopic and macroscopic issues should be taken into account when explaining the post-compression phenomenon. We have seen that with pulses of 55 fs, intensity 1.67×10^{15} W/cm², helium pressure 8 mbar and 2 cm of the propagation in the capillary, we can obtain a spectral width larger than 100 nm and pulse duration less than 10 fs and close to Fourier limit.

To see the model parameters sensibility we considered some other values of intensity and helium pressure. Note that in our approach, changing the pressure is equivalent to changing the propagation length we therefore neglect the impact of this length.

Figures 5.6, 5.7, 5.8 and 5.9 show the resulting ionization dynamics, blue shift, spectrum with compensated phase and temporal profile for few different values of intensity and pressure around the values used for former detailed simulations (section 5.2.2 on page 186).

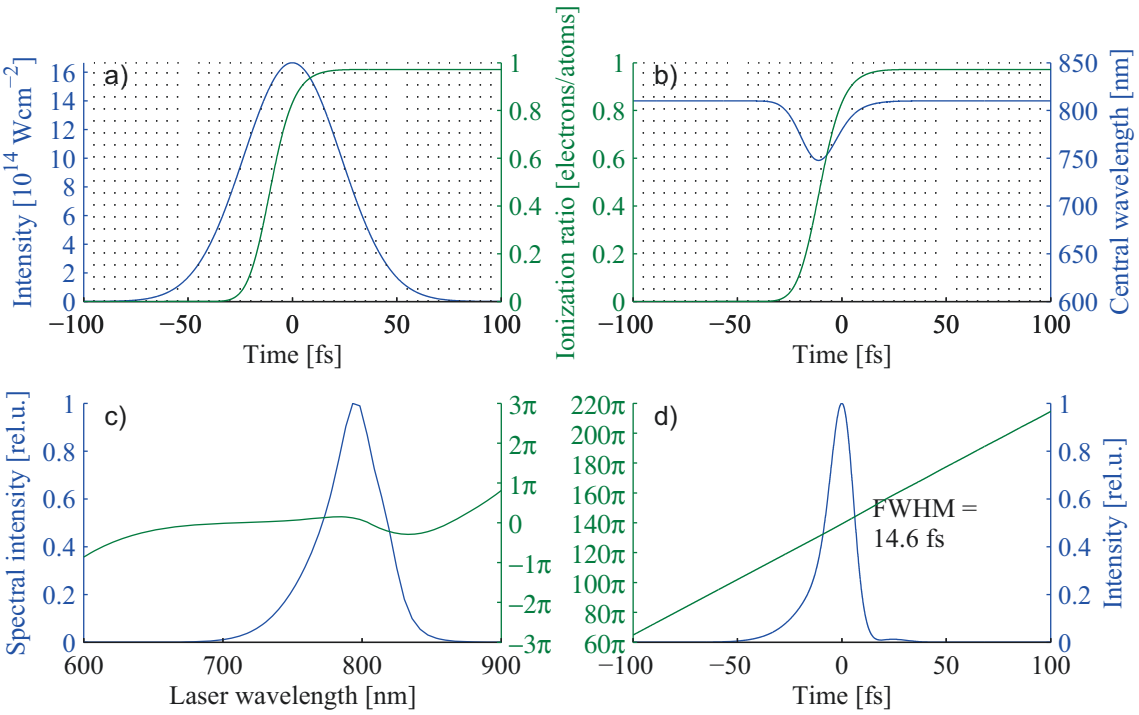

Figure 5.6 – Simulated a) ionization dynamics b) blue shift of central wavelength c) resulting spectrum with compensated quadratic phase d) resulting temporal profile using 4 mbar of helium and peak intensity of 1.67×10^{15} W/cm^2.

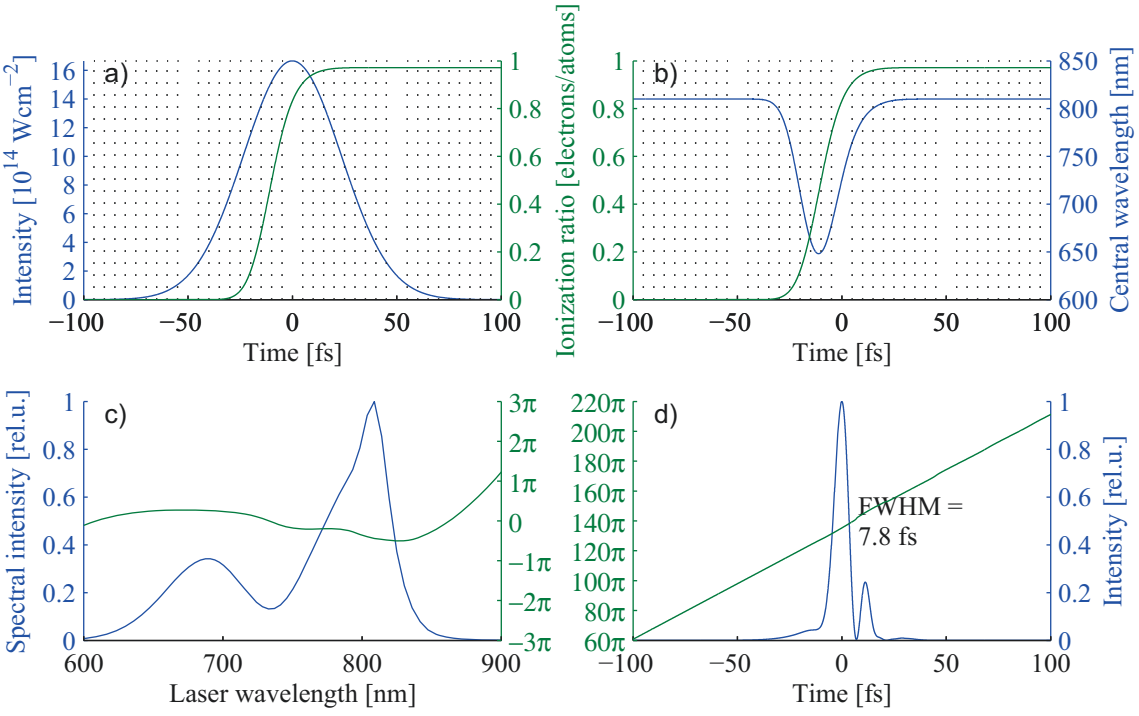

Figure 5.7 – Simulated a) ionization dynamics b) blue shift of central wavelength c) resulting spectrum with compensated quadratic phase d) resulting temporal profile using 12 mbar of helium and peak intensity of 1.67×10^{15} W/cm^2.

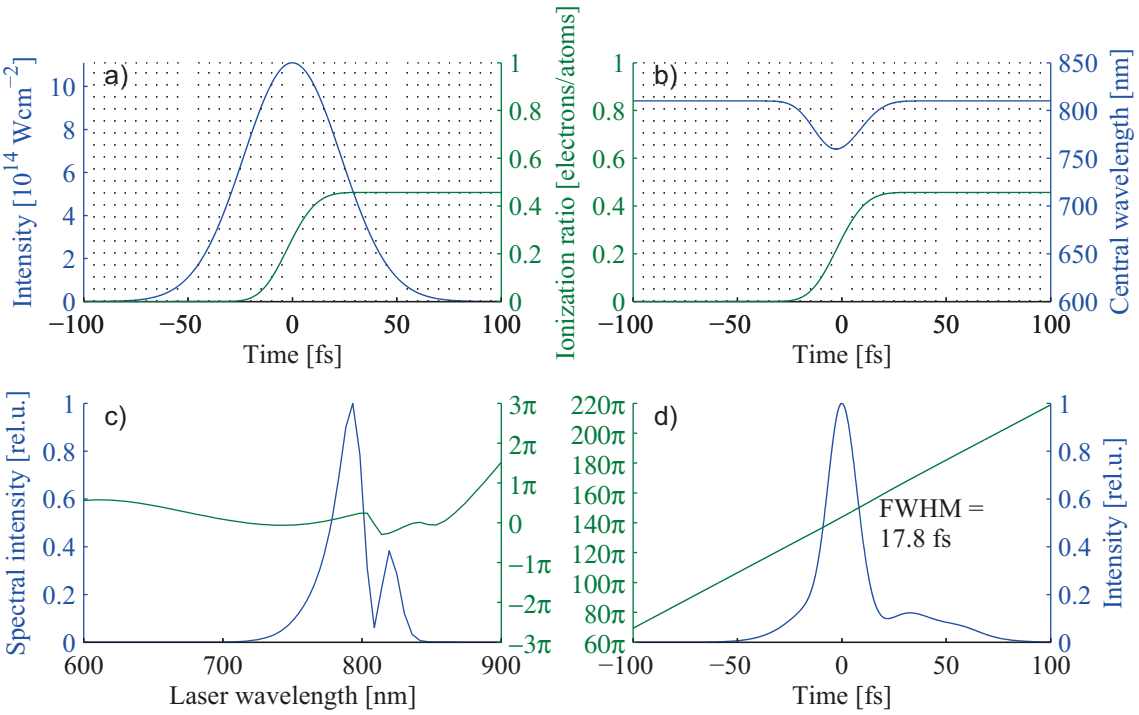

Figure 5.8 – Simulated a) ionization dynamics b) blue shift of central wavelength c) resulting spectrum with compensated quadratic phase d) resulting temporal profile using 8 mbar of helium and peak intensity of 1.11×10^{15} W/cm^2.

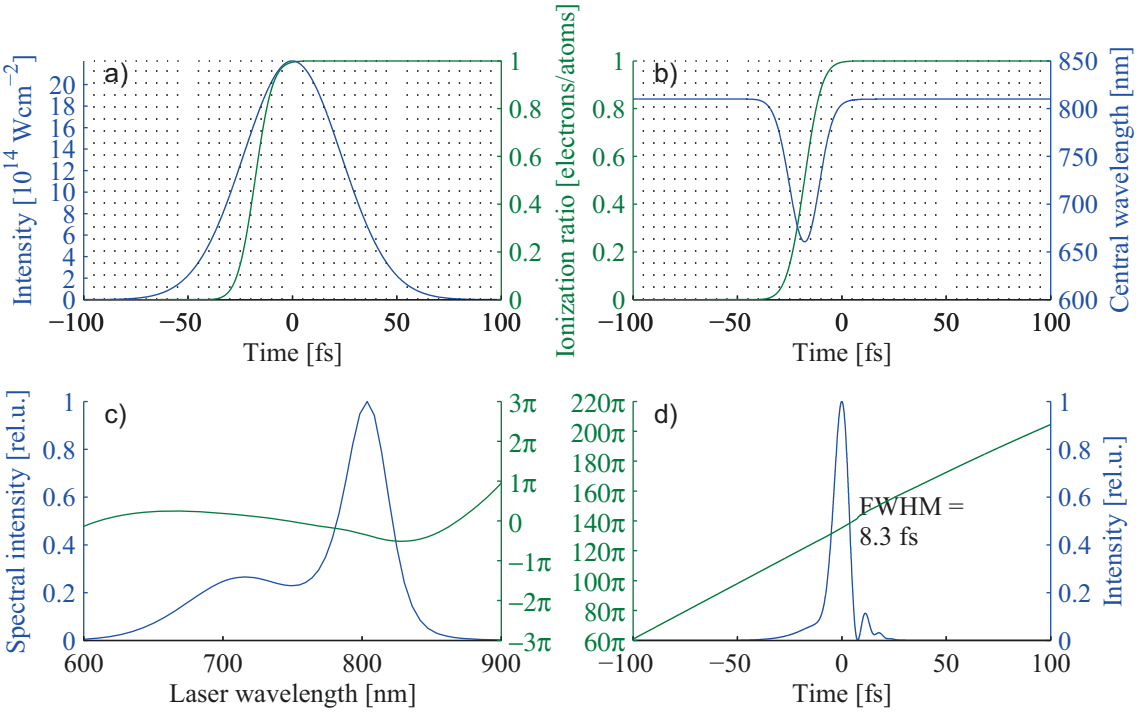

Figure 5.9 – Simulated a) ionization dynamics b) blue shift of central wavelength c) resulting spectrum with compensated quadratic phase d) resulting temporal profile using 8 mbar of helium and peak intensity of 2.22×10^{15} W/cm^2.

One can see that the pressure and intensity influence also the instant of high ionization gradient making the maximal blue-shifted wavelength (e.g. maximal frequency shift) moving along the time profile. This demonstrates itself significantly not only in spectral width but also in spectral structures that correspond to temporal structures in the post-compressed pulse.

As the model used here is relatively simple and extremely sensitive to major parameters change it cannot be used for parameter optimization in order to obtain short energetic pulses with clean temporal profile containing no pedestal. It can however be used to guide us toward the optimal range of parameters (high intensity, few mbar of helium) where the experiments can be performed.

5.3 Experimental setup

We reproduced an ionization-based post-compression feasibility proof as in [Fourcade-Dutin 10]. After the capillary a fraction of energy was recompressed and characterized with slightly better results than the former work mainly due to the better coupling and stabilization of the setup. Then we designed, built and performed a new experiment consisting of successful recompression, characterization and application of full energy femtosecond pulses under vacuum. This chapter is devoted to this high energy post-compression and the application will be discussed in the next chapter.

There is one particular thing that one should not forget when designing the experimental setup for ionization induced post-compression of high energy femtosecond pulses. It is the propagation effects of TW laser pulses in a medium. Recalling equation 5.1 on page 182 for critical power it is clear that in order to avoid self-focusing and therefore also material and beam destruction it is necessary to avoid propagation through any medium including primary vacuum.

Practically it means that the whole beam propagation has to take place under secondary vacuum and only reflective optics (mirrors) are allowed (no lenses or plates). Fortunately the ionization based post-compression requires only few millibars of helium so there is no need for differential pumping or windows in contrast to common (e.g. Kerr effect based) post-compression techniques.

5.3.1 Experimental setup overview

The experimental setup is shown on figure 5.10. The vacuum chambers are also displayed to give an idea of compactness and space requirements. The biggest chambers in the setup are based on DN160KF vacuum tubes (i.e. the inner diameter around 16 cm). That allows

one to pass 3 beams while using standard supports of 2" mirrors. When using chambers of DN100KF one has to use special compact mirror supports.

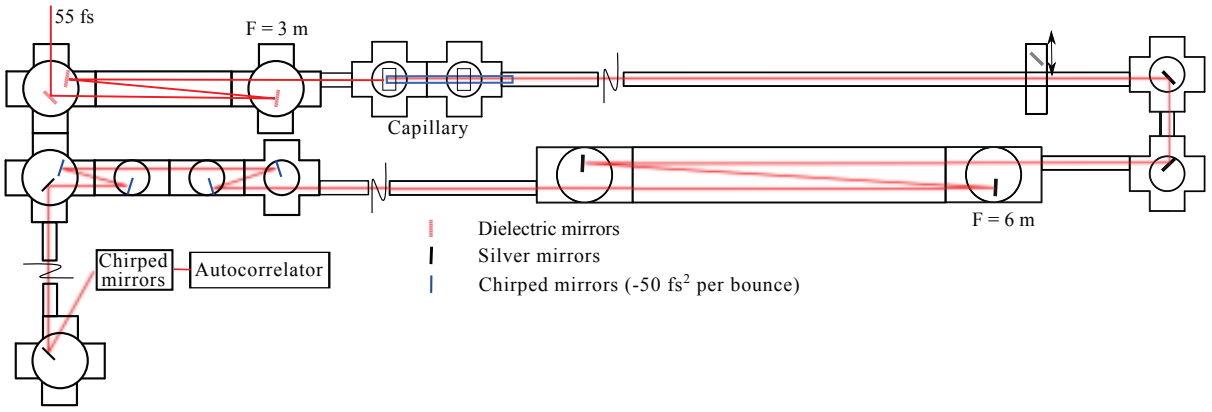

Figure 5.10 – (color) Experimental setup of ionization based post-compression technique

The post-compression setup can be divided in four parts: fundamental laser source, spectral broadening in the capillary, pulse recompression and characterization.

5.3.1.1 Fundamental laser source

We dispose of a Ti:Sapphire chirped-pulse-amplification (CPA) based laser chain delivering pulses of 250 mJ in 400 ps (recompressible to 50 fs) at a repetition rate of 10 Hz. The laser is called Eclipse and is located in CELIA laboratory in Talence. The laser chain consists of Ti:Sapphire oscillator[7] (Femtolasers Synergy), an Offner stretcher, a regenerative amplifier (20 roundtrips) and two multipass amplifiers (4 pass each). The beam is then directed to an experimental room where the post-compression and high harmonic generation (HHG) setup take place. At the entrance of the experimental room there is a homemade 2-gratings based compressor. Because of the low damage threshold of the gratings we do not inject more than $\approx$ 125 mJ to the compressor that gives $\approx$ 75 mJ after compression to 55 fs. Starting from the entrance window of the compressor whole high energy beam path is under vacuum. The laser chain provides a quasi-flat-top spatial profile that is typical for CPA laser chains. The pulse energy tuning is achieved via a half-wave plate and a polarizer cube. The picosecond contrast of the pulses is better than 3 orders of magnitude as shown on figure 5.11.

Note that the narrow peaks are measurement artifacts.

[7]The oscillator, as the rest of the chain, does not provide any stabilization of carrier-envelope phase (CEP).

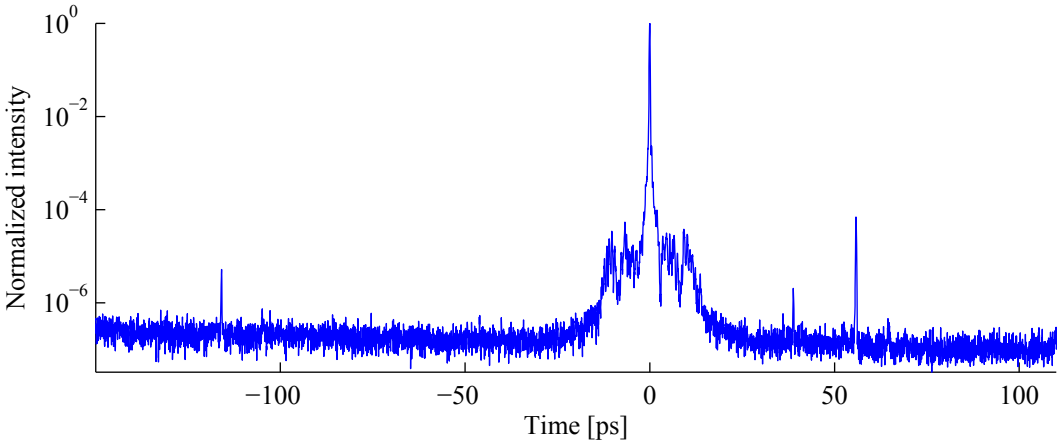

Figure 5.11 – Measured temporal contrast of the Eclipse laser

5.3.1.2 Spectral broadening in the capillary

The beam, propagating under vacuum, is focused by a 3 m focal length spherical mirror into a 40 cm long glass capillary with inner diameter of 420 µm and outer diameter of 6 mm. The capillary is an industrial product with no claim of optical quality. However the roughness of inner wall and the straightness are sufficient to perform our experiment as drilling of the gas injection hole has much higher influence on capillary transmission. The beam focal spot size and position were adjusted to favor monomode coupling: the focus at the capillary entrance and the size $3w = \phi_{cap}$ (w is a waist radius at $^{I_{max}}/_{e^2}$) [Marcatili 64]. A hole of 20 mm diameter was installed after the compressor exit for this purpose. Helium gas was injected in this capillary at controlled pressure via a side hole located 25 cm from the entrance of the capillary.

5.3.1.3 Pulse recompression

After the capillary, a 6 m focal length spherical mirror collimates the output beam to a size of $w = 10\,\text{mm}$ as before the compressor. This is very important because of two reasons. The beam diameter before compressor is the largest possible compatible with 2" optics[8]. The second reason is the compatibility with the second stage of the experimental setup that is not presented here - the high harmonic generation and the application stage. The whole post-compression beam line can be bypassed by removing only 2 mirrors implying relatively easy and fast changeability between post-compressed beam and fundamental beam.

To compensate the chirp of the pulse acquired during the spectrum-broadening process in the capillary, 4 chirped mirrors fabricated by Layertec inducing a -50 fs^2 GVD per

[8]Note that using 3" optics would result also in larger supports and vacuum chambers, multiplying the cost of whole setup.

reflection are located under vacuum. The chirped mirrors support large-bandwidth pulses and are paired to assure the GVD oscillation compensation to minimum. Due to the beam size there is only one reflection per mirror.

5.3.1.4 Characterization

We characterize the output pulses with homemade single-shot SHG autocorrelator and a spectrometer located in air. A fraction of the laser beam is reflected by a uncoated silica wedge, exits the vacuum chamber via a 3 mm thick BK7 window and is sent to single-shot autocorrelator. To compensate for the window and the air dispersion we added 4 additional chirped mirrors (-50 fs^2 each) and a 1 mm silica plate in front of the autocorrelator. In this way, the measured pulse duration was identical to the pulse duration under vacuum. The autocorrelator uses a 10 µm thick BBO crystal and was designed to be compatible with sub-10 fs pulses. Spectra were acquired by a fiber spectrometer located outside between exit window and chirped mirrors. To validate this approach and to be sure that there are no nonlinear effects due to the exit window, we compared these spectra with those obtained by acquiring the beam blocker diffusion located in the vacuum. Both cases gave the same spectra.

5.3.2 Experimental setup optimization

5.3.2.1 Coupling to the fundamental mode

The capillary post-compression can provide at the output a quasi-perfect spatial profile in spite of quasi flat-top input beam spatial profile, ionized gas turbulence and capillary inner wall roughness. However, perfect coupling into fundamental mode is the necessary condition to be fulfilled. The condition is even stronger when considering beam-pointing fluctuation that should be avoided. Bad coupling or large beam-pointing fluctuation can make the post-compressed pulses completely useless or even destroy the capillary.

The proper coupling is achieved by two motorized mirrors as shown on figure 5.12.

Note that trying to couple the beam to the capillary while watching an output spatial profile is very time-consuming and user-frustrating as aligning the spherical mirror would move the beam also on the flat mirror so everyday finding the right x-y position and incident angle on the capillary face is practically not possible. The solution consists in having an alignment reference on the flat motorized mirror so the alignment of the spherical motorized mirror is given and easy. The beam is then properly injected with the flat motorized mirror when watching the capillary face for rough alignment and output beam spatial profile for fine fundamental mode coupling. So the optical axis is well defined by the first reference on the flat motorized mirror and the second spot is the capillary entry. Those two spots

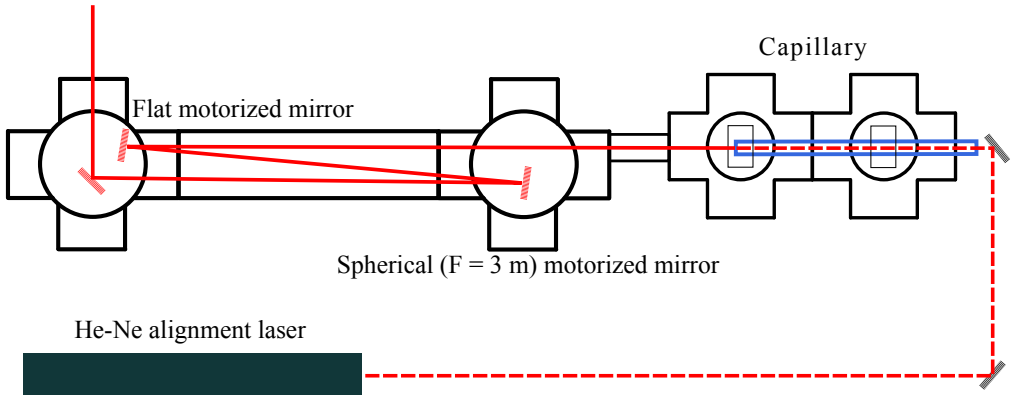

Figure 5.12 – Proper coupling to the capillary by two motorized mirrors. The necessary alignment mark on the flat mirror is provided by the He-Ne beam injected from the other side.

are necessary for alignment to the fundamental capillary mode and have to be visualized with enough precision. We dedicated one CCD camera for each spot that permits the fine alignment.

The first reference on the flat motorized mirror is crucial. To create it with enough of precision we perform a monomode injection, i.e. of a He-Ne laser beam from the other side of the capillary (see fig. 5.12). Then the He-Ne beam on the flat motorized mirror simply defines the spot whose Gaussian fit position is saved on a PC. The fundamental (CPA laser chain) beam is then easily aligned to the saved spot.

The He-Ne coupling into the capillary using mirrors is much easier than the fundamental beam coupling for two major reasons:

1. The He-Ne coupling is performed in air. One can tune both mirrors directly with hands in contrast to fundamental beam coupling where the use of motorized mirrors is necessary. Using both hands to tune both mirrors in the same moment decreases dramatically the alignment time necessary to converge to the final position.

2. As we are in the air the two injecting mirrors for He-Ne can be placed wherever. In contrast to fundamental beam injecting mirrors, where we are strongly limited by the damage threshold, we can place the second mirror nearly in contact with the capillary very close to the focus. This results in decoupling of the two mirrors as the first one defines the position on the capillary rear face and the second one the angle.

The He-Ne quasi-perfect coupling is achieved by minimizing the laser diffusion on capillary inner wall[9] and the beam spatial profile is controlled on the flat motorized mirror using the CCD. After saving the alignment mark the He-Ne injecting mirror is removed and before closing the vacuum chambers one should also check the beam path that follows. Note that

[9]The human eye is very well suitable for such task due to is logarithmic perception.

this alignment procedure requires a perfectly stable capillary that should not move during pumping.

5.3.2.2 Experimental setup stability

Perfect monomode coupling is necessary condition for our post-compression technique. This coupling has to stay for the whole experimental day. We can differentiate two major types of stability improvement: a laser beam stability and a mechanical stability of the setup.

A commercial beam-pointing stabilization was installed at the end of the laser chain. It consists of automatic real-time control of the beam position on two mirrors using two motorized mirrors. Step-motors are used for slow wide-range alignment and piezo tunes the alignment quickly but with reduced range. As the characteristic fluctuation frequency is higher than laser chain repetition rate (10 Hz) the fast compensation via piezo has no practical use and was disabled.

It is necessary to consider mechanical stability of the setup because of long beam path (more than 20 m) and wide range of vibration sources such as vacuum pumps, chillers, air conditioning, power supplies etc. Stable mirror supports and few cm thick vacuum chamber basis were used, the compressor gratings support were reinforced and a special care was taken for post-compression capillary support as for its 40 cm length and 6 mm diameter it is very sensible to vibration. The capillary installation is shown on fig. 5.13 on the next page. Note the robustness of the support and the fact that longitudinally the capillary is held in place almost over its whole length except with a necessary hole for the gas injection cell.

5.4 Experimental results

5.4.1 Capillary transmission

Capillary transmission under vacuum is mainly defined by the coupling conditions and the roughness of the capillary inner wall. Coupling conditions were optimized for best transmission of the fundamental mode as discussed in section 5.3.1.2 on page 195. Note that these conditions maximize the fundamental mode transmission, not the overall transmission of all modes together. The fundamental mode transmission was measured through an iris after long propagation. With He-Ne laser we obtained fundamental mode transmission around 80 %. The main reason of such a huge loss is the side hole for gas injection considering that before drilling the hole the transmission was about 98%.

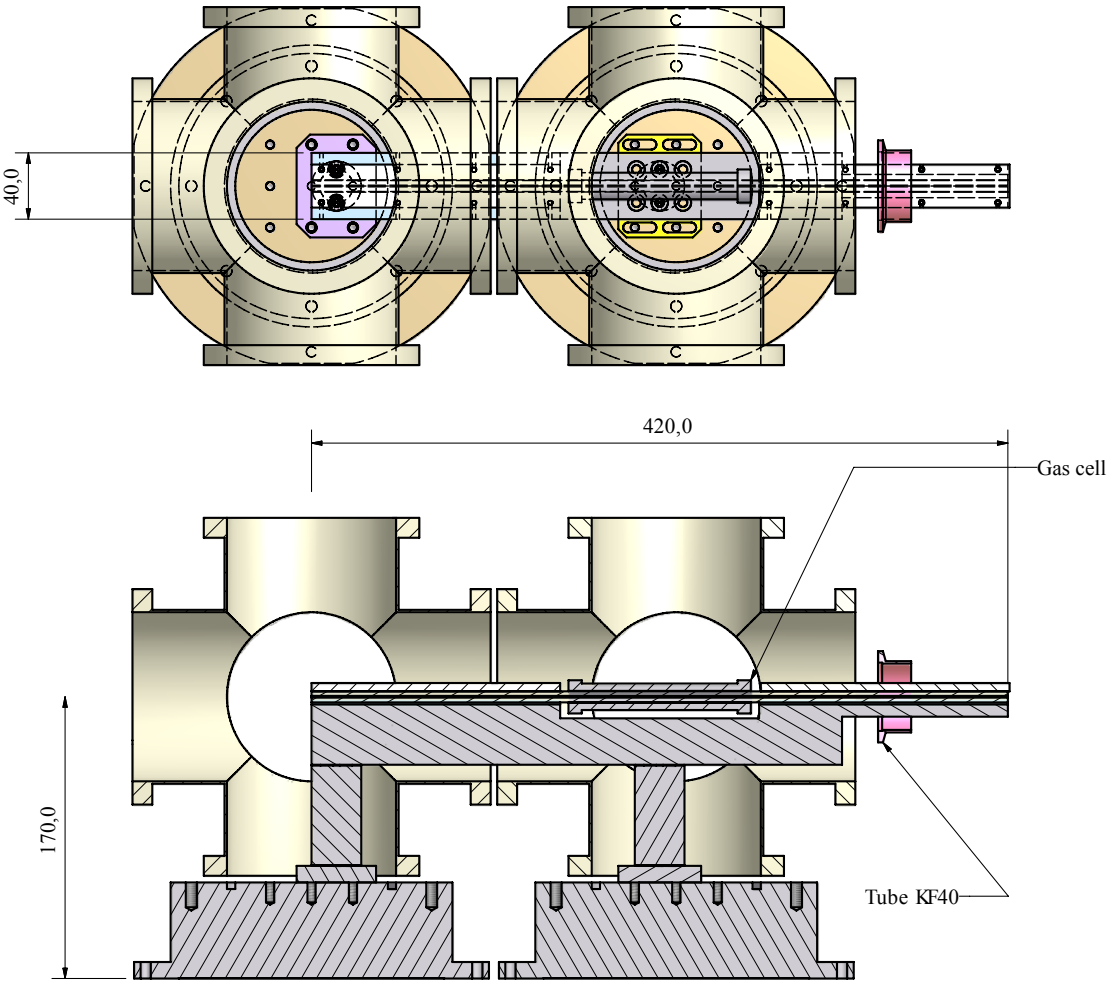

Figure 5.13 – (color) Post-compression capillary support installation: from above and side view. Dimensions in mm.

The Ti:Sapphire laser fundamental mode transmission was measured to 40 - 47 % depending on actual beam pointing fluctuations and quasi-flat-top spatial profile that are the main reasons for such a low transmission. The spatial profile can be improved by spatial filtering, although the overall setup transmission would be similar, or using a lossless spatial shaping device e.g. deformable mirror[10].

5.4.2 Spatial profile

The spatial profile of post-compressed pulse is shown on fig. 5.14 on the following page. The spatial profile and phase were acquired by a Haso wavefront analyzer[11] manufactured by Imagine optics. The intensity spatial profile is close to fundamental mode as expected and

[10]For detailed information about a deformable mirror function and use see section 4.1 on page 153

[11]For more details about wavefront analyzes see section 4.1 on page 153.

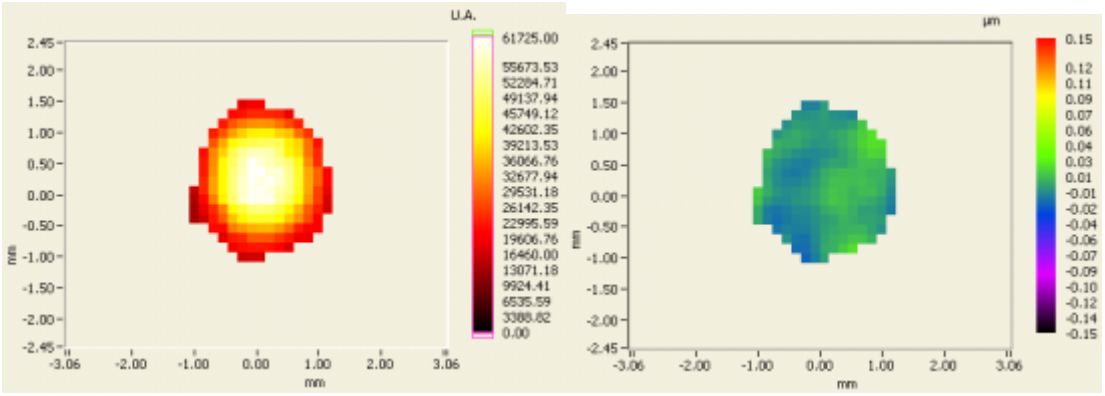

Figure 5.14 – (color) Measured spatial profile of post-compressed pulse (a) and its spatial phase of 8 nm RMS. (b).

the spectral phase is nearly flat with 8 nm RMS. This value is obtained after subtraction of the spherical phase component that is intrinsic to Gaussian beam wavefront out of focus. The direct result is that this beam can be focused and its intensity in focus will be 96% of intensity of a perfect fundamental Gaussian mode (Strehl ratio equals 96%). Note that fundamental quasi-flat-top beam of the Eclipse laser chain has never reached more than 70% of Strehl ratio. This is very important especially for such a nonlinear processes as high harmonic generation where every intensity profile imperfection projects directly multiplied to the harmonic spatial and even spectral profile.

5.4.3 Spectral characteristics of post-compressed pulses

As the high intensity infrared laser pulse propagates through the helium filled capillary its spectrum changes significantly even with a low gas pressure. Both a broadening and a blue shift of the spectra are observed and controlled with the gas pressure and pulse energy. Figure 5.15 shows the evolution of the infrared spectra after post-compression for several helium pressures and for several values of the pulse incident energy. Even 1 mbar of helium is sufficient to broaden the incident pulse spectrum. With gas injected in the capillary the output spectrum broadens and splits into several peaks. The red-side peak position is constant while the blue-side peak position experiences a blue shift increasing with pressure until a saturation is reached (between 7 and 10 mbar) so the overall spectral widths increase rapidly with pressure.

It can be easily seen that 5.15 is divided into two regions 0 to 10 mbar and 10 to 50 mbar respectively where the spectra evolve differently.

The first region is characterized by a rapid evolution of the spectral width and central wavelength.

The second region demonstrates spectra whose shape is not dependent on the helium

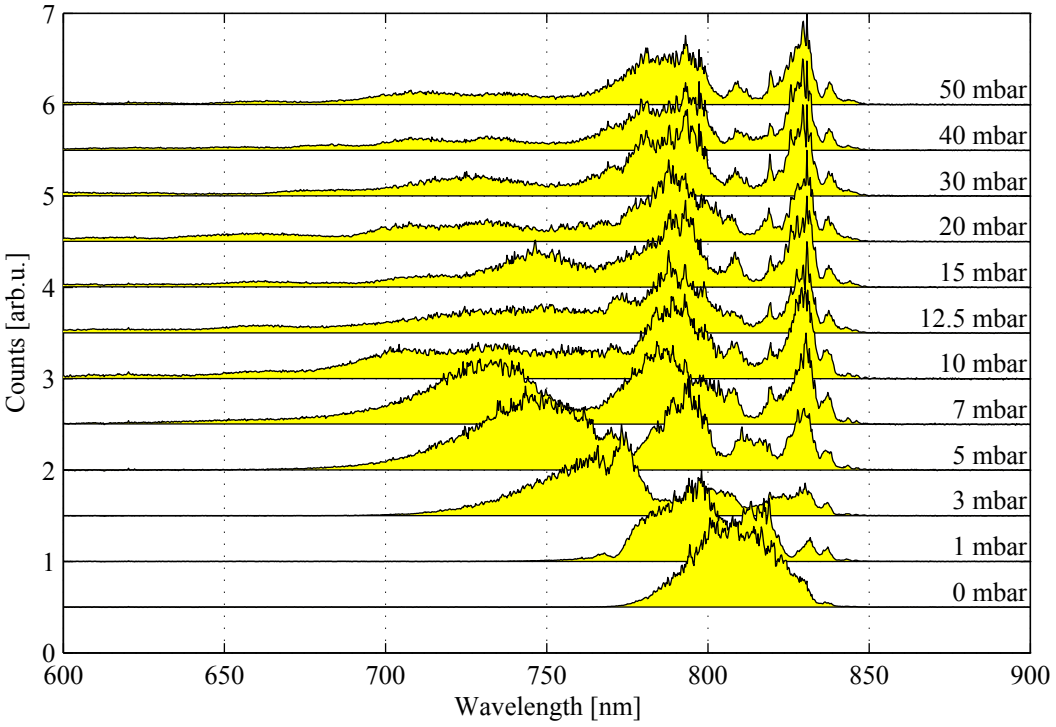

Figure 5.15 – Normalized experimental infrared spectra obtained after guided propagation of the pulse in the capillary for several pressures of helium gas injected in the capillary. The incident energy at the entrance of the capillary is 74.4 mJ and the displayed pressure is the pressure in the capillary. Note that the energy coupled into fundamental mode of the capillary without any helium is only 30 mJ that corresponds to the capillary monomode transmission discussed above.

pressure and most of spectral energy is centered around 800 nm.

Later in this section we will show that the highest peak power output pulses for a given input pulse energy are obtained at the frontier of the two regions i.e. at the saturation pressure threshold. Note that the second region and therefore even complete first region were not observed in the previous work [Fourcade-Dutin 10] because of low input energy of the pulses.

However, the effect of spectral broadening is not restricted to the high energy input pulses only. Fig. 5.16 shows output spectra evolution on input pulse energy for a fixed pressure at 7 mbar of helium in the capillary. We observe that the spectral broadening increases regularly with the pulse energy. That means that in general this laser source has independently tunable spectral width and pulse energy and the only tuning parameters needed are input pulse energy and helium pressure in the capillary. This corresponds to the parameter dependence that we found theoretically in section 5.2.1 on page 185.

At the highest input energy of 75 mJ and 7 mbar of helium, the output spectrum exhibits a regular shape resulting in a large spectral width (120 nm FWHM) and a high output energy of 10.9 mJ. In this regime, the spatial profile of the beam remained also good as studied in [Fourcade-Dutin 10].

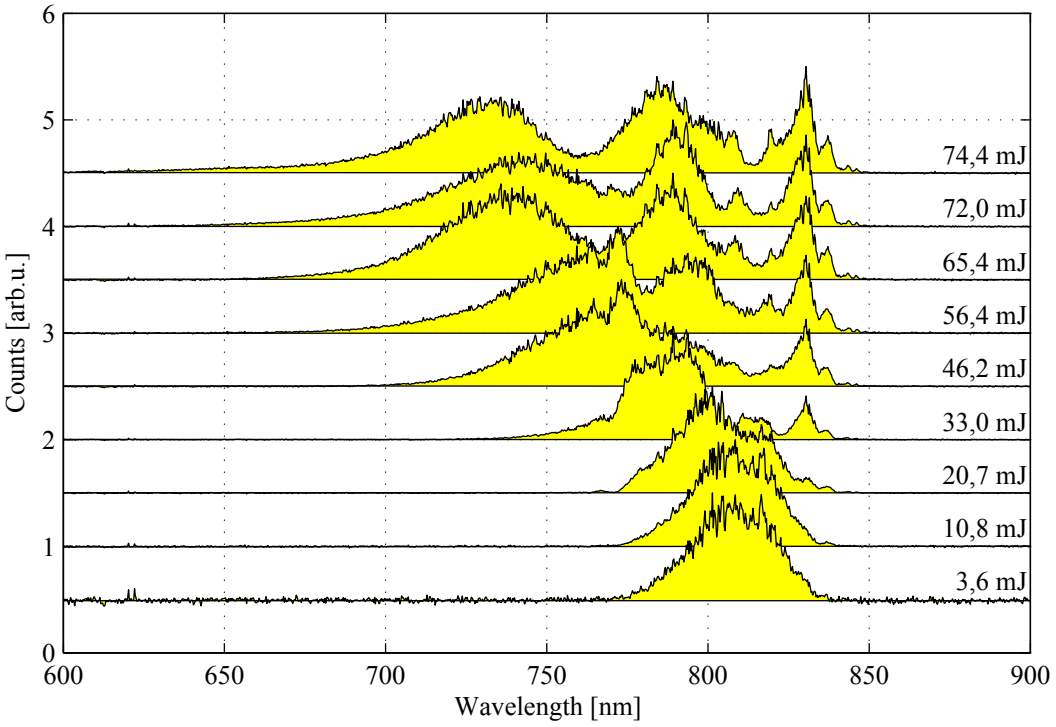

Figure 5.16 – Normalized measured infrared spectra obtained after guided propagation of the pulse in the capillary for several incident energy of the pulse injected in the capillary. Helium pressure in the capillary is 7 mbar.

In general the region of rapid evolution of the spectral width corresponds well to the theory. However the second «saturated» region promotes spectra whose spectral width does not depend on the intensity and on pressure in contrast with theory. This can be explained considering the losses via refraction and high order modes creation that are beyond our 1D model. As the energy or pressure is too high the complete ionization occurs earlier making the high refraction losses occurring earlier reducing the energy that continues to propagate and makes the blue shift. The best solution for more blue shift and broader spectra with more energy seems to be a maximal available input pulse energy and maximal pressure (or longer capillary) adjusted to avoid the saturation.

For the capillary length of 40 cm in the saturation threshold the pulse energy became dependent only on pressure. The experimental optimal helium pressure as a function of the input pulse energy is plotted on figure 5.17. It suggests that the saturation threshold helium pressure can be directly linked to the input pulse energy and that this dependence is monotonous. For highest pulse energies above 70 mJ only 7 mbar of helium are sufficient. On the other side with 20 mbar of helium 33 mJ are needed making this technique useful in wide range of input pulse energies.

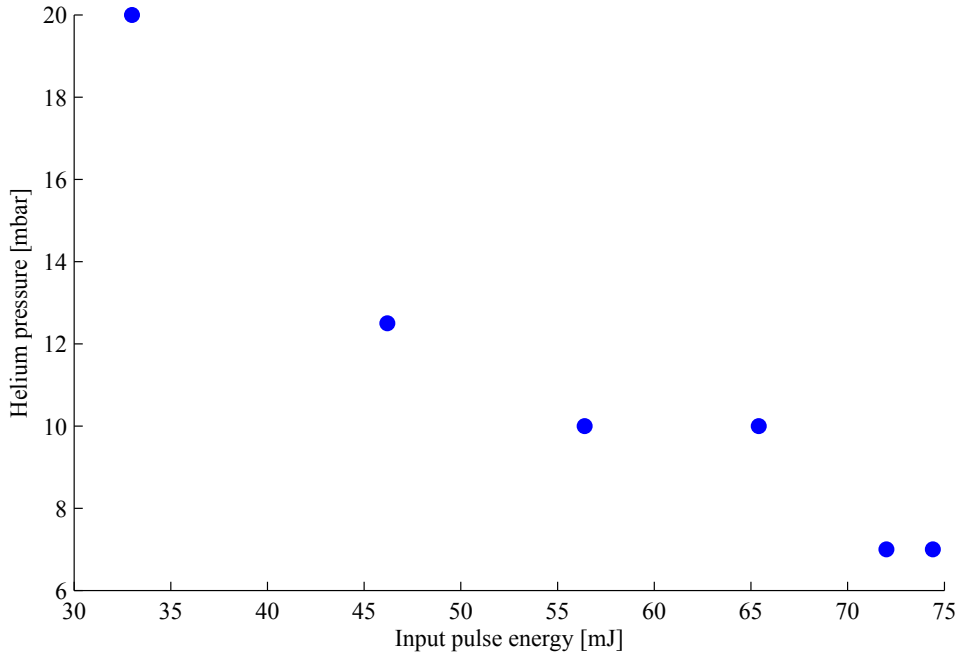

Figure 5.17 – Measured optimal helium pressure of blue shift saturation threshold as a function of input pulse energy before capillary for a capillary of 40 cm.

5.4.4 Duration and energy of the post-compressed pulses

The possibility to obtain short pulses depends both on the spectral extent and on the relative weight of the spectral component. To estimate the shortest pulse duration that could be achieved with the measured spectra shown in previous section we calculated Fourier limit pulse duration as shown on fig. 5.18. The figure shows that shorter pulses can potentially be obtained at higher helium pressure. It also shows that above the saturation pressure (defined in previous section), the pulse duration does not significantly change anymore. We can observe that pulses shorter than 10 fs FWHM could be obtained with perfect compensation of the chirp.

The energy of the output pulses was studied as a function of the helium pressure. To estimate the pulse energy, we measure the energy of the beam that was transmitted through a large-band 90/10 beamsplitter located after the chirped mirrors. In this way, we could effectively select the beam propagating in the fundamental mode of the capillary because high order modes do not fit to the 33 mm diameter beamline aperture. We observed that the pulse energy regularly decreases as the helium pressure increases (fig. 5.19). This is consistent as part of the pulse energy is refracted out of the capillary by a diverging plasma lens made by a gradient of electron density, coupled in high order modes of the capillary and lost to ionize the gas [Tempea 98]. These results also show that output pulses with high energy above 10 mJ and significant spectral broadening can be obtained simultaneously.

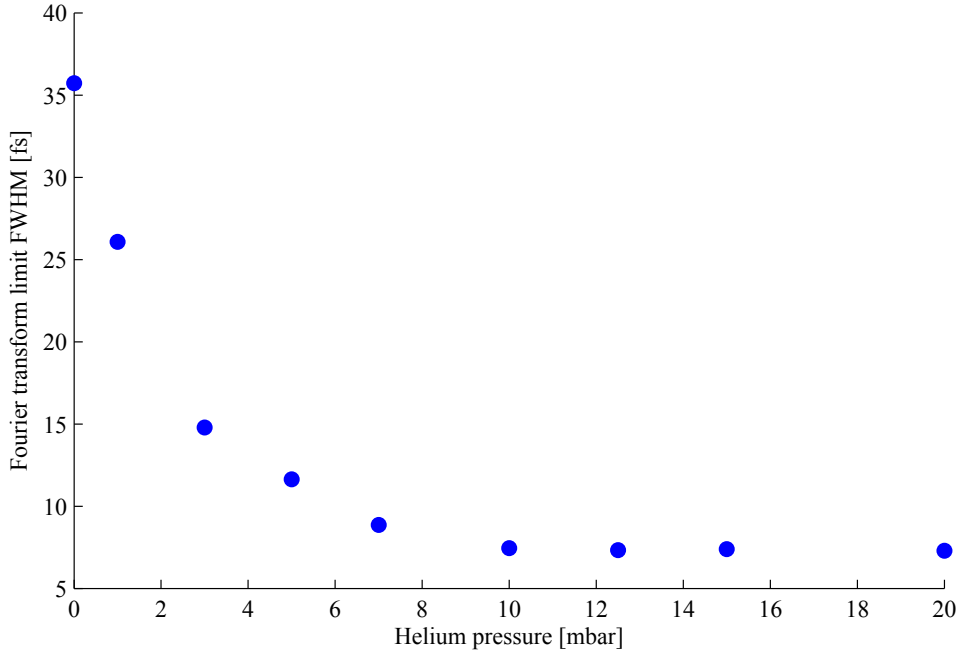

Figure 5.18 – Dependence of the Fourier-transform-limited output pulse length on the pressure of the Helium gas in the capillary measured for incident energy of 75 mJ.

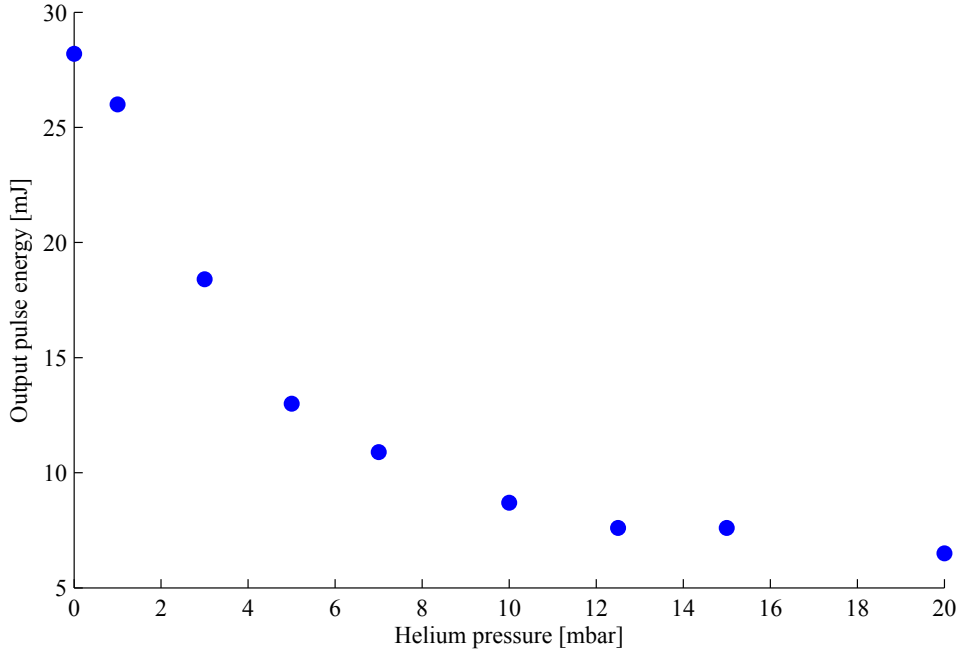

Figure 5.19 – Output pulse energy as a function of the helium pressure for incident pulse energies of 75 mJ.

The recompression of a small part of the pulse energy was already done in previous work [Fourcade-Dutin 10]. In our work, we recompressed the whole energy of the output pulse in a collimated beam. The GVD compensation via chirped mirrors that we used under vacuum was not adjustable as the number of reflections was limited and could not

be changed easily under vacuum. Nevertheless recompression of pulses is relatively easy in this spectral range with 100 nm wide spectra and broadband paired chirped mirrors with compensated GVD oscillations allowed us to recompress the pulses and even to approach the value imposed by the Fourier limit.

Real tunability of the output pulse duration is shown on fig. 5.20 that shows a single-shot second harmonic autocorrelation measurement. It clearly shows that short pulses can be obtained and controlled via pressure tuning. The pulse duration drops to 10 fs at around 7 mbar of the helium pressure. One should also note a stability of the output pulse

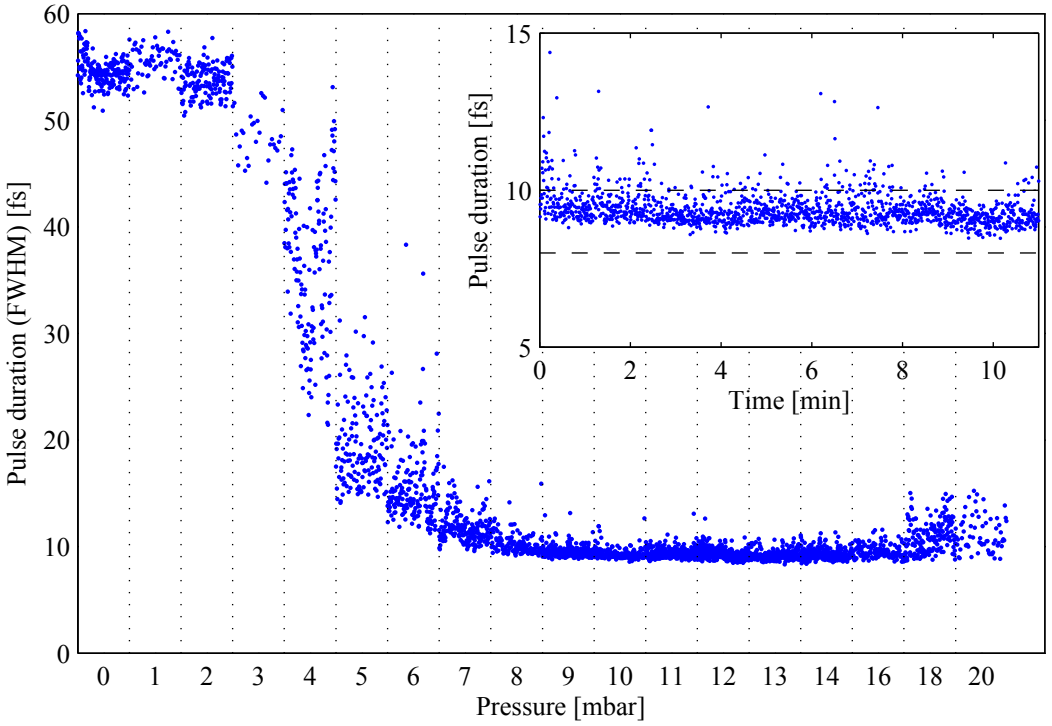

Figure 5.20 – Pressure dependence of the pulse duration showing a single shot real-time response on the pressure of Helium gas in the capillary. There was 1 mm of Si before compressor and the input pulse energy before the capillary was 60 mJ.

duration. The best one can be found between 10 - 13 mbar where the pulse duration stays below 10 fs (inset of fig. 5.20) with 5.6% of RMS.

In general there is nevertheless a trade-off between output pulse duration and energy. That implies limits in achievable values for output pulse duration and energy. Under those limits, one can obtain pulses of desirable energy and duration simply by tuning input pulse energy and helium pressure in a capillary. Further control could also be obtained by changing the capillary diameter and length as well as the gas pressure [Fourcade-Dutin 10] or input pulse duration but this study was not performed here.

5.5 Discussion

To summarize we have demonstrated a TW level laser source adjustable between 55 and 10 fs at 10 Hz with good spatial profile under vacuum. The spectral broadening is achieved via ionization induced self-phase modulation and the generated spectra are recompressible. We generated pulses of 10 mJ in 10 fs with 5.6% RMS of duration fluctuation. Results are in good agreement with 3D simulation [Auguste 12, Auguste 13] and also with our simple simulations provided that we consider an effective length of interaction that is much smaller than the capillary length. The technique is promising for the future as it is compatible with high energy pulses - even higher than the ones we dispose.

Today there are two other techniques besides high energy ionization based post-compression technique: Kerr effect based post-compression and OPCPA laser chain.

Kerr effect based post-compression has been implemented and proved its quality on many places around the world. The world record of 5 mJ in 5 fs of [Bohman 10] was submitted for publishing 4 years ago on January 2010 and to date is not beaten. With the fact that this type of post-compression has been studied and performed by many groups this may indicate that the technique already reached its intrinsic limits in terms of output pulse energy and peak power.

As a large number of scientific groups announced developing high energy OPCPA, it is possible that they will obtain higher energy in shorter duration in comparable spatial mode while using a proper spatial filtering, than us with our post-compression technique.

Simultaneously some groups using a high energy multi-TW laser chains plan to implement our ionization-based post-compression technique and are expecting high performance.

The post-compression technique itself provides a powerful possibility of upgrade of high energy CPA laser chains.

From an other point of view, the implementation and studies of ionization-based post-compression technique will provide us better understanding of laser-gas interaction with parameters that are close to e.g. high harmonic generation at high energy.

Chapter 6

HHG with 10 fs TW pulses

In previous chapters 3 and 4, we have discussed HHG with high energy femtosecond pulses typically with a duration of 50 fs. We have also seen that low intensity 50 fs pulses generates several tens of attosecond pulses and that the number of attosecond pulses generated can be lowered by depletion of harmonic dipole.

Intuitively, with even faster depletion or shorter pulses, one can expect to generate a single attosecond pulse only. Faster depletion can be achieved using higher intensity.

Generation of high energy short duration femtosecond pulses is a difficult task and we developed a high energy TW post-compression technique (described in chapter 5) and successfully generated pulse of 10 mJ and 10 fs duration.

In this chapter, we will describe HHG with such driving pulses.

6.1 Experimental setup

The experimental setup is a combination of the experimental setup of post-compression technique (figure 5.10) and the experimental setup of high harmonic generation (figure 3.4). The schematics of the HHG with 10 fs TW pulses experimental setup are on figure 6.1.

The 10 fs TW pulses delivered by the post-compression technique are loosely focused by a 2 m focal length mirror into an argon gas jet with 250 μm orifice. The generated XUV is then characterized by a XUV flat-field spectrometer described in detail in section 2.3.1 on page 35.

The experimental setup is designed to produce and characterize the XUV radiation both spectrally and spatially on single-shot basis. As we will see later in this chapter, this is crucial characteristic of our setup that allows us observing a lot of features of generated harmonics.

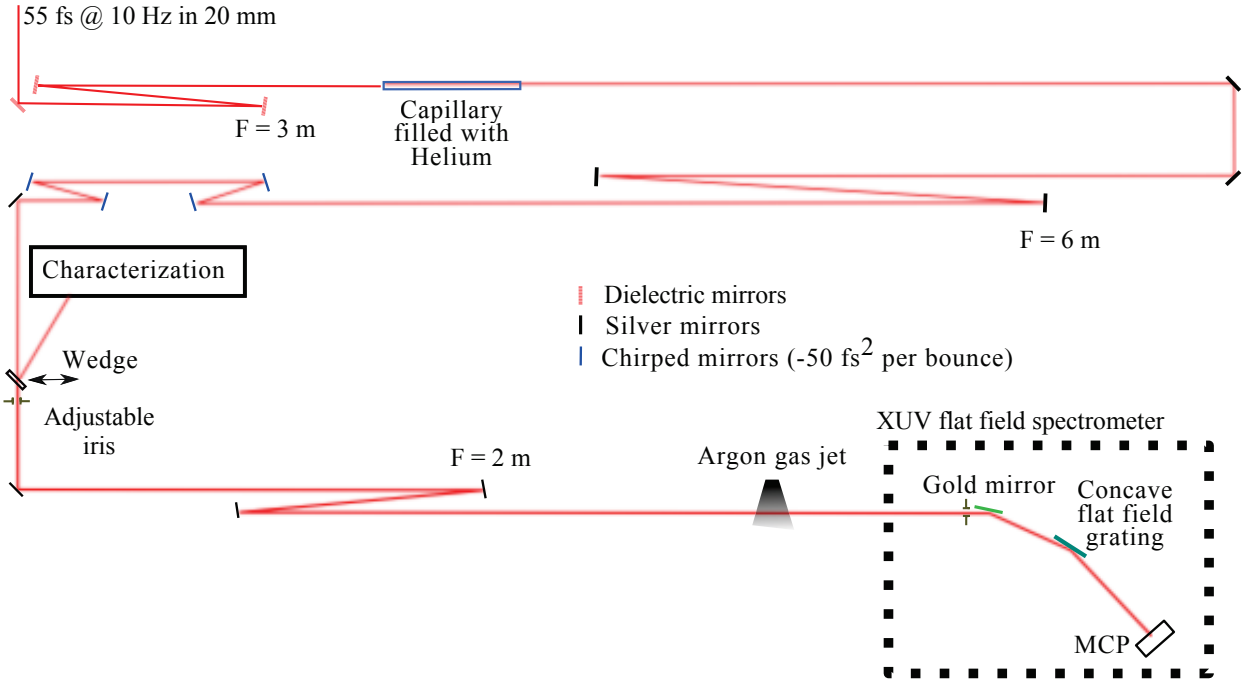

Figure 6.1 – (color) Schematic experimental setup of the HHG with 10 fs TW pulses delivered by ionization-induced self phase modulation.

6.2 Experimental results

6.2.1 Iris diameter dependence

The figure 6.2 shows XUV spatio-spectral profile evolution on iris diameter.

The argon jet is placed 5 cm before the focus and the iris maximal diameter is maximally 14 mm thus the intensity increases with the iris diameter.

6.2.1.1 Reference spectrum

The figure a) is a reference spectrum generated without any helium in the post-compression capillary i.e. with 50 fs long pulses. As the generation took place at high intensity the harmonics are asymmetric and blue-shifted as seen on the figure 6.2 a).

Note that the indicated harmonic lines correspond to harmonics generated with long pulses i.e. centered at 810 nm. Such harmonic lines will be indicated for reference in the whole chapter. One can thus expect that the XUV spectra generated with blue-shifted post-compressed pulses (to 790 nm) would be found much on the blue side of the 810 nm harmonics. However, they would not shift beyond the next harmonic, for that even shorter central wavelength (shorter than 740 nm) would be necessary.

The harmonics on figure 6.2 a) are generated with long 50 fs pulses and therefore they are spectrally relatively narrow. On the blue side we can distinguish thin vertical spectral

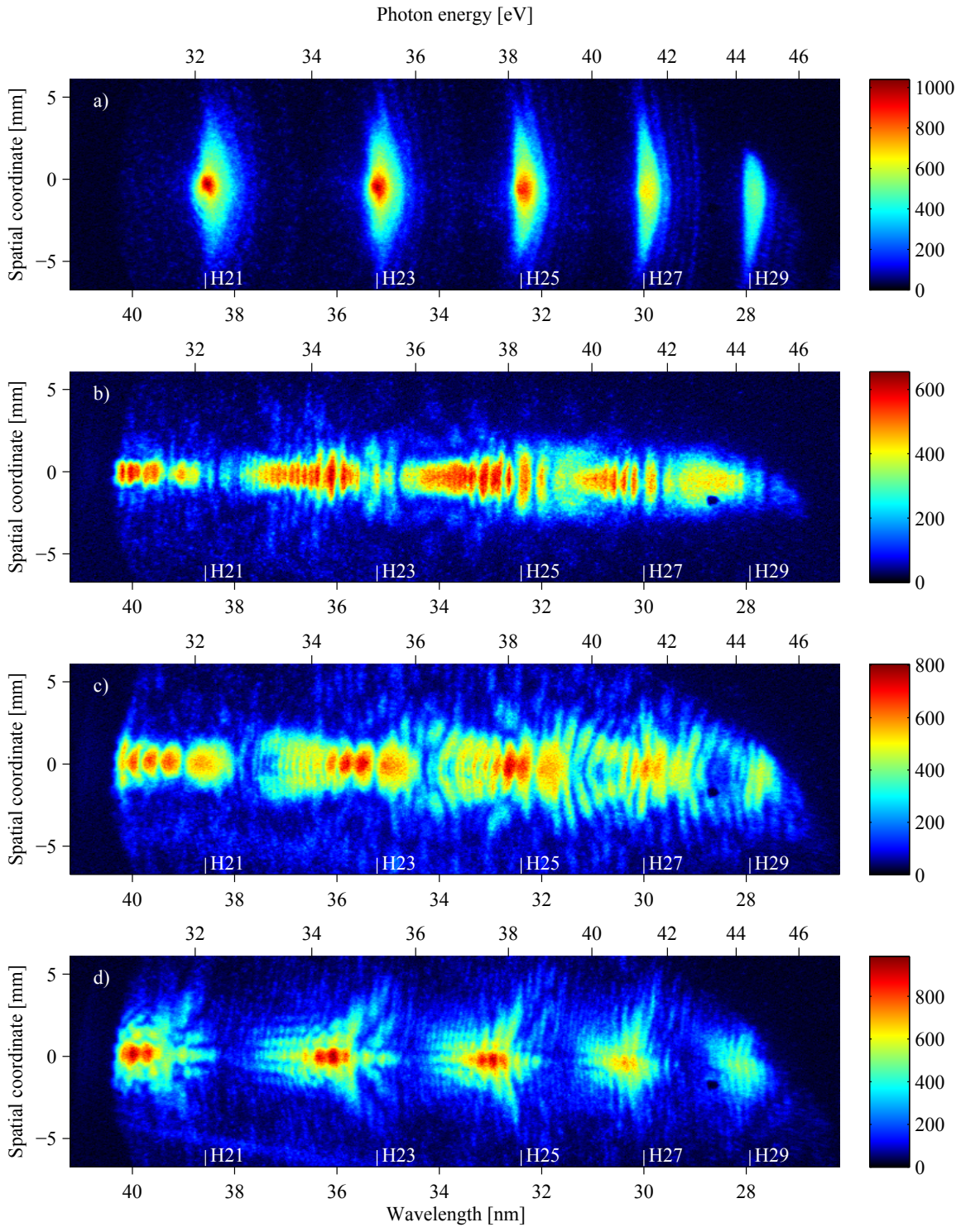

Figure 6.2 – (color) Experimental single-shot spatially and spectrally resolved XUV profiles generated in argon jet. a) is a reference generated with long pulses of 50 fs, iris = 12 mm and peak intensity of 1.2×10^{15} W/cm². b), c) and d) are generated with 10 fs 10 mJ pulses 5 cm before the focus. The iris diameter and corresponding peak intensity was b) 10 mm, 1.2×10^{15} W/cm², c) 12 mm, 1.7×10^{15} W/cm², d) 14 mm, 2.3×10^{15} W/cm².

lines that extent over the whole spatial range. Such structures were identified as due to the long path (interfering with itself) and we have seen them very well already on figure 3.89 d).

We simulate the corresponding reference figure and the result in shown on figure 6.3.

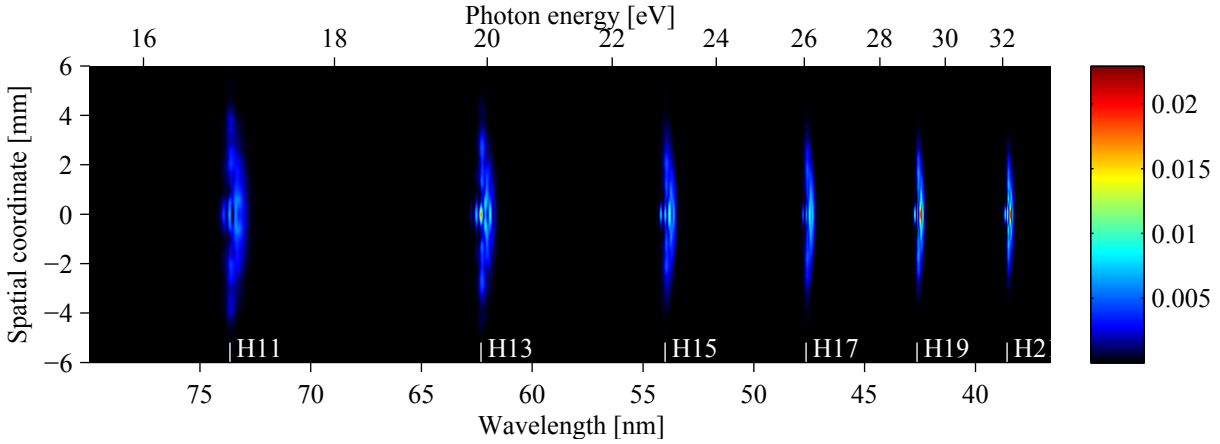

Figure 6.3 – (color) Simulated spatially and spectrally resolved XUV profiles generated in argon with 50 fs pulses, iris diameter of 12 mm and peak intensity of 1.2×10^{15} W/cm^2. That are the same conditions as figure 6.2 a).

The figure shows simulated spatially and spectrally resolved XUV profiles generated in argon with 50 fs pulses in the same conditions as figure 6.2 a). The simulation is in good agreement with the experiment: the harmonics are asymmetric and blue-shifted, the most on axis due to $\alpha \frac{\mathrm{d}I_{IR}}{\mathrm{d}t}$ and spatially they cover few mm above and below the optical axis. From the red side, the harmonics are sharply cut.

6.2.1.2 HHG with post-compressed driving pulses

With post-compressed 10 fs TW pulses, we observe complex and reproducible structures in XUV profiles. Those structures are similar for consecutive harmonics.

On figure 6.2 b), we can see XUV radiation generated with post-compressed pulses at the same intensity as the reference with long pulses. However, the overall shape of the harmonics is completely different. They are spectrally much larger and shifted to the blue wavelength. They are spectrally so large that they form a quasi-continuum. They contains also a lot of spectral fringes (up to 20 for harmonic 21).

Raising intensity (figure c) with iris diameter of 12 mm) does not change the spectral extent of harmonics. It add spatial structures that seem to be more pronounced for higher harmonics.

Opening more the iris to 14 mm (figure d) and thus further increasing the peak intensity in the gas jet, results in spectral separation of harmonics and more spatial structures.

Spectral structures are also very asymmetric. The reduction of the spectral bandwidth could be due to the fact that the XUV emission gets predominant in the leading front of the pulse before reaching the point of highest blue shift caused by $\alpha\frac{\mathrm{d}I_{IR}}{\mathrm{d}t}$. The spatial inter-fringes are smaller on the red side of the harmonics and larger on the blue side, as the spectral fringes.

6.2.2 Dependence on the pulse length

One expects that shorter driving pulses would produce shorter XUV pulses. Related to the helium-pressure dependent pulse duration after post-compression technique described on figure 5.20, we performed a study of HHG as a function of the pulse duration (figure 6.4).

The study is performed for helium pressure of 0, 2, 4, 6 and 8 mbar in the capillary corresponding approximately to 55, 40, 25, 14 and 10 fs. Other experimental parameters than helium pressure in the capillary are not necessary to be controlled to tune the driving pulses duration.

One of the most significant changes of XUV radiation is the spectral width of the detected harmonics. It is increasing with pressure and with 8 mbar of helium in the capillary (figure e) the spectral width of individual harmonics is so high that the harmonics spectrally overlap and create an XUV quasi-continuum.

The spectral width of harmonics is due to 2 phenomena: spectral width of the driving infrared pulse and a blue shift during HHG. As we saw on figure 5.15, the spectral width of the infrared pulses increase with the helium pressure generating directly large spectral width of the harmonics. However, the infrared pulse spectral width is less than $1/7$ of the central photon energy and it cannot explain XUV quasi-continuum. So the main phenomenon making the significant part of the harmonic spectral width is the XUV blue shift caused by $\alpha\frac{\mathrm{d}I_{IR}}{\mathrm{d}t}$. For high energy short pulses (as pulses generated via our post-compression technique), the time derivative of the intensity can become high enough to shift the photon energy close to one octave creating the XUV quasi-continuum. This is therefore a proof of having high energy very short femtosecond pulses available for HHG.

Another thing that one can see on figure 6.4 c), d) and e) are spatio-spectral structures in XUV spatially-resolved spectra. Those structures are robust and similar from one harmonic to the other.

6.2.3 Medium length influence

We studied the influence of propagation and phase-matching on the interference patterns. The figure 6.5 shows harmonic spectra obtained with the same parameters of the driving

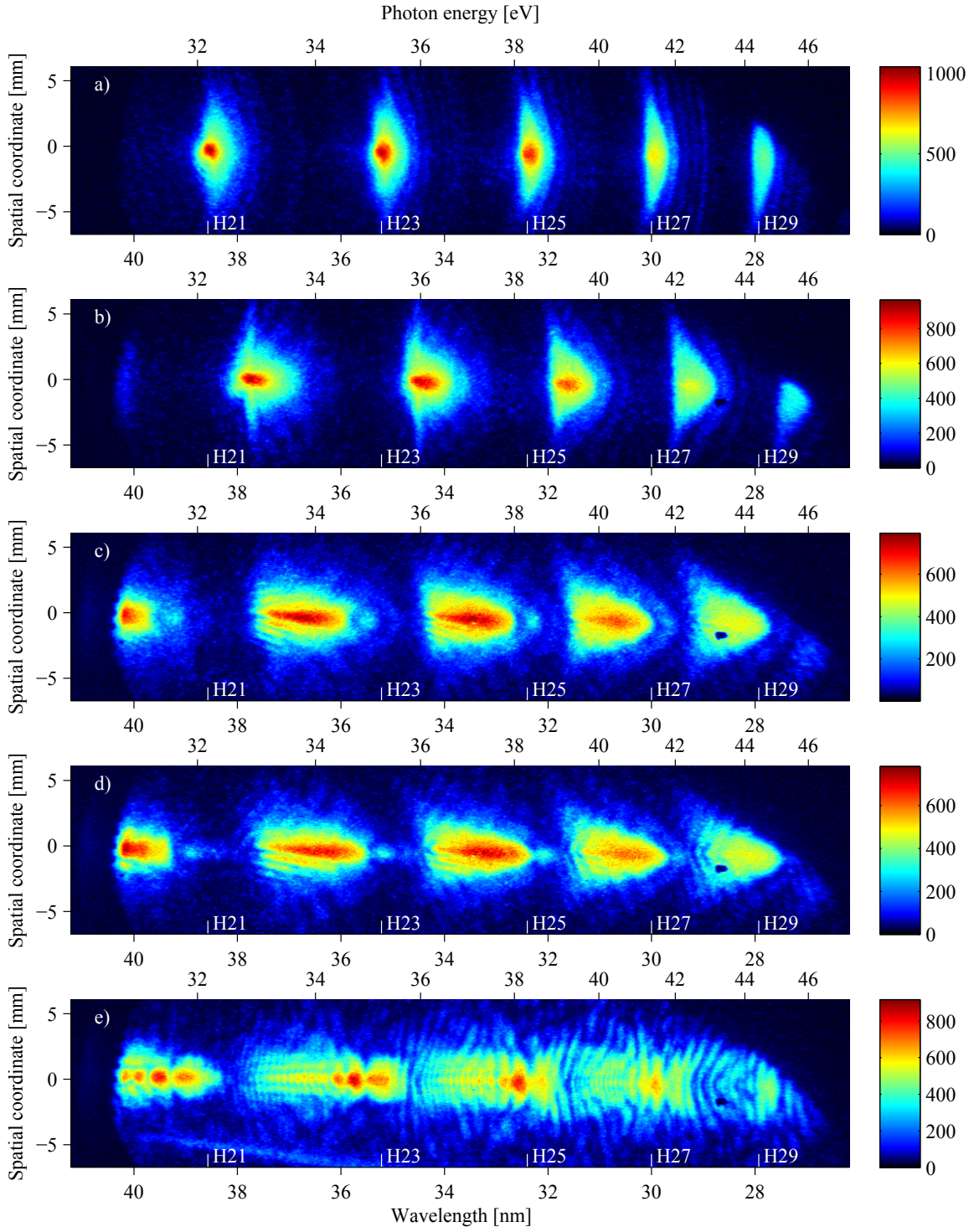

Figure 6.4 – (color) Experimental single-shot spatially and spectrally resolved XUV profiles generated with post-compressed pulses in argon gas jet placed 5 cm in front of the focus. The helium pressure in the capillary of post-compression is a) 0 mbar, b) 2 mbar, c) 4 mbar d) 6 mbar and e) 8 mbar respectively corresponding approximately to pulses of a) 50 fs, b) 40 fs , c) 25 fs, d) 14 fs and e) 10 fs. More details in text.

laser but with different density and length of the generating medium. We were basically changing the distance d_{jet} between the gas jet valve and the driving laser beam propagation axis. The gas expands from the valve in a jet with approximately 55 degrees of divergence[1] and therefore, the more the distance d_{jet} increases, the more the laser will propagate in a longer and more diluted gas medium.

Despite the change of those interaction conditions, all the spectra presented on figure 6.5 are highly structured and complex. However, it is clear that the structures get more pronounced for optimized conditions of short and dense medium where one generates the most of XUV signal. We recall that we machined the gas jet valve to obtain even shorter and denser medium as showed on figure 3.2.

For $d_{jet} = 4\,\text{mm}$ the medium is long and the gas pressure is low (figure a) the XUV divergence is low and similar for all wavelengths, the total signal is relatively low but the spectral interferences are present. For shorter distance of 2.5 mm (figure b), the overall signal gets stronger and its properties are close to the previous figure with a slightly higher XUV beam divergence. The spectral fringes are also very similar considering also small change of the spectral fringes position.

In general, approaching the gas jet valve from 2.5 mm to 1.3 mm on figures b), c), d) and e) does not affect qualitatively the structures. However, the level of overall XUV signal is increasing and the divergence is higher for some part of the spectra.

The integrated signal is on figure 6.6.

There is a clear trend on figure 6.6. The overall XUV signal in the far field decreases with the medium length.

For a very short and dense medium at $d_{jet} = 0.5\,\text{mm}$ corresponding to the medium length of 0.75 mm on figure 6.5 f), there is much more XUV signal and the divergence is the highest. All the fringes are now curved and the spatial fringes are more pronounced. They are stronger for longer wavelength. However the on-axis spectral interferences still exhibit the same patterns as for higher distance between the gas jet and the beam. We also stress that the XUV photon flux is maximum for a short and dense medium which corresponds to the conditions where the structures are most pronounced.

To conclude, structures were observed with different lengths of the generating medium. In other words, the observed structures were influenced but not created by propagation (for propagation-created structures see [He 09, Zhong 02]).

[1] Measured for 4.2 bar of argon backing pressure.

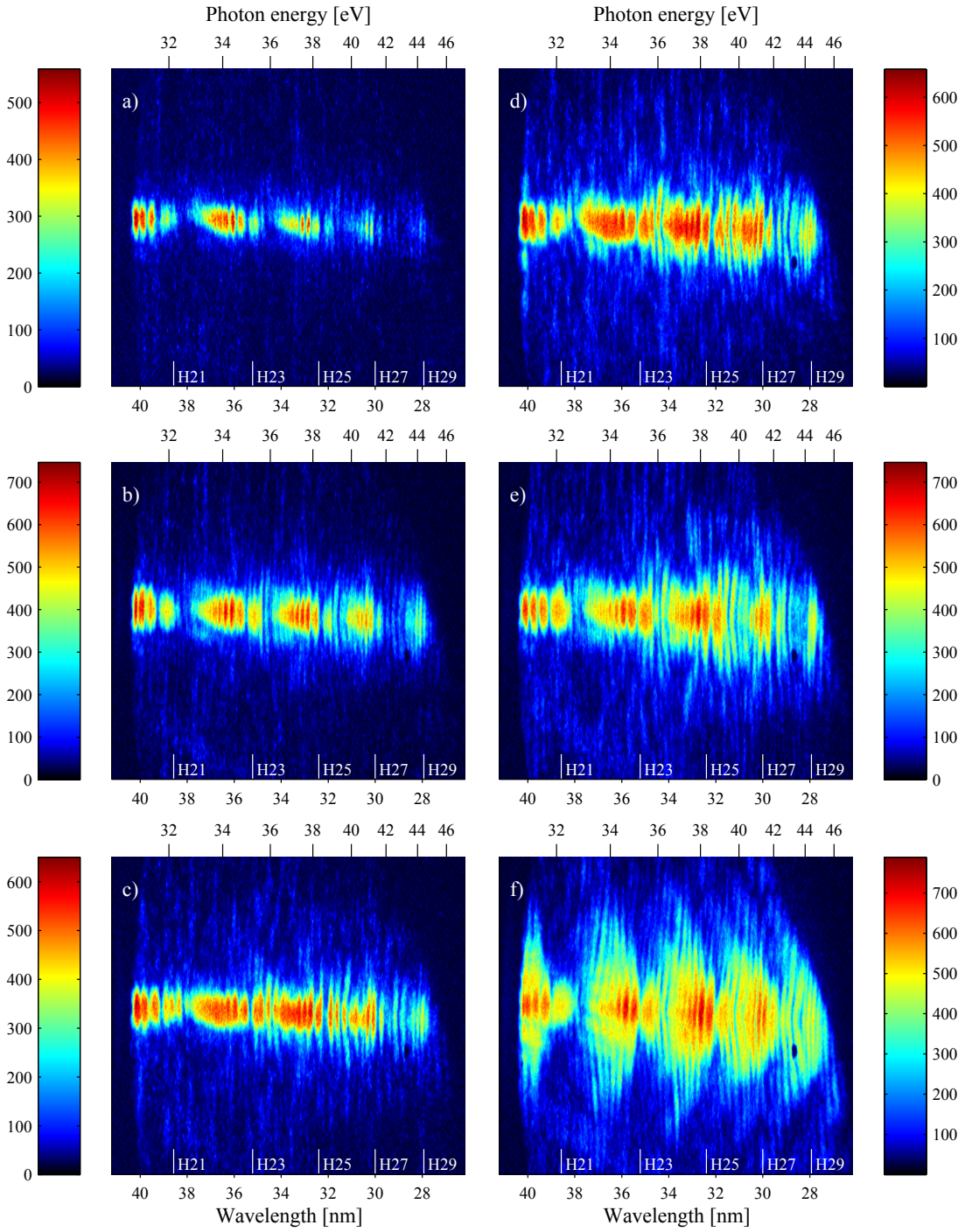

Figure 6.5 – (color) Experimental single-shot spatially and spectrally resolved XUV profiles generated with post-compressed pulses in argon gas jet placed 5 cm in front of the focus. The iris diameter was 12 mm and the argon jet backing pressure 4.5 bar. The distance between the gas jet valve and the beam is a) 4 mm, b) 2.5 mm, c) 2.2 mm d) 1.7 mm, e) 1.3 mm and f) 0.5 mm corresponding to calculated medium length of a) 4.33 mm, b) 2.80 mm, c) 2.49 mm d) 1.98 mm, e) 1.57 mm and f) 0.75 mm. More details in text.

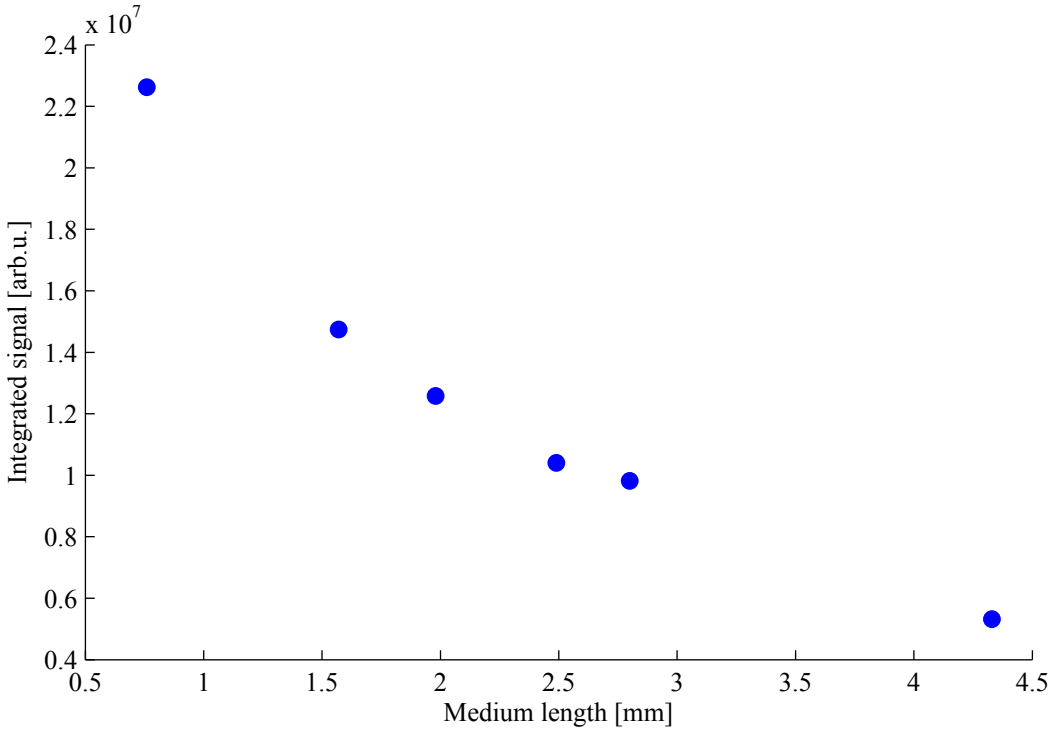

Figure 6.6 – Experimental integrated signal of the spatially resolved XUV spectra of figure 6.5 that decreases with calculated medium length. Note that the pressure decreases as the medium length increase.

6.2.4 Impact of the averaging

6.2.4.1 Averaging over multiple shots

The crucial parameter of presented spectra is the single-shot acquisition. On figure 6.7 a) we present a spatially resolved XUV spectrum obtained by integrating over 20 shots.

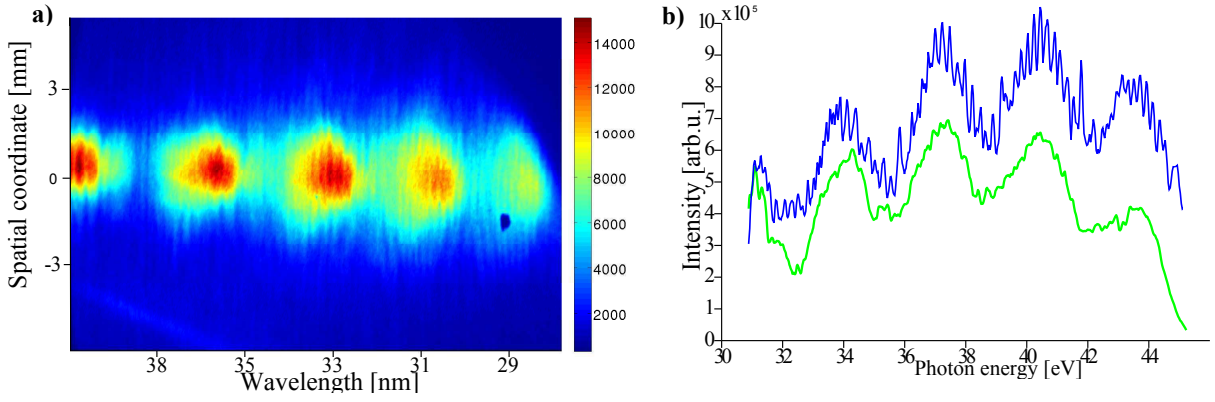

Figure 6.7 – (color) Experimental a) average over 20 shots spatially and spectrally resolved XUV profiles, b) spatially integrated spectra of a) (green) and spatially integrated spectrum of one shot (blue). Spectra weer generated with post-compressed pulses in argon gas jet placed 5 cm in front of the focus. The iris diameter was 12 mm and the argon jet backing pressure 4.5 bar. The single-shot signal (blue) has been multiplied by 20 and the curves have been shifted vertically for visibility.

The spatially integrated spectrum is shown on figure b) in green. From both figures, we can see that the fringes can be barely seen because the contrast is extremely poor. This can be compared to the figure 6.7 b) blue curve which describes the spatially integrated spectral profile of only one shot. One can see that averaging over 20 shots only nearly completely washed out spectral structures.

This is caused by intrinsic driving laser fluctuations of the pulse energy, beam profile, beam pointing, pulse duration, CEP and others. As the structures exact position and shape are very dependent on the driving laser parameters only small change in driving laser can cause the delicate structures to change enough to completely disappear when averaged of only few tens of shots.

6.2.4.2 Averaging over frequency or space

As a lot of structures are not straight vertical or horizontal only, integrating the spatio-spectrally resolved XUV profiles can also lead to loss of information. On figure 6.8 we show spatially resolved XUV spectra already seen on figure 6.2 c) and d) with their spatial and spectral integration.

The single-shot spatially and spectrally resolved XUV profiles on figures a) and d) contain complex spatio-spectral structures.

Integrating over space one can believe to detect a slightly modulated XUV continuum (figure b) and practically clean spectrally large harmonics on figure e).

Integrating over frequency leads to Gaussian-like spatial profile (figure c) without any modulations or triangular spatial profile (figure f) also without modulation or fringes.

We would like to stress in here that those integrated profiles are also single-shot.

6.2.4.3 Conclusion on averaging and integration

To conclude this section we insist that the spatially and spectrally resolved characterization on the single-shot basis is a necessary condition to observe all the structures in the XUV beam. Without the 3 conditions accomplished together one cannot know the XUV beam profile.

Note that such spatio-spectral structures are of major importance when estimating XUV intensity or temporal characteristics as isolated attosecond pulse generation and others. Smooth XUV spectra generated with high energy short pulses observed with averaging can be found in [Kanai 12, Wu 13, Ferrari 10].

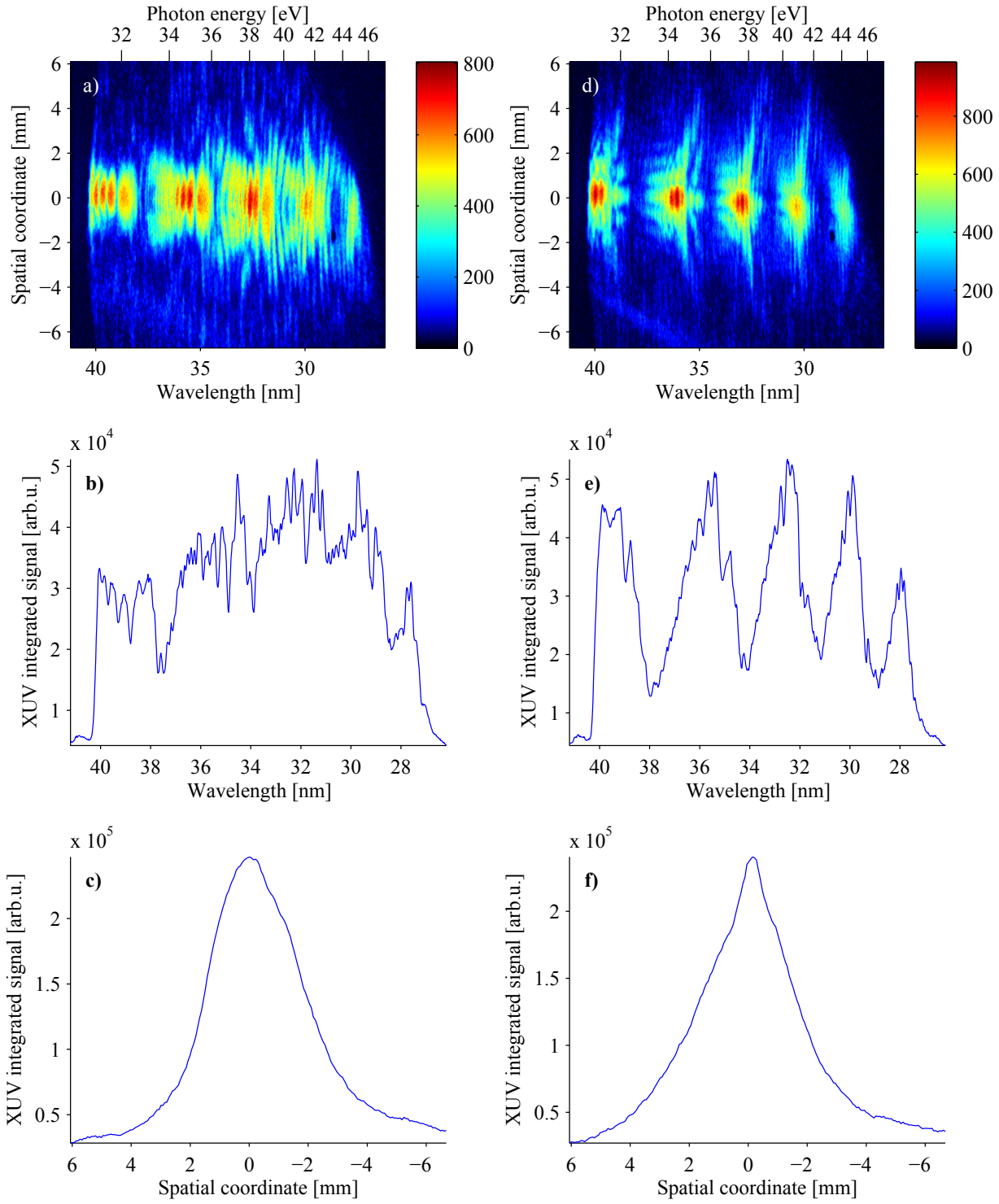

Figure 6.8 – (color) Comparison of single-shot experimental spatially and spectrally resolved XUV profiles a) and d), their spatial integration b) and e) and their spectral integration c) and f). All the figures were generated with 10 fs 10 mJ pulses 5 cm before the focus. Figures The iris diameter and corresponding peak intensity was a), b) and c) 12 mm, 1.7×10^{15} W/cm², d), e) and f) 14 mm, 2.3×10^{15} W/cm².

6.2.5 Iris clipping influence

When generating 5 cm before the focus, we have to check the infrared driving beam for spatial irregularities or structures that can be responsible for such a complex spatio-spectral XUV profiles. Therefore, we plot the driving beam spatial profile in the gas jet on figure 6.9.

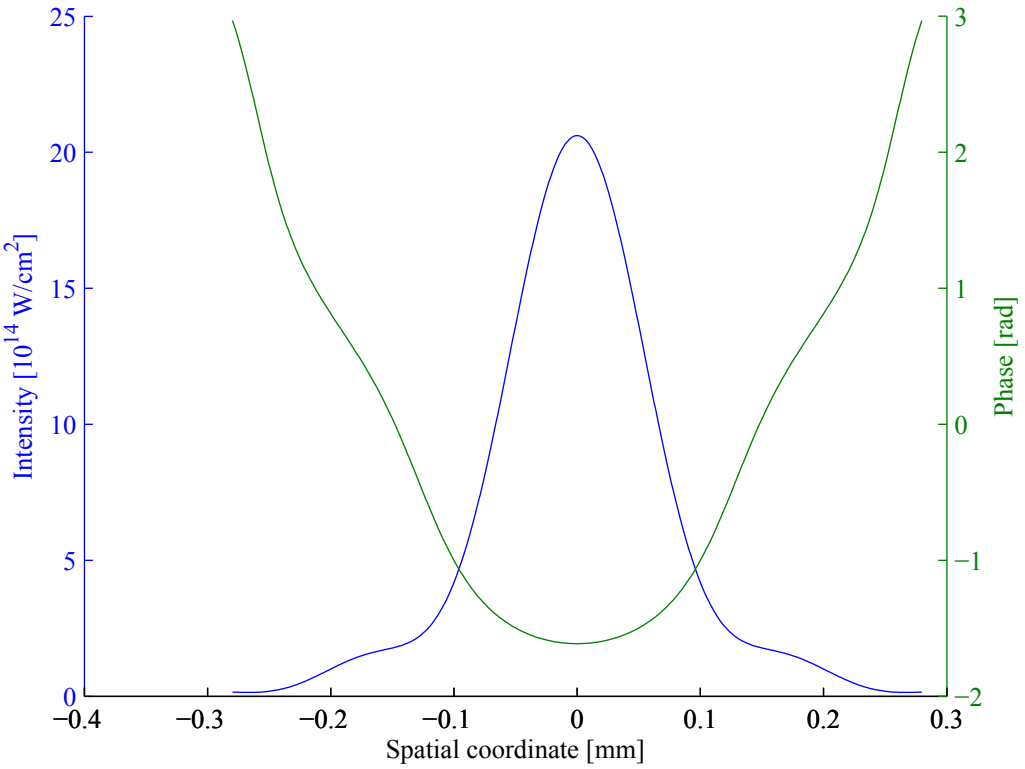

Figure 6.9 – (color) Calculated infrared driving beam spatial and phase profile 5 cm before focus for iris diameter of 14 mm. The profiles are obtained by diffracting a perfect Gaussian beam clipped by iris before diffraction by mean of an Hankel transform (see appendix A.). The focal length is 2 m and the beam w = 10 mm where w is the radius at I_{max}/e^2.

The iris diameter was chosen to simulate the infrared driving spatial and phase profile at the generation conditions of figure 6.2. We can see that the profile is smooth without any sharp modulation same as the phase. There is only small pedestal rising less than 9 % of the peak intensity for the iris diameter of 14 mm.

Indeed, the Rayleigh length[2] equals 10 cm for 10 mm iris diameter and shrinks to 6 cm for 14 mm iris making the iris still too close to cause important irregularities in the spatial profile and phase.

[2]In here we keep the definition of the Rayleigh range as the distance from the waist where the beam radius $w = \sqrt{2} \times w_0$

6.3 Interpretation

6.3.1 Simple simulations

We perform simulations to investigate the observed behavior of the XUV signal. The resulting XUV profiles are on figure 6.10.

We used simulation described in section 3.3 with pulses of 10 mJ, 10 fs and centered on 790 nm (according to experimental results). The generation plane position is 5 cm before focus and the iris diameter was chosen to match the experimental condition of figure 6.2.

The simulated spectra have a lot of common points with the experimental one. There are complex spatio-spectral structures, the harmonics are spectrally very large and the structures are similar for consecutive harmonics.

The low intensity case of 10 mm iris diameter shows simulated harmonics that are more divergent than the experimental one. They also contain intensity maximum on axis. The simulation also shows spectral fringes, but they are not as regular as experimentally observed. Also in simulations, the harmonics are spectrally less large than experimentally.

The middle case of 12 mm the iris diameter shows equally dispersed intensity over the space and spectrum. The harmonics are too divergent compared to the experimental case.

The highest intensity case of 14 mm iris diameter shows the simulated spectra more complex as the experimental one also are. On the other hand the experimental harmonics are less divergent and for the widest iris diameter of 14 mm the maximum of the intensity lies on axis, while the simulated harmonics show huge maxima off axis. This would suggest that the harmonic dipole depletion on axis is not present in the same way as in the simulation.

We have discussed in chapter 3 the influence of the on-axis position of the generating medium on HHG. Therefore, we simulate far-field spatially resolved XUV profiles in different position of the medium on figure 6.11.

We observe clear dependence of the structures on the position of the generating medium. When the medium is 2.5 cm before the focus (figure 6.11 a), the harmonics are spatially and spectrally very large. They contain a lot of regular spatial structures which size depends on wavelength. Compared to the medium located 5 cm before the focus (figure 6.10 c) the maximum of intensity is located on axis. The harmonics are spectrally very large and form a quasi-continuum with spectral structures.

When generated at focus (figure 6.11 b), the harmonics are spatially and spectrally very narrow but they still contain spectral and spatial structures.

When the generating medium is located after the focus (figures 6.11 c) and d), the harmonics become spectrally larger and more spatial and spectral structures appear. However,

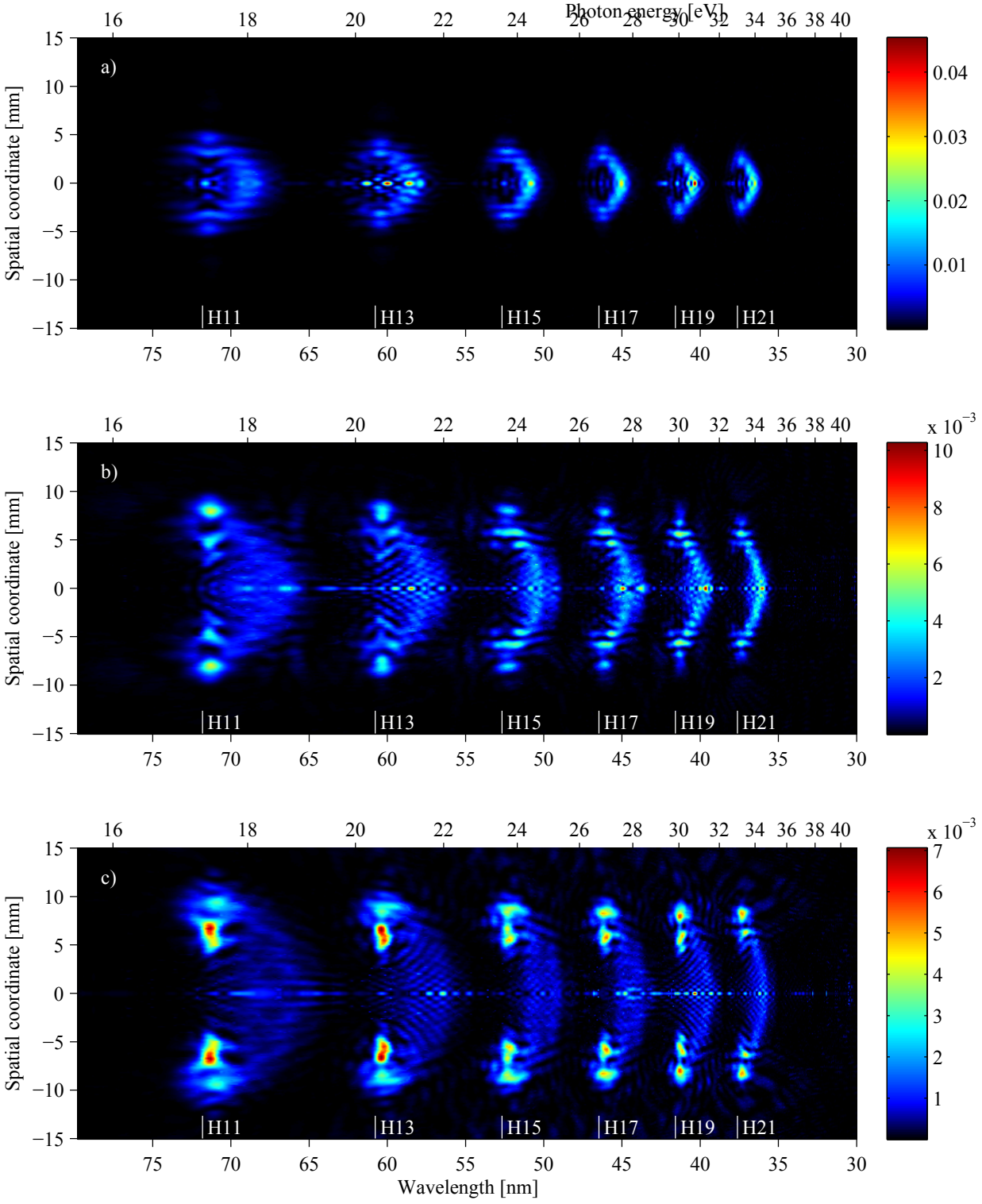

Figure 6.10 – (color) Simulated single-shot spatially and spectrally resolved XUV profiles generated in argon jet with 10 fs 10 mJ pulses 5 cm before the focus. The iris diameter and corresponding peak intensity was a) 10 mm, 1.2×10^{15} W/cm², b) 12 mm, 1.7×10^{15} W/cm² and c) 14 mm, 2.3×10^{15} W/cm². Those simulated figures correspond to the experimental ones on figure 6.2.

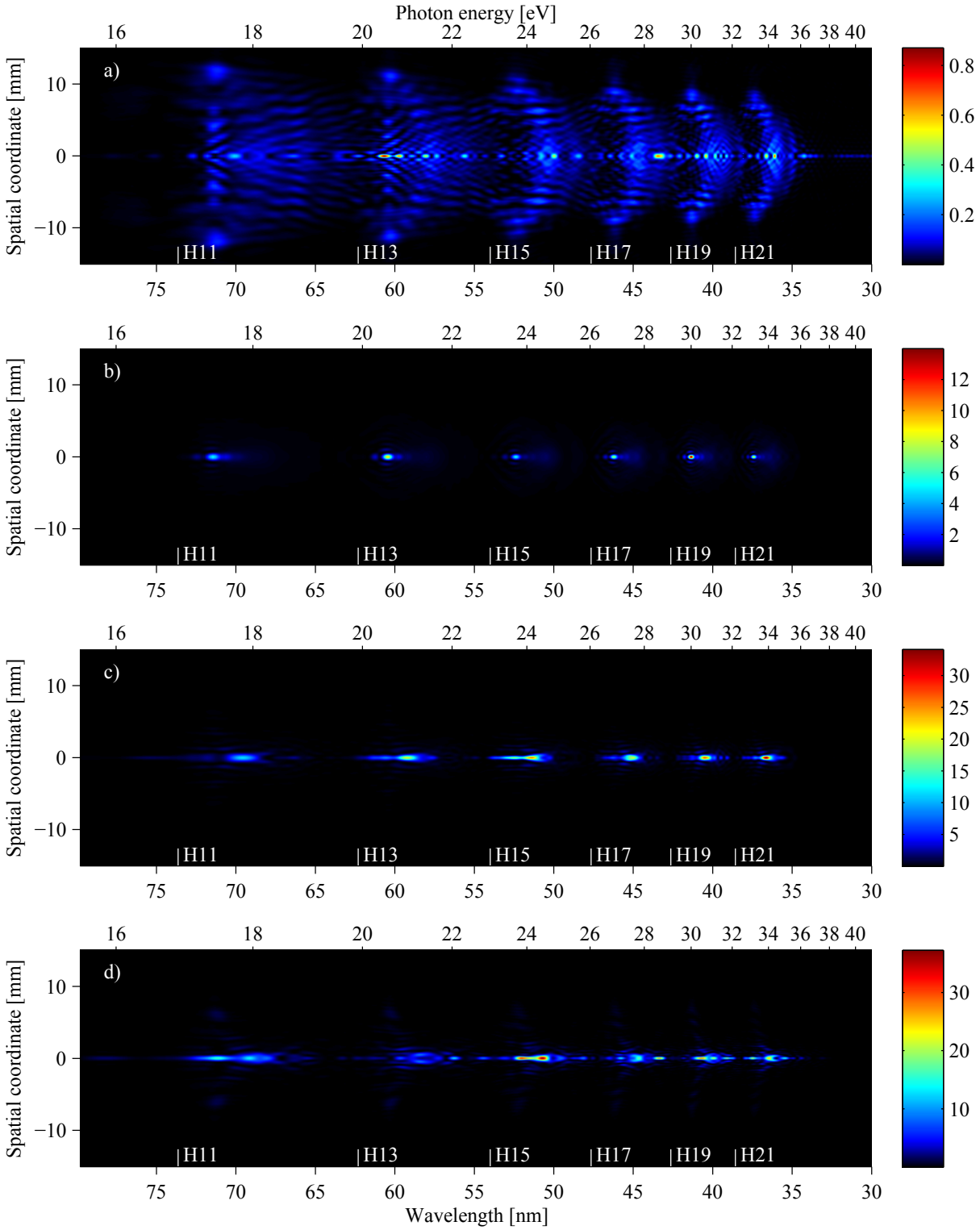

Figure 6.11 – (color) Simulated single-shot spatially and spectrally resolved XUV profiles generated in argon jet with 10 fs 10 mJ pulses. The iris diameter was 14 mm. The generating medium was placed a) 2.5 cm before the focus, b) at focus, c) 2.5 cm after the focus and d) 5 cm after the focus.

the main signal remains on axis.

6.3.2 Numerical simulation

6.3.2.1 Far-field simulation

To compare with our simple simulation, in this section we present a complex simulation performed by Vasily Strelkov. The spatio-spectral XUV profiles in the far field are presented on figure 6.12.

The simulated far-field spatially resolved XUV spectra were calculated using the same conditions as the experimental one on figure 6.2. The generating medium is placed 5 cm before the focus of 2 m focal length mirror. The driving pulse energy is 10 mJ and duration is 10.67 fs with a $\cos^2$ temporal profile that corresponds to 4 cycles. The iris diameter and peak intensity in the generating medium is a) 10 mm, 1.15×10^{15} W/cm², b) 12 mm, 1.85×10^{15} W/cm² and c) 14 mm, 2.34×10^{15} W/cm². The propagation is taken into account through modification of the driving pulse wave front. The length of the medium is 500 µm for an estimated effective pressure of argon of 30 mbar in the gas jet.

In the generating medium the calculation is based on microscopic response of the target medium as a function of time and space using the theory described in [Strelkov 06a]. Being based on the Strong-Field Approximation, this theory uses tabulated ionization rates and estimates more realistic ratio of the different quantum path contributions in the generation process (for a single atom in the near field) than TDSE approach. The microscopic response is used to further calculate the macroscopic XUV signal in the far field using the Hankel transform.

For iris = 10 mm on figure 6.12 a) one can see spatial structures in all harmonics that are little spectrally modulated. The spectral bandwidth of the harmonics is lower than in the experimental case. The spectral structures are practically not present on axis.

Opening iris to 12 mm (figure b), the spectral structures appear on axis and the harmonics become spectrally larger. Also the spatial structures are now present almost over the spectrum.

With iris diameter of 14 mm (figure c) the harmonics become so spectrally large and structured that it is nearly impossible to distinguish individual harmonic from each other. Spatial structures are regular in agreement with the experiment. On the other hand the spectral structures are completely arbitrary that does not correspond to experimental ones.

The role of propagation was also numerically simulated on figure 6.13.

Numerically the propagation in the generating medium does not alter the spectral fringes. This conclusion is in very good agreement with the experimental results shown on figure 6.5. Consequently, propagation in the generating medium and phase-matching are

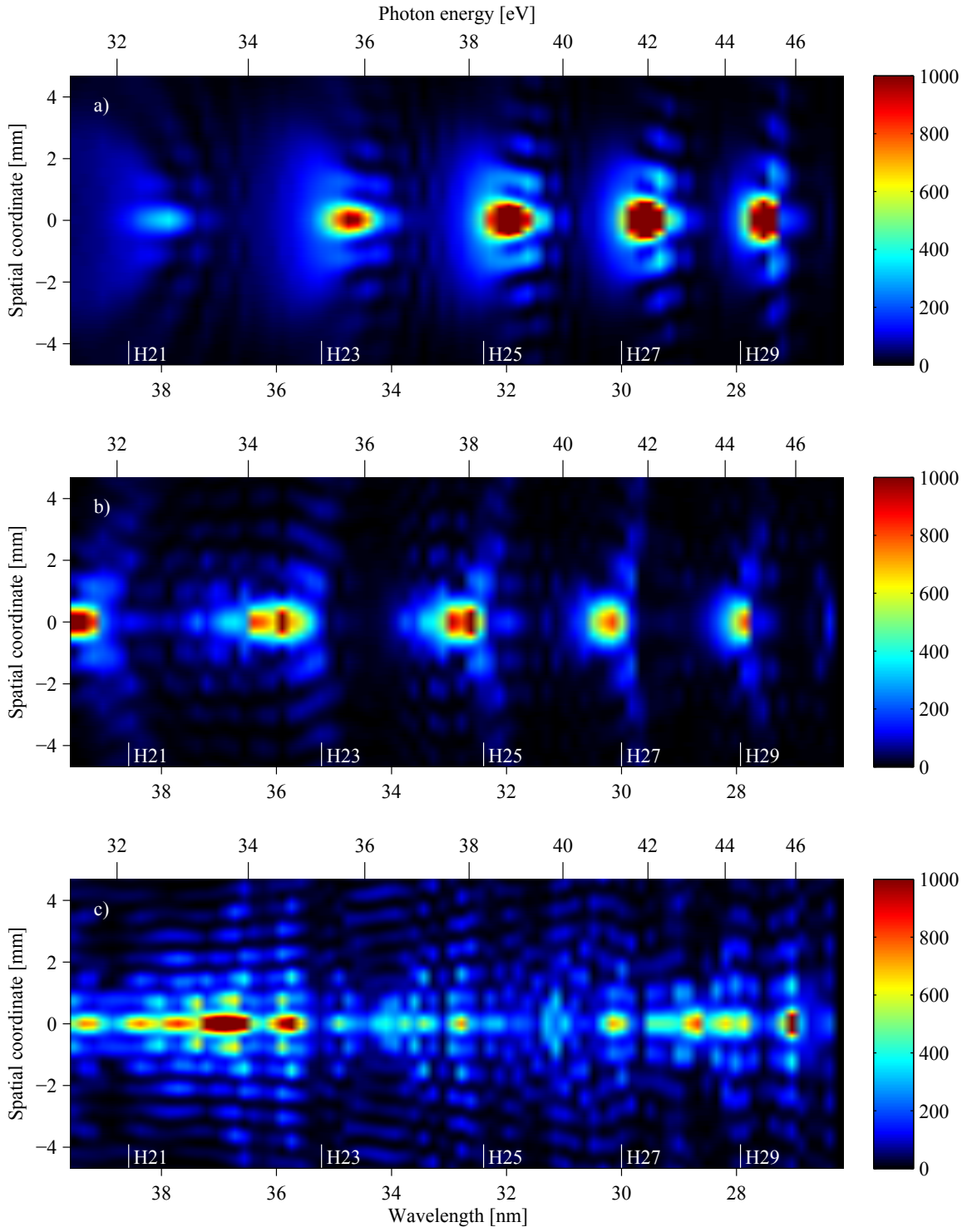

Figure 6.12 – (color) Simulated far-field spatially resolved XUV spectra. The conditions are as the experimental one on figure 6.2. The driving pulse energy is 10 mJ and duration is 10.67 fs with a $\cos^2$ temporal profile. The iris diameter and peak intensity in the generating medium is a) 10 mm, 1.15×10^{15} W/cm², b) 12 mm, 1.85×10^{15} W/cm² and c) 14 mm, 2.34×10^{15} W/cm². The propagation in the medium is considered.

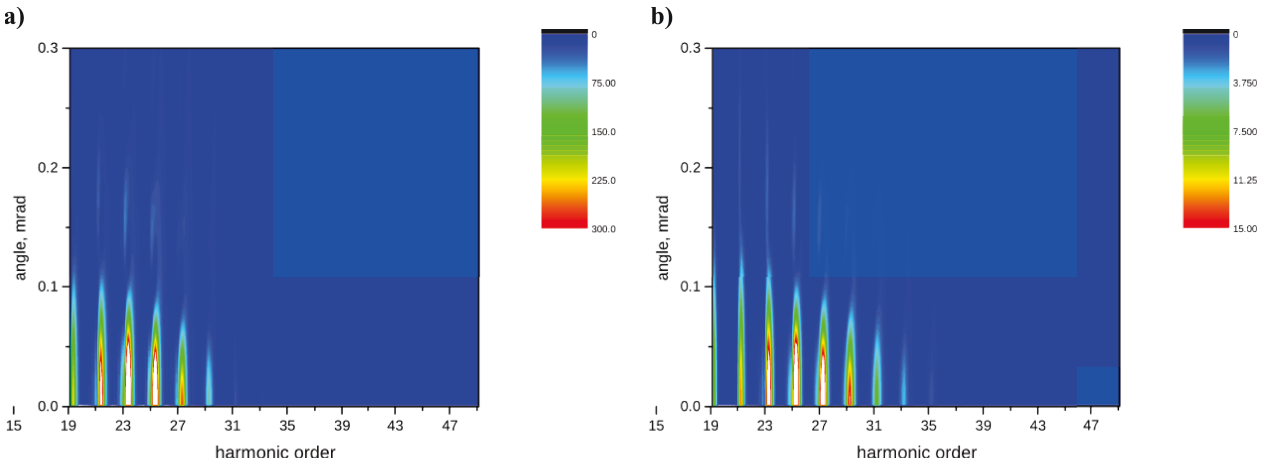

Figure 6.13 – (color) Simulated far-field spatially resolved XUV spectra. The conditions are as the experimental one on figure 6.2. The driving pulse energy is 10 mJ and duration is 10.67 fs with a $\cos^2$ temporal profile. The iris diameter and peak intensity in the generating medium (30 mbar of argon) is 10 mm corresponding to 1.15×10^{15} W/cm^2. The propagation in the medium is a) not considered and b) included in the simulation.

not the dominant mechanism driving the spatio-spectral structures we observed.

6.3.2.2 Conclusion

In general the spectrum obtained at high intensity contains a lot of spatio-spectral structures and the overall shape evolves with the iris diameter. The spatial structures are in very good qualitative agreement with the experiment suggesting that they are principally due to the spatial coherence and diffraction to the far field.

Note that the spatio-spectral structures strongly depend on multiple driving laser characteristics as the intensity spatial profile, temporal profile, the CEP [Strelkov 06b], and others so any impurities or irregularities of the laser will strongly affect obtained XUV structures. Because of this, it is difficult to obtain a good quantitative agreement between the calculated and experimental XUV profile. Thus only qualitative agreement is achieved.

The dominant parameters are the nonlinearity of the atomic response and the depletion of the neutral atoms. Then in the far field this leads to complex structures as already discussed in chapter 3.

6.3.2.3 Near-field XUV profile

To give an insight into the XUV spatio-temporal profile in the gas jet that leads to the far-field spatio-spectral profile presented on figure 6.12 c), we present the first on figure 6.14.

The figure 6.14 demonstrates a fast evolution of the XUV emitting spatial profile during a time shorter than the driving pulse duration. At the leading edge of the driving pulse,

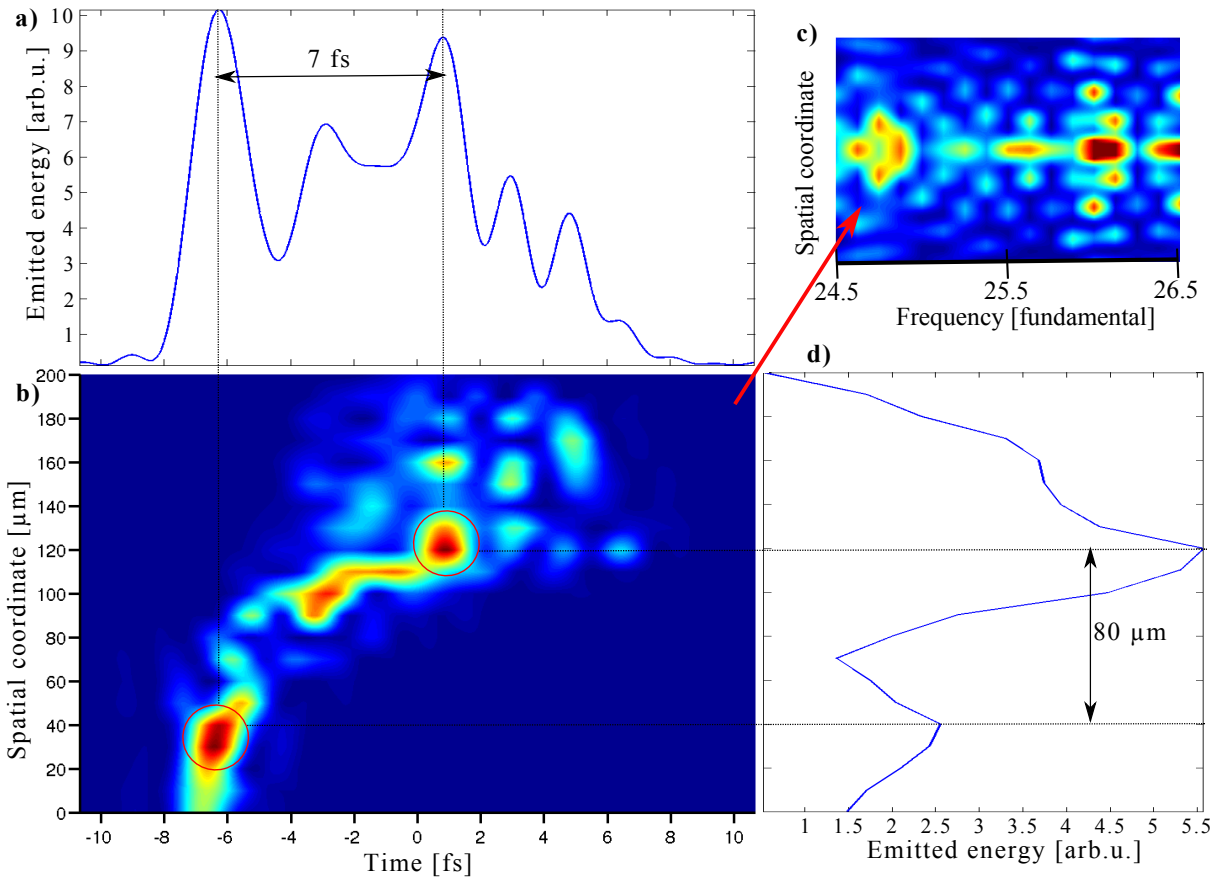

Figure 6.14 – (color) Spatio-temporal XUV profile in the gas jet (near-field) for spectral range from $24.5\omega_0$ to $26.5\omega_0$ that corresponds to spectrally broadened (thus blue-shifted) harmonic 25 (figure c). b) presents the spatio-temporal XUV profile, a) the spatially integrated temporal profile of b) and d) is the temporally integrated spatial profile of b).

around 7 fs before the peak intensity, the XUV emission occurs on axis. Then the medium is depleted so the HHG shifts off axis and continues until there is still enough of intensity i.e. about the peak intensity of the driving pulse.

Moreover, there are two dominant dipole emissions in time and space. On figure they are indicated by red circles. They are separated by 7 fs in time and by 80 μm in the space. Those two maxima create the spatial and spectral interferences observed in the far field. Note that with continuous emission there could be no spectral fringes in the far field.

The harmonic dipole spatial distribution is time-dependent and have to create structures in the far field spatially resolved spectra. This is in good agreement with experimental and calculated far-field profiles.

An interesting thing is that the near-field on-axis emission should produce an isolated attosecond pulse on axis. However, the off-axis near-field signal also contributes to the on-axis far-field signal (and vice versa) so this isolated attosecond pulse will no more be isolated in the far field.

In general, spatial separation of dipoles in the near field can be directly linked to the spatial structures in the far field. Note that the first indicated near-field maximum on the leading edge would be strongly blue-shifted (due to $\alpha\frac{\mathrm{d}I_{IR}}{\mathrm{d}t}$) and the second one red-shifted but closer to the harmonic line. Therefore inside single harmonic the spatial structures are smaller as the wavelength increases as observed on experimental figure 6.2.

From the spatial point of view, the average experimental spatial inter-fringe distance is around 1 mm which is in good agreement with the expected interfringe distance in the near field from two sources separated by 80 μm.

6.3.3 Near-field simulations comparison

To compare our simple simulation with the complex numerical one presented above we show on figure 6.15 the near-field spatio-temporal profile of the harmonic 21 in the gas jet calculated with the first one.

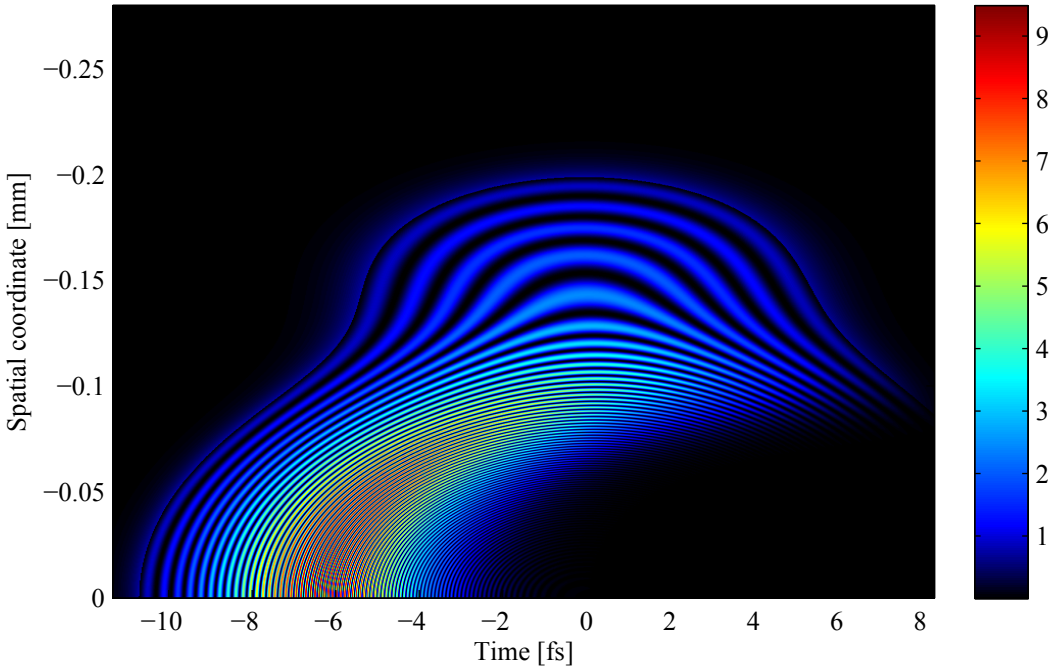

Figure 6.15 – (color) Simulated spatially and temporally resolved profile of the harmonic 21 in the near field (in argon jet) with 10 fs 10 mJ pulses 5 cm before the focus. The iris diameter and corresponding peak intensity was 14 mm and 2.3×10^{15} W/cm^2.

The figure 6.15 shows the spatio-temporal profiles of the harmonic 21 in the gas jet. The figure corresponds to figure 6.14 b). Except that the complex figure is valid only for harmonic 25 but the simple one is for harmonic 21. However, we have seen that in the simple simulation the harmonics are similar.

The overall shape of the time dependent spatial distribution of the emitters is the same

in the simple and the complex simulation, although much more structured in the case of complex numerical simulation. In a simple simulation the XUV emission on axis is longer. Also off axis there is no single maximum but a continuous emission. This is the reason why the far-field spatio-spectral profiles in the simple simulation do not contain regular spectral fringes.

However the depletion of the neutral atoms causes the same spatial modulation and so the spatial distribution of emitters after the temporal intensity peak is also located around 110 μm off axis. This make the same spatial fringes in the far field for both types of simulation.

We plotted near-field spatially resolved temporal profiles of harmonics 11-21 on figure 6.16.

The near-field spatially resolved temporal profiles of harmonics 11-21 (figure 6.16) contains attosecond pulses. When only one harmonic is considered (figure 6.15) the emission is not divided into attosecond pulses.

We can also see that with larger iris diameter the on-axis depletion arrives earlier than with smaller iris diameter. This is due to the higher intensity. The off-axis emission, however, has approximately the same duration for each of three studied iris diameters. With higher intensity one can also generate harmonics at longer distance from axis. The distance between the emitting dipoles in the near field would then define the spatial interfringe distance in the far field.

6.4 Conclusion on HHG with 10 fs TW pulses

In this chapter we have presented an experimental and numerical study of HHG in argon jet using pulses of 10 mJ and 10 fs duration. We have observed that HHG in such extreme conditions lead to spectrally very large harmonics (quasi-continuum) with complex structures both in frequency and space in the far field.

We have demonstrated that such structures are only observable when detecting spatially and spectrally resolved XUV signal on the single-shot basis. Averaging over multiple shots or integration over one of the dimensions would wash out the structures. As the structures are relatively robust, their exact position nevertheless is very sensitive on multiple laser parameters. Thus even with a very good stabilization of carrier-envelope phase (CEP) that reaches typically 320 mrad (RMS) [Feng 13] one would loose the structures while averaging over several shots.

We have shown that the spatial structures are mainly due to the spatial coherence of the XUV source. Considering the depletion of the harmonic dipole due to the high intensity of the driving pulses the near-field XUV spatial profile varies significantly during the time

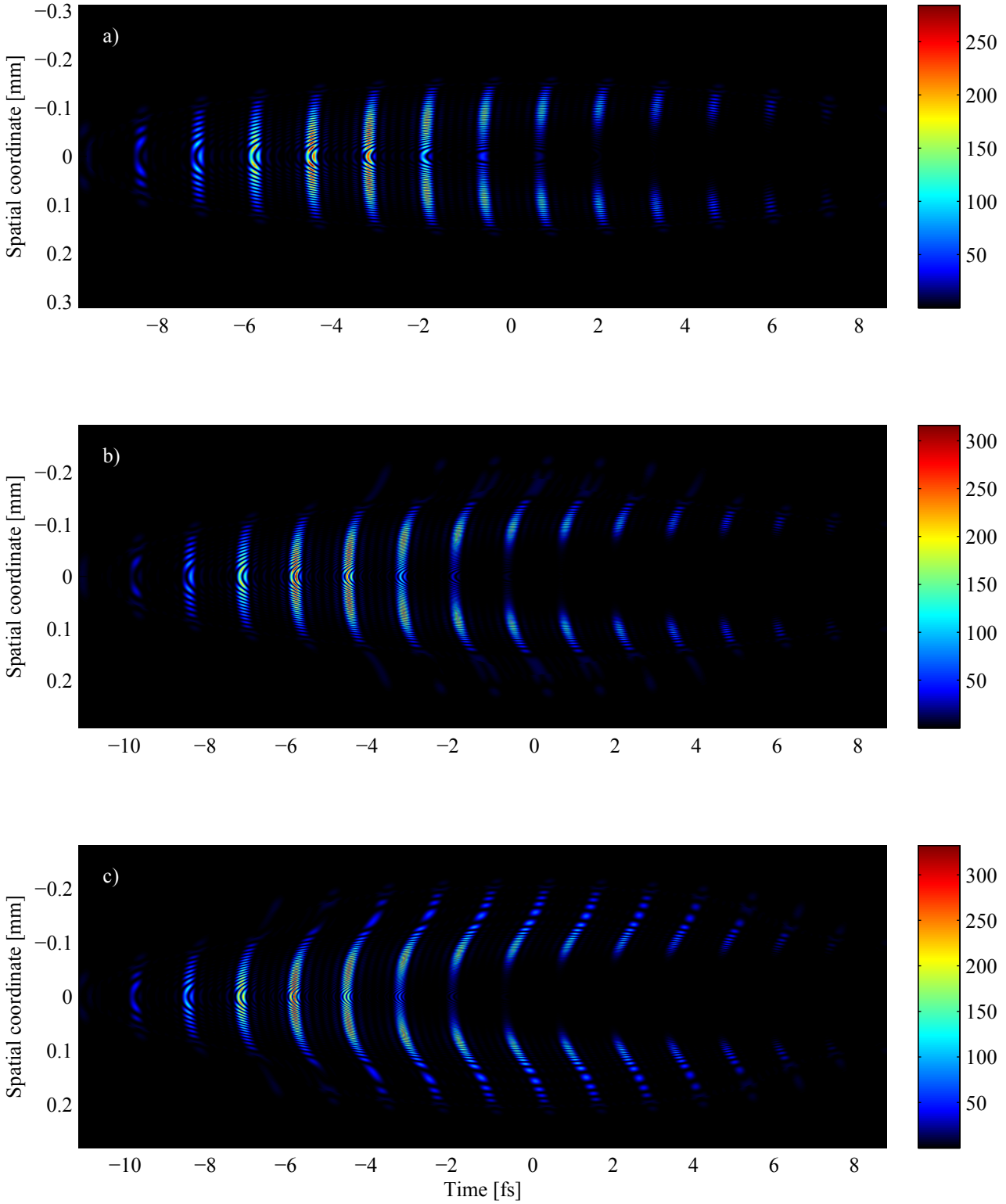

Figure 6.16 – (color) Simulated spatially and temporally resolved XUV profiles in the near field (in argon jet) with 10 fs 10 mJ pulses 5 cm before the focus. The iris diameter and corresponding peak intensity was b) 10 mm, 1.2×10^{15} W/cm², c) 12 mm, 1.7×10^{15} W/cm², d) 14 mm, 2.3×10^{15} W/cm². Those simulated figures correspond to the experimental ones on figure 6.2 and to simulated far-field on figure 6.10.

scale shorter than the driving pulse duration creating a very modulated XUV signal. This complex near-field signal diffracts to the far field creating the spatial fringes.

The spectral structures were explained using the spatial coherence, depletion of the harmonic dipole and the shaping of the driving pulse during propagation. Two time-distinguished maxima were observed in the near field leading to spectral fringes in the far field.

Our simulation that does not consider the driving pulse propagation shaping is in a good agreement with the spatial characteristics of the experimental spectra. The spectral broadening is also explained.

The complex SFA simulation considers also the driving pulse propagation and is consistent with XUV experimental results both in frequency and space. Note that important role of driving pulse shaping during the propagation in the medium was already suggested and discussed in section 3.4.4 on page 119.

We stress that neither phase-matching conditions (as described in section 2.2) nor the propagation of XUV in the gas medium were considered in both types of simulations. As we succeeded to explain the XUV behavior without the phase-matching and XUV propagation in the medium, we can conclude that those effects do not play major role in the structures observed with HHG at high energy TW level pulses generated in a gas jet. This finding is coherent with the experimental study of medium-length influence on the XUV structures.

The direct result of our findings is that the off-axis near-field signal contributes also to on-axis far-field signal. Therefore even if one can obtain a single attosecond pulse on axis in the generating medium (as suggested by the SFA simulation) there are more of such pulses both on and off axis in the far field where the detector and applications are typically placed. Therefore, we observe that the spatial filtering in the far field cannot help to obtain a single attosecond pulses.

Chapter 7

Conclusion & perspectives

In this work, we present scientific progress in our way for the generation of high energy isolated attosecond pulses. We present HHG with high energy femtosecond pulses and developed simple simulations to identify important physics phenomena. We demonstrate two techniques of spatial shaping of the driving pulses and their advantage for HHG. We also show the development of high energy TW level post-compression technique that provides pulses of 10 fs and 10 mJ and HHG with such pulses.

We characterize the generated XUV emission spatially and spectrally at the single-shot basis and we estimate XUV photon number using XUV photodiode. With high energy driving pulses, we observed that HHG in the gas jet with a very short medium length maximizes the XUV photons number as compared to gas cell and gas filled capillary.

We also observed many structures in spatially resolved XUV spectra in the far field. Those structures are very robust and reproducible and have been observed in many different gases and generation geometries. Without spatial and spectral characterization on the single-shot basis the structures are not visible.

We developed simple simulations to identify those structures and we observed similar structures as experimentally. We identified them as a result of spatial coherence of the XUV source and the diffraction to the far field. In the near field, the harmonic amplitude and phase are spatially and temporally dependent and their profiles are strongly modulated. Such modulated profiles diffract to structured spatially resolved spectra in the far field. Those structures are mostly identified with interference of the short path with itself via $\alpha\frac{\mathrm{d}I_{IR}}{\mathrm{d}t}$ and the depletion of the ground state of atoms in generating medium. We observed that propagation of the XUV in the generating medium has little influence on the structures.

We developed a driving beam spatial shaping compatible with high energy TW femtosecond pulses. A TOP mirror allows us obtaining a flat-top beam profile in the focus.

The XUV emission is then temporally confined. We show theoretically that using high intensity flat-top driving beam with 10 fs pulses leads to only 2 attosecond pulses but should lead only to 1 pulse when considering propagation [Strelkov 08]. An adaptive optics allows us to have the driving beam of regular spatial profile and phase even out of focus. Such a beam is used for HHG with a large diameter driving beam and control of the XUV beam is demonstrated.

We developed a high energy TW post-compression technique and we obtained pulses of 10 fs and 10 mJ in a quasi-Gaussian spatial profile. The technique is based on ionization-induced self-phase-modulation and is compatible with high energy TW level pulses. We performed HHG with such pulses and obtained XUV quasi-continuum spectra with spectral and spatial structures. We performed simple simulations and SFA simulations and we observed similar structures even without considering the XUV propagation in the medium.

In the future, the developed techniques should be coupled together. Performing the HHG with 10 fs pulses and flat-top beam should generate high energy isolated attosecond pulses. This was investigated theoretically in this work and we found that the flat phasefront and intensity profile of the driving beam would generate flat phasefront of the XUV beam. Such a beam would thus contain isolated attosecond pulse that withstand propagation to the far-field. To obtain more energy in the attosecond pulses one would perform HHG far from focus where the driving beam is large. However, this is only possible with a regular driving beam (corrected for instance with a deformable mirror).

Afterward a temporal characterization of attosecond pulses is necessary. The techniques based on time (such as XUV autocorrelation) are preferable [Kruse 10, Nikolopoulos 05] to avoid the influence of spatio-spectral XUV structures than techniques that features spatial integration or do not apply to the whole XUV beam [Sansone 06, Paul 01, Bourassin-Bouchet 10, Frumker 12, Mairesse 05].

The structures in the spatially resolved XUV spectra could be also used to characterize the HHG process via inverse imaging. The Coherent Diffraction Imaging technique is nowadays routinely used to retrieve imaged sample objects with numerical algorithms. These algorithms are applied to diffraction pattern in the far field. One can reach nanosecond spatial resolution while illuminating the sample object with X-rays or XUV. In our case, we can consider the generating medium as the diffracting object. We observe diffraction pattern of the generated XUV in the far field and we know the position and size of the medium. Therefore, with Coherent Diffraction Imaging technique it may be possible to retrieve our "sample object" – the generating medium spatial profile. Moreover, as our XUV source is spectrally very broad, one can think about resolving also a time dynamics of our medium.

During our work, the driving pulse duration was around 50 fs and with our post-

compression technique we generated 10 fs pulses. After this work, a dazzler was installed in the Eclipse laser chain and the duration dropped to 30 fs. Therefore, shorter pulses should be generated using the post-compression technique or 10 fs pulses with more energy. Spectral phase of the driving beam is also flat giving more control over the HHG process. With such driving beam it should be easier to generate high energy attosecond pulse that would be suitable to explore new domains such as XUV induced non-linear processes.

Bibliography

[Abel 09] M. J. Abel, T. Pfeifer, P. M. Nagel, W. Boutu, M. J. Bell, C. P. Steiner, D. M. Neumark & S. R. Leone. *Isolated attosecond pulses from ionization gating of high-harmonic emission.* Chemical Physics, vol. 366, no. 1–3, pages 9 – 14, 2009. Attosecond Molecular Dynamics.

Cited on page(s) 20

[Agostini 04] P. Agostini & L. F. DiMauro. *The physics of attosecond light pulses.* Rep. Prog. Phys., vol. 67, page 913, 2004.

Cited on page(s) 19

[Altucci 96] C. Altucci, T. Starczewski, E. Mevel, C.-G. Wahlström, B. Carré & A. L'Huillier. *Influence of atomic density in high-order harmonic generation.* J. Opt. Soc. Am. B, vol. 13, no. 1, pages 148–156, Jan 1996.

Cited on page(s) 129

[Ammosov 86] M. V. Ammosov, N. B. Delone & V. P. Krainov. *Tunnel ionization of complex atoms and of atomic ions in an alternating electromagnetic field.* Sov. Phys. JETP, vol. 64, page 1191, 1986.

Cited on page(s) 57

[Augst 89] S. Augst, D. Strickland, D. D. Meyerhofer, S. L. Chin & J. H. Eberly. *Tunneling ionization of noble gases in a high-intensity laser field.* Phys. Rev. Lett., vol. 63, pages 2212–2215, Nov 1989.

Cited on page(s) 28

[Augst 91] S. Augst, D. D. Meyerhofer, D. Strickland & S. L. Chint. *Laser ionization of noble gases by Coulomb-barrier suppression.* J. Opt. Soc. Am. B, vol. 8, no. 4, pages 858–867, Apr 1991.

Cited on page(s) 28

[Auguste 12] T. Auguste, O. Gobert, C. F. Dutin, A. Dubrouil, E. Mével, S. Petit, E. Constant & D. Descamps. *Application of optical-field-ionization-induced spectral broadening in helium gas to the post-compression of high-energy femtosecond laser pulses.* Journal of the Optical Society of America B: Optical Physics, vol. 29, no. 6, pages 1277–1286, 2012.

Cited on page(s) 183, 187, 206

[Auguste 13] T. Auguste, C. Fourcade Dutin, A. Dubrouil, O. Gobert, O. Hort, E. Mével, S. Petit, E. Constant & D. Descamps. *High-energy femtosecond laser pulse compression in single- and multi-ionization regime of rare gases: experiment versus theory.* Applied Physics B: Lasers and Optics, pages 1–13, 2013. Article in Press.

Cited on page(s) 183, 186, 206

[Balcou 93] Philippe Balcou. *Étude de la génération d'harmoniques d'ordre élevé en champ intense.* PhD thesis, Université Paris 6 Pierre et Marie Curie (France), 1993.

Cited on page(s) 132

[Balcou 97] P. Balcou, P. Sali'eres, A. L'Huillier & M. Lewenstein. *Generalized phase-matching conditions for high harmonics: The role of field-gradient forces.* Phys. Rev. A, vol. 55, pages 3204–3210, Apr 1997.

Cited on page(s) 20

[Baumgartner 79] R. Baumgartner & R. Byer. *Optical parametric amplification.* Quantum Electronics, IEEE Journal of, vol. 15, no. 6, page 432–444, 1979.

Cited on page(s) 182

[Becker 02] W. Becker, F. Grasbon, R. Kopold, D. B. Milošević, G. G. Paulus & H. Walther. Above-threshold ionization: From classical features to quantum effects, volume 48 of *Advances In Atomic, Molecular, and Optical Physics*, pages 35–98. Elsevier, 2002.

Cited on page(s) 32

[Bohman 10] S. Bohman, A. Suda, T. Kanai, S. Yamaguchi & K. Midorikawa. *Generation of 5.0 fs, 5.0 mJ pulses at 1 kHz using hollow-fiber pulse compression.* Optics Letters, vol. 35, no. 11, pages 1887–

1889, 2010.

Cited on page(s) 183, 206

[Bouhal 98] A. Bouhal, P. Salières, P. Breger, P. Agostini, G. Hamoniaux, A. Mysyrowicz, A. Antonetti, R. Constantinescu & H. G. Muller. *Temporal dependence of high-order harmonics in the presence of strong ionization.* Phys. Rev. A, vol. 58, pages 389–399, Jul 1998.

Cited on page(s) 20

[Bourassin-Bouchet 10] C. Bourassin-Bouchet, S. de Rossi, F. Delmotte & P. Chavel. *Spatiotemporal distortions of attosecond pulses.* J. Opt. Soc. Am. A, vol. 27, no. 6, pages 1395–1403, Jun 2010.

Cited on page(s) 40, 232

[Boutu 11] W. Boutu, T. Auguste, O. Boyko, I. Sola, Ph. Balcou, L. Binazon, O. Gobert, H. Merdji, C. Valentin, E. Constant, E. Mével & B. Carré. *High-order-harmonic generation in gas with a flat-top laser beam.* Phys. Rev. A, vol. 84, page 063406, Dec 2011.

Cited on page(s) 166

[Brizuela 13] F. Brizuela, C. M. Heyl, P. Rudawski, D. Kroon, L. Rading, J. M. Dahlstrom, J. Mauritsson, P. Johnsson, C. L. Arnold & A. L'Huillier. *Efficient high-order harmonic generation boosted by below-threshold harmonics.* Sci. Rep., vol. 3, March 2013.

Cited on page(s) 139

[Brunetti 08] E. Brunetti, R. Issac & D. A. Jaroszynski. *Quantum path contribution to high-order harmonic spectra.* Phys. Rev. A, vol. 77, page 023422, Feb 2008.

Cited on page(s) 120, 132, 133

[Canova 07] F. Canova, L. Canova, J.-P. Chambaret, X. Levecq, E. Lavergne, G. Dovillaire & Thomas A. Planchon. *Wavefront correction and aberrations pre-compensation in the middle of Petawatt-class CPA laser chains.* In Lasers and Electro-Optics, 2007. CLEO 2007. Conference on, pages 1–2, May 2007.

Cited on page(s) 157

[Cao 06] W. Cao, P. Lu, P. Lan, X. Wang & G. Yang. *Single-attosecond pulse generation with an intense multicycle driving pulse.* Phys.

Rev. A, vol. 74, page 063821, Dec 2006.

Cited on page(s) 20

[Cao 12] W. Cao, G. Laurent, C. Jin, H. Li, Z. Wang, C. D. Lin, I. Ben-Itzhak & C. L. Cocke. *Spectral splitting and quantum path study of high-harmonic generation from a semi-infinite gas cell.* Journal of Physics B: Atomic, Molecular and Optical Physics, vol. 45, no. 7, page 074013, 2012.

Cited on page(s) 120

[Cavalieri 07] A. L. Cavalieri, N. Muller, Th. Uphues, V. S. Yakovlev, A. Baltuska, B. Horvath, B. Schmidt, L. Blumel, R. Holzwarth, S. Hendel, M. Drescher, U. Kleineberg, P. M. Echenique, R. Kienberger, F. Krausz & U. Heinzmann. *Attosecond spectroscopy in condensed matter.* Nature, vol. 449, no. 7165, pages 1029–1032, 2007.

Cited on page(s) 20

[Christov 96] I. P. Christov, J. Zhou, J. Peatross, A. Rundquist, M. M. Murnane & H. C. Kapteyn. *Nonadiabatic Effects in High-Harmonic Generation with Ultrashort Pulses.* Phys. Rev. Lett., vol. 77, pages 1743–1746, Aug 1996.

Cited on page(s) 142, 146, 147

[Constant 99] E. Constant, D. Garzella, P. Breger, E. Mével, Ch. Dorrer, C. Le Blanc, F. Salin & P. Agostini. *Optimizing High Harmonic Generation in Absorbing Gases: Model and Experiment.* Phys. Rev. Lett., vol. 82, pages 1668–1671, Feb 1999.

Cited on page(s) 20, 33, 51

[Constant 12] E. Constant, A. Dubrouil, O. Hort, S. Petit, D. Descamps & E. Mével. *Spatial shaping of intense femtosecond beams for the generation of high-energy attosecond pulses.* Journal of Physics B: Atomic, Molecular and Optical Physics, vol. 45, no. 7, 2012.

Cited on page(s) 168, 169, 170, 171, 172

[Corkum 93] P. B. Corkum. *Plasma perspective on strong field multiphoton ionization.* Phys. Rev. Lett., vol. 71, pages 1994–1997, Sep 1993.

Cited on page(s) 24, 32, 147

[Corkum 07] P. B. Corkum & F. Krausz. *Attosecond science*. Nature Phys., vol. 3, page 281, 2007.

Cited on page(s) 19

[Covington 11] A. M. Covington, A. Aguilar, I. R. Covington, G. Hinojosa, C. A. Shirley, R. A. Phaneuf, I. Álvarez, C. Cisneros, I. Dominguez-Lopez, M. M. Sant'Anna, A. S. Schlachter, C. P. Ballance & B. M. McLaughlin. *Valence-shell photoionization of chlorinelike Ar+ ions*. Phys. Rev. A, vol. 84, page 013413, Jul 2011.

Cited on page(s) 142

[Daboussi 13] Sameh Daboussi. *Accord de phase et quasi accord de phase en génération d'harmoniques d'ordres élevés : effet de la pression et du guidage laser*. PhD thesis, Université Paris Sud (France), 2013.

Cited on page(s) 146, 147, 150

[De Saint Denis 06] R. De Saint Denis, N. Passilly, M. Laroche, Tayeb Mohammed-Brahim & K. Ait Ameur. *Beam-shaping longitudinal range of a binary diffractive optical element*. Applied Optics, vol. 45, no. 31, pages 8136–8141, November 2006.

Cited on page(s) 166

[Drescher 02] M. Drescher, M. Hentschel, R. Kienberger, M. Uiberacker, V. Yakovlev, A. Scrinzi, Th. Westerwalbesloh, U. Kleineberg, U. Heinzmann & F. Krausz. *Time-resolved atomic inner-shell spectroscopy*. Nature, vol. 419, no. 6909, pages 803–807, 2002.

Cited on page(s) 20

[Dromey 06] B. Dromey, M. Zepf, A. Gopal, K. Lancaster, M. S. Wei, K. Krushelnick, M. Tatarakis, N. Vakakis, S. Moustaizis, R. Kodama, M. Tampo, C. Stoeckl, R. Clarke, H. Habara, D. Neely, S. Karsch & P. Norreys. *High harmonic generation in the relativistic limit*. Nat Phys, vol. 2, no. 7, pages 456–459, 2006.

Cited on page(s) 23

[Du 12] H. Du, L. Luo, X. Wang & B. Hu. *Isolated attosecond pulse generation from pre-excited medium with a chirped and chirped-free two-color field*. Opt. Express, vol. 20, no. 9, pages 9713–9725, Apr 2012.

Cited on page(s) 20

[Dubrouil 11a] A. Dubrouil, Y. Mairesse, B. Fabre, D. Descamps, S. Petit, E. Mével & E. Constant. *Controlling high harmonics generation by spatial shaping of high-energy femtosecond beam.* Opt. Lett., vol. 36, no. 13, pages 2486–2488, Jul 2011.

Cited on page(s) 166

[Dubrouil 11b] Antoine Dubrouil. *Post compression d'impulsions intenses ultra-brèves et mise en forme spatiale pour la génération d'impulsions attosecondes intenses.* PhD thesis, Université Bordeaux 1 (France), 2011.

Cited on page(s) 35, 173

[Durfee 99] C. G. Durfee, A. R. Rundquist, S. Backus, C. Herne, M. M. Murnane & H. C. Kapteyn. *Phase Matching of High-Order Harmonics in Hollow Waveguides.* Phys. Rev. Lett., vol. 83, pages 2187–2190, Sep 1999.

Cited on page(s) 20

[Feng 09] X. Feng, S. Gilbertson, H. Mashiko, H. Wang, S. D. Khan, M. Chini, Y. Wu, K. Zhao & Z. Chang. *Generation of isolated attosecond pulses with 20 to 28 femtosecond lasers.* Physical Review Letters, vol. 103, no. 18, 2009.

Cited on page(s) 20, 181

[Feng 13] C. Feng, J.-F. Hergott, P.-M. Paul, X. Chen, O. Tcherbakoff, M. Comte, O. Gobert, M. Reduzzi, F. Calegari, C. Manzoni, M. Nisoli & G. Sansone. *Complete analog control of the carrier-envelope-phase of a high-power laser amplifier.* Opt. Express, vol. 21, no. 21, pages 25248–25256, Oct 2013.

Cited on page(s) 227

[Ferrari 10] F. Ferrari, F. Calegari, M. Lucchini, C. Vozzi, S. Stagira, G. Sansone & M. Nisoli. *High-energy isolated attosecond pulses generated by above-saturation few-cycle fields.* Nature Photonics, no. 12, page 875–879, 2010.

Cited on page(s) 20, 216

[Ferray 88] M. Ferray, A. L'Huillier, X. F. Li, L. A. Lompre, G. Mainfray & C. Manus. *Multiple-harmonic conversion of 1064 nm radiation in rare gases.* Journal of Physics B: Atomic, Molecular and Optical

Physics, vol. 21, no. 3, page L31, 1988.

Cited on page(s) 19

[Fourcade-Dutin 10] C. Fourcade-Dutin, A. Dubrouil, S. Petit, E. Mével, E. Constant & D. Descamps. *Post-compression of high-energy femtosecond pulses using gas ionization.* Optics Letters, vol. 35, no. 2, pages 253–255, 2010.

Cited on page(s) 183, 186, 193, 201, 204, 205

[Frumker 12] E. Frumker, G. G. Paulus, H. Niikura, A. Naumov, D. M. Villeneuve & P. B. Corkum. *Order-dependent structure of high harmonic wavefronts.* Opt. Express, vol. 20, no. 13, pages 13870–13877, Jun 2012.

Cited on page(s) 232

[Gaarde 99] M. B. Gaarde, F. Salin, E. Constant, Ph. Balcou, K.J. Schafer, K.C. Kulander & A. L'Huillier. *Spatiotemporal separation of high harmonic radiation into two quantum path components.* Physical Review A, vol. 59, no. 2, page 1367, 1999.

Cited on page(s) 20, 70

[Gaarde 02] M. B. Gaarde & K. J. Schafer. *Quantum path distributions for high-order harmonics in rare gas atoms.* Phys. Rev. A, vol. 65, page 031406, Mar 2002.

Cited on page(s) 34, 55, 56

[Gaarde 06] M. B. Gaarde & K. J. Schafer. *Generating single attosecond pulses via spatial filtering.* Opt. Lett., vol. 31, no. 21, pages 3188–3190, Nov 2006.

Cited on page(s) 177

[Gaarde 08] M. B. Gaarde, J. L. Tate & K. J. Schafer. *Macroscopic aspects of attosecond pulse generation.* Journal of Physics B: Atomic, Molecular and Optical Physics, vol. 41, no. 13, page 132001, 2008.

Cited on page(s) 119, 135

[Gaudiosi 06] D. M. Gaudiosi, B. Reagan, T. Popmintchev, M. Grisham, M. Berrill, O. Cohen, B. C. Walker, M. M. Murnane, H. C. Kapteyn & J. J. Rocca. *High-Order Harmonic Generation from Ions in a Capillary Discharge.* Phys. Rev. Lett., vol. 96, page

203001, May 2006.

Cited on page(s) 139, 142, 146, 147

[Gibson 04] E. A. Gibson, A. Paul, N. Wagner, R. Tobey, S. Backus, I. P. Christov, M. M. Murnane & H. C. Kapteyn. *High-Order Harmonic Generation up to 250 eV from Highly Ionized Argon.* Phys. Rev. Lett., vol. 92, page 033001, Jan 2004.

Cited on page(s) 139, 142

[Goulielmakis 10] E. Goulielmakis, Z.-H. Loh, A. Wirth, R. Santra, N. Rohringer, V. S. Yakovlev, S. Zherebtsov, T. Pfeifer, A. M. Azzeer, M. F. Kling, S. R. Leone & F. Krausz. *Real-time observation of valence electron motion.* Nature, vol. 466, no. 7307, pages 739–743, August 2010.

Cited on page(s) 20

[Hamamatsu 06] Hamamatsu. *MCP assembly.* pages 6–8, 2006.

Cited on page(s) 42, 44, 72

[Hauri 05] C. P. Hauri, A. Guandalini, P. Eckle, W. Kornelis, J. Biegert & U. Keller. *Generation of intense few-cycle laser pulses through filamentation - Parameter dependence.* Optics Express, vol. 13, no. 19, pages 7541–7547, 2005.

Cited on page(s) 182

[He 09] X. He, M. Miranda, J. Schwenke, O. Guilbaud, T. Ruchon, C. Heyl, E. Georgadiou, R. Rakowski, A. Persson, M. B. Gaarde & A. L'Huillier. *Spatial and spectral properties of the high-order harmonic emission in argon for seeding applications.* Phys. Rev. A, vol. 79, page 063829, Jun 2009.

Cited on page(s) 213

[Heissler 12] P. Heissler, R. Hörlein, J. M. Mikhailova, L. Waldecker, P. Tzallas, A. Buck, K. Schmid, C. M. S. Sears, F. Krausz, L. Veisz, M. Zepf & G. D. Tsakiris. *Few-cycle driven relativistically oscillating plasma mirrors: A source of intense isolated attosecond pulses.* Physical Review Letters, vol. 108, no. 23, 2012.

Cited on page(s) 182

[Heyl 11] C. M. Heyl, J. Güdde, U. Höfer & A. L'Huillier. *Spectrally Resolved Maker Fringes in High-Order Harmonic Generation.* Phys. Rev.

Lett., vol. 107, page 033903, Jul 2011.

Cited on page(s) 55, 86, 87

[Higuet 10] Julien Higuet. *Études structurelles et dynamiques de systèmes atomiques ou moléculaires par génération d'harmoniques d'ordre élevé*. PhD thesis, Université Bordeaux 1 (France), 2010.

Cited on page(s) 24, 25, 26, 27

[Holler 09] M. Holler, A. Zaïr, F. Schapper, T. Auguste, E. Cormier, A. Wyatt, A. Monmayrant, I. A. Walmsley, L. Gallmann, P. Salières & U. Keller. *Ionization effects on spectral signatures of quantum-path interference in high-harmonic generation*. Opt. Express, vol. 17, no. 7, pages 5716–5722, Mar 2009.

Cited on page(s) 87

[Hong 11] W. Hong, Q. Zhang, X. Zhu & P. Lu. *Intense isolated attosecond pulse generation in pre-excited medium*. Opt. Express, vol. 19, no. 5, pages 4728–4739, Feb 2011.

Cited on page(s) 20

[Itatani 04] J. Itatani, J. Levesque, D. Zeidler, H. Niikura, H. Pépin, J. C. Kieffer, P. B. Corkum & D. M. Villeneuve. *Tomographic imaging of molecular orbitals*. Nature, no. 7019, page 867–871, 2004.

Cited on page(s) 19

[Jullien 08] A. Jullien, T. Pfeifer, M.J. Abel, P.M. Nagel, M.J. Bell, D.M. Neumark & S.R. Leone. *Ionization phase-match gating for wavelength-tunable isolated attosecond pulse generation*. Applied Physics B, vol. 93, no. 2-3, pages 433–442, 2008.

Cited on page(s) 20

[Kanai 12] T. Kanai, Y. Fu, Y. Kamba, S. Bohman, H. Yoshida, T. Kanai, S. Yamaguchi, E.J. Takahashi, Y. Nabekawa, A. Suda & K. Midorikawa. *Generation of Highly Phase-Matched Isolated Attosecond Pulses Using Multi-mJ, Carrier-Envelope Phase Stabilized, Few-Cycle Laser Pulses*. In Kaoru Yamanouchi & Midorikawa Katsumi, editeurs, Multiphoton Processes and Attosecond Physics, volume 125 of *Springer Proceedings in Physics*, pages 105–107. Springer Berlin Heidelberg, 2012.

Cited on page(s) 216

[Kazamias 03a] S. Kazamias, D. Douillet, F. Weihe, C. Valentin, A. Rousse, S. Sebban, G. Grillon, F. Augé, D. Hulin & Ph. Balcou. *Global Optimization of High Harmonic Generation*. Phys. Rev. Lett., vol. 90, page 193901, May 2003.

Cited on page(s) 20

[Kazamias 03b] Sophie Kazamias. *Optimisation d'une source d'harmoniques d'ordres élevés pour l'optique non-linéaire dans l'extrême UV*. PhD thesis, Ecole Polytechnique (France), 2003.

Cited on page(s) 160

[Kazamias 11] S. Kazamias, S. Daboussi, O. Guilbaud, K. Cassou, D. Ros, B. Cros & G. Maynard. *Pressure-induced phase matching in high-order harmonic generation*. Phys. Rev. A, vol. 83, page 063405, Jun 2011.

Cited on page(s) 33

[Keldysh 65] L. V. Keldysh. *Ionization in the field of a strong electromagnetic wave*. Soviet Physics JETP, vol. 20, pages 1307–1314, May 1965.

Cited on page(s) 29

[Kim 02] Jung-Hoon Kim & Chang Hee Nam. *Plasma-induced frequency chirp of intense femtosecond lasers and its role in shaping high-order harmonic spectral lines*. PHYSICAL REVIEW A, vol. 65, page 033801, 2002.

Cited on page(s) 135

[Krausz 09] F. Krausz & M.Yu. Ivanov. *Attosecond physics*. Rev. Mod. Phys., vol. 81, pages 163–234, Feb 2009.

Cited on page(s) 19

[Kruse 10] J. E. Kruse, P. Tzallas, E. Skantzakis, C. Kalpouzos, G. D. Tsakiris & D. Charalambidis. *Inconsistencies between two attosecond pulse metrology methods: A comparative study*. Phys. Rev. A, vol. 82, page 021402, Aug 2010.

Cited on page(s) 232

[Lambert 08] G. Lambert, T. Hara, D. Garzella, T. Tanikawa, M. Labat, B. Carre, H. Kitamura, T. Shintake, M. Bougeard, S. Inoue, Y. Tanaka, P. Salieres, H. Merdji, O. Chubar, O. Gobert,

K. Tahara & M.-E. Couprie. *Injection of harmonics generated in gas in a free-electron laser providing intense and coherent extreme-ultraviolet light.* Nat Phys, vol. 4, no. 4, pages 296–300, April 2008.

Cited on page(s) 139

[Lefaudeux 12] N. Lefaudeux, X. Levecq, G. Dovillaire, S. Theis & L. Escolano. *New deformable mirror technology and associated control strategies for ultrahigh intensity laser beam corrections and optimizations*, 2012.

Cited on page(s) 157

[Lewenstein 94] M. Lewenstein, Ph. Balcou, M. Yu. Ivanov, Anne L'Huillier & P. B. Corkum. *Theory of high-harmonic generation by low-frequency laser fields.* Phys. Rev. A, vol. 49, pages 2117–2132, Mar 1994.

Cited on page(s) 31

[Lewenstein 95] M. Lewenstein, P. Salières & A. L'Huillier. *Phase of the atomic polarization in high-order harmonic generation.* Phys. Rev. A, vol. 52, pages 4747–4754, Dec 1995.

Cited on page(s) 31

[Lide 07] D. R. Lide. CRC Handbook of Chemistry and Physics, 88th Edition (CRC Handbook of Chemistry & Physics). CRC Press, 88 edition, June 2007.

Cited on page(s) 28

[Mairesse 05] Y. Mairesse & F. Quéré. *Frequency-resolved optical gating for complete reconstruction of attosecond bursts.* Phys. Rev. A, vol. 71, page 011401, Jan 2005.

Cited on page(s) 232

[Marcatili 64] E.A.J. Marcatili & R.A. Schmeltzer. *Hollow Metallic and Dielectric Waveguides for Long Distance Optical Transmission and lasers.* Bell System Technical Journal, vol. 43, no. 4P2, pages 1783+, 1964.

Cited on page(s) 142, 195

[McPherson 87] A. McPherson, G. Gibson, H. Jara, U. Johann, T. S. Luk, I. A. McIntyre, K. Boyer & C. K. Rhodes. *Studies of multiphoton production of vacuum-ultraviolet radiation in the rare gases.* J. Opt.

Soc. Am. B, vol. 4, no. 4, pages 595–601, Apr 1987.
Cited on page(s) 19

[Morlens 06] A.-S. Morlens, J. Gautier, G. Rey, P. Zeitoun, J.-P. Caumes, M. Kos-Rosset, H. Merdji, S. Kazamias, K. Cassou & M. Fajardo. *Submicrometer digital in-line holographic microscopy at 32 nm with high-order harmonics.* Opt. Lett., vol. 31, no. 21, pages 3095–3097, Nov 2006.
Cited on page(s) 19

[Mulser 10] P. Mulser & D. Bauer. *The Laser Plasma: Basic Phenomena and Laws.* In High Power Laser-Matter Interaction, volume 238, page 39. Springer Berlin Heidelberg, Berlin, Heidelberg, 2010.
Cited on page(s) 184

[Mével 00] E. Mével, E. Constant, D. Garzella, P. Breger, C. Dorrer, C. Le Blanc, F. Salin & P. Agostini. *Optimizing high order harmonic generation in absorbing gases.* Multiphoton Processes: ICOMP 8th Proc., page 373, 2000.
Cited on page(s) 20

[Nikolopoulos 05] L. A. A. Nikolopoulos, E. P. Benis, P. Tzallas, D. Charalambidis, K. Witte & G. D. Tsakiris. *Second Order Autocorrelation of an XUV Attosecond Pulse Train.* Phys. Rev. Lett., vol. 94, page 113905, Mar 2005.
Cited on page(s) 232

[Nisoli 96] M. Nisoli, S. De Silvestri & O. Svelto. *Generation of high energy 10 fs pulses by a new pulse compression technique.* Applied Physics Letters, vol. 68, no. 20, page 2793, 1996.
Cited on page(s) 149, 182

[Nugent-Glandorf 01] L. Nugent-Glandorf, M. Scheer, D. A. Samuels, A. M. Mulhisen, E. R. Grant, X. Yang, V. M. Bierbaum & S. R. Leone. *Ultrafast time-resolved soft x-ray photoelectron spectroscopy of dissociating Br2.* Phys Rev Lett, vol. 87, no. 19, page 193002, Nov 2001.
Cited on page(s) 19

[Papadogiannis 03] N. A. Papadogiannis, L. A. A. Nikolopoulos, D. Charalambidis, G. D. Tsakiris, P. Tzallas & K. Witte. *Two-Photon Ionization*

of He through a Superposition of Higher Harmonics. Phys. Rev. Lett., vol. 90, page 133902, Apr 2003.

Cited on page(s) 19

[Paul 01] P. M. Paul, E. S. Toma, P. Breger, G. Mullot, F. Augé, Ph. Balcou, H. G. Muller & P. Agostini. *Observation of a Train of Attosecond Pulses from High Harmonic Generation.* Science, vol. 292, no. 5522, pages 1689–1692, 2001.

Cited on page(s) 38, 232

[Pfeifer 07] T. Pfeifer, A. Jullien, M. J. Abel, P. M. Nagel, L. Gallmann, D. M. Neumark & S. R. Leone. *Generating coherent broadbandcontinuum soft-x-ray radiation byattosecond ionization gating.* Opt. Express, vol. 15, no. 25, pages 17120–17128, Dec 2007.

Cited on page(s) 20

[Quéré 06] F. Quéré, C. Thaury, P. Monot, S. Dobosz, Ph. Martin, J.-P. Geindre & P. Audebert. *Coherent Wake Emission of High-Order Harmonics from Overdense Plasmas.* Phys. Rev. Lett., vol. 96, page 125004, Mar 2006.

Cited on page(s) 23

[Rundquist 98] A. Rundquist, C. G. Durfee, Z. Chang, C. Herne, S. Backus, M. M. Murnane & H. C. Kapteyn. *Phase-Matched Generation of Coherent Soft X-rays.* Science, vol. 280, no. 5368, pages 1412–1415, 1998.

Cited on page(s) 20, 50

[Salières 95] P. Salières, A. L'Huillier & M. Lewenstein. *Coherence Control of High-Order Harmonics.* Phys. Rev. Lett., vol. 74, pages 3776–3779, May 1995.

Cited on page(s) 153

[Sansone 06] G. Sansone, E. Benedetti, F. Calegari, C. Vozzi, L. Avaldi, R. Flammini, L. Poletto, P. Villoresi, C. Altucci, R. Velotta, S. Stagira, S. De Silvestri & M. Nisoli. *Isolated Single-Cycle Attosecond Pulses.* Science, vol. 314, no. 5798, pages 443–446, 2006.

Cited on page(s) 232

[Sansone 10] G. Sansone, F. Kelkensberg, J. F. Perez-Torres, F. Morales, M. F. Kling, W. Siu, O. Ghafur, P. Johnsson, M. Swo-

boda, E. Benedetti, F. Ferrari, F. Lepine, J. L. Sanz-Vicario, S. Zherebtsov, I. Znakovskaya, A. L/'Huillier, M. Yu. Ivanov, M. Nisoli, F. Martin & M. J. J. Vrakking. *Electron localization following attosecond molecular photoionization.* Nature, vol. 465, no. 7299, pages 763–766, 2010.

Cited on page(s) 20

[Schafer 93] K. J. Schafer, Baorui Yang, L. F. DiMauro & K. C. Kulander. *Above threshold ionization beyond the high harmonic cutoff.* Phys. Rev. Lett., vol. 70, pages 1599–1602, Mar 1993.

Cited on page(s) 24

[Schapper 10] F. Schapper, M. Holler, T. Auguste, A. Zaïr, M. Weger, P. Salières, L. Gallmann & U. Keller. *Spatial fingerprint of quantum path interferences in high order harmonic generation.* Opt. Express, vol. 18, no. 3, pages 2987–2994, Feb 2010.

Cited on page(s) 87

[Schnürer 98] M. Schnürer, Z. Cheng, S. Sartania, M. Hentschel, G. Tempea, T. Brabec & F. Krausz. *Guiding and high-harmonic generation of sub-10-fs pulses in hollow-core fibers at 1015 W/cm2.* Applied Physics B, vol. 67, no. 2, pages 263–266, 1998.

Cited on page(s) 142

[Schultze 10] M. Schultze, M. Fieß, N. Karpowicz, J. Gagnon, M. Korbman, M. Hofstetter, S. Neppl, A. L. Cavalieri, Y. Komninos, Th. Mercouris, C. A. Nicolaides, R. Pazourek, S. Nagele, J. Feist, J. Burgdörfer, A. M. Azzeer, R. Ernstorfer, R. Kienberger, U. Kleineberg, E. Goulielmakis, F. Krausz & V. S. Yakovlev. *Delay in Photoemission.* Science, vol. 328, no. 5986, pages 1658–1662, 2010.

Cited on page(s) 20

[Sekikawa 04] T. Sekikawa, A. Kosuge, T. Kanai & S. Watanabe. *Nonlinear optics in the extreme ultraviolet.* Nature, vol. 432, no. 7017, page 605, 2004.

Cited on page(s) 20

[Shafir 12] D. Shafir, H. Soifer, B. D. Bruner, M. Dagan, Y. Mairesse, S. Patchkovskii, M. Y. Ivanov, O. Smirnova & N. Dudovich. *Re-*

solving the time when an electron exits a tunnelling barrier. Nature, vol. 485, no. 7398, pages 343–346, May 2012.

Cited on page(s) 32

[Stavros 05] V. G. Stavros, E. Harel & S. R. Leone. *The influence of intense control laser pulses on homodyne-detected rotational wave packet dynamics in O2 by degenerate four-wave mixing.* J. Chem. Phys., vol. 122, page 064301, 2005.

Cited on page(s) 19

[Strelkov 06a] V. V. Strelkov. *Theory of high-order harmonic generation and attosecond pulse emission by a low-frequency elliptically polarized laser field.* Phys. Rev. A, vol. 74, page 013405, Jul 2006.

Cited on page(s) 56, 222

[Strelkov 06b] V. V. Strelkov, A. F. Sterjantov, N. Yu. Shubin & V. T. Platonenko. *XUV generation with several-cycle laser pulse in barrier-suppression regime.* Journal of Physics B: Atomic, Molecular and Optical Physics, vol. 39, no. 3, page 577, 2006.

Cited on page(s) 224

[Strelkov 08] V. V. Strelkov, E. Mével & E. Constant. *Generation of isolated attosecond pulses by spatial shaping of a femtosecond laser beam.* New Journal of Physics, vol. 10, no. 8, page 083040, 2008.

Cited on page(s) 166, 178, 232

[Strelkov 09] V. V.F Strelkov, E. Mével & E. Constant. *Isolated attosecond pulse generated by spatial shaping of femtosecond laser beam.* European Physical Journal: Special Topics, vol. 175, no. 1, pages 15–20, 2009.

Cited on page(s) 166, 178, 181

[Strickland 85] D. Strickland & G. Mourou. *Compression of amplified chirped optical pulses.* Optics Communications, vol. 55, no. 6, page 447–449, 1985.

Cited on page(s) 182

[Takahashi 13] E. J. Takahashi, P. Lan, O. D. Mücke, Y. Nabekawa & K. Midorikawa. *Attosecond nonlinear optics using gigawatt-scale isolated attosecond pulses.* Nature Communications, pages –, 2013.

Cited on page(s) 20

[Tavella 07] F. Tavella, Y. Nomura, L. Veisz, V. Pervak, A. Marcinkevičius & F. Krausz. *Dispersion management for a sub-10-fs, 10 TW optical parametric chirped-pulse amplifier.* Optics Letters, vol. 32, no. 15, pages 2227–2229, 2007.

Cited on page(s) 182

[Tempea 98] G. Tempea & T. Brabec. *Theory of self-focusing in a hollow waveguide.* Optics Letters, vol. 23, no. 10, pages 762–764, 1998.

Cited on page(s) 182, 183, 203

[Tong 05] X. M. Tong & C. D. Lin. *Empirical formula for static field ionization rates of atoms and molecules by lasers in the barrier-suppression regime.* Journal of Physics B: Atomic, Molecular and Optical Physics, vol. 38, no. 15, page 2593, 2005.

Cited on page(s) 57

[Tosa 05] V. Tosa, H. T. Kim, I. J. Kim & C. H. Nam. *High-order harmonic generation by chirped and self-guided femtosecond laser pulses. II. Time-frequency analysis.* Phys. Rev. A, vol. 71, page 063808, Jun 2005.

Cited on page(s) 129

[Tosa 09] V. Tosa, K. T. Kim & C. H. Nam. *Macroscopic generation of attosecond-pulse trains in strongly ionized media.* Phys. Rev. A, vol. 79, page 043828, Apr 2009.

Cited on page(s) 119

[Uiberacker 07] M. Uiberacker, Th. Uphues, M. Schultze, A. J. Verhoef, V. Yakovlev, M. F. Kling, J. Rauschenberger, N. M. Kabachnik, H. Schroder, M. Lezius, K. L. Kompa, H.-G. Muller, M. J. J. Vrakking, S. Hendel, U. Kleineberg, U. Heinzmann, M. Drescher & F. Krausz. *Attosecond real-time observation of electron tunnelling in atoms.* Nature, vol. 446, no. 7136, pages 627–632, April 2007.

Cited on page(s) 20

[Wahlström 93] C.-G. Wahlström, J. Larsson, A. Persson, T. Starczewski, S. Svanberg, P. Salières, Ph. Balcou & Anne L'Huillier. *High-order harmonic generation in rare gases with an intense short-pulse laser.*

Phys. Rev. A, vol. 48, pages 4709–4720, Dec 1993.
Cited on page(s) 55

[Wang 08] Y. Wang, E. Granados, F. Pedaci, D. Alessi, B. Luther, M. Berrill & J. J. Rocca. *Phase-coherent, injection-seeded, table-top soft-X-ray lasers at 18.9 nm and 13.9 nm.* Nat Photon, vol. 2, no. 2, pages 94–98, 2008.
Cited on page(s) 139

[Watanabe 94] S. Watanabe, K. Kondo, Y. Nabekawa, A. Sagisaka & Y. Kobayashi. *Two-Color Phase Control in Tunneling Ionization and Harmonic Generation by a Strong Laser Field and Its Third Harmonic.* Phys. Rev. Lett., vol. 73, pages 2692–2695, Nov 1994.
Cited on page(s) 139

[Wu 13] Y. Wu, E. Cunningham, H. Zang, J. Li, M. Chini, X. Wang, Y. Wang, K. Zhao & Z. Chang. *Generation of high-flux attosecond extreme ultraviolet continuum with a 10 TW laser.* Applied Physics Letters, vol. 102, no. 20, pages –, 2013.
Cited on page(s) 216

[Xu 08] H. Xu, H. Xiong, Z. Zeng, Y. Fu, J. Yao, R. Li, Y. Cheng & Z. Xu. *Fine interference fringes formed in high-order harmonic spectra generated by infrared driving laser pulses.* Phys. Rev. A, vol. 78, page 033841, Sep 2008.
Cited on page(s) 87

[Zaïr 08] A. Zaïr, M. Holler, A. Guandalini, F. Schapper, J. Biegert, L. Gallmann, U. Keller, A. S. Wyatt, A. Monmayrant, I. A. Walmsley, E. Cormier, T. Auguste, J. P. Caumes & P. Salières. *Quantum Path Interferences in High-Order Harmonic Generation.* Phys. Rev. Lett., vol. 100, page 143902, Apr 2008.
Cited on page(s) 87, 134

[Zeitoun 04] Ph. Zeitoun, G. Faivre, S. Sebban, T. Mocek, A. Hallou, M. Fajardo, D. Aubert, Ph. Balcou, F. Burgy, D. Douillet, S. Kazamias, G. de Lacheze-Murel, T. Lefrou, S. le Pape, P. Mercere, H. Merdji, A. S. Morlens, J. P. Rousseau & C. Valentin. *A high-intensity highly coherent soft X-ray femtosecond laser seeded by a high harmonic beam.* Nature, vol. 431, no. 7007, pages 426–429, September

2004.

Cited on page(s) 139

[Zepf 07] M. Zepf, B. Dromey, M. Landreman, P. Foster & S. M. Hooker. *Bright Quasi-Phase-Matched Soft-X-Ray Harmonic Radiation from Argon Ions.* Phys. Rev. Lett., vol. 99, page 143901, Oct 2007.

Cited on page(s) 140, 142, 146, 147

[Zhao 12] K. Zhao, Q. Zhang, M. Chini, Y. Wu, X. Wang & Z. Chang. *Tailoring a 67 attosecond pulse through advantageous phase-mismatch.* Opt. Lett., vol. 37, no. 18, pages 3891–3893, Sep 2012.

Cited on page(s) 20

[Zhong 02] F. Zhong, Z. Li, Z. Zeng, Z. Zhang, R. Li & Z. Xu. *Spectral splitting of high-order harmonic emissions from ionizing gases.* Phys. Rev. A, vol. 65, page 033808, Feb 2002.

Cited on page(s) 213

Appendix A

Diffraction simulation

To calculate an arbitrary beam propagation numerically let's consider following scheme (fig. A.1).

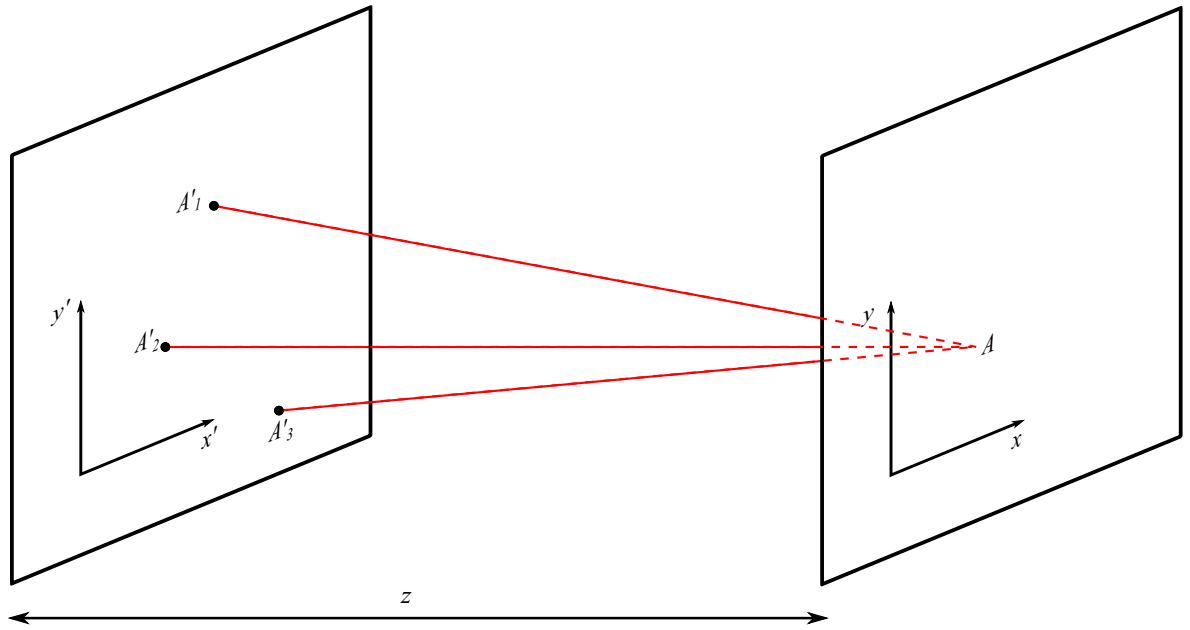

Figure A.1 – Schematic principle of beam propagation simulation. The source plane and the observation plane are separated with a distance z. Electric field in each point A of the observation plane equals a sum of electric fields propagated on the distance $\sqrt{z^2+(x-x')^2+(y-y')^2}$ of all points A'_n of the source plane divided by a normalizing factor. n denotes the number of points in source plane.

For every frequency component of ultrashort pulse electric field we can define its spatial distribution at source plane ($z = 0$) that projects to the distant plane electric field spatial distribution. Every point of the source plane is expected to emit to every point of the observation plane. Thus the observation plane is filled with coherent sums of source field averaged in amplitude. Because of paraxial approximation all of the field components have

the same weight and the resulting field can be expressed as

$$\mathcal{E}(x,y,z) = \frac{1}{n}\sum_{x'}\sum_{y'}\mathcal{E}'(x',y')\, e^{ik\left((x-x')^2+(y-y')^2+z^2\right)}$$

where the double sum has to be calculated for every x' and y' that is computationally extremely heavy and time consuming.

Alternative approach to calculate a beam diffraction is to use the Fresnel integral that reads

$$\mathcal{E}(x,y,z) = -\frac{ik}{2\pi z}e^{ikz}\iint \mathcal{E}'(x',y')\, e^{ik\frac{(x-x')^2+(y-y')^2}{2z}}\mathrm{d}x'\mathrm{d}y'$$

where the phase term in the integral can be expanded to

$$e^{ik\frac{(x-x')^2+(y-y')^2}{2z}} = e^{ik\frac{x^2-2xx'+x'^2+y^2-2yy'+y^2}{2z}} = e^{ik\frac{x^2+y^2}{2z}}e^{ik\frac{x'^2+y'^2}{2z}}e^{-ik\frac{xx'+yy'}{z}}$$

where only first term can be put in front of integral. So the electric field in the observation plane xy at the distance z from the source plane can be expressed as

$$\mathcal{E}(x,y,z) = -\frac{ik}{2\pi z}e^{ikz}e^{ik\frac{x^2+y^2}{2z}}\iint \mathcal{E}'(x',y')\, e^{ik\frac{x'^2+y'^2}{2z}}e^{-ik\frac{xx'+yy'}{z}}\mathrm{d}x'\mathrm{d}y' \tag{A.1}$$

This still contains 4 variables x, y, x', y'. To proceed in simplification we will assumed that the source is symmetrical with the optical axis of beam propagation acting as the axis of symmetry. This is justified assuming a Gaussian beam with no asymmetric aberrations and clipped by a centered circular aperture. So we transform from Cartesian to polar coordinates using transform relations

$$\begin{aligned} x' &= \rho'\cos\theta \\ y' &= \rho'\sin\theta \\ \frac{kx}{z} &= \rho\cos\phi \\ \frac{ky}{z} &= \rho\sin\phi \end{aligned}$$

and hence

$$\begin{aligned} \rho' &= \sqrt{x'^2+y'^2} \\ \rho &= \frac{k}{z}\sqrt{x^2+y^2} \end{aligned}$$

Substitution into equation A.1 and using $\cos\phi\cos\theta+\sin\phi\sin\theta=\cos(\theta-\phi)$ gives

$$\mathcal{E}(\rho,z)=-\frac{ik}{2\pi z}e^{ikz}e^{i\frac{\rho^2 z}{2k}}\int_0^\infty \rho'\mathcal{E}'(\rho')\,\mathrm{e}^{\mathrm{ik}\frac{\rho'^2}{2z}}\mathrm{d}\rho'\int_0^{2\pi}\mathrm{d}\theta e^{-ik\frac{\rho\cos\phi z\rho'\cos\theta+\rho\sin\phi z\rho'\sin\theta}{kz}}$$

$$\mathcal{E}(\rho,z)=-\frac{ik}{2\pi z}e^{ikz}e^{i\frac{\rho^2 z}{2k}}\int_0^\infty \rho'\mathcal{E}'(\rho')\,\mathrm{e}^{\mathrm{ik}\frac{\rho'^2}{2z}}\mathrm{d}\rho'\int_0^{2\pi}\mathrm{d}\theta e^{-i\rho\rho'\cos(\theta-\phi)}$$

$$\mathcal{E}(\rho,z)=-\frac{ik}{z}e^{ikz}e^{i\frac{\rho^2 z}{2k}}\int_0^\infty \rho'\mathcal{E}'(\rho')\,\mathrm{e}^{\mathrm{ik}\frac{\rho'^2}{2z}}\mathrm{J}_0(\rho\rho')\,\mathrm{d}\rho'$$

where we have used $\int_0^{2\pi}\mathrm{d}\theta e^{-i\rho\rho'\cos(\theta-\phi)}=2\pi J_0(\rho\rho')$. J_0 is the Bessel function of the first kind and zeroth order.

So we have reduced a 4-dimensional problem of variables x',y',x,y to 2-dimensional problem (ρ',ρ).

When using MATLAB to perform the calculation one can use MATLAB built-in functions as `besselj` for Bessel function of the first kind and `integral`[1] for the numerical integration. The `integral` function calculates the integral using global adaptive quadrature and default error tolerances. The main advantage is a very fast convergence of the method and short runtime.

[1]The `integral` function is available in MATLAB version R2012a and newer.